



Technische Universität München
TUM School of Engineering and Design

Cell-Level Improvement Strategies for Large-Scale Implementation of Hydrogen Production by PEM Water Electrolysis

Dipl.-Ing. Univ. Maximilian Christopher Möckl

Vollständiger Abdruck der von der TUM School of Engineering and Design der
Technischen Universität München zur Erlangung des akademischen Grades eines

Doktors der Ingenieurwissenschaften (Dr.-Ing.)

genehmigten Dissertation.

Vorsitz: Prof. Dr.-Ing. Harald Klein
Prüfer der Dissertation: 1. Prof. Dr.-Ing. Andreas Jossen
2. Prof. Dr.-Ing. Hartmut Spliethoff

Die Dissertation wurde am 28.06.2022 bei der Technischen Universität München eingereicht und
durch die TUM School of Engineering and Design am 14.03.2023 angenommen.

Abstract

For the future use of proton exchange membrane water electrolysis (PEMWE) for large-scale hydrogen production with renewable electricity, two improvement measures at cell level are indispensable: First, the use of thin membranes for high current and power densities, and second, the use of improved oxygen evolution reaction (OER) catalysts which allow for reduced iridium loadings ($\text{mg}_{\text{Ir}}/\text{cm}^2$). The combination of these two measures will enable to reach sufficiently low power-specific iridium loadings ($\text{g}_{\text{Ir}}/\text{kW}$) to circumvent an iridium shortage due to a possible massive expansion of PEMWE. In this context, several issues need to be investigated for the practical applicability of the described concept. At first, the basic suitability of PEMWE for the reduction of greenhouse gas emissions in comparison with fossil hydrogen production and the positive influence of an increase in power density will be demonstrated by means of a life cycle analysis. Subsequently, the technical feasibility of using very thin membranes down to $30\ \mu\text{m}$ in PEMWE will be investigated experimentally and thermal limitations at high current densities will be verified. Peak values in the laboratory up to $25\ \text{A}/\text{cm}^2$ are achievable, a long-term technical application up to $10\ \text{A}/\text{cm}^2$ seems possible. In addition, the influence of high current densities on hydrogen permeation in PEMWE cells is investigated. A strong increase of the permeation at high current densities for low cathode pressures is shown, for higher pressures the increase is moderate. It follows that the integration of recombination catalysts is necessary for most applications when thin membranes are used. Furthermore, the degradation of iridium-based OER catalysts is found to be very low for uninterrupted operation and even with approximately eight times lower iridium loadings, high lifetimes in the range of 10^4 to 10^5 h should be possible with tailored catalyst designs.

Kurzfassung

Für den zukünftigen Einsatz von Protonenaustauschmembran-Wasserelektrolyse (PEMWE) zur großskaligen Wasserstoffproduktion mit erneuerbarem Strom sind zwei Verbesserungsmaßnahmen auf Zellebene unverzichtbar: Zum einen der Einsatz von dünnen Membranen für hohe Strom- und Leistungsdichten sowie zum anderen die Verwendung von verbesserten Sauerstoffevolutionsreaktions-(OER) Katalysatoren, die verringerte Iridiumbeladungen ($\text{mg}_{\text{Ir}}/\text{cm}^2$) erlauben. Die Kombination dieser beiden Maßnahmen ermöglicht ausreichend niedrige leistungsspezifische Iridiumbeladungen ($\text{g}_{\text{Ir}}/\text{kW}$) um eine Iridiumverknappung durch einen möglichen massiven Ausbau der PEMWE zu umgehen. In diesem Zusammenhang müssen mehrere Punkte für die praktische Anwendbarkeit des geschilderten Konzepts untersucht werden. Die grundsätzliche Eignung der PEMWE zur Verringerung von Treibhausgasemissionen im Vergleich mit fossiler Wasserstoffproduktion und der positive Einfluss einer Steigerung der Leistungsdichte wird mittels einer Lebenszyklusanalyse nachgewiesen. Anschließend wird die technische Umsetzbarkeit des Einsatzes von sehr dünnen Membranen bis $30\ \mu\text{m}$ in PEMWE untersucht und thermische Limitierungen bei hohen Stromdichten überprüft. Spitzenwerte im Labor bis $25\ \text{A}/\text{cm}^2$ sind erzielbar, ein langfristiger technischer Einsatz bis $10\ \text{A}/\text{cm}^2$ erscheint möglich. Ferner wird der Einfluss hoher Stromdichten auf die Wasserstoffpermeation in PEMWE Zellen untersucht. Es zeigt sich ein starker Anstieg der Permeation bei hohen Stromdichten für niedrige Kathodendrücke, für höhere Drücke ist der Anstieg moderat. Daraus folgt, dass eine Integration von Rekombinationskatalysatoren beim Einsatz von dünnen Membranen in den meisten Einsatzbereichen notwendig sein wird. Weiters zeigt sich, dass die Degradation von Iridium-basierten OER Katalysatoren bei ununterbrochenem Betrieb sehr gering ist und auch bei ungefähr achtfach niedrigerer Beladung mit angepasstem Katalysatordesign hohe Lebensdauern im Bereich von 10^4 bis 10^5 h möglich sein sollten.

Contents

Abstract	II
Kurzfassung	III
List of Acronyms	V
List of Symbols	VI
1 Introduction	1
2 Theory of Proton Exchange Membrane Water Electrolysis	4
2.1 Overview Functional Principle	4
2.2 Membrane	8
2.3 Electrodes and Catalysts	13
2.4 Porous Transport Layers	14
2.5 Flow Fields and Bipolar Plates	16
2.6 Thermodynamics and Reversible Cell Voltage	17
2.7 Cell Voltage and Efficiency during Operation	18
2.8 Operation Characteristics	24
3 Main Research Questions	33
4 Methods & Experimental Techniques	34
4.1 Electrode and MEA Preparation	34
4.2 Electrochemical Cells & Stacks	35
4.3 Test Environment	37
4.4 Electrochemical Test Procedures	39
4.5 Additional Methods	42
5 Results	43
5.1 Life Cycle Assessment of Hydrogen from Proton Exchange Membrane Water Electrolysis in Future Energy Systems	43
5.2 Proton Exchange Membrane Water Electrolysis at High Current Densities: Investigation of Thermal Limitations	56
5.3 Analysis of Gas Permeation Phenomena in a PEM Water Electrolyzer Operated at High Pressure and High Current Density	69
5.4 On the Limitations in Assessing Stability of Oxygen Evolution Catalysts Using Aqueous Model Electrochemical Cells	83
5.5 Durability Testing of Low-Iridium PEM Water Electrolysis Membrane Electrode Assemblies	94
6 Conclusion	108
References	111
Acknowledgments	121

List of Acronyms

ATO	antimony doped tin oxide
BOL	begin of life
BOP	balance of plant
CAPEX	capital expenditures
EIS	electrochemical impedance spectroscopy
GDL	gas diffusion layer
HER	hydrogen evolution reaction
HHV	higher heating value
IEA	international energy agency
LEL	lower explosive limit
LHV	lower heating value
MEA	membrane electrode assembly
NTO	niobium doped titanium oxide
OER	oxygen evolution reaction
PEMWE	proton exchange membrane water electrolysis
PFSA	perfluorosulfonic acid
PGM	platinum group metal
PV	photovoltaics
PTFE	polytetrafluoroethylene
PTL	porous transport layer
SEM	scanning electron microscope
SHE	standard hydrogen electrode

List of Symbols

Constants

F	Faraday's constant	96485 C/mol
R	universal gas constant	8.3145 J/(mol K)

Greek symbols

$\alpha_{a/c}$	anodic/cathodic charge transfer coefficient	(-)
Δ	difference of a physical value	(-)
ΔE	overpotential	V
η	efficiency	(-)
H	Henry coefficient of solubility	mol/(l bar)
ϑ	temperature	°C
λ	membrane water content	mol _{H₂O} /mol _{SO₃H}
ν	ratio	(-)
ρ	density	g/cm ³
σ	electrical conductivity	S/m

Latin symbols

a	thermodynamic activity	mol/l
D	permeation coefficient	(mol μ m)/(cm ² s bar)
E	potential	V
E_a	specific activation energy	kJ/mol
EW	membrane equivalent weight	g/mol _{SO₃H}
G	Gibbs free energy	kJ/mol
H	enthalpy	kJ/mol
i	current density	A/cm ²
i_0	exchange current density	A/cm ²
I	current	A
k	permeation coefficient prefactor	(mol μ m)/(cm ² s bar)
m	mass	g
M	molar mass	g/mol
n	molar quantity	mol
p	pressure	bar
P	power	W
R	area specific resistance	Ω cm ²
rf	roughness factor	cm ² _{metal} /cm ² _{geometric}
S	entropy	kJ/mol
t	thickness	μ m
T	temperature	K
x	volumetric share	(-)
z	number of electrons transported per molecule reacted	(-)

Subscripts

act	referring to activation
an	referring to the anode
aniso	referring to anisotropy only in through-plane direction
cath	referring to the cathode
cell	referring to the electrolysis cell
dry	referring to the dry state
el	referring to electricity
eo	referring to electroosmosis
f	referring to / abbreviation for faradaic
HER	referring to the hydrogen evolution reaction
HHV	referring to the higher heating value of hydrogen
in	referring to a cell/stack inlet port
iso	referring to isotropy
LHV	referring to the lower heating value of hydrogen
m	referring to the membrane
OER	referring to the oxygen evolution reaction
ohm	referring to ohmic resistances
out	referring to a cell/stack outlet port
perm	referring to permeation
PEMWE	referring to the PEMWE system
produced	referring to a produced quantity
rev	referring to reversibility
s	referring to saturation
tn	referring to thermoneutrality
tr	referring to transport resistances
wet	referring to the wet state
wb	referring to a water-bound process

1 Introduction

The rapid development of mankind, especially during the last 200 years, both in terms of population and technology, has led to an enormous increase in energy consumption on earth by humans. According to a recent report by the International Energy Agency (IEA), the global energy consumption in 2018 was 166,500 TWh [1]. This very large number becomes more tangible when divided by the number of fellow citizens on earth ($7.6 \cdot 10^9$ [1]) which results in an average per capita consumption of ≈ 22 MWh per year. This, in turn, is approximately the thermal energy released when burning 2200 liter of Diesel or the average yearly heating energy consumption for a large single-family house with ≈ 170 m² living space in Germany [2] or roughly the amount of Kerosene burnt per passenger during 5 intercontinental flights of ≈ 12.000 km [3]. Nevertheless, there is a clear regional disparity between higher and lesser developed countries. At the moment, the vast majority (133,200 TWh or ≈ 80 %) of the energy used comes from fossil sources such as coal, oil and gas. However, this is associated with high CO₂ emissions that continue to accumulate in the atmosphere, affecting the Earth's radiative heat balance. The resulting global climate change and its implications are forcing society to react quickly if extremely far-reaching consequences for mankind and the environment are to be avoided. In this context, the 2015 Paris climate agreement adopted a maximum warming target of 1.5 to 2 °C by the end of the 21st century [4]. To reach this goal, the CO₂ emissions need to be cut very fast and significant and a net zero CO₂ emission status has to be reached until the mid of the 21st century [5]. This poses a strong need to transform our current mostly fossil based energy system towards a system that uses mainly renewable sources. An inherent characteristic of renewable energy sources such as wind power and photovoltaics (PV) is their volatility. Thus, when renewable sources make up a very high proportion of a power system, intermediate storage is required to compensate for periods of low supply. Since the primary form of energy from renewable sources is electric power, electrical energy storage would be particularly well suited for this purpose and would enable to keep a high share of the exergy during storage. However, electrical energy storage devices such as batteries also have disadvantages: For very large amounts of energy, the amount of storage material required also becomes very large and heavy as the specific energy density is usually below 200 Wh/kg [6], which can limit availability and usability. Furthermore, with most electrical energy storage systems, the relatively low gravimetric energy density means that transport of stored energy over long distances, to use it decoupled in time and location from production, is usually not economical. At least a spacial decoupling is possible by electric grids. However, electric grids are not economic over very long distances [7]. Here, energy storage and transport based on chemical energy, especially in the form of hydrogen are advantageous. Hydrogen can be produced by electrolysis from purified water alone and has the highest gravimetric energy density of all materials on earth (≈ 33 kWh/kg (LHV)). Also the volumetric energy density stays relatively high if high pressures, liquefied hydrogen or other forms of chemical storage are used (e.g. Ammonia) [8] which in turn facilitates the use of bulk transport, for example by ships. Thus, a production at a site with optimum renewable energy yield at low cost and subsequent storage and transport to a consumer also over long distances is technically possible with hydrogen and can offer economic benefits [9]. Furthermore, the hydrogen can be used in many different sectors of the energy system (figure 1). In particular, as a fuel for long-distance and heavy-duty transport, for industry as a basic material or reducing agent, and, if hydrogen production costs are low enough, also for reconversion into electricity or for heating applications.

However, for widespread use of hydrogen technologies, the power required for the energy converters (i.e., on the production side, the electrolyzers) is very large. Since our current energy system

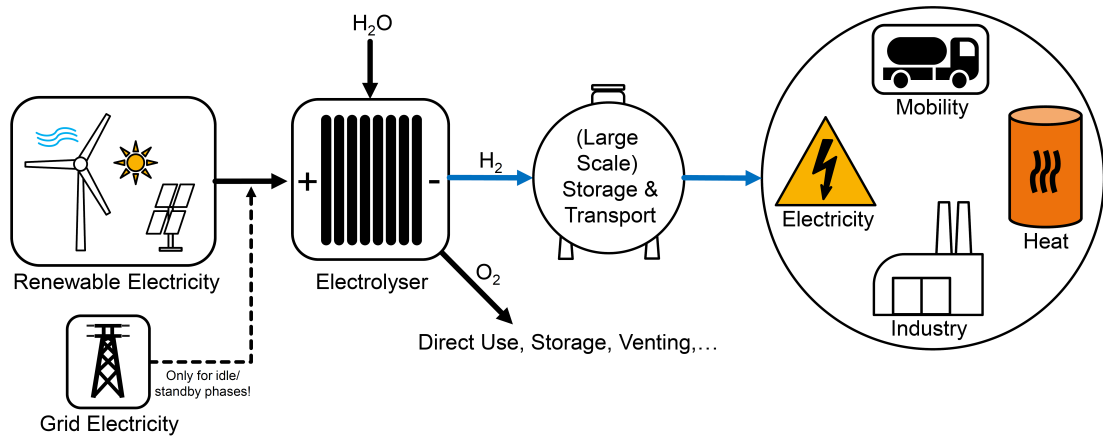


Figure 1: Principle use case scheme for hydrogen production by water electrolysis and subsequent usage of the hydrogen in different sectors.

is multi-layered, it is reasonable to consider only one sector for an initial estimate of the required power. For the global mobility sector alone, Bernt et al. [10] estimated an annual primary energy demand of 10^{20} joules. If this complete energy demand is to be provided by electrolytic hydrogen (700 Mt/y), the authors indicate a necessary annual installation of 150 GW electrolysis capacity by the end of the 21st century, taking already into account the volatility of renewable energies and the resulting necessary surplus installation of electrolysis power. Although there are other electrolysis technologies on the market (most notably alkaline electrolysis and at a lower technology readiness level also solid-oxide electrolysis), proton exchange membrane water electrolysis (PEMWE) is considered to have the greatest overall future potential for large scale application [11] [12]. The already comparably high current and power density, the ability to produce hydrogen at the cathode directly at higher pressures (typically up to 30 bar) and high purity [13], independent of the pressure of the oxygen side (anode), as well as the high load spread and high dynamics predetermine this electrolysis technology for coupling to volatile renewable electricity sources such as wind power and photovoltaics. Also the investment costs for PEMWE systems (CAPEX), which are at the moment between 1000 and 2000 EUR/kW, are expected to fall significantly in the future to values around 300 EUR/kW [11]. While large PEMWE systems with a capacity of several MW are already being built and connected to the grid today [14], the current annual addition rate of 25 MW (electrolysis in general, IEA Report 2020) would need to be increased by a factor of ≈ 6000 to meet the required target.

Thesis Outline

This thesis addresses the issue of what measures can be taken at cell level to enable a sustainable addition of PEMWE systems at a high rate of more than 100 GW per year - a scale necessary for a deep defossilization of the mobility sector alone [10]. In a first step, the PEMWE technology is explained starting with a brief overview of the general functional principles followed by a more detailed look on the individual components of the cell/stack. Here, all necessary information is provided for setting up a basic temperature and pressure dependent performance model of a PEMWE cell/stack and system. Several parameters used for the model are based on own laboratory measurements. By analyzing the operational characteristics of a PEMWE system with the model, two key strategies can be identified which together should technically enable a large-scale deployment of PEMWE for renewable hydrogen production: i) Thin membranes for high efficiency and high power density as well as ii) low-iridium catalyst loadings at the anode.

Following the selected path, among many other problems that might come up, five central research questions are raised: i) Will renewable hydrogen production by PEMWE be sustainable from a life cycle assessment point of view and what is the influence of increased power density? ii) Are there thermal limitations when using thin membranes at high and very high current densities? iii) How much do thin membranes and high current densities have an influence on the hydrogen permeation losses? iv) Are iridium catalysts stable enough for long-term operation and what influences the stability? v) How is the long-term performance of low-iridium loaded anodes?

Subsequently, the experimental methods for finding answers to the raised questions are presented and the results are included in the form of five peer-reviewed journal papers, each one for one of the research questions.

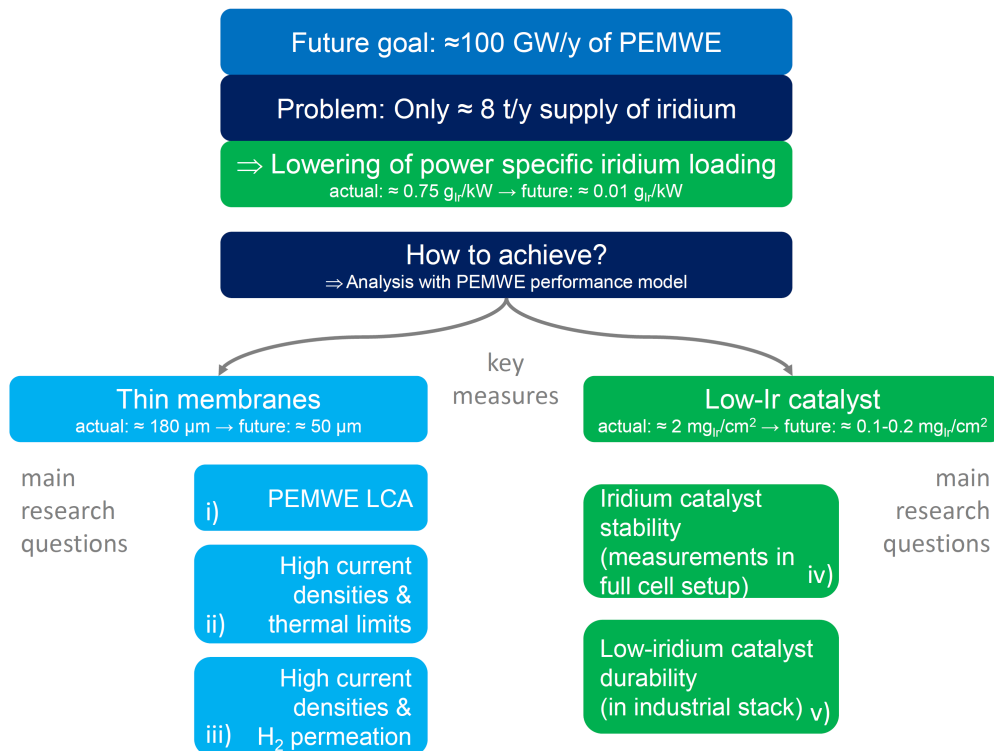


Figure 2: Thesis outline.

2 Theory of Proton Exchange Membrane Water Electrolysis

2.1 Overview Functional Principle

In order to be able to identify possible limitations and improvement potentials for PEMWE on cell level, a description of the system, its properties and the boundary conditions during operation is helpful. Therefore, a basic explanation of the functional principle of a PEMWE cell is provided first.

As in any electrolysis, a chemical substance, in this case pure water, is split by means of electrical energy. As shown in figure 3, water is supplied to the anode side of the PEMWE cell and is split into oxygen, protons as well as electrons by supplying energy, as given in equation 1, the anode partial reaction or Oxygen Evolution Reaction (OER). For each mole of water, half a mole of gaseous oxygen is released which mainly bubbles out from the anode towards the anode side flow channel. The two moles of protons released during decomposition are transported to the cathode via the proton-conducting phase of the anode, the so-called ionomer, the proton-conducting membrane and finally the equivalent proton-conducting phase of the cathode. There, the protons are reduced to hydrogen with the electrons transported via the external electrical circuit, see equation 2, of the cathode partial reaction or Hydrogen Evolution Reaction (HER). One mole of hydrogen is thus produced per mole of decomposed water, which, like the oxygen on the anode side, mainly bubbles out from the cathode to the flow channel on the cathode side. Smaller parts of the gas volumes produced on both sides, depending on the operating pressures, can also permeate through the membrane and are then lost for usage, which will be discussed later more into detail. Combining OER and HER gives the net reaction for water splitting (equation 3).

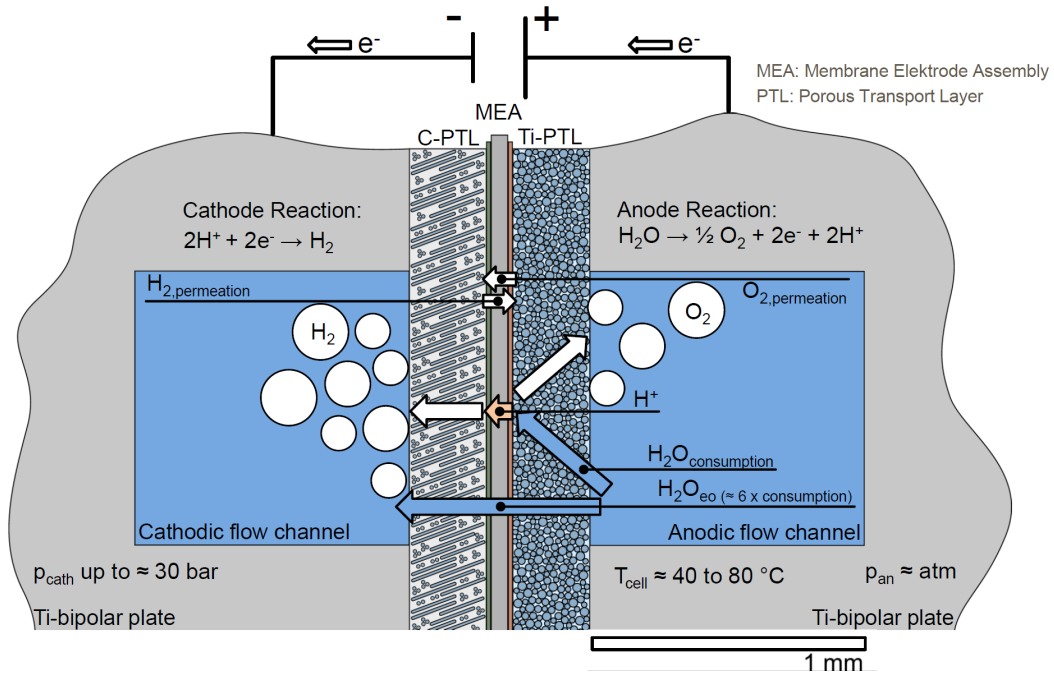
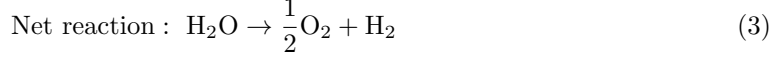
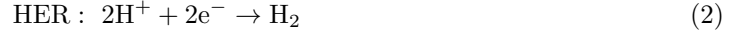
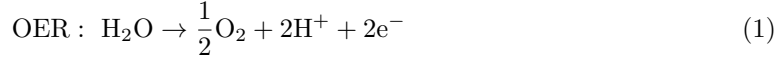


Figure 3: Schematic cross section of a typical PEMWE cell. All dimensions are roughly to scale. The cutout shows only a small part of a unit cell with the flow field channels on both sides. Real devices have significantly larger active cell areas (laboratory cells ≈ 5 cm², current industrial cells ≈ 30 to 1000 cm²) with a multitude of channels. The active area of the cell is defined as the geometric electrode area of the membrane electrode assembly (MEA).



Another important aspect of a PEMWE cell is its relatively easy water management. On their way from anode to cathode, the protons draw water molecules with them. This process, also called electroosmosis, is relatively strong and ≈ 6 times more water is transported from anode to cathode than is consumed at the anode [15]. As a result, active wetting of the cathode side of the PEMWE cell is not necessary, which greatly simplifies its operation. The pressures of both compartments can be changed individually as the membrane is tight for convective transport of gases. Typical operation pressures range between 20 bar and 50 bar (hydrogen pressure) at cell temperatures between 40 °C and 80 °C [11]. However, the anode side is mostly kept at ambient pressure which makes water supply and water treatment for maintaining high water purity easier. The core of the cell where the reactions take place is the membrane electrode assembly (MEA), exemplary depicted in figure 4. It consists of the proton-conducting membrane (typical thickness

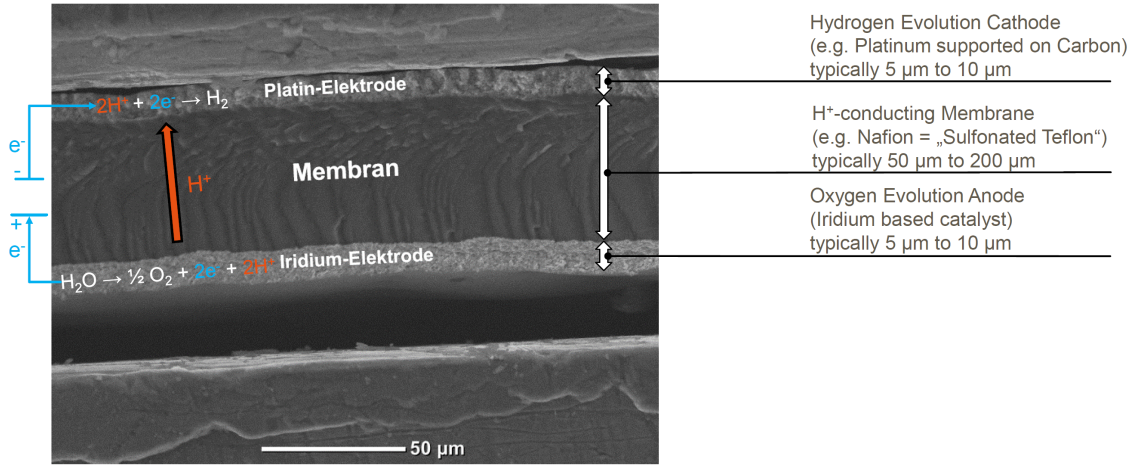


Figure 4: Scanning electron microscope cross sectional image of a typical PEMWE MEA based on 50 μm thick Nafion[®] 212. SEM graph provided by Maximilian Bernt, ZAE Bayern.

is between 50 μm and 200 μm) onto which thin electrode layers (≈ 5 to 10 μm) are applied on both sides which can be deposited in several ways. Most common are a direct coating of the membrane by spray coating or the decal transfer process [16], where electrodes are coated first on a transfer film and are then sandwiched with the membrane. This sandwich is finally hotpressed to obtain a permanent assembly. The active area of the cell, which is defined as the geometric area of the electrodes of the MEA, is typically small for laboratory devices like single cells and short-stacks (≈ 5 to 50 cm^2) and is significantly larger for stacks which are used in industrial applications (up to $\approx 1000 \pm 500 \text{ cm}^2$ [17]). Porous transport layers (PTL) with thicknesses around 200 μm to 300 μm are placed between the MEA and the flow fields. Ideally, these PTLs allow good electrical contact to the electrodes, uniform mechanical support of the MEA and good transport of water, the product gases and heat. Typically at the cathode side carbon cloth or carbon paper is

used as PTL material. However, at the anode side, carbon materials are not stable at the high electrode potentials exceeding 1.23 V vs. standard hydrogen electrode (SHE) potential. Thus, mainly titanium materials made from sintered powders or fibers are used instead [18]. Also the flowfields itself with the ≈ 1 mm deep and wide machined or forged channels are typically made from titanium for the same stability reasons. The thin, compact and stable passivation layer of titanium dioxide forming at the surface of the bulk titanium is responsible for the good applicability at operating conditions prevailing at anode sides of PEMWE cells. Nevertheless, the protective passivation layer can significantly increase the contact resistance between the titanium elements and between PTL and anode. Thus, both flowfields and titanium PTLs at the anode side of the cells are frequently coated with a thin platinum-group metal (PGM) layer. Mostly platinum is used to ensure low and stable contact resistances. Gold can be used as a coating of the flowfields, but it will dissolve in direct contact with the ionomer (low pH) from the electrode or membrane at elevated cell potential [19] and is thus not suited as a PTL coating. A PGM coating is especially necessary when using thin and brittle anode catalyst layers with lower in-plane conductivity [10]. In contrast at the cathode side, the high bulk conductivity of the carbon PTL and its full stability at the local operating conditions without passivation effects makes a coating obsolete.

However, single cells are not commonly used outside of laboratory applications, since their voltage-to-current ratio is rather unfavorable for significant power conversion. In current state-of-the-art systems a relatively low terminal voltage around 1.8 V (corresponding to ≈ 70 % efficiency based on lower heating value (LHV)) would correlate to a relatively high current density of ≈ 1.5 A/cm² [11]. Thus, in order to operate PEMWE cells reasonably, they are usually arranged in a stack. Exemplary, figure 5 shows an industrial PEMWE short-stack (H-TEC Systems GmbH, Germany) with 10 cells in a laboratory test rig at ZAE Bayern electrochemistry laboratory and a graphic representation of the relevant parts and their assembly. Note that manifolds and gaskets are not shown in this graphic. In this case, the cells are arranged one behind the other. The monopolar plates of the single cell thus are complemented in the stack by a certain number of bipolar plates, depending on the number of cells contained. The current through all cells in the stack is the same, but the individual cell voltages add up to the stack voltage at the terminal clamps. In this way, a more favorable ratio of voltage to current can be reached, which is better suited to the specifications of conventional power electronics.

In order to run the stack in a PEMWE system, several other components are necessary. As depicted in figure 6, a basic system needs a water cycle at the anode side with a water setup tank, a heat exchanger to regulate the system temperature, a circulation pump and an ion exchange filter before the stack. The task of keeping high water quality while running a PEMWE system is very important for a stable performance. Ionic impurities can accumulate in the membrane or in the ionomere phases of the electrodes and deteriorate the ionic conductivity or directly affect the platinum group metal (PGM) catalysts [21] [22] [23]. Therefore, the water conductivity of the supplied or cycled water in a PEMWE should always be close to the conductivity of ultrapure water (≈ 0.1 μ S/cm at 25 °C). This is achieved by using mixed-bed deionizer resins to clean up the water constantly and by using metal free (plastic) piping and setup components in contact to the process water wherever possible. As mentioned before, at the cathode side no water cycling is necessary due to a constant net water transport from anode to cathode via electroosmotic drag. The gases produced on both sides are separated from the water and, depending on the use case, are dried and purified to reach a defined quality. Furthermore, power and control electronics as well as safety equipment are essential for the operation of a PEMWE system. Systems up to a power class of about 1 MW can be fitted into standardized 20 or 40 ft cargo containers [24] whereas

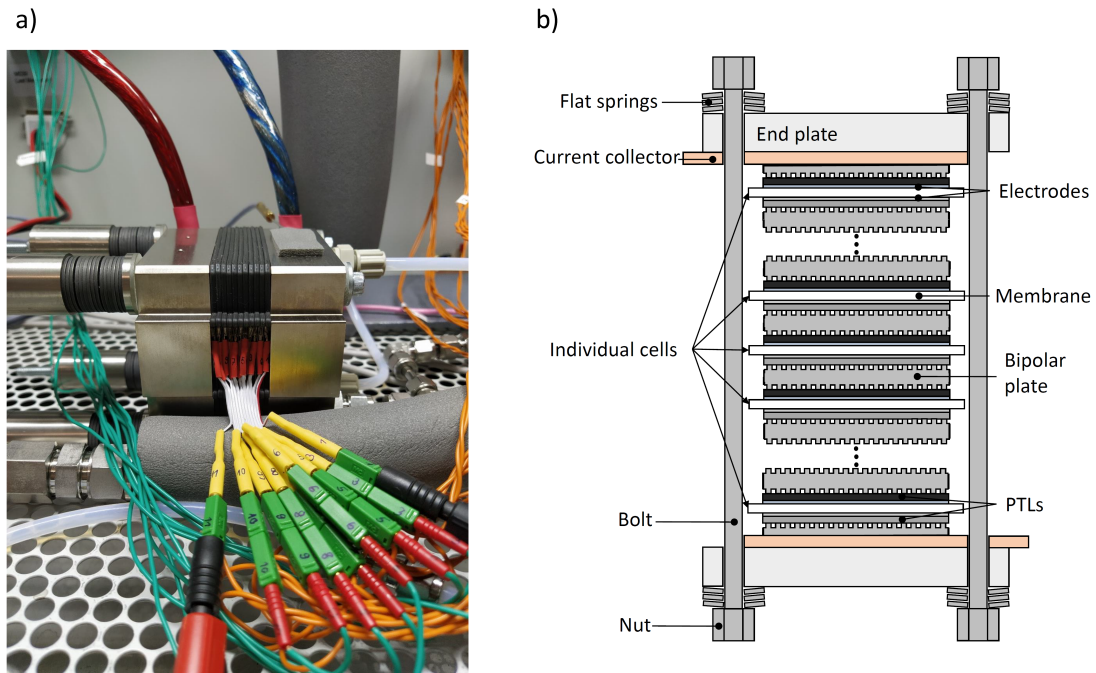


Figure 5: a) Industrial 10-cell PEMWE short stack from H-TEC Systems GmbH with 30 cm² active area inside the stack test rig at ZAE Bayern electrochemistry laboratory, Garching. b) Schematic drawing of the relevant parts and their assembly in a PEMWE stack [20]. Manifolds and gaskets are not shown in this simplified graphic.

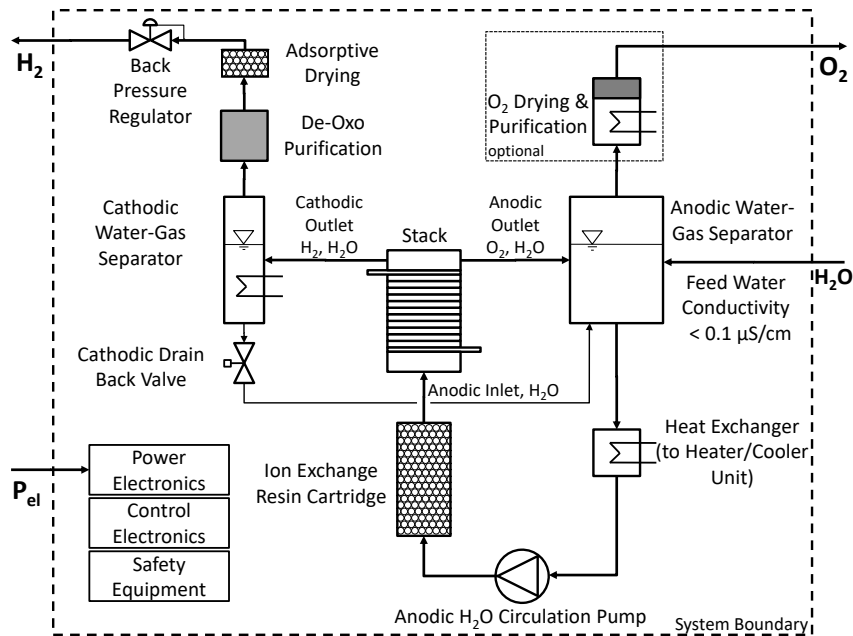


Figure 6: Schematic representation of all relevant components of a PEMWE system. Taken from [20].

larger systems are usually integrated into a special dedicated building [14].

After this short overview of the functionality, the main components and the commonly used materials, a more detailed description of the core elements of a PEMWE cell follows. These are

concretely the membrane, electrodes, PTLs as well as the flow fields.

2.2 Membrane

As briefly described in the overview, the membrane in a PEMWE cell serves three important purposes: The electrical separation of the two electrodes, the ionic connection between the anode and cathode and the gas-tight separation of the compartments at the respective operating pressures. To ensure the appropriate conductivity for protons while simultaneously guarantee high chemical and mechanical stability, membranes based on a PTFE backbone with sulfonic acid groups at the end of ether-linked perfluorinated side chains are used in most cases [25]. The most widely employed membrane type in this class of perfluor-sulfonic-acid (PFSA) materials is Nafion[®] from Dupont. In addition to a large number of similar PFSA materials, hydrocarbon-based membranes in particular are in focus, as they might be produced cheaper in the long run and also should exhibit lower gas permeation at low ohmic resistance compared to PFSA materials [26]. Structural reinforcement, for example with integrated PTFE fibres in a PFSA membrane or a PTFE matrix filled with PFSA ionomer [27], is particularly useful for thin membranes and applications at the limit of the thermomechanical stability of the PFSA base material ($T_{\text{cell}} > 90 \text{ }^\circ\text{C}$) [28] [29].

Water Uptake, Swelling and Conductivity

As typical PFSA materials like Nafion[®] can take up a significant amount of water, most of their physicochemical properties depend on the water content λ , which is defined by equation 4 as the number of moles of water per mole of sulfonic acid groups in the polymer electrolyte membrane [30].

$$\lambda = \frac{n_{\text{H}_2\text{O}}}{n_{\text{SO}_3\text{H}}} \quad (4)$$

A practical calculation of the water content based on measured values and material properties can be done with equation 5 [31].

$$\lambda = \frac{WU \cdot EW}{M_{\text{H}_2\text{O}}} \quad (5)$$

Here, WU denotes the water uptake of the membrane (defined by equation 6), EW , the "equivalent weight" of the membrane type, which is defined by the quotient of the dry weight of the ionomer per mole of sulfonic acid in ($\text{g/mol}_{\text{SO}_3\text{H}}$) and $M_{\text{H}_2\text{O}}$, the molar mass of water. For the calculations in this thesis, an EW of $1100 \text{ g/mol}_{\text{SO}_3\text{H}}$ for Nafion[®] membranes is used based on the data given in [30].

$$WU = \frac{m_{\text{wet}} - m_{\text{dry}}}{m_{\text{dry}}} \quad (6)$$

The water uptake and thus also the water content of a PFSA membrane in contact with liquid water is highly dependent on the actual temperature and also the pretreatment history of the membrane [32] [33]. At full hydration in contact to liquid water, Nafion[®] reaches a water content of $\lambda \approx 21\text{-}22$ [34]. However, if Nafion[®] membranes are dried at elevated temperatures close to or above glass transition temperature [15], they do not directly reach full hydration again at subsequent contact with liquid water [35]. Typical dry membrane thicknesses in state of the art systems are between $125 \text{ } \mu\text{m}$ (Nafion[®] 115) and $175 \text{ } \mu\text{m}$ (Nafion[®] 117) [36]. However, the actual wet thickness $t_{m,\text{wet}}$ varies with the water content λ as the membrane swells during water uptake. Two extreme cases of swelling are possible: Isotropic swelling in all directions (e.g. if the membrane is freely immersed in water without fixation or if a MEA is externally hydrated

previously to mounting in the cell setup) with the lowest thickness change and anisotropic swelling only in through-plane direction with the maximum possible thickness change (very likely to occur if a membrane or MEA is mounted in a dry state in the cell and subsequently hydrated in the fully built cell setup). The following equations adapted from [31] can be used to calculate the membrane thicknesses t_m for isotropic and anisotropic (only in through-plane direction) swelling:

$$t_{m,\text{wet,iso}} = \sqrt[3]{\left(\frac{M_{\text{H}_2\text{O}} \cdot \rho_{m,\text{dry}} \cdot \lambda}{\rho_{\text{H}_2\text{O}} \cdot EW} + 1\right)} \cdot t_{m,\text{dry}} \quad (7)$$

$$t_{m,\text{wet,aniso}} = \left(\frac{M_{\text{H}_2\text{O}} \cdot \rho_{m,\text{dry}} \cdot \lambda}{\rho_{\text{H}_2\text{O}} \cdot EW} + 1\right) \cdot t_{m,\text{dry}} \quad (8)$$

Here, $\rho_{m,\text{dry}}$ denotes the dry membrane density which is $\approx 2 \text{ g/cm}^3$ for Nafion[®] [37]. For a known λ and cell temperature T_{cell} , also the membrane conductivity of Nafion[®], σ_m in S/cm, can be calculated by equation 9 fitted to measurement data and published by Springer et al. [38], which is in good agreement with other published data [15].

$$\sigma_m = (0.005139\lambda - 0.00326) \cdot \exp\left[1268 \cdot \left(\frac{1}{303} - \frac{1}{T_{\text{cell}}}\right)\right] \quad (9)$$

Mass Transport through PFSA Membranes

As described earlier, the membrane prevents direct convective transport of gases from anode to cathode and vice versa, but still a certain amount of gases can permeate through the material. This is especially of concern for the hydrogen permeating from the mostly pressurized cathode side of the cell to the anode side. As the anode is running at a potential of typically $> 1.4 \text{ V vs. SHE}$, the permeated hydrogen is not oxidized at the anode and mixes with the produced oxygen. If the hydrogen content exceeds a concentration of $\approx 4 \%$ H_2 in O_2 (lower explosive limit, LEL), the gas mixture exiting the anode compartment is explosive which poses a considerable safety issue for the cell/stack and the other downstream electrolyser plant components [39]. Thus, measures have to be taken to limit the H_2 in O_2 concentration to about 2 % (50 % LEL). One option to allow safe operation is to choose a certain minimum membrane thickness, depending on the operating conditions (temperature, pressures, minimum current density/part load ratio).

Although several transport mechanisms for gases take place in parallel in the membrane (water-bound transport of dissolved gases driven by differential pressure and electroosmosis vs. diffusive transport [40]), in a first order approximation, pure diffusion has the biggest influence for the hydrogen transport from cathode to anode. Equation 10 gives the diffusive through-plane molar hydrogen permeation flux based on Fick's law:

$$\dot{n}_{\text{H}_2,\text{perm}} = D_{\text{H}_2,\text{perm}}(T) \cdot \frac{\Delta p_{\text{H}_2}}{t_m} \quad (10)$$

$$D_{\text{H}_2,\text{perm}}(T) = k_{\text{dry,H}_2} \cdot e^{\left(\frac{-E_{a,\text{dry,H}_2}}{RT}\right)} + \nu_{\text{H}_2\text{O}} \cdot k_{\text{wet,H}_2} \cdot e^{\left(\frac{-E_{a,\text{wet,H}_2}}{RT}\right)} \quad (11)$$

$$k_{\text{dry,H}_2} = 1.57 \cdot 10^{-4} \text{ (mol } \mu\text{m)/(cm}^2 \text{ s bar)} \quad (12)$$

$$E_{a,\text{dry,H}_2} = 20.28 \text{ (kJ/mol)} \quad (13)$$

$$k_{\text{wet,H}_2} = 4.5 \cdot 10^{-4} \text{ (mol } \mu\text{m)/(cm}^2 \text{ s bar)} \quad (14)$$

$$E_{a,\text{wet,H}_2} = 18.93 \text{ (kJ/mol)} \quad (15)$$

Here, $D_{H_2,perm}$ denotes the effective permeation coefficient for hydrogen in the membrane, Δp_{H_2} the hydrogen partial pressure difference between cathode and anode side and t_m the membrane thickness. The universal equation for Nafion[®] permeability (equation 11) gives an Arrhenius fit for the temperature dependence of $D_{H_2,perm}$ [30]. The values for the prefactors and activation energies k_{dry,H_2} , E_{a,dry,H_2} , k_{wet,H_2} and E_{a,wet,H_2} are also taken from [30]. The volume fraction of water ν_{H_2O} (cm³ of water per cm³ of hydrated polymer) is calculated by equation 16 [30]. Note that the unity correction factor $\frac{mol}{cm^3}$ is missing in the original reference. As stated above, a fully hydrated membrane at 80 °C typically has a water content of $\lambda \approx 21$.

$$\nu_{H_2O} = \frac{\lambda \cdot 18}{\lambda \cdot 18 + \frac{EW}{\rho_{m,dry}} \cdot \frac{mol}{cm^3}} \quad (16)$$

Vice versa, also oxygen transport from anode to cathode side takes place and can be diffusive in nature (equation 17 to 22) or water bound (equation 27). Analogous to hydrogen permeation, $D_{O_2,perm}$ (equation 18) is the effective permeation coefficient for oxygen in Nafion[®] and, together with the prefactors and activation energies given by equations 19 to 22, taken from [30].

$$\dot{n}_{O_2,perm} = D_{O_2,perm} \cdot \frac{\Delta p_{O_2}}{t_m} \quad (17)$$

$$D_{O_2,perm}(T) = k_{dry,O_2} \cdot e^{\left(\frac{-E_{a,dry,O_2}}{RT}\right)} + \nu_{H_2O} \cdot k_{wet,O_2} \cdot e^{\left(\frac{-E_{a,wet,O_2}}{RT}\right)} \quad (18)$$

$$k_{dry,O_2} = 0.674 \cdot 10^{-4} \text{ (mol } \mu\text{m)/(cm}^2 \text{ s bar)} \quad (19)$$

$$E_{a,dry,O_2} = 21.28 \text{ (kJ/mol)} \quad (20)$$

$$k_{wet,O_2} = 5.05 \cdot 10^{-4} \text{ (mol } \mu\text{m)/(cm}^2 \text{ s bar)} \quad (21)$$

$$E_{a,wet,O_2} = 20.47 \text{ (kJ/mol)} \quad (22)$$

As already mentioned, water transport takes place in the cell primarily from anode to cathode via electroosmosis (equation 23). Here, n_{drag} denotes the drag coefficient, which relates a water flow to the proton current from anode to cathode in the cell. Figure 7 shows measured electroosmotic drag coefficients for a MEA based on Nafion[®] 117 in comparison with literature data [41] [42]. The resulting temperature dependence of n_{drag} is given by the linear fit in equation 24.

$$\dot{n}_{H_2O,eo} = n_{drag} \cdot \frac{I}{F} \quad (23)$$

$$n_{eo}(\vartheta) \text{ (mol}_{H_2O} \text{ / mol}_{H^+}) = 0.012(1/^\circ\text{C}) \cdot \vartheta + 2.17 \quad (24)$$

Also a differential pressure driven reverse transport of water from cathode to anode is possible (equation 25), but is usually significantly less intense compared to the electroosmotic water transport. However, the pressure driven reverse transport of water from cathode to anode becomes important for high differential pressures and thin membranes. In order to estimate the differential pressure driven transport, a simple measurement was done with a 60 cm² PEMWE cell by Sylatech GmbH, Germany. The water transport rate is measured for three current densities (0.17 A/cm², 0.5 A/cm² and 0.83 A/cm² and two temperatures, 40 °C and 80 °C, at balanced ambient pressure and for a pressure difference of 5 bar between cathode and anode. In both cases the water transport is measured gravimetrically by weighing the exhaust water at the cathode side. The results are shown in figure 8. In general, a linear dependency of the water transport rate with

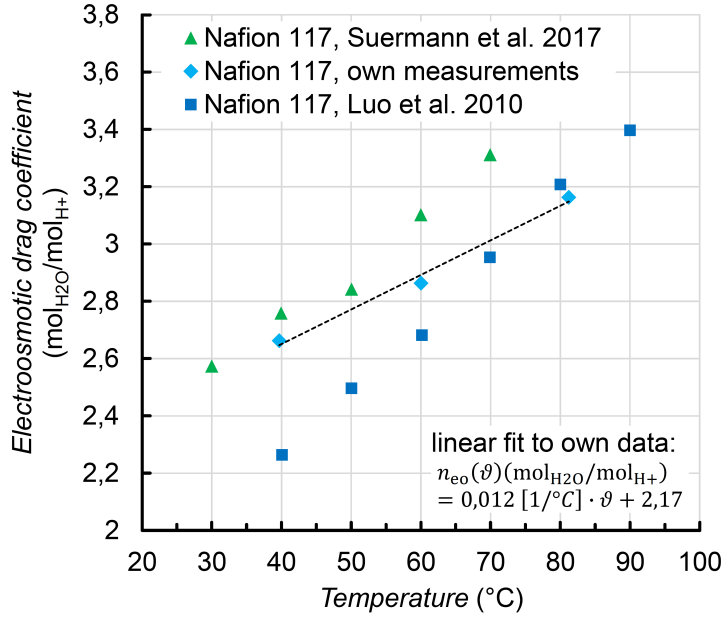


Figure 7: Measured data for n_{drag} in a temperature range from 40 °C to 80 °C at a mean current density of 0.5 A/cm² for a commercial MEA based on Nafion[®] 117 made by HIAT, Germany. The catalyst loading is 2 mg_{Ir}/cm² at the anode and 1 mg_{Pt}/cm² at the cathode. The measured drag coefficients are comparable to literature data by Luo et al. [41] and Suermann et al. [42]. The water transport is measured gravimetrically by weighing the exhaust water at the cathode side.

the current density is visible for all sets of measurements. As expected, the measurements with elevated cathode pressure (5 bar pressure difference) show an offset towards lower transport rates. Furthermore, the transport rate is higher at higher temperature which results in a steeper increase of the water transport rate with current density at higher temperatures (80 °C) compared to lower temperatures (40 °C).

$$\dot{v}_{\text{H}_2\text{O},\text{dp}} = D_{\text{H}_2\text{O},\text{dp}} \cdot \frac{\Delta p_{\text{cath,an}}}{t_{\text{m}}} \quad (25)$$

$$D_{\text{H}_2\text{O},\text{dp}}(\vartheta) \text{ ((mL } \mu\text{m)) / (s cm}^2 \text{ bar)} = 4.12 \cdot 10^{-6} (1/^\circ\text{C}) \cdot \vartheta + 1.29 \cdot 10^{-4} \quad (26)$$

Using the set of datapoints (40 °C and 80 °C at 0 and 5 bar pressure difference) from figure 8 and by assuming a linear temperature dependence of the transport coefficient for differential pressure driven water flow through the membrane leads to equation 26 for the calculation of $D_{\text{H}_2\text{O},\text{dp}}(\vartheta)$. It is important to note, that the membrane reference thickness for the calculation of the transport coefficient was assumed to be that of a fully anisotropically (only in through-plane direction) swollen Nafion[®] 212 membrane at $\lambda = 21$ ($t_{\text{m}} = 77 \mu\text{m}$).

In dependence of the operation parameters, a net water transport as a sum of differential pressure and electroosmotic driven water transport results, which in turn leads to a transport of soluted oxygen from anode to cathode (equation 27).

$$\dot{n}_{\text{O}_2,\text{wb}} = \dot{v}_{\text{H}_2\text{O},\text{m}} \cdot H_{\text{O}_2} \cdot p_{\text{O}_2,\text{an}} \quad (27)$$

$$H_{\text{O}_2}(T) = 1.3 \cdot 10^{-3} \text{ (mol / (l} \cdot \text{bar))} \cdot \exp \left(1700 \text{ K} \cdot \left(\frac{1}{T} - \frac{1}{298.15 \text{ K}} \right) \right) \quad (28)$$

Here, $\dot{v}_{\text{H}_2\text{O},\text{m}}$ denotes the area specific volumetric flow rate of water from anode to cathode and

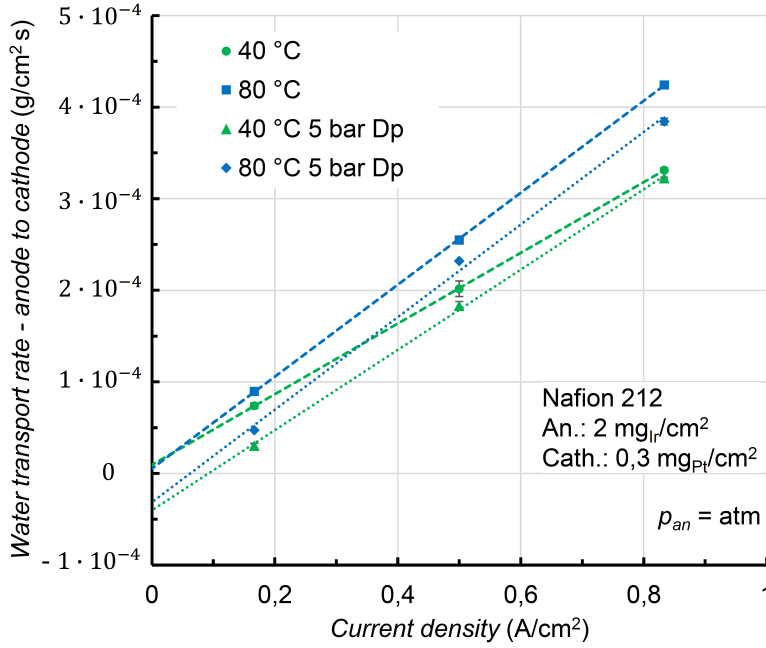


Figure 8: Measured data for water transport rate at balanced atmospheric pressure and 5 bar differential pressure at 40 °C and 80 °C and 0.17 A/cm², 0.5 A/cm² and 0.83 A/cm² for a MEA based on Nafion[®] 212. The catalyst loading is 2 mg_{Ir}/cm² at the anode and 0.3 mg_{Pt}/cm² at the cathode. The water transport is measured gravimetrically by weighing the exhaust water at the cathode side. Each point shown is the average of three individual measurements.

H_{O_2} the Henry coefficient for the solubility of oxygen in water. The temperature dependence of H_{O_2} is given by equation 28 taken from [43]. In the case of oxygen transport from anode to cathode, safety aspects are less critical as most of the oxygen reacts with the hydrogen at the cathode catalyst layer (potential < 0 V vs. SHE) back to water and does not remain in the product gas stream. Nevertheless, a faradaic efficiency loss is linked to both permeation losses, either of hydrogen or oxygen and also to the water-bound oxygen transport. Thus, for the calculation of the Faraday efficiency, the total transported oxygen $\dot{n}_{O_2, tr}$ is relevant which is the sum of water-bound-transported (equation 27) and permeated (equation 17) oxygen:

$$\dot{n}_{O_2, tr} = \dot{n}_{O_2, wb} + \dot{n}_{O_2, perm} \quad (29)$$

For low material consumption and high cost efficiency, optimized cells with low losses are necessary which in turn can reach significantly higher current and power densities than conventional state-of-the-art cells. This can be achieved in particular by using thin membranes to reduce the ohmic losses associated to the proton transport through the membrane. Since the permeation of the product gases is also stronger in this case, the associated safety issues have to be carefully addressed. Especially when a high part load range is desired and standard PFSA membranes are used, the integration of recombination catalysts, mostly platinum based, in the MEA or the cell/system is unavoidable. Technical solutions for recombination catalysts can be built into the MEA [44] [45] [46], or at some point in the O₂ stream at the anode side of the electrolyzer or in the anode side PTL [47].

2.3 Electrodes and Catalysts

As visible in figure 4, the approximately 5 to 10 μm thick anode and cathode electrode layers are arranged on both sides directly on the membrane to form the MEA. The individual reactions during water electrolysis take place at the electrodes, which are the OER at the anode and the HER at the cathode, and thus make the electrodes crucial components of the overall PEMWE system. In order to allow high turnover rates (= high current densities) at low losses, the porous electrodes need to have large specific surface areas and a well balanced ratio of electrical conducting phase, ionic conducting phase (ionomer), open pores for transport of water and product gases (void volume) and particularly catalytic active surfaces (catalyst) optimized for the respective reaction [16] [10]. Usually, PGM catalysts are used in PEMWE, as they are highly active and show the best stability at the challenging operating conditions with low pH values around 0 in presence of the highly acidic polymer electrolyte. At the cathode side, the potential of < 0 V vs. SHE [48] enables the use of Pt-catalysts with high surface area carbon support materials, which are widely used in PEM fuel cells [49]. The state of the art loading for PEMWE applications is usually between 0.5 and 1 $\text{mg}_{\text{Pt}}/\text{cm}^2$ [50]. Due to the very fast reaction kinetics for the HER with Pt-based catalysts, the cathode side loading can be lowered significantly (≈ 10 -fold) without detrimental effects on performance [10] [51] [52] [53]. Even non-noble metal catalysts can be applied at the cathode side, e.g. cobalt-based [54] or molybdenum-based systems [55] [56] [57]. Nevertheless, they have so far tended to be used on a laboratory scale only and not for industrial applications.

At the anode side however, platinum is not the most active PGM catalyst for the OER. Iridium and ruthenium show higher activities [58], but due to stability reasons at the high anode potentials during operation of > 1.4 V vs. SHE [48], iridium or its oxides are the current state-of-the-art catalyst materials [50]. The operating conditions also impede the use of carbon as a conductive support material. Thus, different designs are used: Typical industrial OER catalysts are unsupported iridium (Ir-black) as well as iridium dioxide supported on non-conductive titanium oxide particles with a comparatively thick and compact iridium layer for sufficient electrical conductivity (e.g. Umicore Elyst Ir75 0480). Consequently, the resulting iridium loadings are high at 1 to 2 $\text{mg}_{\text{Ir}}/\text{cm}^2$ [50]. Today, the mean current density reached by industrial PEMWE systems is about 1.5 ± 0.5 A/cm^2 at a cell voltage efficiency of 70 % (lower heating value, LHV) [11], which equals a cell voltage of 1.79 V. At this operating point, the resulting mean power density of the system is 2.69 W/cm^2 . This, in turn, results in a mean power-specific iridium loading of about 0.75 $\text{g}_{\text{Ir}}/\text{kW}_{70\% \text{ (LHV)}}$ for state-of-the-art PEMWE systems. However, iridium is one of the nine rarest stable elements on Earth [59]. Annual mining and recycling in 2018 was only about 7.8 tons, while the demand was in the range of 6.6 to 6.8 tons [60] [61]. Thus, if all the iridium available annually were used solely for PEMWE, plants of about 10 GW capacity per year could be added at today's power-specific loading. This is in stark contrast to the already mentioned rate of around 150 GW/year, which would be necessary to change the worldwide mobility sector completely to renewable hydrogen until the end of the 21st century. To overcome this limitation, the power-specific iridium loading would have to be reduced significantly to values around ≈ 0.01 $\text{g}_{\text{Ir}}/\text{kW}_{70\% \text{ (LHV)}}$ [10] [36]. Yet, if the loading is to be reduced significantly, the use of commercial state of the art catalysts is limited: At loadings below about 0.5 $\text{mg}_{\text{Ir}}/\text{cm}^2$, the resulting electrodes are getting thin and brittle with insufficient in-plane conductivity and high contact resistances to the anode PTL [10] [62].

Therefore, the development of new or improved catalyst systems for PEMWE anodes is a critical task for a future large scale application. One possible direction would be the use of a conductive support material just like the high surface area carbon support materials in HER catalysts. In

this case, the active iridium particles could be very finely dispersed and the necessary electrical conductivity would be supplied by the support material and not by the iridium itself. Several promising candidates for conductive support materials exist, for example antimony-doped tin oxide (ATO) [63] [64], niobium-doped titanium oxide (NTO) [65] [66] or tungsten doped titanium oxide [67]. However, long term stability testing of such support materials in PEMWE acidic environment is still to be conducted. A different approach is the use of thin iridium films, directly coated on highly structured membranes [68] or on nano structures (e.g. whiskers) on the membrane surface [69]. Finally, also the consistent optimization of the catalyst concept applying a non-conductive titanium dioxide support with a compact conductive iridium layer on top is possible. First laboratory tests with such materials show higher begin-of-life (BOL) performance compared to established commercial products at 8-fold lowered iridium loading [70]. Nonetheless, the long-term stability needs to be further investigated.

2.4 Porous Transport Layers

As already briefly explained, the porous transport layers (PTL) between MEA and flow fields are multifunctional components of a PEMWE cell setup. Besides well-proportioned mechanical mounting of the MEA [71], the PTLs serve for electrical as well as thermal contact of the MEA to the flowfields [72]. Furthermore, their preferably high open porosity allows for good through-plane and, to a certain extent, also in-plane media transport from the flow field channels to the electrodes and vice versa [71] [73]. The materials used differ for anode and cathode side due to the different potentials present. At the cathode side, the potential stays slightly below 0 V vs. SHE during operation [48]. Thus, carbon-based materials can be used here as a PTL, which are in general similar to the gas diffusion layers (GDL) used in PEM fuel cells [74]. In contrast to the fuel cell operation, where a clogging of the pores with water is detrimental to the gas transport [75], in PEMWE cells carbon cloth or paper without or with only slight hydrophobic characteristic (= with low PTFE content) are used. A typical carbon fibre cathode side PTL is shown in the SEM graph in figure 9 in panel c). At the cathode side, the mixture of water and hydrogen gas exits the setup from the electrode to the flow field and usually no reverse water crossflow occurs inside the PTL. Typical uncompressed thicknesses range between 300 and 400 μm [16] [76]. Due to their compressibility, carbon-based PTLs also have a compensative effect for mechanical stress and act as an elastic element in the otherwise mainly rigid cell setup. Especially when using thin membranes with thicknesses below 50 μm , the use of a micro porous layer (MPL) at the interface between PTL and MEA can be necessary to avoid short circuits [77]. The individual carbon fibres with thicknesses around 20 μm which compose the PTL have sharp tips and can perforate thin MEAs even at standard cell compression rates of 1.5 to 2 MPa [16]. Such compression rates are necessary to reach overall low electric contact resistances in the cell. However, due to the high bulk electric conductivity of the carbon PTL and the carbon catalyst support in the cathode, the resulting contact resistances at the cathode side are low, even at very low catalyst loadings around 0.03 $\text{mg}_{\text{Pt}}/\text{cm}^2$ [10].

As already mentioned, the local potential during operation at the anode side is higher than 1.4 V vs. SHE [48] at which carbon materials are not stable and would quickly corrode to carbon dioxide [78]. Thus, mostly titanium-based PTLs are used instead. Different PTL designs are possible, with sintered titanium meshes and fibres (figure 9, panel b)) or sintered titanium particles (panel a)) being the most-used structures [79]. Also thin titanium foils with etched, electron-beam/ laser-cut or punched micro perforations could be possible anode PTL designs [80] [81] [82] [83]. For sintered

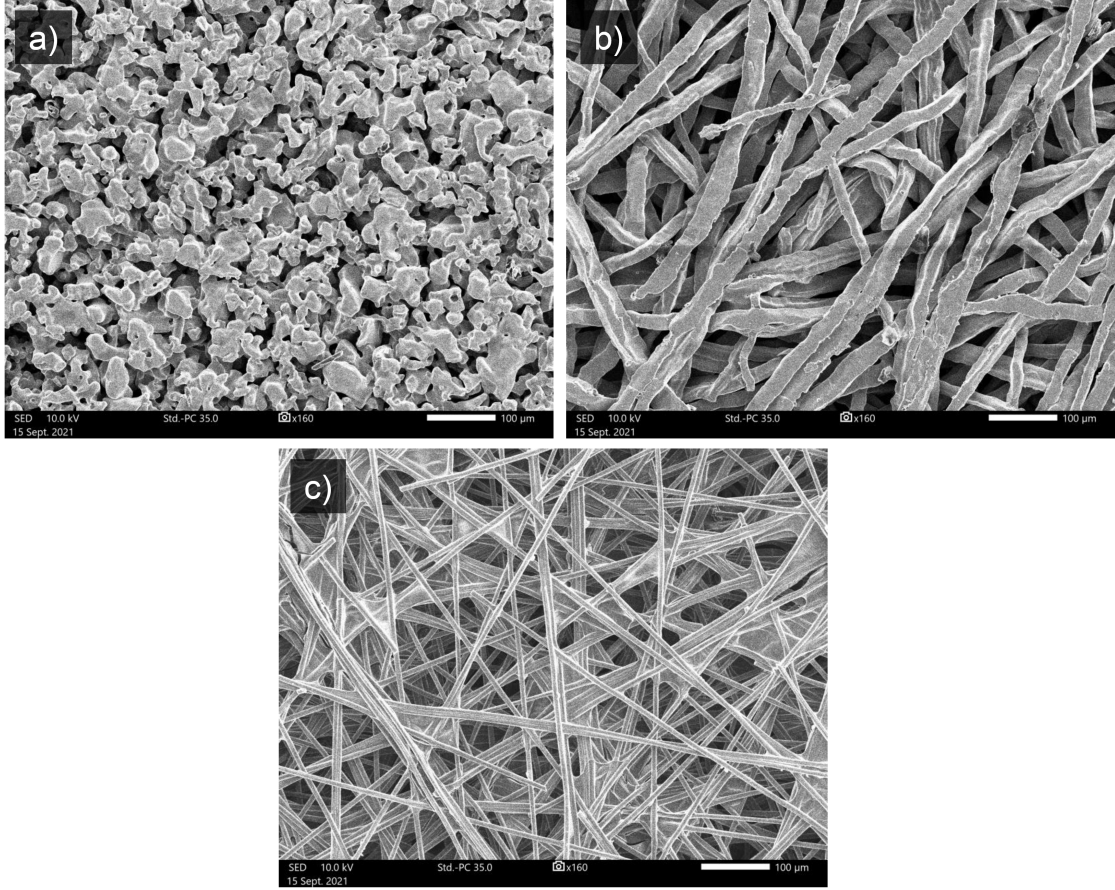


Figure 9: SEM graphs of three different PEMWE PTL materials: a) Titanium sinter anode side PTL made from spherically shaped titanium powder (Mott, USA). b) Titanium sinter anode side PTL made from titanium fibres (Bekaert 10-0.25, Germany). c) Carbon fibre cathode side PTL (Toray TGP-H-120, Japan). The magnification factor of 160 is the same for all three graphs.

PTL materials, optimum pore sizes vary around 10 to 13 μm , whereas the mean open porosity should be between 30 and 50 % [84] [73]. In contrast to the low electric contact resistances present with carbon-based cathode side PTLs, titanium-based PTLs have the drawback of low-conductivity of the protective titanium dioxide film which inevitably forms at their surface during operation. Thus, the contact resistances are significantly higher at the anode side and are especially of concern if thin electrodes with low iridium loadings are used, which typically have higher in-plane resistances than standard anodes with high catalyst loadings around 2 $\text{mg}_{\text{Ir}}/\text{cm}^2$ [42]. In order to lower the contact resistance between PTL and anode, MPL-like structures can be implemented at the interface of anode to PTL [85] [86] [87]. Also a surface roughening by pulsed laser can be done to build up a microstructure on top of an existing coarser PTL [88]. However, pure titanium structures with higher surface area might be more prone to continuous oxide layer growth which could outweigh the positive effect of the initially lowered contact resistance. Thus, to ensure low contact resistances which are stable during the long expected service life of PEMWE systems in the range of 60,000 to 90,000 h [12], also thin platinum coatings can be applied [89]. However, with a platinum density of 21.45 g/cm^3 [90], a 100 nm thick homogeneous protective layer already equals an additional platinum loading of $\approx 0.2 \text{ mg}_{\text{Pt}}/\text{cm}^2$ in the cell. Yet, this extra amount of platinum could be problematic at large scale applications as it is roughly seven times higher

than possible optimized cathode catalyst loadings around $0.03 \text{ mg}_{\text{Pt}}/\text{cm}^2$ [10]. Therefore, also alternative coating options are under investigation, for example with niobium [85].

2.5 Flow Fields and Bipolar Plates

On both sides, each cell unit is terminated by plates which separate the cell from the adjacent cells (= bipolar plates) or from the end plates in the stack (= monopolar plates). To allow media transport from and to the cell, a gas and water perfusable, planar structure with the same dimensions as the active cell area is used. These structures are also called flow-fields and can be realized in several ways: In most cases, channel structures are directly integrated in the mono/bipolar plates and can be machined, etched, laser/water cut or embossed/deep-drawn/hydroformed. Also the use of coarse expanded metal mesh is possible to allow a water and media flow in combination with a solid bipolar plate that separates a compartment from the adjacent one. In addition to the mentioned supply of water and removal of product gases, also waste heat, which is produced during water splitting under most operating conditions, has to be transported away from the cell mainly via the process water flow. Furthermore, the stable mechanical bearing of the PTLs and MEA by the flow-fields and the mono/bipolar plates is important. Finally, sealings and manifolds for the two separate media flows of the anode and cathode sides are integrated in the edge areas of the plates.

Similar to PTLs, the choice of materials is limited by the operating conditions on both sides of the cell. However, since the flow fields are not in direct contact with the acidic polymer electrolyte, the conditions are somewhat less demanding compared to the PTL. Nevertheless, the pH of the usually cycled water decreases from neutral values to a slightly acidic range during prolonged operation of the cell. Langemann et al. measured pH values in the cycled feedwater of 3.5 at the anode side and 4.5 at the cathode side after 50 h of continuous electrolysis. [91]. In order to withstand these conditions, titanium (grades 1 and 2) is usually employed at the anode. Carbon / graphite could be used at the cathode, but a titanium-carbon composite construction is less advantageous from a manufacturing point of view. For this reason, normally, titanium is used at the cathode as well and single-material bipolar plates are built. High-alloy stainless steels may be coated with various materials (titanium, niobium, titanium nitride, platinum) and under these circumstances may likewise be used on both sides [91] [92] [93] [94]. Also laboratory tests with bipolar plates made by injection molding of conductive plastic and subsequent application of titanium coatings by a plasma process for providing stability under PEMWE operating conditions have been conducted [95]. However, a long service life ($\approx 60,000$ to $90,000$ h [12]) of all components in a PEMWE stack is a critical factor that must be taken into account when using novel materials.

In older systems, relatively thick bipolar plates are used with thicknesses up to 3 mm [20]. However, due to the relatively high material cost of titanium (approximately 3-fold higher than stainless steel) and the difficult machining of solid titanium, in newer systems the plate thicknesses are significantly lowered. This is done by the use of formed (mostly embossed) titanium sheet metal with sheet thicknesses down to 0.3 mm [20]. This is analogous to the development observed in PEMFC stacks. Here, embossed metal bipolar plates (stainless steel) with sheet thicknesses of around $50 \mu\text{m}$ have in many cases replaced the significantly thicker graphite-based bipolar plates [96]. The minimum thickness that can be used in PEMWE cells depends to a certain extent on the mechanical stability of the material under differential pressures and under the high compression forces necessary for low contact resistances. In particular, failure based on nonlinear buckling must be considered.

2.6 Thermodynamics and Reversible Cell Voltage

In order to split water into hydrogen and oxygen in a PEMWE cell, a supply of energy is required. A Legendre-transformation of the general Gibbs-Helmholtz equation shows the relationship between the reaction enthalpy change ΔH , the change in Gibbs free energy ΔG , the temperature T and the entropy change ΔS :

$$\Delta H = \Delta G + T\Delta S \quad (30)$$

A minimum electric work $\Delta G^0 = 237$ kJ/mol at standard conditions (298.15 K and 1 bar) is necessary for maintaining the net reaction shown in equation 3. However, the total energy supply needs to be higher at $\Delta H^0 = 286$ kJ/mol. The difference of $T\Delta S^0 = 49$ kJ/mol can also be provided in the form of heat/thermal energy. The minimum electric work ΔG^0 and the enthalpy ΔH^0 can be translated into the equivalent reversible cell voltage E_{rev}^0 and E_{tn}^0 (thermoneutral cell voltage):

$$E_{\text{rev}}^0 = \frac{\Delta G^0}{zF} = 1.23V \quad (31)$$

$$E_{\text{tn}}^0 = \frac{\Delta H^0}{zF} = 1.48V \quad (32)$$

Here, the Faraday constant F (96485 As/mol) and the number of electrons transmitted in the net reaction ($z = 2$) are applied. In contrast to an operation between the reversible voltage E_{rev}^0 and E_{tn}^0 , where the electrolyser cell would require external heat input to not cool down, the thermoneutral voltage E_{tn}^0 is the voltage at which a perfectly thermally insulated PEMWE cell runs without changing its temperature. At cell voltages exceeding E_{tn}^0 , heat is released which has to be removed, for example by the process water, to maintain a constant cell temperature.

If the reversible voltage has to be calculated for non-standard conditions, it is possible to correct the values for concentration or activity differences of the product gases by applying the Nernst equation and by using a fit for the temperature dependency of E_{rev}^0 based on data from [97]:

$$E_{\text{rev}} = E_{\text{rev}}^0 + \frac{RT}{2F} \ln \left(\frac{a_{\text{H}_2} \cdot a_{\text{O}_2}^{1/2}}{a_{\text{H}_2\text{O}}} \right) \quad (33)$$

$$E_{\text{rev}}^0 = 1.2291 - 0.0008456 \text{ V} \cdot (T - 298, 15 \text{ K}) \quad (34)$$

Here, the activity for water $a_{\text{H}_2\text{O}}$ in the liquid phase is always 1 whereas the activities of the product gases $a_{i,\text{gas}}$ can be calculated by a normalization of the respective prevailing partial pressures $p_{i,\text{gas}}$ by the standard pressure of 1 bar:

$$a_{i,\text{gas}} = \frac{p_{i,\text{gas}}(\text{bar})}{1 \text{ bar}} \quad (35)$$

In this context, it is particularly important to note that the individual partial pressures of hydrogen and oxygen are influenced by the prevailing, temperature-dependent saturated vapor pressure of water, especially at low total pressures, e.g. operation at atmospheric pressure. The so-called Buck equation [98] provides a good approximation for the water saturation pressure dependence from temperature ϑ in °C, valid between 0 °C and 100 °C with less than 0.1 % greatest error ($p_{s,\text{H}_2\text{O}}$ in mbar):

$$p_{s,\text{H}_2\text{O}}(\vartheta) = 6.1121 \exp \left(\left(18.678 - \frac{\vartheta}{234.5} \right) \cdot \left(\frac{\vartheta}{257.14 + \vartheta} \right) \right) \quad (36)$$

2.7 Cell Voltage and Efficiency during Operation

If a PEMWE cell is operated, several overpotentials caused by the current flowing through the cell and all its parts are added to the reversible cell voltage. Equation 37 contains a simplified sum of the most important overpotentials ΔE_i (ohmic, activation and transport overpotentials) which are added to the reversible voltage E_{rev} and thus give as a result the cell voltage E_{cell} which can be measured from the outside at the terminal clamps:

$$E_{\text{cell}} = E_{\text{rev}} + \Delta E_{\text{ohm}} + \Delta E_{\text{act}} + \Delta E_{\text{tr}} \quad (37)$$

Ohmic Overpotential

The ohmic overpotential ΔE_{ohm} can be further broken down to the main ohmic resistances present in the cell, the sum of membrane resistance R_{m} and the lumped electric resistance of all electric conducting cell components R_{el} , both area specific with the unit $\Omega \cdot \text{cm}^2$, times the current density i in A/cm^2 :

$$\Delta E_{\text{ohm}} = i \cdot (R_{\text{m}} + R_{\text{el}}) \quad (38)$$

Taking equation 9 for the membrane conductivity σ_{m} and equations 8 or 7 for the anisotropic ($t_{\text{m,wet,aniso}}$) or isotropic ($t_{\text{m,wet,iso}}$) wet membrane thickness, the membrane resistance R_{m} can be calculated by the following equation:

$$R_{\text{m}} = \frac{t_{\text{m,wet}}}{\sigma_{\text{m}}} \quad (39)$$

For all model calculations in this thesis anisotropic swelling only in through-plane direction is assumed, which is most likely to occur for a dry mounted MEA and subsequent hydration in the fully built cell setup as the MEA is fixed in the in-plane direction by the PTLs. The remaining lumped electric resistance of the cell R_{el} is usually small compared to the membrane resistance R_{m} . The largest part of R_{el} is typically the contact resistance R_{c} between PTLs and MEA [16]. It was found by Bernt and Gasteiger to be $\approx 12 \text{ m}\Omega \text{ cm}^2$ for the standard 5 cm^2 laboratory cell setup used also in this thesis.

Activation Overpotential

The second important source of overpotentials is the activation overpotential ΔE_{act} which results from irreversible processes at the electrode surfaces while driving the reactions involved in water splitting at a desired rate. It is the sum of the individual activation overpotentials at the cathode (ΔE_{HER}) and anode side (ΔE_{OER}) of the cell.

$$\Delta E_{\text{act}} = \Delta E_{\text{HER}} + \Delta E_{\text{OER}} \quad (40)$$

As the HER is a fast reaction [52] [53], the corresponding overpotential ΔE_{HER} on typically used Pt-C catalysts is small around $\approx 1 \text{ mV}$ at high current densities of $3 \text{ A}/\text{cm}^2$ (linearized resistance $R_{\text{HER}} \approx 0.3 \text{ m}\Omega \text{ cm}^2$) [16]. It can thus be neglected in the further analysis. However, ΔE_{OER} is comparably large and must be included in the calculation of E_{cell} [99]. In general, the relation between current density and activation overpotentials can be described by the Butler-Volmer equation which is shown here according to the definition used in [100] and [101]:

$$i_{+/-} = i_0 \cdot r f \cdot \left[\exp\left(\frac{\alpha_{\text{a}} \cdot F}{R \cdot T} \cdot \Delta E\right) - \exp\left(-\frac{\alpha_{\text{c}} \cdot F}{R \cdot T} \cdot \Delta E\right) \right] \quad (41)$$

Here, the current density $i_{+/-}$ is related to the overpotential ΔE (positive for anodic reaction and negative for cathodic reaction) via an electrode and reaction specific exchange current density i_0 (A/cm²) and an electrode roughness factor rf (cm²_{metal}/cm²_{geometric}) which are multiplied with a sum of the exponential current to overpotential relations for the anodic reaction (left expression, positive current) and the cathodic reaction (right expression, negative current). The surfaces used

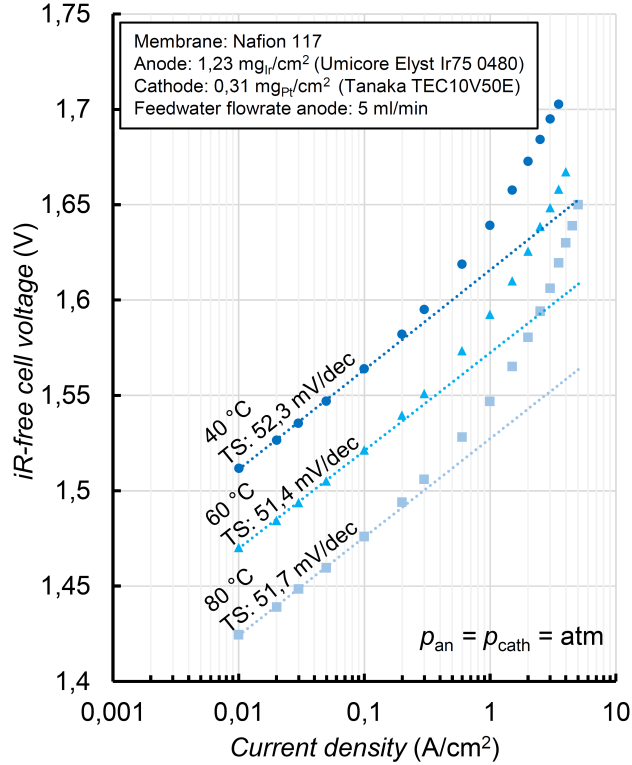


Figure 10: Tafel-slope analysis for three different temperatures (40 °C, 60 °C and 80 °C). Measurement data for iR-free cell voltage obtained from a MEA based on Nafion[®] 117 with an IrO_x-TiO₂ OER catalyst (Umicore Elyst Ir75 0480) at 1.23 mg_{Ir}/cm² and a Pt-C HER catalyst (Tanaka TEC10V50E) at 0.31 mg_{Pt}/cm². All curves were recorded at atmospheric pressure and with 5 ml/min anode side water flowrate in a 5 cm² laboratory cell (see figure 23, panel a)). The resulting Tafel-slopes are almost constant at ≈ 52 mV/dec.

for the calculation of the roughness factor are defined in this work as follows: The metal surface is the electrochemically active surface of the catalyst, e.g. the iridium surface accessible to species, ionomer and electric charge. In contrast, the geometric surface is defined as the flat surface of the electrode. This means that, e.g. for a theoretical roughness factor of $rf = 600$, for each cm² of electrode geometric surface, 600 cm² of electrochemically active iridium metal (or more precisely: metal-oxide) surface is present. The anodic and cathodic charge transfer coefficients α_a and α_c describe the symmetry of the overpotential-to-current characteristic and also the number of electrons transferred in the rate limiting step of the reaction. They can take values between $\alpha_{a,c} = 0.5$ and $\alpha_{a,c} = 2.5$ [100]. For the large positive overpotentials that prevail during OER at the anode, the Butler-Volmer equation can be simplified to the Tafel equation containing only one exponential relation:

$$i_{\text{OER}} = i_0 \cdot rf \cdot \left[\exp \left(\frac{\alpha_a \cdot F}{R \cdot T} \cdot \Delta E_{\text{OER}} \right) \right] \quad (42)$$

Inverting the Tafel equation allows to analytically calculate ΔE_{OER} for a given current density i_{OER} . Using the decadic logarithm of the actual current density i_{OER} normalized by the exchange current density $i_{0,\text{OER}}$ times the electrode roughness rf , all the remaining constants give the so-called Tafel-slope (equation 44) which can be extracted from a linear fit to measured iR-free polarization curves at low current densities ($< 100 \text{ mA/cm}^2$) plotted over a logarithmic current density scale:

$$\Delta E_{\text{OER}} = \frac{2.303 \cdot R \cdot T}{\alpha_a \cdot F} \cdot \log \left(\frac{i_{\text{OER}}}{i_{0,\text{OER}} \cdot rf} \right) \quad (43)$$

$$\text{Tafel Slope} := \frac{2.303 \cdot R \cdot T}{\alpha_a \cdot F} \quad (44)$$

Measured begin of life (BOL) Tafel-slopes for OER catalysts in this work have been 45 mV/dec for a novel $\text{IrO}_2/\text{TiO}_2$ catalyst with low iridium loading ($0.25 \text{ mg}_{\text{Ir}}/\text{cm}^2$) and 52 mV/dec for a Benchmark $\text{IrO}_2/\text{TiO}_2$ catalyst ($2 \text{ mg}_{\text{Ir}}/\text{cm}^2$). This is in good agreement to the results obtained by Bernt et al. for similar catalysts (45 to 50 mV/dec) [16] [10]. For a temperature dependent calculation of the OER activation overpotential, an analysis of measurement data at different temperatures is necessary. Figure 10 contains the iR-free cell voltage of a PEMWE cell at 40 °C, 60 °C and 80 °C, measured in a 5 cm^2 active area laboratory cell setup. The used MEA is based on Nafion[®] 117 with an $\text{IrO}_x\text{-TiO}_2$ OER catalyst (Umicore Elyst Ir75 0480) at a loading of $1.23 \text{ mg}_{\text{Ir}}/\text{cm}^2$. The cathode side uses a Pt-C HER catalyst (Tanaka TEC10V50E) at $0.31 \text{ mg}_{\text{Pt}}/\text{cm}^2$. Using a logarithmic scale for the current density, the Tafel-slopes can be extracted from the linear curve fits in the low current density regime $< 100 \text{ mA/cm}^2$. The resulting Tafel-slopes are relatively constant at $\approx 52 \text{ mV/dec}$ for all three temperatures. At 60 °C this would correspond to a value of $\alpha_a \approx 1.3$, which is within the range of 0.5 to 2.5 given in [100]. In order to calculate the activation overpo-

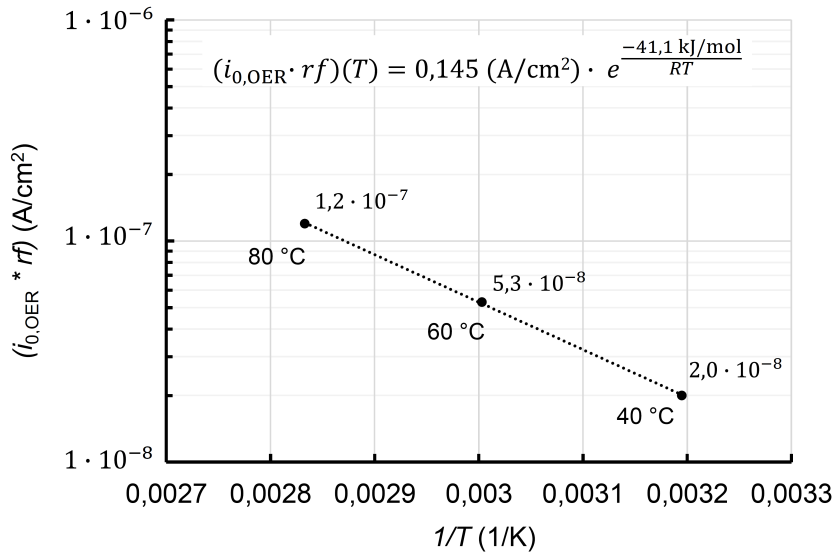


Figure 11: Fitted anode OER exchange current density times electrode roughness factor ($i_{0,\text{OER}} \cdot rf$) over inverted temperature. The analysis is based on the measurement data from figure 10. An Arrhenius approach is well suited to describe the temperature dependence.

tential ΔE_{OER} , also the product of exchange current density and roughness factor ($i_{0,\text{OER}} \cdot rf$) has to be extracted from measurements. Using the data shown in figure 10, the values of ($i_{0,\text{OER}} \cdot rf$) can be fitted to match the measured iR-free cell voltage curves. Figure 11 shows the values for ($i_{0,\text{OER}} \cdot rf$) over the inverted temperature $1/T$. Using a logarithmic scale for the effective exchange

current density in (A/cm^2), a linear trend is visible and thus an Arrhenius approach can be used to describe the temperature dependence. The resulting parameters for rate constant and activation energy are shown in equation 45:

$$(i_{0,\text{OER}} \cdot rf)(T) = 0.145 (\text{A}/\text{cm}^2) \cdot \exp\left(\frac{-41.1 (\text{kJ}/\text{mol})}{RT}\right) \quad (45)$$

With the kinetic parameters Tafel-slope and $(i_{0,\text{OER}} \cdot rf)$ obtained from measurement data as shown in both figures 10 and 11, the activation overpotential ΔE_{OER} can be well described in the relevant temperature range. Nevertheless, the parameters are only valid for the OER catalyst used and, strictly speaking, only at atmospheric pressures and for the specific setup with which the data was recorded. For any other OER catalyst and for higher operating pressures, individual parameters have to be determined. However, the $\text{IrO}_x\text{-TiO}_2$ OER catalyst (Umicore Elyst Ir75 0480) used represents a good standard for PEMWE anodes and thus relatively good estimates can be made with the obtained kinetic parameters.

Transport Overpotentials

The third major source of overpotentials are transport overpotentials. These can be caused by various mechanisms. On the one hand, proton transport in the electrodes causes sheet resistances which are not represented in the high-frequency resistance (HFR) of the cell when the system is analyzed with EIS. The sheet resistances become visible at lower frequencies than the HFR (typically between 0.1 to 10 kHz) and produce the so-called 45°-region in the Nyquist plot [102]. On the other hand, real mass transport overpotentials can be caused by depletion of the water at the reaction zone, e.g. due to local dry running, or an enrichment of the product gases due to restrained removal. Furthermore, mass transport overpotentials can have a strongly nonlinear behavior and, due to the complexity of the multiphase gas-water flow, have so far been sparsely investigated in the field of PEMWE [103]. Following the analysis by Bernt and Gasteiger [16] for electrodes with optimized ionomer content, the proton transport resistance in anode and cathode accounts to ≈ 20 mV and mass transport losses to ≈ 30 mV at $3 \text{ A}/\text{cm}^2$ and atmospheric pressure. Assuming linear behavior, both proton and mass transport losses would sum up to a lumped transport resistance of $R_{\text{tr}} \approx 17 \text{ m}\Omega \text{ cm}^2$. For the further analysis in this thesis, this lumped resistance R_{tr} is used to account for modeling transport overpotentials ΔE_{tr} according to the following equation:

$$\Delta E_{\text{tr}} = i \cdot R_{\text{tr}} \quad (46)$$

Cell Efficiency

In general, calculating the energetic efficiency η of a technical process is done by normalizing the useful net energy output by the net energy input:

$$\eta = \frac{\text{useful energy output}}{\text{energy input}} \quad (47)$$

In this context, it is important to emphasize that different efficiencies can result for the same process depending on how the system boundary is placed. The first approach to evaluate the efficiency of a PEMWE cell is to compare the energy content of the produced hydrogen with the electrical energy input to the cell. Depending on which reference value is used for the energy content of hydrogen, slightly different values result. If the hydrogen is subsequently utilized as a

material, the higher heating value ($\text{HHV} = \Delta H^0 = 286 \text{ kJ/mol}$) is often used as the reference value. In comparison, the lower heating value ($\text{LHV} = 242 \text{ kJ/mol}$) differs by the standard enthalpy of vaporization of water ($\Delta H_{\text{vap}, \text{H}_2\text{O}} = 44 \text{ kJ/mol}$). However, the LHV is also almost equal to the minimum electrical energy requirement for water splitting $\Delta G^0 = 237 \text{ kJ/mol}$ and is thus often used as a reference value if the hydrogen is for example subsequently used to generate electricity in a fuel cell. As it was shown already in equations 31 and 32, specific enthalpies or energy quantities ΔH can be translated into an electrical potential difference E using the Faraday constant F and the number of electrons transferred z , with $z = 2$ for water electrolysis:

$$E = \frac{\Delta H}{zF} \quad (48)$$

Thus, with equation 48 also electrical potential differences can be used directly to evaluate the electric or voltage efficiency of the cell, e.g. in reference to the HHV of hydrogen η_{elHHV} :

$$\eta_{\text{elHHV}} = \frac{\Delta H^0}{\Delta H_{\text{el}, \text{in}}} = \frac{\frac{\Delta H^0}{zF}}{\frac{\Delta H_{\text{el}, \text{in}}}{zF}} = \frac{E_{\text{HHV}}^0}{E_{\text{cell}}} = \frac{1.48 \text{ V}}{E_{\text{cell}}} \quad (49)$$

For η_{elLHV} and $\eta_{\text{el}\Delta G^0}$, the respective reference potentials are lower at 1.25 V and 1.23 V:

$$\eta_{\text{elLHV}} = \frac{1.25 \text{ V}}{E_{\text{cell}}} \quad (50)$$

$$\eta_{\text{el}\Delta G^0} = \frac{1.23 \text{ V}}{E_{\text{cell}}} \quad (51)$$

However, the voltage efficiency η_{el} of the cell does not account for permeation losses of the product gases. Therefore, to calculate the real cell (or stack) efficiency η_{cell} , the voltage efficiency needs to be multiplied with the faradaic efficiency η_{f} which relates the usable hydrogen molar flow $\dot{n}_{\text{H}_2, \text{out}}$ to the molar flow of total produced hydrogen $\dot{n}_{\text{H}_2, \text{produced}}$

$$\eta_{\text{f}} = \frac{\dot{n}_{\text{H}_2, \text{out}}}{\dot{n}_{\text{H}_2, \text{produced}}} = 1 - \frac{\dot{n}_{\text{H}_2, \text{perm}} + 2 \cdot \dot{n}_{\text{O}_2, \text{tr}}}{\dot{n}_{\text{H}_2, \text{produced}}} = 1 - \frac{i_{\text{H}_2, \text{perm}} + i_{\text{O}_2, \text{tr}}}{i_{\text{cell}}} \quad (52)$$

$$\eta_{\text{cell}} = \eta_{\text{el}} \cdot \eta_{\text{f}} \quad (53)$$

The faradaic efficiency varies with current density with low values in the part load regime and approaches high values close to 1 at high current densities. This topic is discussed more into detail in sections 2.8 and 5.3.

System Efficiency

Finally, the overall efficiency of a PEMWE system η_{PEMWE} is influenced by several additional energy consumptions and losses of the systems auxiliary components like pumps, power electronics, safety and control equipment, heaters, coolers etc. Nevertheless, to simplify the calculation of the overall system efficiency, a lumped balance of plant efficiency η_{BOP} can be generated. However, it has to be stated that in contrast to η_{cell} , the BOP efficiency η_{BOP} depends not on the current density i , but on the relative normalized system power P_{sys} which in turn strongly depends on the definition of the systems maximum current/power density. Thus, to use the following equation 54, the relation of current density i to the correspondent relative system power needs to be known.

$$\eta_{\text{PEMWE}} = \eta_{\text{el}}(i) \cdot \eta_{\text{f}}(i) \cdot \eta_{\text{BOP}}(P_{\text{sys}}) \quad (54)$$

Typically, η_{BOP} is $\approx 90\%$ for most of the operating range [11]. However, especially in the lower partial load regime, η_{BOP} can be lowered significantly due to the relatively high constant power consumption of BOP components compared to the actual electrolysis stack power and furthermore due to the poor transfer characteristics of the power electronics below $\approx 20\%$ net load [104]. A straightforward way to model the BOP efficiency curve is to assume a constant BOP power consumption of 2.5 % of the PEMWE system peak power, which is a typical value for larger systems between 1 and 100 MW [105]. In this case, the maximum BOP efficiency is reached at the systems maximum power. Additionally, the transfer efficiency of the power electronics for intermediate and high normalized power greater 20 % is also assumed to be constant and reaching high maximum values $\eta_{\text{pel,max}} > 95\%$ [106]. Combining both assumptions results in equation 55 for η_{BOP} :

$$\eta_{\text{BOP}}(P_{\text{sys}}) = \frac{P_{\text{sys}} - P_{\text{BOP}}}{P_{\text{sys}}} \cdot \eta_{\text{pel,max}} \quad (55)$$

Figure 12 shows the calculated curve (straight blue line) of η_{BOP} (equation 55) for a constant BOP power consumption of 2.5 % of the peak power and a maximum power electronics efficiency $\eta_{\text{pel,max}} = 97.5\%$. Furthermore, figure 12 contains the BOP efficiency curve extracted from real life data of the Energiepark Mainz 6.5 MW peak power PEMWE system from Siemens (dashed blue line). Here, η_{BOP} is derived from the total system efficiency (HHV) given in [14] and the Siemens Silyzer PEMWE system polarization curve given in [11] which allows for a calculation of η_{el} . The missing faradaic efficiency η_{f} to obtain η_{BOP} is modelled for operating parameters of 35 bar cathode pressure and 60 °C cell temperature assuming a Nafion[®] 117 based MEA. The resulting synthetic polarization curve closely resembles the given Siemens Silyzer polarization curve from [11]. The dot-dashed line in green in figure 12 shows a 10 % optimized η_{BOP} curve of the Energiepark Mainz system. As the modelled η_{BOP} curve is in the corridor of the current and optimized Energiepark Mainz η_{BOP} curves, it should be a reasonable approximation of real BOP efficiencies over the power range of larger PEMWE systems with peak powers greater 1 MW. Figure 12 shows also

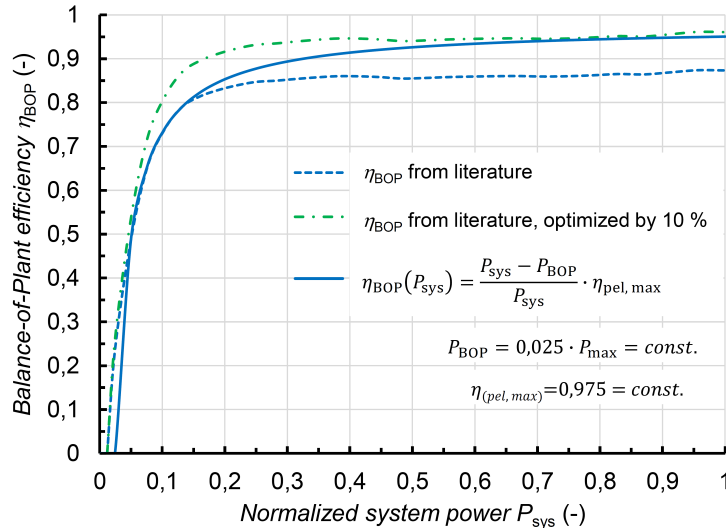


Figure 12: BOP efficiency curves over the peak power normalized system power P_{sys} of the Energiepark Mainz Siemens Silyzer system extracted from literature data [14] [11], blue dashed line and 10 % optimized BOP efficiency green dot-dashed line. The straight blue line shows the synthetic BOP efficiency for an assumed constant BOP power consumption of 2.5 % of the system peak power and a maximum power electronics efficiency of 97.5 %.

that $\eta_{\text{BOP}}(P_{\text{sys}})$ is zero for peak power normalized powers smaller than the constant BOP power. As the electrolyzer stack has its zero power and current density at $P_{\text{sys}} = P_{\text{BOP}}$, a slightly different BOP efficiency calculation is convenient for a current density based calculation and visualization of η_{PEMWE} .

$$\eta_{\text{BOP}}(i) = \frac{P_{\text{stack}}}{P_{\text{stack}} + P_{\text{BOP}}} \cdot \eta_{\text{pel,max}} \quad (56)$$

Here, the electrolyzer stack power P_{stack} is used, which is defined by the following equation 57:

$$P_{\text{stack}} = P_{\text{sys}} - P_{\text{BOP}} \quad (57)$$

2.8 Operation Characteristics

In this chapter the influences of the operating parameters temperature, pressure and current density as well as a variation of the membrane thickness on the overall PEMWE cell and system efficiency is discussed. All calculations shown in the following are based on the theory, equations and data presented in the preceding chapters.

Influence of Temperature and Pressure on Cell Voltage

Figure 13 contains PEMWE cell polarization curves for three different temperatures (40 °C, dot symbols, 60 °C, triangle symbols and 80 °C, square symbols) at 10 bar cathode pressure and atmospheric anode pressure. In addition for 60 °C, the polarization curves for 1 bar (dashed line) and 100 bar (dot-dashed line) cathode pressure are shown as well. For all curves, a Nafion[®] 117 membrane at a water content of $\lambda = 21$ and anisotropic swelling in through-plane direction only is assumed. This swelling only in through-plane direction is most likely to happen at dry mounting of the membrane in the cell and subsequent hydration inside the fully built cell setup where the membrane is fixed in the in-plane direction by the PTLs. It is clearly visible, that higher temperatures significantly lower the cell voltage due to a lowered membrane resistance and a lowered activation overpotential. At a cell voltage of 1.8 V, the current density can be more than doubled from 0.6 A/cm² at 40 °C to 1.3 A/cm² at 80 °C. However, using thinner membranes, the reduction in cell voltage at increased cell temperature is less intense, as the share of the membrane resistance in total cell resistance is lowered as well. Furthermore, an increase in operating temperature can be detrimental for the stability of various cell components such as membranes, electrodes and PTLs. For a future large scale application where high service life ideally up to 90,000 h [12] is desired, a limitation to intermediate temperatures around 60 °C seems a good trade of between high efficiency and sufficient stability [107] [108] [109].

In contrast, an increase in cathode pressure causes an increase in cell voltage of approximately 33 mV per decade at 60 °C, which is constant over the current density range. Though the compression of hydrogen in the PEMWE cell itself is efficient compared to the use of external compressors [110], at high cathode pressures also the Faraday efficiency decreases due to permeation losses of the product gases. Thus, determining an optimum operating pressure for a PEMWE system is a difficult multiparametrical task and depends strongly on the pressure target value which is demanded by the application for which the hydrogen is produced. Looking at future large scale applications, where the produced hydrogen is to be subsequently transported over long distances, cryo-hydrogen seems to be a reasonable form of storage. In this case, the hydrogen production pressure of the PEMWE system can be limited to low values between ≈ 10 bar to 20 bar [111]. As shown by Tjarks et al. [112], this rather low pressure level is well suited for high current density

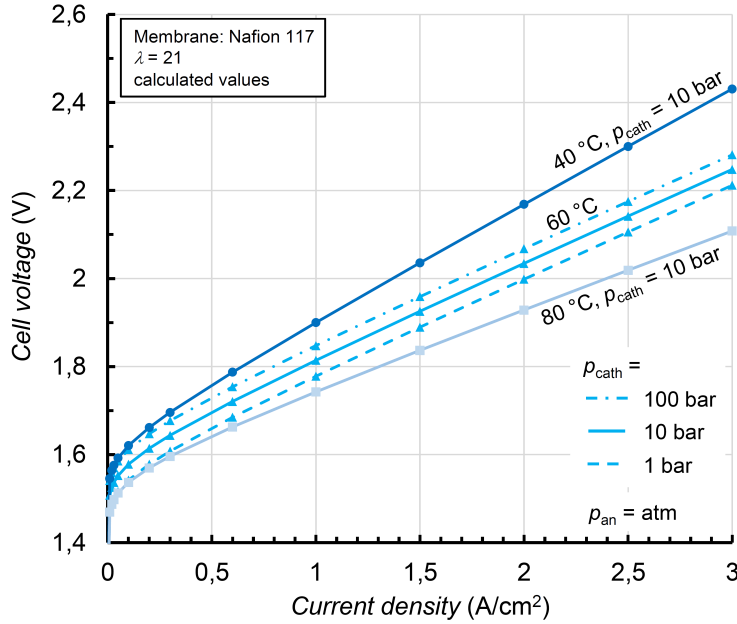


Figure 13: Calculated polarization curves for a MEA based on Nafion[®] 117 with a water content of $\lambda = 21$ (anisotropic swelling only in through-plane direction) at three temperatures (40 °C, 60 °C and 80 °C) and 10 bar cathode pressure and 1 bar anode pressure. For 60 °C, also curves for 1 bar and 100 bar cathode pressure are included.

operation with thin membranes. Thus, for the further analysis of the cell and system efficiency, a cathode pressure of 10 bar and atmospheric anode pressure are chosen.

Influence of Membrane Thickness on Cell Voltage

As mentioned before, a significant share of losses in PEMWE cells arise due to the membrane resistance. Thus, using thinner membranes can effectively reduce the cell voltage with the greatest effect at high current densities. In order to visualize the possible loss reduction and lowering of the cell voltage, figure 14 contains calculated polarization curves for PEMWE cells using Nafion[®] membranes of different thicknesses at 10 bar cathode pressure, atmospheric anode pressure and 60 °C. Comparing the current density at a cell voltage threshold for 70 % (LHV) voltage efficiency at 1.79 V shows a possible increase from 0.9 A/cm² for Nafion[®] 117 (178 μm dry thickness) to 2.1 A/cm² for Nafion[®] 212 (51 μm dry thickness) and 2.8 A/cm² (28 μm dry thickness) for Nafion[®] XL. If a theoretical 15 μm membrane would be possible to manufacture and integrate into a PEMWE cell/stack, even a 3.7-fold increase in current density up to 3.4 A/cm² would be gainable. Using a 60 % (LHV) voltage efficiency threshold at 2.08 V instead of 70 % (LHV), the attainable current densities are ≈ 2.5 to 3 times higher, reaching 5.5 A/cm² for Nafion[®] 212 and 7.5 A/cm² for Nafion[®] XL.

Influence of Membrane Thickness on Power-Specific Iridium Loading

As illustrated above, thin membranes allow for a significant increase in current and power density of a PEMWE system and thus also directly facilitate the realisation of lower power specific anode side iridium catalyst loadings. To discuss this effect in more detail, figure 15 shows the relationship between the membrane thickness and the achievable power-specific iridium loading at 70 % (LHV)

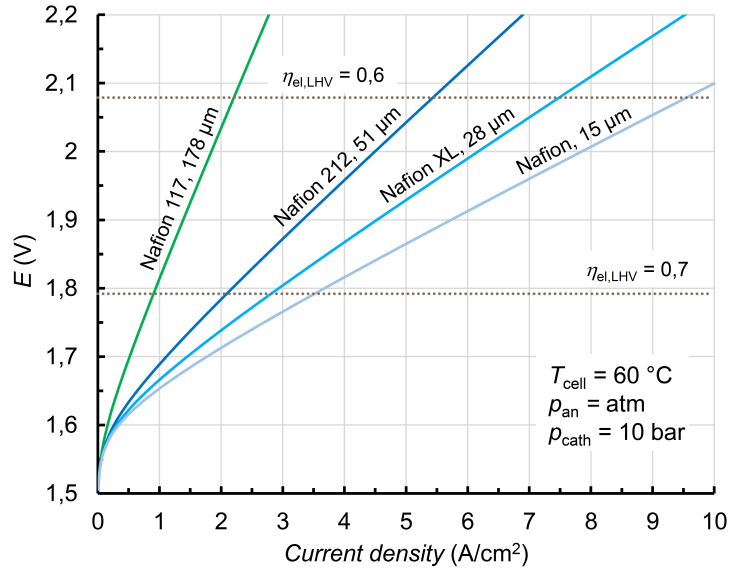


Figure 14: Calculated polarization curves for PEMWE cells with different membrane thicknesses from current industry standard of 178 μm (Nafion[®] 117) down to a theoretical value of 15 μm . The assumed membrane material is Nafion[®] at a water content of $\lambda = 21$ (anisotropic swelling only in through-plane direction). The cell temperature is 60 $^{\circ}\text{C}$, anode pressure is at 1 bar and cathode pressure at 10 bar.

voltage efficiency and an anode catalyst loading of 1 $\text{mg}_{\text{Ir}}/\text{cm}^2$ at temperatures of 40 $^{\circ}\text{C}$, 60 $^{\circ}\text{C}$ and 80 $^{\circ}\text{C}$. The main takeaways are:

- Reducing the membrane thickness drastically from about 178 μm to 15 μm would reduce the power-specific iridium loading by about half an order of magnitude.
- The same power-specific iridium loading can be reached for Nafion[®] 212 at 80 $^{\circ}\text{C}$ as for Nafion[®] XL at 60 $^{\circ}\text{C}$. Thus, at lower membrane thicknesses, high operating temperatures are less crucial for reaching high efficiency and low power-specific iridium loading.
- Also at very low membrane thicknesses, still a 10 to 20-fold reduction of the anode side catalyst loading is necessary to reach power-specific iridium loadings in the target region around $\approx 0.01 \text{ g}_{\text{Ir}}/\text{kW}_{70\% \text{ (LHV)}}$ for a future large scale application of PEMWE.

Influence of Membrane Thickness on Faraday Efficiency

In contrast to the significantly improved voltage efficiency, the faradaic efficiency is lowered when using thinner membranes. As discussed before, Nafion[®] membranes are gas tight in terms of convective transport, but gases can nevertheless permeate through the membrane material. According to equation 11 and 18, the molar flux of hydrogen and oxygen due to permeation is indirect proportional to the membrane thickness. Thus, thinner membranes increase the permeation losses and decrease the faradaic efficiency of the cell. Furthermore, a second effect comes to play with product gas transport across the membrane which was already briefly explained before: The oxygen which is permeating or transported via water from anode to cathode is only lowering the faradaic efficiency of the cell as it is reacting back to water at the cathode catalyst layer (besides small oxygen fractions up to 700 ppm that can still be present in the cathode gas stream due to edge

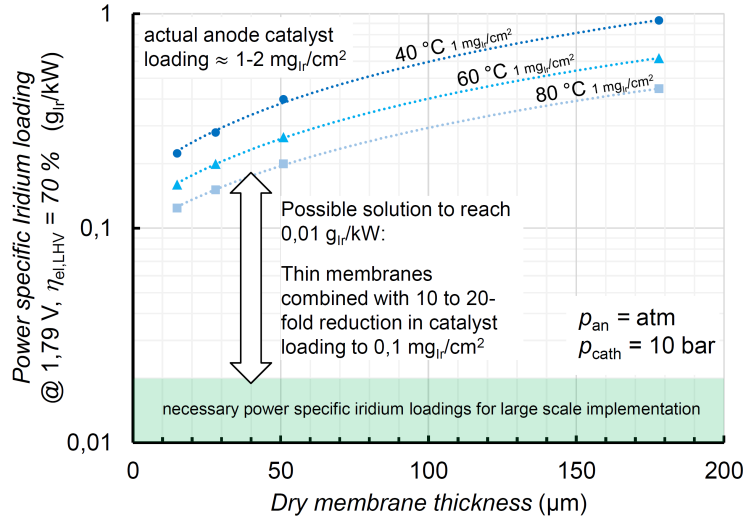


Figure 15: Calculated values for power-specific iridium loading in dependence of operating temperature and membrane thickness for a PEMWE cell with $1 \text{ mg}_{\text{Ir}}/\text{cm}^2$ anode catalyst loading.

effects [113]). In contrast, the permeated hydrogen is causing a security problem at the anode side. It is not reacting back to water at the anode catalyst layer and persists in the anode gas stream. The lower explosive limit for hydrogen in oxygen is at $\approx 4 \%$ and with a 50 % safety margin, a hydrogen concentration at the anode side of 2 % should never be exceeded during operation. To visualize these two effects, Figure 16 shows the influence of a lowered membrane thickness on faradaic efficiency as well as on the critical minimum current density below which the hydrogen concentration at the anode side is exceeding 2 %. At the depicted operating conditions, for all

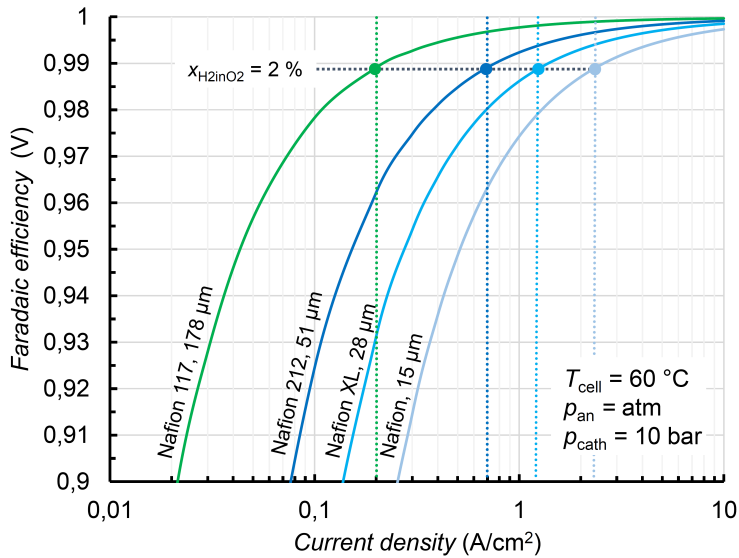


Figure 16: Calculated faradaic efficiency curves for different membrane thicknesses at $60 \text{ }^\circ\text{C}$ and 10 bar cathode and 1 bar anode side pressure. Minimum current densities for less than 2 % hydrogen in oxygen are marked by dotted lines.

membrane thicknesses a faradaic efficiency greater 99 % is reached for current densities above $\approx 2 \text{ A}/\text{cm}^2$. Thus, the effect of the reduced faradaic efficiency on the cell efficiency is limited, as

with thinner membranes also higher current densities are possible as discussed before and shown in figure 14. Nevertheless, the minimum current densities for less than 2 % hydrogen in oxygen are increasing by an order of magnitude for a reduction of dry membrane thickness from 178 μm (0.2 A/cm²) to 15 μm (2.4 A/cm²). This is especially restraining an operation of cells with thin membranes at low current densities: A very high cell efficiency could be reached, but operation without a recombination catalyst will produce flammable gas mixtures at the anode side. Therefore, without a recombination catalyst, a tuning of maximum current and power density of the system is necessary to allow operation at both high efficiency and safety. In the case of an emergency stop of the electrolyser (= instant reduction of current density to $i = 0$ A/cm²), usually the high pressure tubings and vessels downstream of the electrolyser stack should be rapidly disconnected via solenoid valves and the cathode compartment of the cell or stack should be vented to reduce the hydrogen pressure quickly. Additionally, also a purging of the anode side compartment with compressed air can be helpful to prevent a possible hydrogen accumulation due to permeation processes of the still present hydrogen inventory in the MEA.

Cell Efficiency at Variable Membrane Thickness

Since, as already described, the faraday efficiency and the voltage efficiency develop in opposite ways when the membrane thickness is reduced, a separate presentation of the cell efficiency in dependence of the membrane thickness is useful. Two graphs show the development of the calculated cell efficiency over the current density for different membrane thicknesses at 60 °C (figure 17) and 80 °C (figure 18) at 10 bar cathode and 1 bar anode pressures. As both figures show a qualitatively similar general behaviour with only quantitative differences, they are discussed at once in the following. Two general trends for the cell efficiency are visible when lowering the

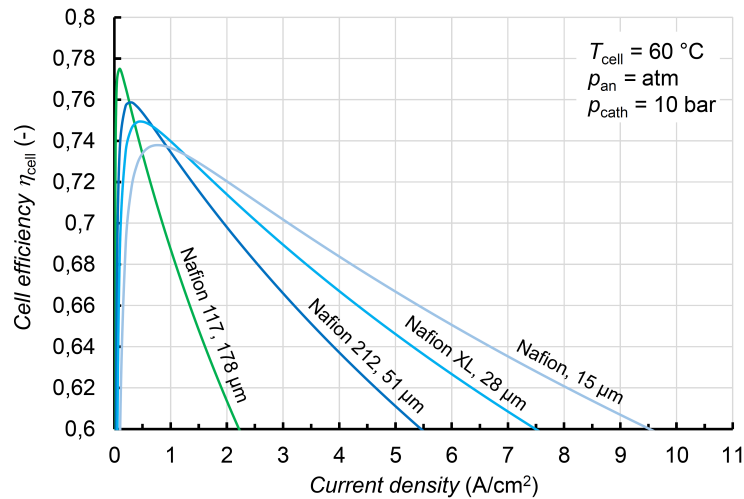


Figure 17: Calculated cell efficiency for PEMWE MEAs at 60 °C based on Nafion[®] membranes of different dry thicknesses at a water content of $\lambda = 21$ (anisotropic swelling only in through-plane direction).

membrane thickness: In the low current density regime up to ≈ 1.5 A/cm², the highest obtainable cell efficiency can be reached with thicker membranes as the faradaic efficiency is higher and the voltage efficiency is still high, also for thick membranes. In contrast, at current densities higher than ≈ 1.5 A/cm², the trend is inverted and cells with thinner membranes reach significantly higher efficiencies than cells with thicker membranes. At 60 °C and 60 % (LHV) as the lower cell

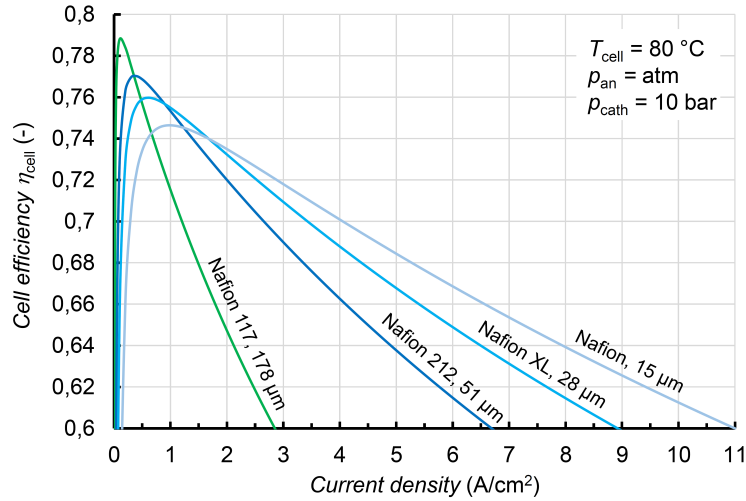


Figure 18: Calculated cell efficiency for PEMWE MEAs at 80 °C based on Nafion[®] membranes of different dry thicknesses at a water content of $\lambda = 21$ (anisotropic swelling only in through-plane direction).

efficiency threshold, it seems possible to reach current densities as high as 7.5 A/cm² with Nafion[®] XL membranes. Even higher current densities around 9 A/cm² could be possible at 80 °C. Looking at a higher cell efficiency threshold of 70 % (LHV), the curves for different membrane thicknesses are closer together and the maximum current densities are significantly reduced. However, a cell equipped with a Nafion[®] XL membrane would still reach 2.5 A/cm² at 60 °C and 3.5 A/cm² at 80 °C - in both cases a ≈ 3 -fold higher maximum current density is reached than for cells with Nafion[®] 117. Based on both figures, the definition of the maximum operating point and its influence on the final system efficiency will be discussed in the following.

System Efficiency at Variable Membrane Thickness

Compared to the cell efficiency described above, which can be given as a straightforward function of current density, the system efficiency depends on the more or less arbitrary definition of a maximum operating point of the PEMWE cell or stack. Thus, in this last section on the operation characteristics, the effect of two different maximum working points at 60 % and 70 % (LHV) cell efficiency is visualized and explained. Again, the results are shown for 60 °C and 80 °C cell temperature with all other operating parameters staying the same. Additionally, the calculated minimum current densities for a hydrogen in oxygen content less than 2 % are marked for each curve.

Looking at the first two figures 19 and 20 for a maximum current density set at 60 % (LHV) cell efficiency reveals several key findings:

- The maximum system efficiencies are only slightly different for 60 °C and 80 °C (≈ 1 % higher at higher temperatures) and are furthermore only weakly lowered when using thinner membranes (≈ 1 % difference between Nafion[®] 117 with 178 μm dry thickness and a fictive Nafion[®] with 15 μm dry thickness).
- Mean system efficiencies over the operating range are close to 60 % (LHV) for all membrane thicknesses.

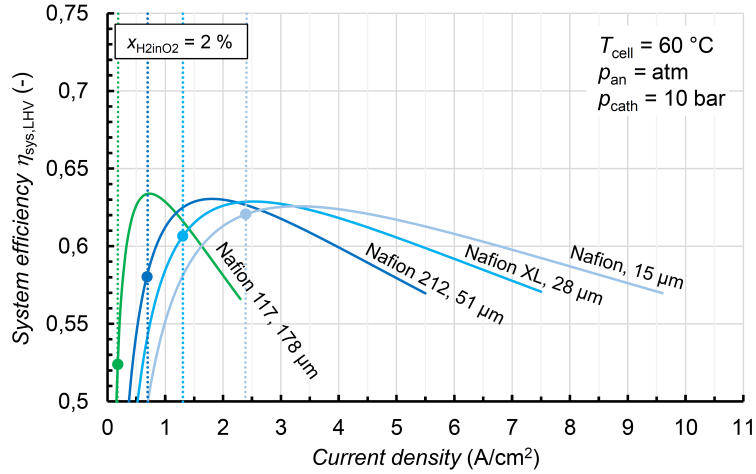


Figure 19: Calculated system efficiency for PEMWE MEAs at 60 °C based on Nafion® membranes of different dry thicknesses at a water content of $\lambda = 21$ (anisotropic swelling only in through-plane direction). The maximum current density is set at the downward crossing of the cell efficiency curve with a 60 % (LHV) threshold. Additionally, calculated minimum current densities for a hydrogen in oxygen content in the anode product gas of less than 2 % are marked for each curve.

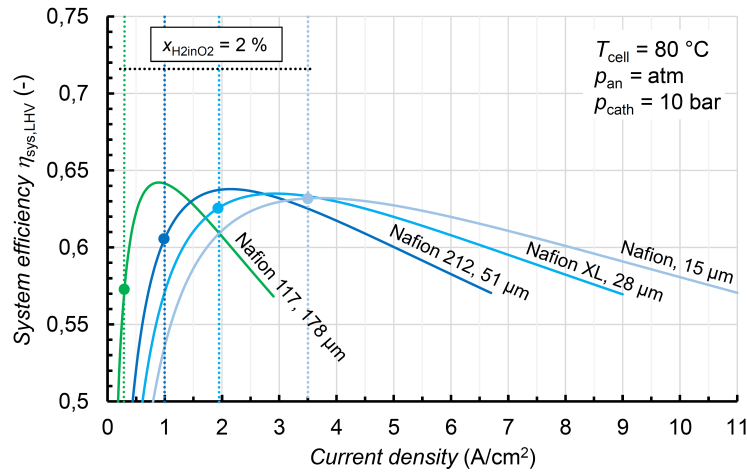


Figure 20: Calculated system efficiency for PEMWE MEAs at 80 °C based on Nafion® membranes of different dry thicknesses at a water content of $\lambda = 21$ (anisotropic swelling only in through-plane direction). The maximum current density is set at the downward crossing of the cell efficiency curve with a 60 % (LHV) threshold. Additionally, calculated minimum current densities for a hydrogen in oxygen content in the anode product gas of less than 2 % are marked for each curve.

- Operation at 80 °C allows for higher maximum current densities, with a stronger effect for thin membranes (e.g. up to 11 A/cm² for the fictive Nafion® with 15 μm dry thickness and still up to 9 A/cm² for Nafion® XL).
- The minimum current densities for less than 2 % hydrogen in oxygen content in the anode side product gas are shifted towards higher current densities at higher operating temperatures.
- The current density turndown ratio without recombination catalyst (= the maximum current density divided by the minimum current density for operation at less than 2 % hydrogen in oxygen) is lowering with thinner membranes and higher temperatures. A maximum value of

12 is reached for Nafion[®] 117 at 60 °C. A minimum of 3.2 results for a fictive Nafion[®] with 15 μm dry thickness at 80 °C.

Changing the definition of the peak power set point to 70 % (LHV) cell efficiency leads to the results shown in figures 21 and 22. Again, several key findings can be gathered:

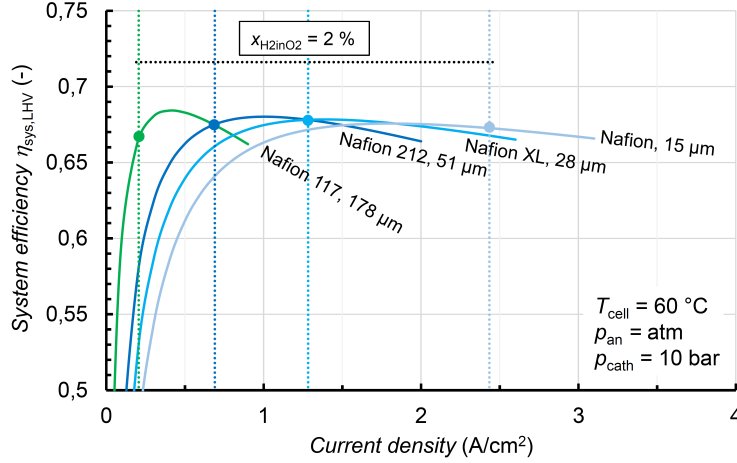


Figure 21: Calculated system efficiency for PEMWE MEAs at 60 °C based on Nafion[®] membranes of different dry thicknesses at a water content of $\lambda = 21$ (anisotropic swelling only in through-plane direction). The maximum current density is set at the downward crossing of the cell efficiency curve with a 70 % (LHV) threshold. Additionally, calculated minimum current densities for a hydrogen in oxygen content in the anode product gas of less than 2 % are marked for each curve.

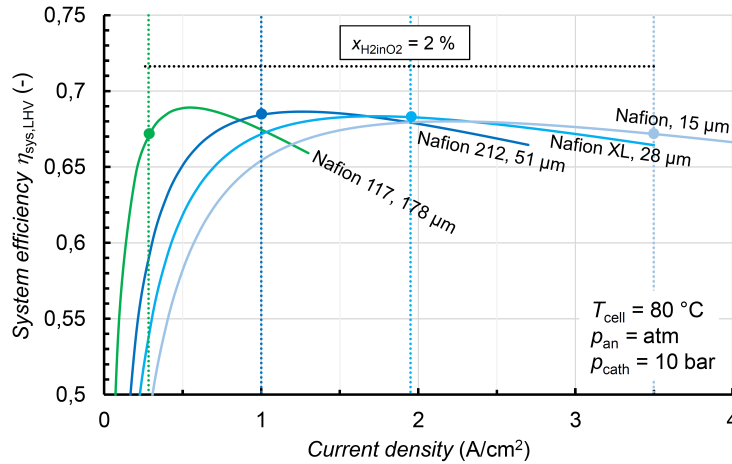


Figure 22: Calculated system efficiency for PEMWE MEAs at 80 °C based on Nafion[®] membranes of different dry thicknesses at a water content of $\lambda = 21$ (anisotropic swelling only in through-plane direction). The maximum current density is set at the downward crossing of the cell efficiency curve with a 70 % (LHV) threshold. Additionally, calculated minimum current densities for a hydrogen in oxygen content in the anode product gas of less than 2 % are marked for each curve.

- The achievable maximum system efficiencies are about 5 % higher than the ones for a 60 % (LHV) cell efficiency peak power definition. However, none of cells with different membrane thicknesses has a maximum system efficiency higher than 70 % (LHV).

- The course of the system efficiency curves is very similar to the ones obtained with 60 % (LHV) cell efficiency peak power definition in terms of maximum and mean system efficiency differences at varying membrane thicknesses.
- As the minimum current densities for less than 2 % hydrogen in oxygen in the anode side product gas are invariant with the peak power current density definition, the current density turndown ratios for a safe operation without a recombination catalyst are significantly lowered approaching a minimum value of 1.1 for a fictive Nafion[®] with 15 μm dry thickness at 80 °C, which is equivalent to a single constant working point.

3 Main Research Questions

With the theoretical background from the previous chapters and the analysis conducted in the last section towards PEMWE operation characteristics, several research questions towards cell improvement strategies can be derived, that arise when PEMWE is to be used on a large scale at an installation rate of ≈ 100 to 200 GW/year.

As shown in figure 15, in order to reach the target values of $0.01 \text{ g}_{\text{Ir}}/\text{kW}_{70\% \text{ (LHV)}}$ for the power specific iridium loading of PEMWE anodes, two measures have to be taken at once: The first one is the use of thin membranes ($\approx 50 \text{ }\mu\text{m}$) to increase the power density and the second one is the application of improved or newly developed OER catalysts with 10 to 20-fold lower iridium loading around $0.1 \text{ mg}_{\text{Ir}}/\text{cm}^2$. Furthermore, thin membranes allow for an effective lowering of the CAPEX for PEMWE systems due to a significantly higher maximum operating current density while keeping high efficiency. As an example, the use of a Nafion[®] XL membrane with $28 \text{ }\mu\text{m}$ dry thickness instead of a Nafion[®] 117 membrane with $178 \text{ }\mu\text{m}$ dry thickness could theoretically allow for a ≈ 3 -fold increase in current density, as shown in figure 17. Thus, at $\approx 50\%$ share for the stack in total system CAPEX [50], the use of thin membranes has the potential to lower the overall CAPEX by $\approx 40\%$, or with ≈ 1000 to 2000 EUR/kW CAPEX cost [11], a direct cost reduction of 400 to 800 EUR/kW might be possible. However, all the effort in reducing the power specific iridium loading and CAPEX is to no purpose, if the system shows significant degradation and shortened lifetime. Furthermore, not only low cost but also the ecological impact of PEMWE systems is of high relevance.

Therefore, the main questions regarding the use of thin membranes and low-loaded OER catalysts in future large scale PEMWE systems which shall be addressed by this thesis are listed below:

- Does the operation of PEMWE systems for hydrogen production in future energy systems have a positive effect in terms of lowering of the overall greenhouse gas emissions compared to fossil hydrogen production? What is the impact of higher current densities on the results?
- Is the fabrication, integration and operation of thin MEAs (e.g. Nafion[®] XL) in PEMWE cells possible? Are the achievable current densities and voltage efficiencies in line with the calculated results? Is the high power density and heat generation associated with high current density operation posing a problem?
- Is the hydrogen permeation from cathode to anode side influenced by high current density operation?
- How stable are iridium OER catalysts and what are the main influences in their stability?
- How is the performance of PEMWE cells with low iridium loaded anodes using tailored catalyst designs and what are the long-term catalyst degradation rates?

4 Methods & Experimental Techniques

4.1 Electrode and MEA Preparation

For the experiments both industrial MEAs (Greenerity GmbH, Germany) and self-made MEAs were used. In the following, the electrode and MEA preparation techniques applied for producing self-made MEAs are explained.

Electrode Preparation

Starting from the catalyst powders, the first step towards functional PEMWE electrodes is the preparation of catalyst inks. For the cathodes a HER catalyst based on platinum nanoparticles supported on highly disperse carbon (46.7 wt% Pt/C TEC10V50E by Tanaka, Japan on Vulcan XC72 carbon) was used. In contrast, for the anode side OER depending on the actual conducted experiments two different catalysts were used: An IrO₂ based catalyst (Elyst Ir75 0480 by Umicore, Germany with 75 wt% Iridium content) on a TiO₂ support and an Ir-black catalyst (Alfa Aesar IrO_x 2H₂O Premion). All catalyst inks were prepared by mixing catalyst powder, analytic grade isopropanol or acetone and ultrapure water with Nafion[®] ionomer solution (20 wt% of ionomer content, type D2021 by IonPower, USA) on a roller mill with 5 mm zirconia grinding balls (\approx 1 g/ml ratio of weight of zirconia balls to mixing recipient volume) for 24 h at 180 rpm. Plastic recipients were used for mixing and were sealed with Parafilm[®] to prevent random opening of the bottles during mixing. Special care has to be taken when initially pouring the solvent in non-oxidic PGM powders (e.g. Ir-black, Pt-C catalysts) to prevent ignition. Thus, for safety reasons the ink components are blended in a glovebox under nitrogen atmosphere.

With the finished inks, various processes can be used to manufacture electrodes for PEMWE cells [114]. For the electrodes in the present work, Mayer-rod coating was used exclusively. Here, the catalyst ink is coated on a substrate (typically high temperature resistant plastic film) by the use of Mayer-rods (K Bar, RK PrintCoat Instruments Ltd) of different sizes to obtain different coating thicknesses. The coating machine used to drive the Mayer-rods in a controlled speed (\approx 3 cm/s) over the plastic decal film (typically 50 μ m thick PTFE foil from Angst+Pfister, Germany) was a K Control Coater by RK PrintCoat Instruments Ltd. To achieve a good coating quality, a thoroughly cleaned glass pane support with a bubble-free, clean plastic film on top, adhered by isopropanol, is essential. The plastic film is ideally of a conical shape with the wider section at the beginning of the coating to prevent wrinkling at the edges when the coating rod moves over the film. After the coating process, the decal films need to be dried to remove all solvent from the electrode layer. This is done at room temperature first until the coating looks superficially dry, followed by about 0.5 h to 1 h in a ventilated oven at 60 °C. Subsequently, the coated decal films can be die cut to obtain the desired active area format.

MEA Preparation

In the next step, a hot-press is used to produce MEAs from the previously coated electrodes on plastic decal films and membranes. The hot-pressing technique is characterized by an increase of the temperature of the press plates above the glass-transition-point of the membrane ionomer and ionomer phases of the electrodes. Thus, when applying an elevated pressure by the press on the sandwich of membrane and electrodes, membrane ionomer and ionomer phases of the electrodes fuse together at their interfaces. In this way, a durable composite, the membrane-electrode-assembly (MEA), is formed. The assembly process starts with sandwiching membrane and the electrode

decals blister-free between cleaned and dust-free Kapton[®] foils. The cathode and anode decals are weighed before the hot pressing and need to be aligned accurately in the middle of the membrane with the film sides pointing to the Kapton[®] foils. Expanded PTFE sheets on both sides of the sandwich (Gylon[®], Type 3545, 2 mm thick, Garlock[®], ENPRO Industries Inc.) on top of the Kapton[®] foils are used to balance the pressure on the surface during hot-pressing. The sandwich is pressed for 3 min at 155 °C and 2.5 MPa (Collin P200 hot-press). Finally, the plastic decal films are removed carefully and weighed to calculate the catalyst loadings based on the ink recipes and the weight differences of the decal films before and after hot-pressing. The MEAs are now ready for use in the different cell hardware.

4.2 Electrochemical Cells & Stacks

In this work, several questions concerning PEMWE cells are addressed with respect to their applicability for large-scale hydrogen production in the GW scale. This also requires different specialized cells and stacks, which were either developed in-house, reused from earlier developments at ZAE Bayern, or provided by industry partners. The three different systems used in this thesis are depicted in figure 23 and are described in the following.

Single Cell, 5 cm² Active Area

The basic laboratory cell setup (see figure 23, panel a)) used in this work was originally developed by Bernt and Gasteiger [16] at ZAE Bayern and Chair of Electrochemistry, Technical University of Munich (TEC-TUM). The cell setup is suitable for pressurized operation up to 30 bar on both anode and cathode side and for high temperatures exceeding 80 °C. Furthermore, the cell design is optimized for low loss operation by using gold-plated flow fields and a high quality anode side PTL sinter material (from Mott Corporation, USA) with a porosity of $\approx 50\%$ and a thickness of $280 \pm 10 \mu\text{m}$. In combination with the well balanced pressure distribution over the flow field active area, the cell reaches a typical overall electronic resistance (= total electronic resistance of the cell setup and electronic contact to MEA) of $\approx 12 \text{ m}\Omega\text{cm}^2$ [16]. With these specifications, this high-performance cell setup is well suited for testing PEMWE limitations at high current density operation.

The cell assembly is done following the description in [16] using hard-stop PTFE flat gaskets (nominal thickness 250 μm) for sealing and thin PTFE subgaskets (nominal thickness 10 μm) at anode and cathode side of the cell for short-circuit protection at the edges of the PTLs. The gasket thickness was chosen in order to reach a good compression of the cathode side carbon paper PTL (TGP-H-120T from Toray, no MPL, 20 wt% PTFE, 370 μm uncompressed thickness) and thus also a good overall cell compression of $\approx 1.7 \text{ MPa}$ on the active cell area [16]. Expanded PTFE sheets (Gylon[®], Type 3545, 2 mm thick, Garlock[®], ENPRO Industries Inc.) are used on both sides of the cell between the current collectors and the end plates for a balanced pressure distribution in the cell. A maximum torque of 10 Nm was set on each of the 12 bolts of the cell, with several intermediate steps until reaching full stress.

Galvanic Redeposition Free Single Cell, 5 cm² Active Area

In addition to the existing laboratory cell design, another specialized 5 cm² cell (see figure 23, panel b)) was developed. The basic design is based on the previously described 5 cm² cell hardware (ZAE/TEC-TUM), but deviates in a crucial point: For the determination of a possible catalyst

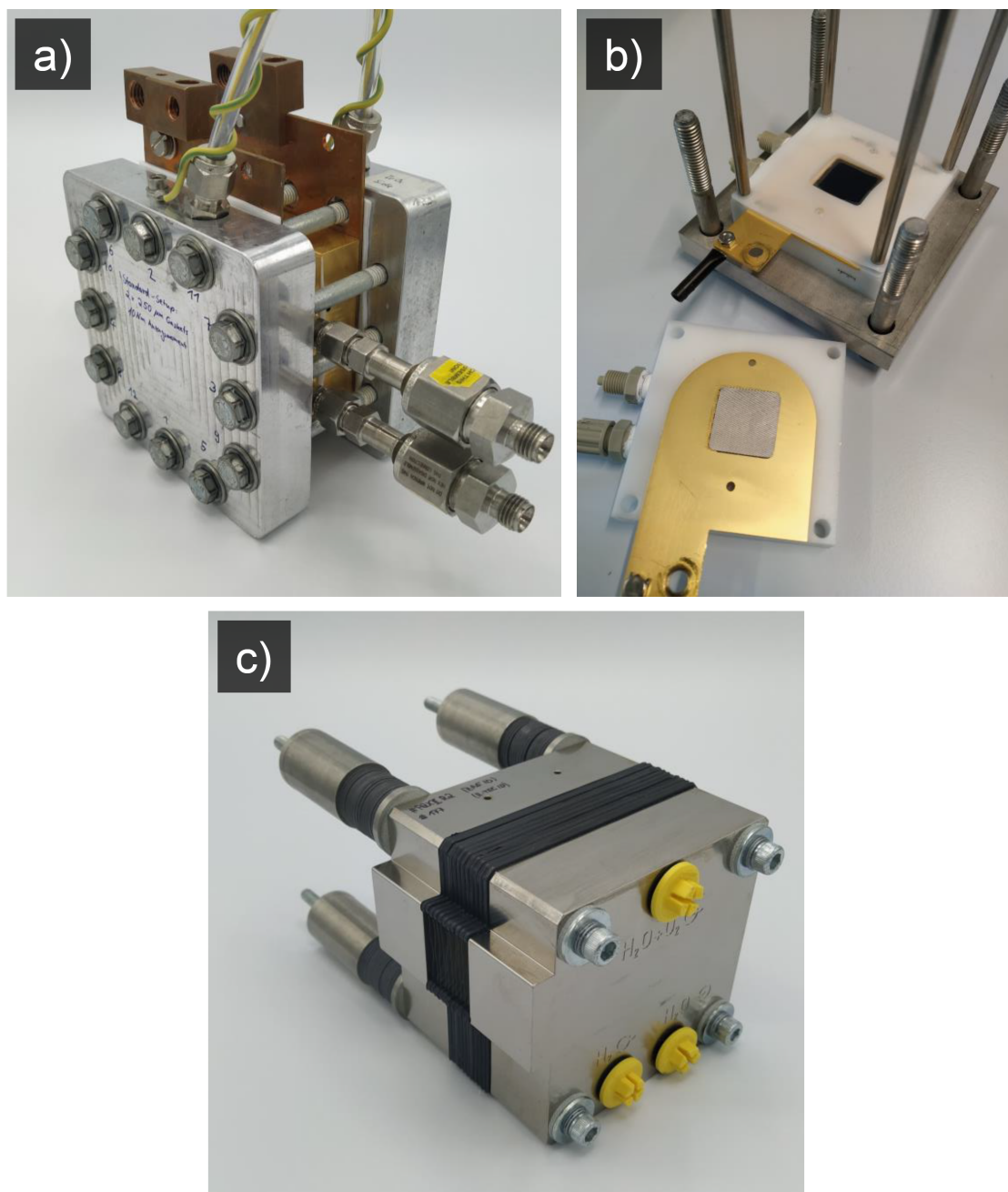


Figure 23: Photographs of the three different cell designs used in this thesis: a) 5 cm² single cell; b) 5 cm² galvanic redeposition free single cell; c) 30 cm² industrial short stack with 10 cells, H-TEC Systems GmbH ELS-30

dissolution under real operating conditions, all the parts in contact with the media (deionized water, hydrogen and oxygen) must either be made of inert material (glass or plastic) or, in the case of metals, a stable PGM coating (e.g. platinum or gold) must be applied on all surfaces. This is necessary because the dissolved precious metal ions from the catalyst (iridium, platinum) could redeposit on non-noble metal surfaces in the cell setup such as titanium or stainless steel and would thus no longer be detectable in the process water [115]. Therefore, a two-piece monopolar plate design is used with a flow field plate made from 3 mm titanium grade 2 sheet metal with laser-cut serpentine flow field (equal 1 mm land and 1 mm channel spacing) which is fitted into

a plastic body made from POM or PTFE for the mechanical support and media supply. The titanium flow field is gold plated (0.5 μm PVD and 5 μm galvanic coating on top). At the face sides of the plastic body, PP fittings are used for connection to the test rig tubing. At the cathode side, a carbon paper PTL is used (TGP-H-120T from Toray, no MPL, 20 wt% PTFE, 370 μm uncompressed thickness), whereas at the anode side an expanded titanium metal sheet (250 μm thickness, Sylatech, Germany) with 5 μm platinum coating is employed as PTL. Hard-stop PTFE flat gaskets (nominal thickness 250 μm) are used for sealing and thin PTFE subgaskets (nominal thickness 10 μm) at anode and cathode side protect the cell setup from short-circuiting due to sharp edges or fibres of the PTLs. Finally, 10 mm stainless steel endplates are used together with 4 M8 bolts for cell compression. A maximum torque of 5 Nm is applied on all bolts in several steps until reaching full stress. The cell is designed for temperatures up to 80 °C at ambient pressure.

Industrial Short Stack (H-TEC Systems GmbH), 30 cm² Active Area

For the long term experiments conducted within the framework of the Kopernikus P2X project phase II, several industrial stacks were provided by the project partner H-TEC Systems GmbH. The ELS-30 type stacks (see figure 23, panel c)) had an active cell area of 30 cm² and a maximum of 10 cells. Thus, a power rating of \approx 1 kW was achieved at the nominal operating parameters. Nevertheless, H-TEC's stack configuration is transferable to larger active cell areas and already optimized for large-scale deployment. A very similar design is used also in H-TEC's MW class stacks ELS-450 with 450 cm² active cell area. Thus, despite the relatively small cell areas, the test results can be used for the optimization of future PEMWE systems in the MW power class. The H-TEC stacks ELS-30 are designed for a maximum operating pressure of 30 bar at the cathode side and a maximum operating temperature of \approx 60 °C. However, the process water flow needs to be adjusted to maintain a maximum temperature increase of 5 K between water inlet and outlet at the anode side. All different cell potentials in the stack are accessible from the outside by fine titanium pins welded to the mono- and bipolar plates. Thus, all individual cell voltages can be monitored and cell impedances can be analyzed by EIS during prolonged testing of the stack. The industrial stacks were always equipped with industrial MEAs and were not opened or modified due to non-disclosure agreements. Thus, no further information can be given about internal parts or design features of the stacks.

4.3 Test Environment

In order to run and examine PEMWE cells and stacks, a controlled test environment is necessary. In the course of this work, two different test systems were planned, purchased and commissioned at the electrochemistry lab at ZAE Bayern in Garching. The first system is a single cell PEMWE test station from Greenlight Innovation, Canada and the second a single cell / short-stack test station for up to 10 cells from Fuelcon, Germany. Both systems are briefly presented in the following.

Greenlight Single Cell Test Station

The single cell test rig from Greenlight Innovation (type nr. G-16-1640) is suitable for fully automated test procedures controlled by scripts. It allows independent pressure adjustment of anode and cathode up to 30 bar by pre-pressure control and temperature control of the cell up to 80 °C by heating cartridges, fans and a feed water preheater. A maximum of 10 ml/min of water can be supplied to either anode (standard) or cathode with an HPLC pump, also during

pressurized operation. The process water is used only once (no water cycling) and is drained off after passing the cell. Anode and cathode gas streams can be diluted using nitrogen, oxygen (anode) or hydrogen (cathode). The test stand uses a Gamry Reference 3000 potentiostat with 30 A booster. This allows common potentiostatic or galvanostatic measurement methods as well as EIS to be performed on single cells. Furthermore, the test rig is equipped with a mass spectrometer gas analyzer (Cirrus 3XD, MKS, UK), which allows precise on-line measurements of hydrogen permeation to the oxygen side.

For measuring catalyst dissolution, a dedicated process water cycle was developed and integrated into the test rig. Here, only glass or plastic components with contact to the media are used in order to prevent galvanic redeposition of PGM catalyst species on non-noble metal surfaces. A membrane pump (KNF, Switzerland) transports the anode side process water via PTFE/PE tubes from the setup recipient (1 to 1.5 l borosilicate glass bottles, Schott, Germany) to a mixed-bed resin (Leycopure, Leyco, Germany) deionizer cartridge integrated in a borosilicate glass bottle (VWR, Germany) to clean the process water from ionic impurities. The polishing filter can be bypassed during testing in order to prevent removing also possible PGM catalyst species from the water. After leaving the deionizer, the water enters the cell setup where a small fraction is electrolysed or transported to the cathode side via electroosmotic drag. The surplus water exits the cell mixed with the produced oxygen. On the way back to the setup tank, a valve allows water samples to be tapped. The cell heating during catalyst dissolution tests with the specialized cell setup is done by the process water stream alone. Therefore, the setup tank glass bottle is placed on a heater plate which is set to a certain power to reach the desired cell temperature in steady-state. A small volume of ≈ 10 ml effluent water from the cathode compartment is intermediately stored in a plastic bottle with an overflow tube in order to be able to take also cathode water samples.

Fuelcon Stack Test Station

For testing single cells at high current densities, larger single cells and cell stacks up to 10 cells, another fully automated test station (Evaluator-S 70620) was purchased from Fuelcon AG (now Horiba-Fuelcon GmbH, Germany). Similar to the single cell test rig also with this system the PEMWE test items can be examined at pressures up to 30 bar and temperatures up to around 80 °C. In contrast to the single cell test rig, the power supply is significantly larger with a maximum current of 600 A and a maximum voltage of 30 V. Also the process water treatment differs, as considerably higher water flows of up to 2 l/min for each side need to be handled by the system. Thus, the water is not drained off after passing the cell but is instead cycled in the test rig. This requires the use of high capacity ion exchange cartridges (5 l volume, Leyco, Germany) to constantly clean up the process water from ionic impurities released by the cell setup or parts of the test rig. The cell/stack heating is done typically by the process water flow alone, though a connection of heater cartridges and fans is possible as well. Similar like the potentiostat paired with the booster in the Greenlight single cell test rig, a combination of a high-output power supply, several smaller four-quadrant power supplies for fine control, and an EIS analyzer is used in the stack test rig. With this setup, EIS is possible in the whole DC current range up to 600 A at AC frequencies up to 20 kHz and 5 A maximum AC amplitude. In order to do automated EIS at all 10 cells without manually changing sense cables, a multiplexer unit is integrated.

4.4 Electrochemical Test Procedures

For the analysis of PEMWE systems, two basic diagnostic methods, polarization curves and EIS, are of special importance. Both methods are briefly explained in the following.

Polarization Curves

As explained in section 2.7, every electrochemical cell has a certain voltage to current characteristic which depends on the reversible voltage at the actual operating conditions and additional losses due to irreversibilities. In order to record these polarization or UI curves as comparably as possible, it is necessary to keep the operating parameters temperature and pressure as constant as possible or at least to use the same procedures repeatedly for comparative measurements [116]. In this case, systematic errors still exist, but in relative terms the error between two measurements becomes smaller. Most experiments in this work have been conducted at ambient pressure. Therefore, especially a relatively constant cell temperature during testing was desired.

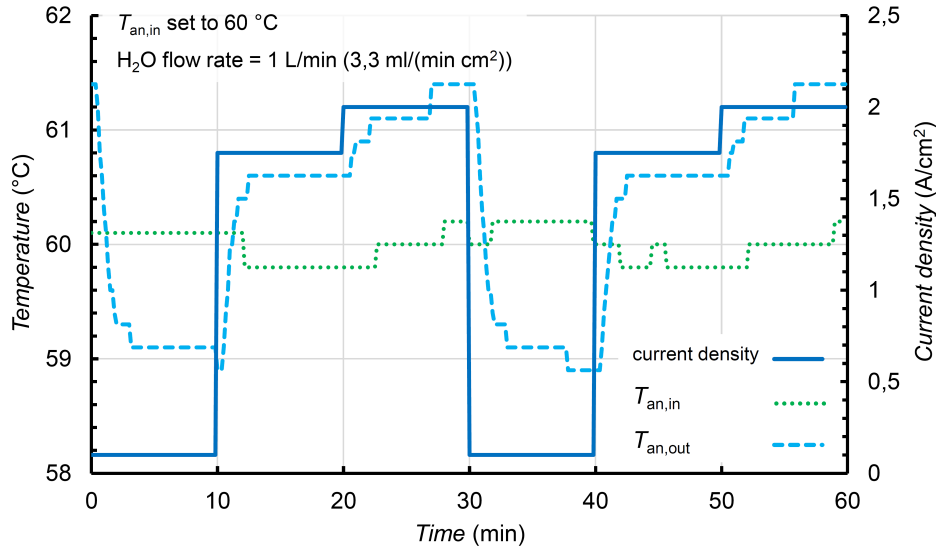


Figure 24: Anode inlet (green dotted line) and outlet (blue dashed line) temperature of the H-TEC ELS-30 stack (see figure 23, panel c)) during current cycling between 0.1 A/cm², 1.75 A/cm² and 2 A/cm² for 10 min each step. The water flowrate at the anode side is set to 1 L/min (3.3 ml/(min cm²)) and the anode inlet temperature setpoint is 60 °C.

Figure 24 shows the anode water inlet and outlet temperatures of an industrial stack (H-TEC ELS-30, 10 cells; see figure 23, panel c)) during a current cycling for 10 min for each current density at 0.1 A/cm², 1.75 A/cm² and 2 A/cm². The water flow was constant at 1 l/min and the system was set to maintain a stack inlet temperature of 60 °C. The resulting maximum deviation of the inlet temperature during testing was ± 0.5 K (after longer runtimes and with good control stability even smaller around ± 0.2 K as visible in figure 24). The temperature dependence in cell voltage is ≈ 5 mV/K, obtained from a measurement at constant current density of 1 A/cm² with the same stack and MEAs once at 60 °C and at 50 °C. Translating the temperature into a voltage perturbation, a maximum error of ± 2.5 mV due to the test systems temperature control quality of ± 0.5 K results for the used stack and MEAs. Nevertheless, this value can be different for different systems (stack and MEAs), but should in general be of the same order of magnitude for comparable PEMWE systems.

Figure 25, panel a) shows the polarization curves for a MEA based on Nafion[®] 117 for three different temperatures (40 °C, 60 °C and 80 °C). The catalyst loadings are 1.23 mg_{Ir}/cm² at the anode (Umicore Elyst Ir75 0480) and 0.31 mg_{Pt}/cm² at the cathode (Tanaka TEC10V50E). Usually, polarization curves are recorded in current control mode. Thus, several current density

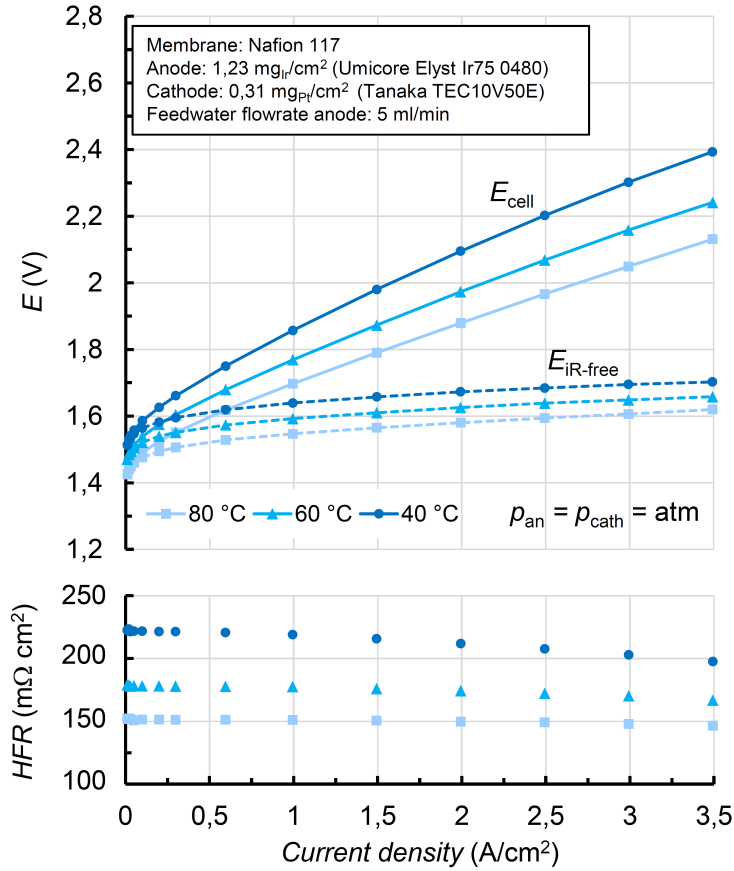


Figure 25: a) Polarization curves (straight lines) for three temperatures (40 °C, 60 °C and 80 °C) for MEA based on Nafion[®] 117. Both cathode and anode side pressures are at ambient level. The MEA has electrodes with catalyst loadings of 1.23 mg_{Ir}/cm² at the anode (Umicore Elyst Ir75 0480) and 0.31 mg_{Pt}/cm² at the cathode (Tanaka TEC10V50E). Dashed lines show the HFR corrected iR -free cell voltages. The 5 cm² laboratory cell (see figure 23, panel a)) uses a platinumized (0.5 μm platinum, coated by Umicore Galvanotechnik, Germany) titanium sinter (Mott Corporation, USA) as anode side PTL. b) Corresponding HFR values obtained by electrochemical impedance spectroscopy (EIS).

steps are held for a certain time (≈ 10 min) in order to reach a steady state in the cell or stack temperature and thereby also in the cell voltage. As the polarization curves of PEMWE show a strong non-linear behaviour at low current densities, a smaller distance of measuring points is appropriate here. Typically, the lowest current density chosen is between 0.05 and 0.1 A/cm². Especially for further analysis of the catalyst activity, a higher resolution in the low current density region is advantageous. After ≈ 1 A/cm², in the linear region of the polarization curve, the point spacing can be higher without loss of information. In dependence of the used cell and MEA system, mass transport losses can occur at high current densities which in turn cause nonlinear behaviour of the polarization curve. If these nonlinearities are only weakly pronounced, it is not essential to reduce the point spacing again.

In addition to the full cell voltage polarization curve recorded in a scheme as described above, a

high frequency resistance (HFR) corrected, iR -free polarization curve can give more insight into the loss structure of the PEMWE cell. To obtain the iR -free cell voltage, the pure ohmic voltage losses, which are calculated by multiplying the HFR values, depicted in figure 25 panel b), with the respective current densities, are subtracted from the full cell voltage values of the polarization curve. Thus, in the ideal case, the remaining iR -free polarization curve shows the sum of all non-ohmic overpotentials present in the cell at different current densities. In the case of PEMWE, the anode activation overpotential is the highest non-ohmic overpotential present. Therefore, in a first approximation and especially at low current densities, the iR -free polarization curve closely resembles the anode activation overpotential. The HFR, in turn, can be obtained by EIS which is usually performed during the recording of the polarization curve at all or some of the current densities.

Electrical Impedance Spectroscopy (EIS)

Electrochemical impedance spectroscopy (EIS) is a versatile measurement method for determining the impedance (= complex electrical resistance) of an electrochemical system over a wide frequency range. EIS on PEMWE cells typically uses a current excitation and measures the amplitude and phase of the voltage response of the system. In order to obtain accurate results, the AC excitation amplitude must be small compared to the DC current at the cell to remain within a sufficiently small pseudo-linear range of the UI characteristic. As a rule of thumb, a factor of 10 times lower AC amplitude compared to DC current was used for the measurements in this work. The frequency range relevant for the analysis for PEMWE cells is approximately between 20 kHz and 100 mHz. By measuring the impedance as a function of frequency, various resistances (e.g. high frequency resistance (HFR), charge transfer resistance (R_{ct}) and mass transfer resistance (R_{diff})) of the cell can be extracted from the resulting Nyquist plot by using equivalent circuit models for the analyzed system. In the present work however, the main focus of applying EIS was to determine the HFR of the cells at different current densities. Figure 26 contains Nyquist plots of

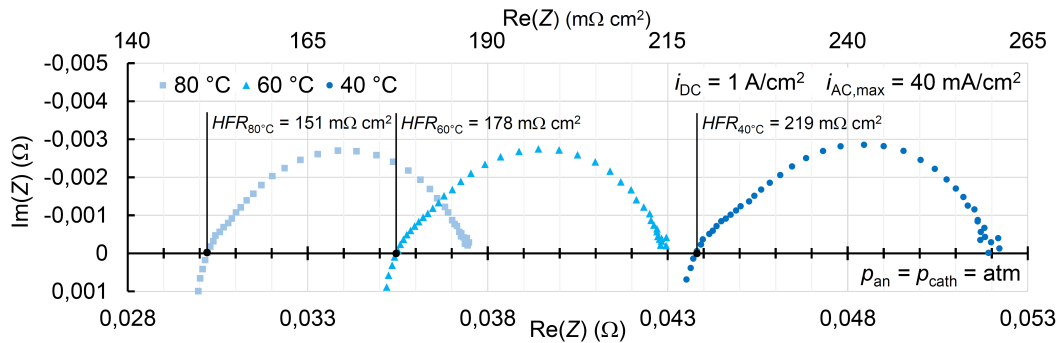


Figure 26: Electrochemical impedance spectra for three temperatures (40 °C, 60 °C and 80 °C) of a PEMWE cell (5 cm² active area, see figure 23, panel a)) at 1 A/cm² DC current density and 40 mA/cm² AC excitation amplitude. The used MEA is based on Nafion[®] 117. Both cathode and anode side pressures are at ambient level. The MEA has catalyst loadings of 1.23 mg_{Ir}/cm² at the anode (Umicore Elyst Ir75 0480) and 0.31 mg_{Pt}/cm² at the cathode (Tanaka TEC10V50E).

impedance spectra at three different temperatures (40 °C, 60 °C and 80 °C) recorded at 1 A/cm² DC current density with 40 mA/cm² AC excitation amplitude. The same cell and MEA is used as in figure 25. The HFR can be determined relatively easy from a Nyquist plot. It is the pure ohmic resistance at the intersection of the impedance curve with the real axis in the high frequency

region. As described above and shown in figure 25, the HFR can be used to subtract the ohmic overpotentials from a recorded polarization curve and obtain an iR -free curve of the cell which shows only non-ohmic overpotentials. For PEMWE cells, the remaining overpotential is, especially at low current densities, mainly composed of the electrode activation overpotential of the anode side catalyst. Thus, using polarization curves and EIS as an analysis tool in regular intervals enables the identification of changes at the electrodes, in particular at the anode.

4.5 Additional Methods

In addition to the main experimental methods and techniques described before, several other ancillary methods were used. These methods were employed, for example, in collaborative publications by other authors or were applied by the author itself, but only to a minor extent. Therefore, the presentation here is very brief and only for the sake of completeness. More detailed information is given in the respective publications in the results chapter.

SEM

For the analysis of MEA cross sections and for visualization of PTL materials, a IB-19520CCP cryo cross section polisher and a JSM-IT200 SEM, both from JEOL, Japan were used. The cross section analysis was performed with the help of Matthias Kornherr from TEC-TUM, Munich.

ICP-MS

In order to measure the iridium concentration of water samples taken from PEMWE water cycles, ICP-MS was used. ICP-MS measurements were performed by Julius Knöppel from HIERN, Erlangen, with a NexIon 300 spectrometer from Perkin Elmer, USA.

LCA

To analyze the global warming impact of electrolytic hydrogen from renewable electricity and to compare it with fossil hydrogen production by steam reforming, a standardized life cycle assessment framework was used which was applied according to the ISO 14040 and 14044 standards (ISOa, 2006 and ISOb, 2006). The life cycle assessment framework and the calculations were set up and performed by Kay Bareiss and Cristina de la Rúa, ENS-TUM, Munich.

XPS

XPS measurements were performed at IrO_x - TiO_2 OER catalyst powders to determine the iridium-oxide film thickness on the TiO_2 support material. An Axis Supra System by Kratos, UK, was used. The measurements were performed by Matthias Kornherr, TEC-TUM, Munich.

5 Results

After the introduction to the field of PEMWE, the subsequent description of possible improvement strategies on cell level and an explanation of the applied experimental methods, in the following results chapter the research articles are presented which are included in this PhD thesis. At first in section 5.1, a life cycle assessment (LCA) of hydrogen produced by PEMWE under different energy system scenarios is done to investigate the possible reduction in global warming potential of electrolytic hydrogen compared to conventional hydrogen production by steam methane reforming (SMR). In section 5.2, the thermal limitation of PEMWE at high current densities due to necessary heat removal is investigated followed in section 5.3 by an analysis of the hydrogen crossover in PEMWE cells at high current densities. In section 5.4, the stability of Iridium based PEMWE anodes is investigated with a dedicated setup to measure possible dissolved Iridium species in the process water at anode and cathode side. Finally in section 5.5, the durability of low-iridium loaded PEMWE MEAs is investigated in an industrial short stack over a period of 3700 h with a focus on the catalyst.

5.1 Life Cycle Assessment of Hydrogen from Proton Exchange Membrane Water Electrolysis in Future Energy Systems

The article "Life Cycle Assessment of Hydrogen from Proton Exchange Membrane Water Electrolysis in Future Energy Systems" [20] was submitted in July 2018 and published as an open access article in the peer-reviewed journal *Applied Energy* in January 2019, distributed under the terms of the Creative Commons Attribution 4.0 License (CC BY-NC-ND). The permanent web-link to the article is <https://doi.org/10.1016/j.apenergy.2019.01.001>.

In this study we analyze the possible reduction potential in global warming footprint of hydrogen production when using PEMWE instead of the reference process steam methane reforming (SMR). A life cycle assessment is used as a framework for the analysis. At first, the basic working principles of both reference process SMR and PEMWE are explained and compared to gain insight into the physical limits of their respective energy consumptions and associated direct CO₂ emissions for the production of a unit amount of hydrogen. In a next step, the core element of the PEMWE system, the cell stack, is modelled into detail for a current state-of-the-art and an improved future configuration at a reference net electric power rating of 1 MW. Also the other necessary system components of a PEMWE besides the stack, such as facilities, pumps, power electronics and process technology, are integrated in the analysis but at a lower level of detail. As the origin of the input electricity plays a crucial role for the global warming footprint of hydrogen from PEMWE, three current and future energy scenarios are modelled: In the first scenario grid electricity based on the German energy mix from 2017 is used to supply the PEMWE system, whereas in the second scenario an extrapolated theoretic grid electricity for the year 2050 with higher share of renewables is used. Finally in the third scenario, electricity exclusively from renewable sources (PV and wind energy) is used for the production of electrolytic hydrogen. The main results of the LCA are:

1. For all energy scenarios the material based emissions for the PEMWE stack and the PEMWE system balance of plant are small compared to the emissions by the used electricity. Even for the case with 100 % renewable electricity feed of the PEMWE, the footprint of stack and system is not more than 4 % of the overall emissions.
2. A significant reduction in carbon dioxide emissions associated with the production of hydro-

gen from 11.5 kg_{CO₂,eq}/kg_{H₂} for the reference SMR process to 3.3 kg_{CO₂,eq}/kg_{H₂} for PEMWE in combination with 100 % renewable electricity is possible. However, electrolysis with the current German grid electricity (2017 values) produces about 2.5 times more carbon dioxide per kg of hydrogen as if a SMR process is used for the hydrogen production. Also in the future (2050), grid electricity has a considerably higher specific CO₂ emission per kWh than electricity from renewables like wind energy and PV systems and thus also the specific emissions for hydrogen from PEMWE in combination with future grid electricity are still quite high at 11.6 kg_{CO₂,eq}/kg_{H₂}.

3. Higher current densities and lowered catalyst loadings significantly reduce the critical material usage (iridium, platinum, copper, titanium etc.). Nevertheless, the direct influence on carbon dioxide emissions due to material reduction is very small as the electricity consumption and the associated carbon footprint to produce the electricity is the governing factor.
4. The standard databases for LCA (ecoinvent v3.3 was used in this study) are relatively old and static. Therefore, projections for future developments with improved or new technology can give misleading results with quite high specific global warming potentials. Especially feedback effects due to a rising share of renewable energy in all sectors can not be represented in the analysis in a straightforward way. The specific carbon dioxide emissions for hydrogen production by PEMWE driven by renewable electricity should be significantly lower than the value obtained in this study. Nevertheless, also with our "conservative" approach, a significant reduction of about 70 % is shown for electrolytic hydrogen from PEMWE fed with 100 % renewables compared to fossil hydrogen from SMR.

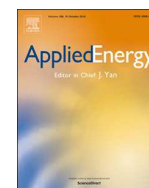
Author Contributions

K.B., C.d.l.R. and M.M. conceived and developed the idea. K.B. coordinated the work and developed the energy scenarios. M.M. and K.B. established the PEMWE inventory. K.B. and C.d.l.R. set up the LCA framework. K.B. performed the LCA calculations. K.B., C.d.l.R. and M.M. wrote the manuscript. All authors discussed the results and revised the manuscript.



Contents lists available at ScienceDirect

Applied Energy

journal homepage: www.elsevier.com/locate/apenergy

Life cycle assessment of hydrogen from proton exchange membrane water electrolysis in future energy systems



Kay Bareiß^a, Cristina de la Rua^a, Maximilian Möckl^b, Thomas Hamacher^a

^a Technical University of Munich, Department of Electrical and Computer Engineering, Chair of Renewable and Sustainable Energy Systems, Lichtenbergstrasse 4a, D-85748 Garching, Germany

^b ZAE Bayern, Electrochemical Energy Storage, Walther-Meißner-Str. 6, D-85748 Garching, Germany

HIGHLIGHTS

- The paper provides a detailed inventory for a PEM water electrolyser system.
- An energy model was built to analyse the future energy mixes required by the system.
- LCIA results prove the relevance of the electricity mix for most impact categories.
- By 2050, the analysed system has less impact compared to the reference system.

ARTICLE INFO

Keywords:

Proton exchange membrane water electrolysis (PEMWE)
Life cycle assessment (LCA)
Energy modeling

ABSTRACT

This study discusses the potential of H₂ production by proton exchange membrane water electrolysis as an effective option to reduce greenhouse gas emissions in the hydrogen sector. To address this topic, a life cycle assessment is conducted to compare proton exchange membrane water electrolysis versus the reference process - steam methane reforming. As a relevant result we show that hydrogen production via proton exchange membrane water electrolysis is a promising technology to reduce CO₂ emissions of the hydrogen sector by up to 75%, if the electrolysis system runs exclusively on electricity generated from renewable energy sources. In a future (2050) base-load operation mode emissions are comparable to the reference system. The results for the global warming potential show a strong reduction of greenhouse gas emissions by 2050. The thoroughly and in-depth modeled components of the electrolyser have negligible influence on impact categories; thus, emissions are mainly determined by the electricity mix. With 2017 electricity mix of Germany, the global warming potential corresponds to 29.5 kg CO₂ eq. for each kg of produced hydrogen. Referring to the electricity mix we received from an energy model emissions can be reduced to 11.5 kg CO₂ eq. in base-load operation by the year 2050. Using only the 3000 h of excess power from renewables in a year will allow for the reduction of the global warming potential to 3.3 kg CO₂ eq. From this result we see that an environmentally friendly electricity mix is crucial for reducing the global warming impact of electrolytic hydrogen.

1. Introduction

Climate change is at the top of today's agenda in most countries and many policies have been put in place to face this global challenge. The European Union is approaching the deadline to reach the European 2020 climate and energy targets, but it has already established three new key targets for 2030: (i) reducing greenhouse gas (GHG) emissions at least by 40% compared to 1990 levels, (ii) increasing the share of renewable energy at least to 32%, and (iii) improving the energy efficiency at least to 27% [1]. Germany is a key player and aims to lead the European energy transition by setting even more ambitious objectives. The energy industry, in general, and the electricity sector, in particular, have been identified as targets due to their high contribution to GHG. In 2015, 37% of the energy-related GHG emissions were produced in the

energy economy, followed by the transportation sector, which contributed with almost 18%. From the total amount of GHG emissions, 85% are related to the energy sector [2].

Electricity production in Germany from renewable energy sources accounted to 3% of the total share in 1990, while it represented already 32% in 2016 [3]. The country expects to cover 80% of its electricity demand from renewable energy sources until 2050 [3]. Most of this energy will be produced from solar and wind power. Besides the clear benefits of renewable energy sources for the environment, the integration of fluctuating energy sources in the energy system is still under discussion. Its availability depends on weather and season as well as on the time of the day. This intrinsic characteristic leads to situations in which electricity production exceeds electricity demand and the capacity of the electric system is surpassed [4]. Under these

<https://doi.org/10.1016/j.apenergy.2019.01.001>

Received 25 July 2018; Received in revised form 27 November 2018; Accepted 1 January 2019
0306-2619/ © 2019 Elsevier Ltd. All rights reserved.

circumstances, energy storage is foreseen as one potential solution [5]. Schill [6] used an optimization model to determine the storage capacities required for taking up renewable surpluses under several scenarios in Germany with three storage options: batteries, pumped hydro storage and power-to-hydrogen. Taking into account the German expectations for 2050 in terms of renewable energy, the use of hydrogen can be seen as a promising solution [7,8]. Electrolytically produced hydrogen can help balancing the electric grid (storage), while also providing an energy carrier to be used in other sectors. A good example is the mobility sector. The need for decarbonizing mobility has placed hydrogen in a better position for future alternatives. Fuel cell vehicles (FCVs) convert hydrogen into electrical energy through a fuel cell. They do not emit any exhaust pollutant but water and have a longer driving range compared to battery electric vehicles (BEVs) [9–11].

Besides its potential for balancing the electric grid and decarbonizing the mobility sector, hydrogen is essential for a variety of industrial processes. Around 65 Mtons of hydrogen are produced yearly worldwide [12]. More than 90% of the hydrogen is used by two main industries, the petroleum recovery and refining industry (47%) and the ammonia production industry (45%) [13–15]. Hydrogen offers a versatility which makes it valuable for achieving the 2030 and 2050 targets from different perspectives. However, before deciding which pathways should be addressed first, it is necessary to study the whole supply chain of hydrogen production and to estimate the potential environmental impacts. This way it will be possible to identify critical issues and processes and propose measures to improve them. For that purpose, we present a life cycle assessment (LCA) of hydrogen production by proton exchange membrane water electrolysis (PEMWE) under different future energy scenarios.

2. Hydrogen production methods

Hydrogen can be supplied through several routes. A first division can be done based on the energy source used in the production. Hydrogen can be produced from both fossil energy sources and renewable energy sources [16]. To date, 48% of the hydrogen has been produced from natural gas, 30% from heavy oils and naphtha, and 18% from coal. From a technological perspective, there are four main production methods: (i) hydrocarbon reforming, (ii) hydrocarbon pyrolysis, (iii) biomass processing, and (iv) water splitting. Steam methane reforming (SMR) is the most common technology among the hydrocarbon reforming technologies, while electrolysis is the most established and well-known method in water splitting. The schematic processes of both SMR and electrolysis are shown in Fig. 1.

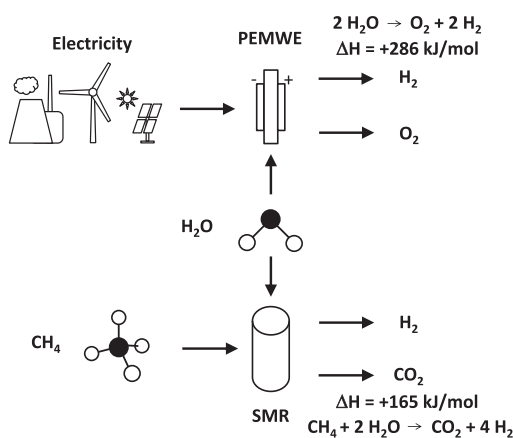
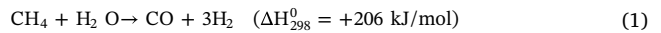


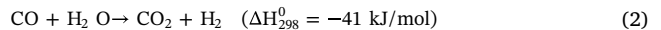
Fig. 1. Schematic drawing of the hydrogen production paths discussed in this paper. The focus is on PEMWE technology, SMR is used as a reference only. Electricity can be provided by renewables only or by a mixture of fossil power plants and renewables.

2.1. Steam methane reforming

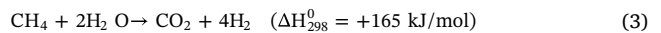
The SMR method is a catalytic conversion of methane and steam to hydrogen and carbon dioxide. The method entails three steps: reforming or synthesis gas generation, water-gas shift and gas purification. The whole process happens under high temperatures and pressures up to 3.5 MPa. Eq. (1) shows the reforming process using methane as feed:



In order to achieve a higher hydrogen yield a second step, the water-gas shift reaction, is used according to Eq. (2):



The net reaction of the SMR process is the sum of Eq. (1) and (2):



With a net enthalpy of $\Delta H_{298}^0 = +165 \text{ kJ/mol}$ the reaction is endothermic and needs external heat input. This is usually done by using natural gas (mainly methane) also as a fuel for heating. It is evident that in practice additional losses will occur. These are compensated by a higher methane consumption than theoretically necessary. The most significant loss is due to excess steam production [17]. The hydrogen production efficiency of a SMR plant can be defined as the power flux of the hydrogen produced divided by the power flux of the methane consumed:

$$\eta_{\text{SMR}} = \frac{P_{\text{H}_2}}{P_{\text{fuel}}} = \frac{\dot{m}_{\text{H}_2} \cdot \text{LHV}_{\text{H}_2}}{\dot{m}_{\text{CH}_4} \cdot \text{LHV}_{\text{CH}_4}} \quad (4)$$

The efficiency of exemplary industrial SMR plants calculated with Eq. (4) is around 74% [18,19]. Thus, the production of 1 kg H₂ leads to direct emission of about 8.8 kg CO₂. Taking into account not only the direct emissions from natural gas but the whole life cycle of the SMR, total CO₂ emissions are naturally higher.

2.2. Water electrolysis

Among the water splitting technologies, electrolysis is the most efficient method. The oldest and most mature type is the alkaline electrolyzer [20]. It consists of a cathode and an anode separated by a thin porous ceramic diaphragm submerged in an alkaline electrolyte. A newer generation of electrolyzers, also known as proton exchange membrane water electrolyzers (PEMWE), does not use a liquid electrolyte but a thin solid polymer electrolyte (membrane) instead [21]. This proton conducting membrane has a typical thickness of 60–200 μm. Nafion® is commonly used in commercial systems. On both sides of the membrane, thin electrodes of about 10 μm thickness are directly bonded to the surface. The electrodes contain noble metal catalysts, typically platinum-based at the cathode and iridium-based at the anode [22]. Some advantages of this technology are high energy efficiency, the provision of highly compressed and pure hydrogen and the flexible dynamic operation [23]. The still evolving PEMWE technology is currently more expensive compared to alkaline electrolyzers, mainly due to the use of critical and valuable materials such as titanium, platinum, iridium and the proton exchange membranes. Hence, there are current development efforts aiming to reduce their required amount [24]. The general operation process of a PEMWE cell is shown in Fig. 2. De-ionized water is supplied to the anode side of the cell. The membrane electrode assembly (MEA) is clamped between the porous transport layers (PTL) and the bipolar plates. The porous transport layers are typically carbon paper on the cathode side (thickness 280 μm, compressed) and sintered titanium foam or felt (thickness 280 μm) on the anode side [25]. The bipolar plates are made from titanium as well, and they usually feature channel-like structures (flow-field) for water and gas transport. In some designs, spatially stretched titanium mesh is

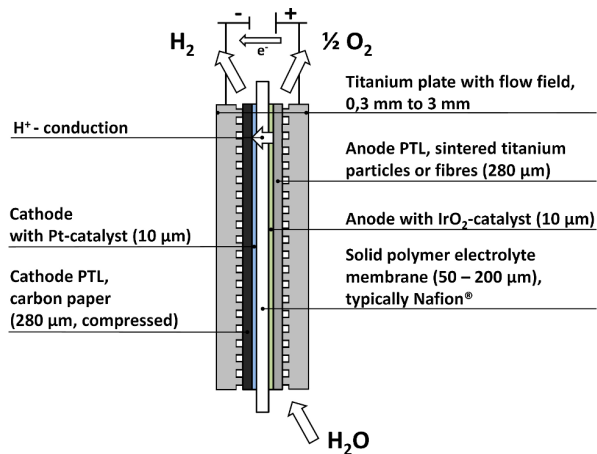
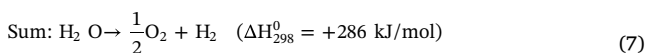


Fig. 2. Parts of a typical PEMWE cell.

also used to generate channels between the PTLs and the bipolar plates [26]. Titanium is one of the few materials which are suitable for the use on the anode side as it forms thin compact oxide layers, which are highly stable under the PEMWE operating conditions of low pH and high electrical potentials [27]. If a voltage greater than 1.23 V is applied to the cell, the necessary Gibbs free energy ($\Delta G_{298}^0 = 237$ kJ/mol) is supplied and the water is split with the integration of thermal energy from the environment. The value of ($\Delta G_{298}^0 = 237$ kJ/mol) is very close to the lower heating value (LHV = 242 kJ/mol) of hydrogen and thus is used synonymously in most publications [28]. For supplying the whole reaction enthalpy of ($\Delta H_{298}^0 = 286$ kJ/mol) a minimum voltage of 1.48 V is necessary. The cathode (negative terminal) produces hydrogen, while the anode (positive terminal) produces oxygen according to the following reactions:



The protons are conducted from the anode to the cathode through the solid polymer electrolyte, whereas the electrons are driven through the external electric circuit. The cell's efficiency can be calculated from the cell voltage E_{cell} with the following equation:

$$\eta_{\text{cell,LHV}} = \frac{1.23\text{V}}{E_{\text{cell}}} \quad (8)$$

Under typical operating conditions, the cell voltages are between 1.5 V and 2 V [28]. The corresponding cell efficiencies are between 62% and 82% based on LHV. The PEMWE system efficiencies with all utilities (electronics, pumps, safety equipment, infrastructure, etc.) and faradaic losses included to deliver H₂ at industry grade 5.0 (99.999%) and 30 bar pressure are typically around 10–20% points lower than the cell efficiencies [29] and are in the range of 50–70% (LHV). As can be seen in Fig. 1, the direct CO₂ emissions of a PEMWE system are zero. However, from a life cycle analysis point of view, the use of this technology for hydrogen production is associated with certain CO₂ emissions. One important factor is the amount of emissions connected to the production of the input electricity.

2.3. LCA reference values for hydrogen production

As described above, many technologies are currently available for hydrogen production. They differ in many parameters, such as process efficiency and energy requirements. Taking into account this variety, it

is understandable that a large amount of hydrogen's life cycle assessment was published during the last decade. Lee and colleagues [30] published recently the life cycle greenhouse gas emissions of hydrogen production as a by-product from chlor-alkali processes. Under different scenarios, hydrogen production creates 1.3–9.8 kg CO₂ eq. per kg of H₂. Utgikar and Thiesen [31] examined global warming and acidification impacts of a combined advanced nuclear-high temperature electrolysis plant. Producing 1 kg of H₂ leads to 2 kg of CO₂ equivalent (eq.) and 0.15 g H⁺ eq. for each impact category. Cetinkaya [32] and her colleagues analyzed the global warming potential along the life cycle for five methods of hydrogen production. Electrolysis using wind emerged as the best option, emitting 0.97 kg CO₂ eq. per kg of H₂, followed by solar electrolysis, with 2.4 kg of CO₂ eq.. Conventional production of H₂ in a steam reforming process with natural gas would emit 11.9 kg of CO₂ eq. per kg of H₂. Dufour [33] also analyzed the impacts of electrolysis using different electricity technologies. From all analyzed sources, the production of H₂ using electricity from the grid leads to the largest GHG emissions, 28 kg of CO₂ eq. per kg of H₂ respectively. The study also assesses SMR with carbon capture and sequestration which results in 3.3 kg of CO₂ eq. In this direction, Verma and Kumar [34] estimated the GHG emissions of hydrogen production from underground coal gasification with and without carbon capture sequestration. Emissions were calculated to be 0.91 and 18 kg CO₂ eq. per kg of H₂.

Most articles focus on global warming potential, while few of them include other impact categories such as cumulative energy demand, acidification or eutrophication. One of them is the article published by Hajjaji [35], which compares eight alternative ways for hydrogen production including nine impact categories. Lastly, Wang and co-authors [36] have investigated GHG emissions along the life cycle of a new alternative to produce hydrogen, which couples chemical looping combustion with steam reforming. This technology would produce 3 kg of CO₂ eq. per kg of H₂.

In this regard, our paper aims to enlarge the current knowledge in the field from two different perspectives. Most reviewed articles provide aggregated data of the PEMWE stack. In this sense, we have made a big effort to describe each component of the stack as it is today and to estimate the future expected improvements based on the work developed in the Kopernikus project Power-to-X [37]. Besides, most studies analyze hydrogen production using a single energy technology as energy source, without considering the actual availability of that source within the energy system. In our study, we have integrated the life cycle analysis and an optimization energy model in line with the scope of the study. This way it is possible to understand how the energy system will react to the demand of hydrogen, and then to identify which energy sources will provide the energy required by the PEMWE.

3. Life cycle analysis

Life cycle assessment (LCA) is one of the most established methods for estimating the environmental performance associated to the life cycle of products and services. The first LCA framework was published by the Society of Environmental Toxicology and Chemistry [38]. After many modifications, the practice of LCA was regulated and nowadays its application follows the ISO 14040 and 14044 standards (ISOa, 2006 and ISOb, 2006).

The LCA comprises four phases: (i) goal and scope definition, (ii) inventory of inputs and outputs, (iii) impact assessment, and (iv) interpretation of results. This study will address the four stages as established in the ISO standards.

3.1. Goal and scope of the study

The main objective of this study is to quantify the potential environmental impacts of hydrogen produced by PEMWE in Germany under different energy scenarios. The LCA has been modeled from an

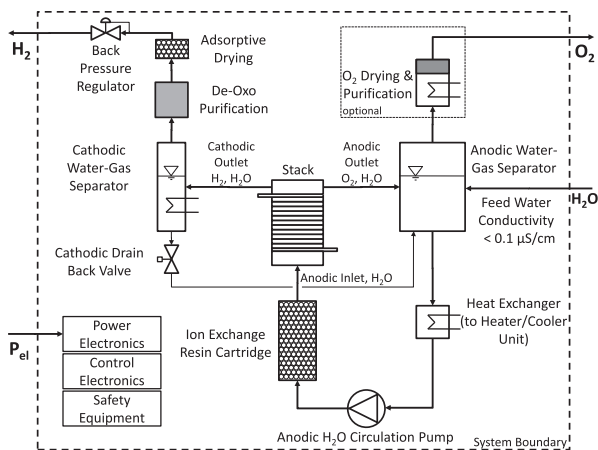


Fig. 3. Scheme of the analyzed PEMWE system layout showing all essential parts for hydrogen 5.0 production at 30 bar pressure, modified from [39,40]. The anode gas drying and purification system is optional and not necessary unless the produced O_2 is used as well.

attributional approach as a cradle to gate system. However, it must be noted that systems outside these boundaries might be affected by the new demand of hydrogen. This is the case of the German electric system. In order to reflect these consequences, the study includes results from an energy model, described in Section 4, which will reflect the potential German electric system under the new demand of H_2 . Fig. 3 shows the processes and components included within the system boundaries. The chosen functional unit is defined as 1 kg of dried hydrogen produced in Germany in a PEMWE plant, with a standard quality of 5.0 and 30 bar pressure at 60 °C operating temperature. First, de-ionized water is fed to the anode water-gas separation tank. To avoid certain system degradation issues, water conductivity has to be lower than 0.1 $\mu S/cm$ [41]. The water is pumped to the cell stack, the core part of the system. Previous to the stack there is an ion exchange resin cartridge for maintaining a low water conductivity. The water leaves the stack at the anode outlet together with the produced oxygen. It is cycled back to the water-gas separation tank. A heat exchanger in the anodic cycle allows the system to maintain a certain working temperature. Typically the working temperatures are in a range between 60 °C and 80 °C [42]. The produced oxygen is usually vented. Gas treatment of the oxygen (drying and purification) is only done if the oxygen is used in a subsequent process. The water circulation is done on the anode side. On the cathodic side of the stack in most cases no water cycling is necessary because there is a net transport of water from the anode to the cathode during operation due to the electro-osmotic drag [43]. Hydrogen and water leave the stack at the cathodic outlet. The gas-water mixture is cooled down close to ambient temperature and liquid water is separated and drained back to the anodic water-gas separation tank. The water-saturated hydrogen is fed to a catalytic de-oxo purification device to reduce the oxygen content to a level of less than 5 ppm. A subsequent adsorptive dryer finally reduces the water content to values lower than 5 ppm [29]. The pressure on the cathodic side typically can reach up to 30 bar. In most cases, the oxygen side is kept at ambient pressure for easier system design and less cross permeation [44]. Further obligatory system components are the power electronics (rectifier and voltage transformer), control electronics and safety equipment. In many applications the whole PEMWE system is integrated in standardized 20 ft or 40 ft containers as depicted in Fig. 4. The balance of plant (BOP) lifetime is assumed to be 20 years [45].

Although the technology is already quite developed, it is expected to further improve in the near future. In addition, the energy mix in Germany will also vary its current configuration to fulfill the policy targets. For this reason, we have extended the initial time horizon from



Fig. 4. Typical containerized PEMWE system in the 1 MW power range at Windgas Hamburg, Reitbrook project site. (Copyright ©Uniper SE).

2017 to 2050, so that our results can reflect these changes.

Data for the foreground system has been collected from different sources. An important part of the data has been taken from laboratory measurements and was reviewed by several industrial partners. Other sources, such as literature review, scientific articles and technical information from commercial sources, have been used when necessary.

Data for the background system has been taken from the ecoinvent v3.3 database. Whenever the available datasets provided in the database did not reflect the geographical and time horizon previously defined in this study, they were modified using additional information. The analysis has been modeled using the software SimaPro. There are currently a large variety of impact assessment methods. The Joint Research Centre (JRC) published in 2011 an extensive review of different methods using criteria such as completeness of the scope, environmental relevance and scientific robustness among others [46]. As result of this review, they proposed an umbrella method, which comprises the best scored method for each impact category. Although the use of this method could be appropriate, we have chosen the most updated version of the ReCiPe Midpoint method to carry out this study [47]. Some of the weaknesses highlighted by the review from the JRC report have been surpassed in the most updated version. Besides, by using one unique method for all impact categories, we can assume that the underlying limitations and assumptions for each category are consistent with each other. The following impact categories have been included in the analysis:

- Climate change (CC)
- Ozone depletion (OD)
- Terrestrial acidification (TA)
- Human toxicity (HT)
- Particulate oxidant formation (POF)
- Particulate matter formation (PM)
- Metal depletion (MD)

3.2. Life cycle inventory

This section describes the different processes within the system boundaries. Inventory data are shown as well in this section, together with the main assumptions and hypothesis taken along the study.

3.2.1. PEMWE stack

The stack as the core component of a PEMWE system is basically a connection of several single cells in series. This is schematically shown in Fig. 5.

The individual cells of the same principle as shown in Fig. 2 are separated by titanium bipolar plates. At the upper and lower end of the

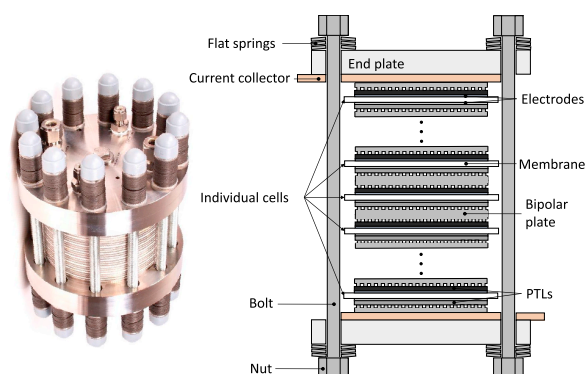


Fig. 5. Picture and simplified schematic drawing of a PEMWE stack of the lower power class up to 100 kW. More powerful systems in the MW class are very similar in their components, the main difference is the size of the active cell area. (Picture: Copyright ©HIAT gmbH).

cell stack current collectors, mainly made of copper or aluminum [25], are installed for the electrical connection. Thick end plates made of aluminum or steel together with several bolts and sets of stacked flat springs are used to ensure an even compression of the cells. The stack lifetime of commercial systems is typically 40000–60000 h and is planned to reach 90000 h or roughly 10 years of continuous service in near future systems [24]. The main parts prone to degradation are the MEA and the anodic PTL [48]. These can be substituted by new components in an overhaul process.

Table 1 shows an overview over some key parameters of the PEMWE system, which are important for the LCA. Current state-of-the-art values (2017) and their estimated development for the near future are gathered. Today's mean cell efficiencies are 70% at corresponding cell voltages of 1.79 V and current densities of around 1.5 A/cm² [28]. The system efficiencies including all utilities are about 10 percentage points lower at 60% [28]. Typical anode catalyst loadings are 2 mg/cm² iridium [22]. In contrast, the cathode catalyst loadings are about ten fold lower with 0.2 mg/cm² platinum. This is possible as the cathodic reaction kinetics are several orders of magnitude faster [49]. The titanium bipolar plate thickness in current state-of-the-art PEM electrolyzers is about 3 mm [50] as there are machined or etched channels on both sides of the bipolar plates with depths of about 1 mm each [51]. Polysulfonic acid membranes for proton conduction (mostly Nafion®) with thicknesses of about 200 µm are used as electrolyte [42].

Research efforts are undertaken to intensify the current density and to lower the catalyst loadings while keeping the high efficiency level [42]. Also, design improvements are expected to reduce the material usage, especially of the expensive and difficult to manufacture titanium bipolar plates. Possible ways to achieve these goals are presented in the following:

Table 1
Current and estimated near future PEMWE system parameters.

Parameter	2017	Near future
Cell voltage level (V)	1.79	1.79
Current density (A/cm ²)	1.5	3
Power density (W/cm ²)	2.7	5.4
η_{cell} (LHV)	0.7	0.7
η_{system} (LHV)	0.6	0.6
Anode Ir. loading (mg/cm ²)	2	0.2
Cathode Pt. loading (mg/cm ²)	0.2	0.05
Ti. bipolar plate thickness (mm)	3	0.3
Membrane thickness (µm)	200	50
Single cell format (cm ²)	500	1000
Stack lifetime (years)	7	10
BOP lifetime (years)	20	20

- **Reduced catalyst loadings:** At the cathode for the hydrogen evolution reaction (HER), the platinum loadings can be reduced by a factor of 8 from today 0.2 mg_{Pt}/cm² to 0.025 mg_{Pt}/cm² without significantly influencing cell performance [52]. With a security factor included for possible degradation issues, 0.05 mg_{Pt}/cm² seems a reasonable value for cathode loadings for the near future. At the anode, the oxygen evolution reaction (OER) is much slower and therefore more catalyst surface area is necessary. As iridium is only mined in a quantity of approximately 4 t/y [42], it was estimated by Bernt et. al. that the power specific iridium loading should get down to 0.01 g_{Ir}/kW at efficiencies similar to today's (≈ 70%) so PEMWE can be used on a large scale with about 150 GW installation per year [52]. By using improved catalysts with higher surface area, a ten fold reduction of the iridium content down to 0.2 mg_{Ir}/cm² at increased current densities of 3 A/cm² is assumed to be possible in the near future.
- **Thinner membranes:** A reduction of membrane thickness from 200 µm to 50 µm in the coming years seems a possible goal. Experimental tests with thinner membranes showed good results [25]. Similar reductions of membrane thickness were achieved in PEM fuel cell technology [53,54]. This facilitates an operation at higher current densities, as the ohmic resistance of the cell is significantly reduced [42]. At the same time, it has to be ensured that the permeation losses and degradation processes are not increasing too much with the thinner membranes [55,56].
- **Thinner bipolar plates:** Bipolar plates can be produced faster and with less material usage by forging of thin sheet metal instead of destructive milling or etching of thicker base material. Similar approaches were done in PEM fuel cell technology, where sheet metals with thicknesses of 50 µm are stamped or forged to manufacture flow fields [57]. In PEMWE systems, with higher operating pressures and thus tighter mechanical restrictions of the minimum bipolar plate thickness, possible reductions are assumed to be ten-fold down from initial 3 mm [50] to 0.3 mm in the near future.

3.2.2. Gas purification

After passing the cathodic water-gas separator unit the produced hydrogen is saturated with water vapor. The water vapor pressure depends on the water-gas separator temperature. In most cases, this device is cooled down slightly above ambient temperature. Average values are assumed to be about 20 °C which corresponds to a water vapor pressure of 23 mbar. At the cathode, total pressures of 30 bar result in a water vapor content of about 770 ppm or 7 g H₂O per kg of H₂. Some oxygen is also present in the cathodic product gas due to permeation processes across the membrane. According to findings by Trinke et al. [58] the mean oxygen impurity level is estimated to be about 800 ppm. For removing these impurities, a de-oxo unit is used, which catalytically cold burns the oxygen traces with hydrogen to water. The produced water from the de-oxo unit, together with the water vapor from the water-gas separator, is reduced to less than 5 ppm by a subsequent adsorptive drying process.

- **De-Oxo**
Different types of de-oxo purification units are available on the market. One possibility is the use of platinum group metals to remove the oxygen content in the hydrogen gas stream in a catalytical recombination device. The reaction is as follows:
$$2\text{H}_2 + \text{O}_2 \rightarrow 2\text{H}_2\text{O} \quad (9)$$
While removing the 800 ppm of oxygen, about 15 g of H₂O is produced per kg of H₂. The product water from the de-oxo device together with the 7 g of H₂O per kg of H₂ from the gas-water separator is subsequently removed in an adsorption process.
- **Adsorption Process**
In most applications, silica gel is used as adsorbent. The silica gel adsorbs water at its surface until it is completely covered and

Table 2
Materials for a 1 MW PEMWE stack, state-of-the-art and near future.

Material (kg)	2017	Near future
Titanium	528	37
Aluminum	27	54
Stainless steel	100	40
Copper	4.5	9
Nafion®	16	2
Activated carbon	9	4.5
Iridium	0.75	0.037
Platinum	0.075	0.010

saturated [59]. Silica gel needs to be baked out before it can be used again. Thus, to maintain a continuous drying process, two silica tanks in a batch process are considered in the study. Energy and material requirements to produce silica gel have been taken from the literature [60]. Between 7100 and 8400 kJ are required to evaporate 1 kg H₂O from silica [59]. This results in an energy demand of 0.05 kWh per kg dried H₂ at 30 bar pressure.

The life cycle inventory (LCI) has been collected for each described process. Taking into account the system parameters for 2017 and the near future shown in Table 1, the required materials for a 1 MW stack have been estimated. The total active cell area for a 1 MW stack is 37 m² for state-of-the-art and 18.5 m² in the future. Subsequently, the material quantities have been estimated assuming a simple layered design as shown in Figs. 2 and 5. Quadratic cell formats with active areas of 500 cm² for 2017 and 1000 cm² for the near future are chosen for estimating the size of the endplates and current collectors. Based on demonstration systems, the end plate thickness is assumed to be 10 cm and the current collector thickness to be 5 mm. Furthermore, the mass of the stainless steel bolts and screws is conservatively estimated. The mass of sealing material and inlet and outlet fittings has been neglected. Table 2 contains the LCI of the main materials for the state-of-the-art and future 1 MW stack.

Titanium is the material that contributes the most to the total mass of the stack in its current configuration. The need for a reduction of its use is mainly driven by its high cost [61] and the difficulty of machining or etching thick titanium bipolar plates. It can be noticed that the effect of higher power density, reduction of the bipolar plate and membrane thickness and reduction of catalyst platinum group metal loadings will lead to a strong decrease in material usage. Especially the application of cost intensive materials like iridium, platinum and also titanium and Nafion® is reduced by 85–95%. Only for the construction materials aluminum and copper a higher usage can be assumed for the future as the active cell area format is doubled.

3.2.3. Balance of plant

The BOP materials are more difficult to estimate, as there is only few publicly accessible information from PEMWE system manufacturers, in most cases only in form of technical specifications as in [62–64]. However, a rough estimation for the materials with a high safety margin is attempted in the following. The assumed system is a containerized solution in a standard 20 ft container with a structural weight of 3.9 t. The foundation is made from concrete realized by 4 point-foundations with a thickness of 25 cm each and a squared area of 1.5 m edge length. The total weight of concrete for the foundation amounts to 5.4 t. To ensure a sufficient water flow, a pump with 10 kW is required. The power electronics, which includes the rectifier and the voltage adaption, weighs 1 t and the control electronics accounted for 100 kg of gross mass. In addition, some construction and process material such as steel elements, plastic and stainless steel piping, adsorbents and lubricants are included in the analysis. The integrated system materials and their estimated masses are specified in Table 3. Fig. 6 shows the mass shares of the BOP components and the PEMWE

Table 3
Main materials and assumed masses of the PEMWE BOP.

Materials	Mass (t)
Low alloyed steel	4.8
High alloyed steel	1.9
Aluminum	< 0.1
Copper	< 0.1
Plastic	0.3
Electronic material (power, control)	1.1
Process material (adsorbent, lubricant)	0.2
Concrete	5.6

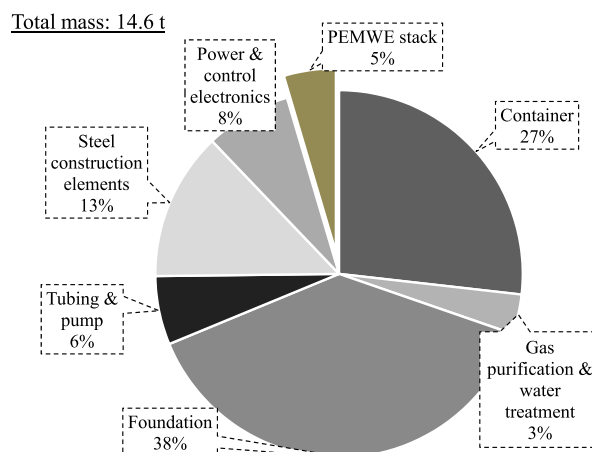


Fig. 6. Mass shares of the components belonging to the electrolyzer system (2017).

stack for 2017. It is clearly visible that the highest mass share (78%) refers to construction elements (foundation, steel construction, container) whereas only 5% is used for the actual electrochemical device, the PEMWE stack.

4. Energy scenarios

After the static PEMWE system has been described, we investigate the dynamic plant operation. Water splitting is an energy demanding process using electricity and some heat. In our system, the heat is also provided by electricity. From stoichiometry results, we know that 9 kg H₂O are required for producing 1 kg H₂. In addition, 55 kWh of electricity are necessary for water splitting at an efficiency of 60% LHV. The choice of energy sources has an important impact on the results as shown by Valente et al. in their extended reviews [65,66]. The energy sources determine the GHG emissions as well as the cumulative energy demand (CED) of the whole life cycle. The potential effects of the electricity mix on our final results make a more detailed analysis of the current and expected development of Germany's energy system necessary. There are numerous studies focusing on energy modeling in Germany [67–70]. However all of them have their own assumptions on different aspects which are not in line with our scope of research. In addition most available studies are published in an aggregated and already interpreted form, which do not provide the necessary degree of freedom. In our premise, we see FCVs as an important component in the course of the energy transition concerning the mobility sector. For this reason, an amount of H₂ requirement was assumed, which is covered by the PEMWE. The capacity expansion of PEMWE and the use of available storage capacities, however are determined endogenously, taking into account the hourly optimized electricity mix by the model. In order to illustrate this complex approach, a linear optimization problem tailored to this research question has been set up. We have built an energy model to computationally answer the question about a

future power mix. A linear optimization problem was described with the open source model-generator "urbs" [71], which was created at the chair of "Renewable and Sustainable Energy Systems" at TUM. The model consists of 16 nodes (for every state of Germany) and does not allow international energy exchanges. Each region (node) is connected to its surroundings with transmission lines. Energy demands (electricity and hydrogen) are given, which have to be covered by different technologies. Three premises were set:

1. A largely electrified private traffic is assumed to match the goal of decarbonization in the private transportation sector. The analysis of the average distance kilometers traveled per trip is based on reference to [72]. Journey distances shorter than 250 km have been assumed to be suitable to be operated by BEV. Due to the limited battery capacity and longer charging time of BEV, hydrogen vehicles are more suitable for longer journeys [73]. Thus, remaining mileage is satisfied by FCV. The electricity requirement of BEVs is added proportionally to the general electricity demand. The battery storage of the vehicles is not included in the power grid as storage. From the analysis, we state 71% of the mileage is provided by BEVs accordingly remaining mileage demand is covered by FCVs. BEVs have an overall higher rate of efficiency (0.57 MJ/km) compared to FCVs (0.73 MJ/km) [67]. Electricity consumption for BEV accounts to 60 TWh, while covering H₂ demand including the efficiency of the PEM system amounts to 35 TWh.
2. The tolerated CO₂ emission limits is made up of the sectors energy economy and private traffic in 2050. Total CO₂ emissions are 80% lower compared to 1990 emissions from private transport (19 Gtons) and energy economy (43 Gtons).
3. The maximum installable capacity of wind is calculated by the share of non-occupied land like settlements, rivers or roads, in Germany. From this share we assume an occupancy of 5% of suitable space in Germany as not all useful space will be allocated to wind farms. By assuming 5 MW turbines in 250 m distance each, a potential of 20 MW/m² is available, which corresponds to 198 GW onshore capacity. This value is slightly higher than the 178 GW stated in [74] (Scenario: "Energiewende- Referenz") but much lower than the 930 GW from [75] as they allow a higher share of Germany for wind-farming. The quality of a wind location is characterized by the amount of full load hours of their corresponding wind time series [76]. 1/3 of the capacity is assigned to very good wind locations (the best third of each region). As a simplification, the remaining 2/3 are assigned to the second best third of wind locations. The maximum capacity of photovoltaic systems is not limited. The use of conventional power plants is determined by the model.

To cover the energy demand, 0.1 TWh pump storage and 0.5 TWh hydrogen storage are set as readily installed. The hydrogen storage represents the capability of existing fuel storage as our hydrogen demand results from FCVs. The efficiency of FCV is given with 0.73 MJ/km [78] and for BEV (300 km range) 0.57 MJ/km [67]. The model solves the problem cost optimally on an hourly time base by keeping the direct maximum CO₂ emissions under a given limit. Finally, we investigated the specific CO₂ emissions of the hourly electricity mix which is plotted in Fig. 7. From the curve, we stated two different operation modes of PEMWE and therefore two load profiles. For a future hydrogen production via PEMWE, based solely on renewable energy, we get 3000 full load hours as a result. The operation time will increase to 8760 h when 40% of the energy is supplied by combined cycle gas turbine (CCGT). All assumptions and further details are published in a working paper [77]. The results from the two different scenarios are shown in Table 4.

5. Results and discussion

In this section we present the potential environmental impacts

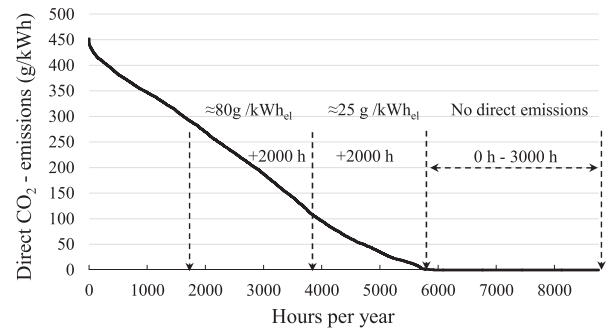


Fig. 7. In descending order sorted CO₂ emissions curve; only direct CO₂ emissions from burning fossil fuels in conventional power-plants are taken into account. Energy from renewables do not have any emissions in the model (figure taken from [77] and translated).

Table 4

Share of power generation from the different scenarios (%).

Power plant	2017	2050	2050
	baseload [79]	baseload [77]	3000 h [77]
Hard coal	15	0	0
Lignite	24	0	0
Nuclear	12	0	0
Natural gas	14	40	0
Oil	1	0	0
Wind energy	17	39	65
Photovoltaic	6	21	35
Biomass	8	0	0
Hydro power	3	0	0

associated with the production of hydrogen by a PEMWE under three different energy scenarios from a life cycle approach. The electricity mixes resulting from the energy model for the different scenarios are shown in Table 4. For today's electricity mix, the GWP is 29.5 kg CO₂ eq. for each kg of produced hydrogen as shown in Fig. 8. This amount is reduced by 60% if the electricity required by the system is produced as described in the 2050 base-load operation scenario. In this case, the production of 1 kg hydrogen causes the emission of 11.5 kg CO₂ equivalent. The most favorable scenario (3.3 kg CO₂ eq.) assumes that

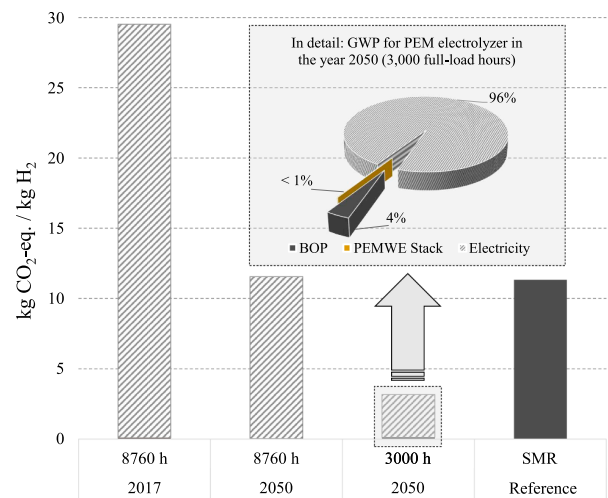


Fig. 8. Global warming impact from CO₂ emissions of the PEMWE system. Emissions are separated into BOP, PEMWE Stack and Electricity. As BOP and PEMWE Stack contribute with a maximum of 4% to the GWP, a pie chart is added in the case of the scenario with 3000 full-load hours.

the PEMWE is operating 3000 h using only electricity produced by renewable sources. Fig. 8 also shows the contribution of the different system components to the GWP for the best case. The modeled components of the PEMWE stack (near future design) have negligible influence, with less than 1%. The PEMWE BOP accounts for only around 4% while the electricity supply is responsible for 96% of total GHG emissions. The contribution of the PEMWE stack and BOP is even lower for the other scenarios. Comparing our results with Bukhardt et al. [80], a distinctly higher proportion of nearly 20% is attributable to the electrolyzer's manufacture supply chain. This divergence can be explained, beside the material choice, by the lower power density of alkaline electrolyzers [28], the system is correspondingly larger than a PEMWE. A comparison of the mass balance shows that the alkaline electrolyzer (including foundation) weighs, with 30 tons, twice as much compared to the PEMWE system examined in this study. Thus, hydrogen production by PEMWE with its high power density should result in lower GWP compared to alkaline electrolysis when using the same input electricity. Although the production of hydrogen in a SMR process is out of the scope of our study, in the figure we have included the GHG emissions associated to this technology (11.5 kg CO₂ eq./kg of H₂) in order to have a reference value. This value has been extracted from the GaBi database.

Since hydrogen as fuel is a premise of our energy scenario, we briefly describe how FCV can contribute to a sustainable transportation sector for the year 2050. First of all, FCVs are more efficient (0.73 MJ/km compared to internal combustion engine (1.2 MJ/km) [67]. Secondly, GWP of gasoline is around 84 g CO₂ eq. per MJ [81], which results in 101 g CO₂ eq. per vehicle kilometer (vkm). Hydrogen from PEM, even in base-load operation (11.5 kg CO₂ eq./kg of H₂) leads to 70 g CO₂ eq. per vkm (hydrogen from SMR will result in similar results). Using the flexibility of PEMWE and matching the hydrogen production with the fluctuating power generation of renewables (3000 h) will further reduce the emissions to 20 g CO₂ eq per vkm.

The change of energy sources in the electricity mix over time does not only contribute to the reduction of GWP but also to the cumulative energy demand indicator. This indicator serves as reference to measure the system's efficiency in terms of energy consumed and produced, considering the whole supply chain. The aim is not only to decrease the CED of the system, but also to decrease the contribution of non-renewable energy sources. Therefore, in this paper we distinguish between renewable and non-renewable cumulative energy demand. The result for the cumulative energy demand of the individual operating modes is shown in Fig. 11. In the base scenario (2017), the production of 1 kg hydrogen requires around 550 MJ along the whole system. Under the second and third energy scenarios, the CED is reduced by 23% and more than 53%, respectively. Producing 1 MJ of H₂ requires around 4.6 MJ along the supply chain in the current scenario, but only 2.1 MJ in the best case scenario, 2050 (3000 full load hours). When analyzing the indicator divided into the two subcategories, renewable and non-renewable, it is possible to perceive that besides an improvement in energy efficiency, there is also an increase in renewable energy source's contribution to the cumulative energy demand. In the current situation, 77% of the CED has a non renewable source, which includes fossil and nuclear energy. This value decreases by 15% when the electricity is produced under the 2050 scenario with 3000 full load hours. As in the case of GWP, we have included the CED from SMR as reference. Although this process demands lower cumulative energy along the supply chain compared to any other scenario, 99% of this energy has a non renewable origin. Table 5 shows the potential environmental impact for each impact category under the three energy scenarios. It can be noticed that the highest values for most categories occur in the current scenario. However, there are two categories in which the trend is different. Human toxicity decreases due to the phase-out of lignite in scenario 2050 (8760 h) compared to the current scenario, but it increases again in 2050 (3000 h) because of the high demand of copper for the wind turbines. In the case of metal depletion,

Table 5
Impact categories for PEMWE in 2017 and 2050.

Impact (unit)	2017 baseload	2050 baseload	2050 3000 h
CC (kg CO ₂ eq.)	29.5	11.6	3.0
OD (10 ⁻⁶ kg CFC-11 eq.)	2.6	2.6	2.3
TA (10 ⁻² kg SO ₂ eq.)	4.7	2.5	2.1
HT (kg 1,4-DB eq.)	24.8	3.9	5.6
POF (10 ⁻² kg NMVOC)	3.4	2.0	1.3
PM (10 ⁻² kg PM10 eq.)	1.6	1.2	1.1
MD (kg Fe eq)	0.53	0.93	1.5

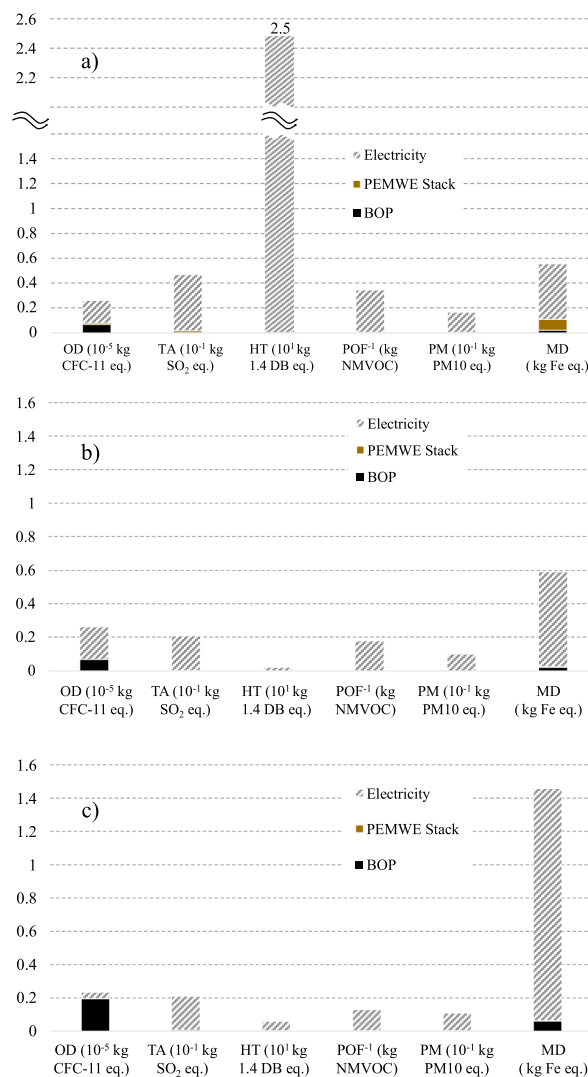


Fig. 9. Impact assessment results per functional unit from the following scenarios: (a) 2017, (b) 2050 (8760 h), (c) 2050 (3000 h).

the potential impact is larger both in 2050 (8760 h) and 2050 (3000 h). Although there is an important reduction of metals (titanium, iridium) used in the PEMWE stack from 2017 to 2050, total MD increases due to the higher share of wind (copper) and PV (silicon, iron) energy in the electricity mix. From these results shown in Fig. 9, we see that the electricity mix is crucial for reducing most environmental impacts, although it might lead to the increase of some other categories. In order to better understand the reasons behind these effects, it is necessary to further investigate the impacts of each energy technology in each

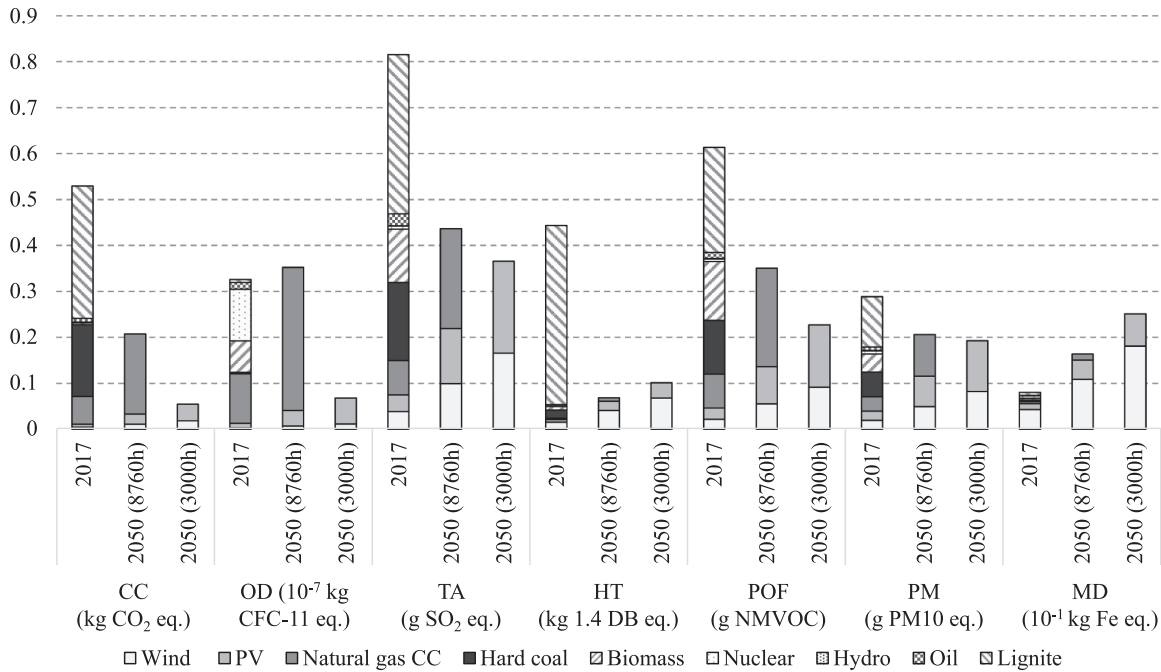


Fig. 10. Further environmental impacts. All impact categories are related to 1 kWh electricity.

energy scenario.

Fig. 10 shows the potential environmental impacts of producing 1 kWh of electricity in each energy scenario, taking into account the different contribution of each energy technology. As expected from the results shown in Table 5, most environmental impacts associated with the production of 1 kWh of electricity decrease in the energy scenarios with higher share of renewable energy sources. In 2017, the environmental impacts are mostly associated with fossil energy sources such as lignite and hard coal. Biomass and natural gas also contribute to the acidification potential and photochemical ozone formation. In the energy scenario 2050 (8760 h), all impacts are driven by natural gas. In some categories, such as climate change or ozone depletion, this energy technology represents more than 90% of the total impact, while in other

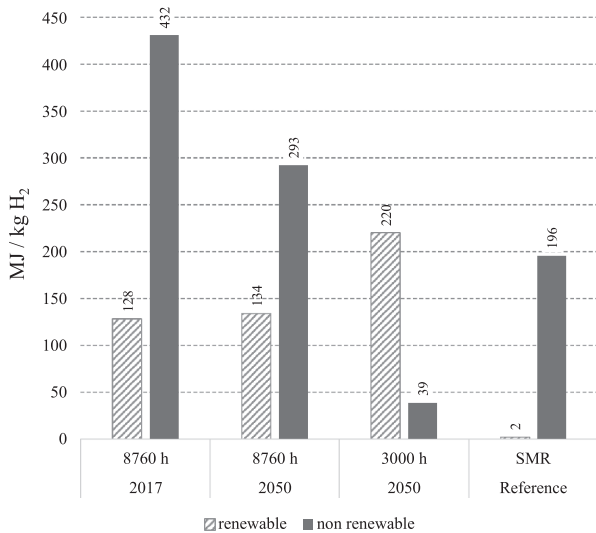


Fig. 11. A significant reduction in energy from non-renewable is observed starting from 2017 until 2050. In contrast to that, the amount of energy from renewable sources is only rising moderately.

categories, such as acidification potential or particulate matter, its contribution does not exceed 50%. Lastly, in 2050 (3000 h), the lack of natural gas as energy source leads to the reduction of most environmental impacts. With a share of 35%, solar energy plays an important role in most categories except in metal depletion, mainly associated with wind energy.

Besides the potential environmental impacts included in a classic LCA, the use of critical materials in the supply chains has recently become a new important topic. The European Commission periodically renews the list of critical materials. These depend on several parameters. The most important are:

- The importance of the material to the EU economy in terms of the cost of material substitution (SIEI Index).
- The security of supply by the supplying regions depending on the development of the respective government and trade performance.

Favorable substitution possibilities or reprocessing of these critical raw materials have a risk-reducing effect on their evaluation in the considered life cycle [82]. The platinum group metals are identified as critical raw materials [83] in this study. It is estimated that the use of iridium in the PEMWE stack can be reduced by 90% by 2050. The platinum loading is reduced by 75%. To cover the H₂ demand from the energy model an installed PEMWE power between 7 GW in full-load and 20 GW in the 3000 h scenario is necessary. With a typical stack lifetime of 7 years the iridium demand (excluding recycling) is between 0.8 t and 2.1 t per year in Germany only. In contrast, the average worldwide production rate of iridium, which is a co-product of platinum, is between 3.5 t [84] and 4 t per year [42]. Therefore, it is crucial to reduce their amount if PEMWE is seen as a roll-out technology for future energy systems. In addition FCV will need a certain amount of platinum for their fuel cell stacks. However, this is outside our system boundaries.

6. Conclusion

We have reported that for different impact categories of hydrogen produced by proton exchange membrane water electrolysis, the

influence of system components plays a minor role. Our investigation has shown that mainly the composition of the electricity mix determines the impacts like global warming potential. A reduction of the used materials causes only very little reduction in global warming potential. Nevertheless, there is a clear influence of material reduction on the critical materials. Three different operation modes of the proton exchange membrane water electrolysis were investigated; for each, a specific process electricity was developed. Further investigation shows that hydrogen production with proton exchange membrane water electrolysis in the future (2050) is definitely an alternative to conventional steam methane reforming production. However, the operation mode by proton exchange membrane water electrolysis is flexible enough for fitting into hours with volatile electricity production having very high shares of renewables. Due to the flexibility of the plants, proton exchange membrane water electrolysis can play an important role in integrating renewables. With the appropriate storage capacity, surplus of hydrogen produced can be used for later re-conversion to stabilize future energy systems or as fuel for fuel cell vehicle. By subsidizing fossil oil in the private transportation sector, even in the baseload scenario, global warming potential is reduced by 30%. Due to the capability of flexible load behavior, proton exchange membrane water electrolysis can contribute to a high reduction of greenhouse gas emitted by the transportation sector by up to 80%, as we have shown. However, our results are subject to the restriction of using existing databases for the background data. These data are based on state of the art or based on older processes. In order to depict future value chains, which also use electricity in production steps, these data sets would also have to be updated for reasons of consistency which is outside of our focus. Therefore, feedback effects of future energy mixes regarding indirect emissions cannot be taken into account. For further investigations of innovative technologies, new datasets should be created which allow increases of efficiency in the production of energy production technologies e.g. solar panels through a lower emission factor of used electricity. This would further reduce the global warming potential of renewable hydrogen production by proton exchange membrane water electrolysis.

Acknowledgement

The authors gratefully acknowledge funding by the German Federal Ministry of Education and Research (BMBF) within the Kopernikus Project P2X: Flexible use of renewable resources – exploration, validation and implementation of ‘Power-to-X’ concepts.

References

- [1] Rat E. Tagung des Europäischen Rates (23./24. Oktober 2014) – Schlussfolgerungen, Tech. rep., Europäischer Rat, 2014. URL: <<https://www.bundesregierung.de/Content/DE/Reiseberichte/2014-10-22-europaeischer-rat-oktober.html>>, [accessed June 27, 2018].
- [2] Strogies M, Gniffke P. Berichterstattung unter der Klimarahmenkonvention der Vereinten Nationen und dem Kyoto-Protokoll 2017. Tech. rep., Umweltbundesamt; 2017.
- [3] BMUB M, Weiß MW. PtJ, Klimaschutz in Zahlen Fakten, Trends und Impulse deutscher Klimapolitik, Tech. rep., Bundesministerium für Umwelt, Naturschutz, Bau und Reaktorsicherheit (BMUB); 2017.
- [4] Hart EK, Stoutenburg ED, Jacobson MZ. The potential of intermittent renewables to meet electric power demand: current methods and emerging analytical techniques. *Proc IEEE* 2012;100(2):322–34. <https://doi.org/10.1109/JPROC.2011.2144951>.
- [5] Zhang X, Bauer C, Mutel CL, Volkart K. Life cycle assessment of power-to-gas: approaches, system variations and their environmental implications. *Appl Energy* 2017;190:326–38. <https://doi.org/10.1016/j.apenergy.2016.12.098>.
- [6] Schill W-P. Residual load, renewable surplus generation and storage requirements in Germany. *Energy Pol* doi:<https://doi.org/10.1016/j.enpol.2014.05.032>.
- [7] Ozarslan A. Large-scale hydrogen energy storage in salt caverns. *J Energy Storage* 2012;19:14265–77. <https://doi.org/10.1016/j.jhydene.2012.07.111>.
- [8] Klumpp F. Comparison of pumped hydro, hydrogen storage and compressed air energy storage for integrating high shares of renewable energies – potential, cost-comparison and ranking. *Int J Hydrogen Energy* 2016;8:119–28. <https://doi.org/10.1016/j.est.2016.09.012>.
- [9] Gurz M, Baltacioglu E, Hames Y, Kaya K. The meeting of hydrogen and automotive: a review. *Int J Hydrogen Energy* 2017;42(36):23334–23346. <https://doi.org/10.1016/j.jhydene.2017.02.124>.
- [10] Wilberforce T, El-Hassan Z, Khatib F, Al-Makky A, Baroutaji A, Carton J, et al. Developments of electric cars and fuel cell hydrogen electric cars. *Int J Hydrogen Energy* 2017;42:25695–734. <https://doi.org/10.1016/j.jhydene.2017.07.054>.
- [11] Simons A, Bauer C. A life-cycle perspective on automotive fuel cells. *Appl Energy* 2015;157:884–96. <https://doi.org/10.1016/j.apenergy.2015.02.049>.
- [12] Weger J, Abánades A, Butler T. Methane cracking as a bridge technology to the hydrogen economy. *Int J Hydrogen Energy* 2017;42:720–31. <https://doi.org/10.1016/j.jhydene.2016.11.029>.
- [13] Miler EL. Hydrogen production & delivery program-plenary presentation-. Tech. rep. US Department of energy; 2017.
- [14] Ausfelder F, Beilmann C, Bertau M, Bräuninger S, Heinze A, Hoer R, et al. Energy storage technologies as options to a secure energy supply. *Chem Ing Tech* 2015;87:17–73. <https://doi.org/10.1002/cite.201400183>.
- [15] Bazanella AM, Ausfelder F. Low carbon energy and feedstock for the European chemical industry. Tech. rep., DECHEMA, 2017. URL:https://dechema.de/en/Low_carbon_chemical_industry.html [accessed June 27, 2018].
- [16] Nikolaidis P, Poullikkas A. A comparative overview of hydrogen production processes. *Renew Sustain Energy Rev* 2017;67:597–611.
- [17] Peng X. Analysis of the thermal efficiency limit of the steam methane reforming process. *Ind Eng Chem Res* 2012;51:16385–92. <https://doi.org/10.1021/ie3002843>.
- [18] Spath PL, Mann MK. Life cycle assessment of hydrogen production via natural gas steam reforming. *Natl Renewable Energy Lab doi*:<https://doi.org/10.2172/764485>.
- [19] Linde Engineering, Hydrogen; 2018.
- [20] Santos D, Sequeira C, Figueiredo J. Hydrogen production by alkaline water electrolysis. *Quim Nova* 2013;36:1176–93. <https://doi.org/10.1590/S0100-40422013000800017>.
- [21] Barbir F. Pem electrolysis for production of hydrogen from renewable energy sources. *Sol Energy* 2005;78:661–9. <https://doi.org/10.1016/j.solener.2004.09.003>.
- [22] Carmo M, Fritz D, Mergel J, Stolten D. A comprehensive review on pem water electrolysis. *Int J Hydrogen Energy* 2013;38:4901–34. <https://doi.org/10.1016/j.jhydene.2013.01.151>.
- [23] Aricò A, Siracusano S, Briguglio N, Baglio V, Di Blasi A, Antonucci V. Polymer electrolyte membrane electrolysis: status of technologies and potential applications in combination with renewable power sources. *J Appl Electrochem* 2013;43:107–18.
- [24] Schmidt O, Gambhir A, Staffell I, Hawkes A, Nelson J, Few S. Future cost and performance of water electrolysis: an expert elicitation study. *Int J Hydrogen Energy* 2017;42:30470–92. <https://doi.org/10.1016/j.jhydene.2017.10.045>.
- [25] Bernt M, Gasteiger H. Influence of ionomer content in IrO₂/TiO₂ electrodes on pem water electrolyzer performance. *J Electrochem Soc* 2016;163:F3179–89. <https://doi.org/10.1149/2.0231611jes>.
- [26] Rozain C, Millet P. Electrochemical characterization of polymer electrolyte membrane water electrolysis cells. *Electrochim Acta* 2014;131:160–7. <https://doi.org/10.1016/j.electacta.2014.01.099>.
- [27] Lædre S, Kongstein O, Oedegaard A, Karoliussen H, Seland F. Materials for proton exchange membrane water electrolyzer bipolar plates. *Int J Hydrogen Energy* 2017;42:2713–23. <https://doi.org/10.1016/j.jhydene.2016.11.106>.
- [28] Buttler A, Spliethoff H. Current status of water electrolysis for energy storage, grid balancing and sector coupling via power-to-gas and power-to-liquids: A review. *Renew Sustain Energy Rev* 2018;82:2440–54. <https://doi.org/10.1016/j.rser.2017.09.003>.
- [29] Kopp M, Coleman D, Stiller C, Scheffer K, Aichinger J, Scheppat B. Energiepark mainz: technical and economic analysis of the worldwide largest power-to-gas plant with pem electrolysis. *Int J Hydrogen Energy* 2017;42:13311–20. <https://doi.org/10.1016/j.jhydene.2016.12.145>.
- [30] Lee D-Y, Elgowainy A, Dai Q. Life cycle greenhouse gas emissions of hydrogen fuel production from chlor-alkali processes in the united states. *Appl Energy* 2018;217:467–79. <https://doi.org/10.1016/j.apenergy.2018.02.132>.
- [31] Utgikar V, Thiesen T. Life cycle assessment of high temperature electrolysis for hydrogen production via nuclear energy. *Int J Hydrogen Energy* 2006;31(7):939–44. <https://doi.org/10.1016/j.jhydene.2005.07.001>.
- [32] Cetinkaya E, Dincer I, Naterer G. Life cycle assessment of various hydrogen production methods. *Int J Hydrogen Energy* 2012;37(3):2071–80. <https://doi.org/10.1016/j.jhydene.2011.10.064>.
- [33] Dufour J, Serrano DP, Gálvez JL, González A, Soria E, Fierro JL. Life cycle assessment of alternatives for hydrogen production from renewable and fossil sources. *Int J Hydrogen Energy* 2012;37(2):1173–83. <https://doi.org/10.1016/j.jhydene.2011.09.135>. [10th International Conference on Clean Energy 2011].
- [34] Verma A, Kumar A. Life cycle assessment of hydrogen production from underground coal gasification. *Appl Energy* 2015;147:556–68. <https://doi.org/10.1016/j.apenergy.2015.03.009>.
- [35] Hajjaji N, Pons M-N, Renaudin V, Houas A. Comparative life cycle assessment of eight alternatives for hydrogen production from renewable and fossil feedstock. *J Cleaner Prod* 2013;44:177–89. <https://doi.org/10.1016/j.jclepro.2012.11.043>.
- [36] Li ZWL, Zhang G. Life cycle greenhouse gas assessment of hydrogen production via chemical looping combustion thermally coupled steam reforming. *J Cleaner Prod* 2018;179:335–46.
- [37] Ausfelder F, Dura HE. 1. Roadmap des Kopernikus-Projektes Power-to-X Flexible Nutzung erneuerbarer Ressourcen (P2X) - Optionen für ein nachhaltiges Energiesystem mit Power-to-X Technologien. Tech. rep., DECHEMA; 2018.
- [38] Consoli F. SETAC, Guidelines for life-cycle assessment: a code of practice, Conference proceedings, SETAC (Society); 1993.

- [39] Smolinka T, Rau S, Hebling C. Polymer electrolyte membrane (PEM) water electrolysis. Wiley-VCH, Weinheim; 2010.
- [40] Suermann M, Pätua A, Schmidt T, Büchi F. High pressure polymer electrolyte water electrolysis: test bench development and electrochemical analysis. *Int J Hydrogen Energy* 2017;42:12076–86. <https://doi.org/10.1016/j.ijhydene.2017.01.224>.
- [41] Rakousky C, Reimer U, Wippermann K, Carmo M, Lueke W, Stolten D. An analysis of degradation phenomena in polymer electrolyte membrane water electrolysis. *J Power Sources* 2016;326:120–8. <https://doi.org/10.1016/j.jpowsour.2016.06.082>.
- [42] Babic U, Suermann M, Buechi FN, Gubler L, Schmidt TJ. Review-identifying critical gaps for polymer electrolyte water electrolysis development. *J Electrochem Soc* 2017;164:F387–99. <https://doi.org/10.3929/ethz-b-000190719>.
- [43] Luo Z, Chang Z, Zhang Y, Liu Z, Li J. Electro-osmotic drag coefficient and proton conductivity in nafion membrane for pemfc. *Int J Hydrogen Energy* 2010;35(7):3120–4. <https://doi.org/10.1016/j.ijhydene.2009.09.013>.
- [44] Bensmann B, Hanke-Rauschenbach R, Arias IP, Sundmacher K. Energetic evaluation of high pressure pem electrolyzer systems for intermediate storage of renewable energies. *Electrochim Acta* 2013;110:570–80. <https://doi.org/10.1016/j.electacta.2013.05.102>.
- [45] Smolinka T, Günther M, Garche J. Stand und Entwicklungspotenzial der Wasserelektrolyse zur Herstellung von Wasserstoff aus regenerativen Energien. Tech. rep. Fraunhofer ISE; 2011.
- [46] Wolf M-A, Pant R, Chomkhamrims K, Sala S, Pennington D. International reference life cycle data system (ILCD) handbook - recommendations for life cycle impact assessment in the european context. Tech. rep. European Commission-Joint Research Centre -Institute for Environment and Sustainability; 2011.
- [47] Goedkoop M, Heijungs R, Huijbregts M, Schryver AD, Struijs J, van Zelm R. Recipe 2008 a life cycle impact assessment method which comprises harmonised category indicators at the midpoint and the endpoint level. Tech. rep. Ruimte en Milieu - Ministerie van Volkshuisvesting, Ruimtelijke Ordening en Milieubeheer; 2009.
- [48] Feng Q, Yuan X, Liu G, Wei B, Zhang Z, Li H, et al. A review of proton exchange membrane water electrolysis on degradation mechanisms and mitigation strategies. *J Power Sources* 2017;366:33–55. <https://doi.org/10.1016/j.jpowsour.2017.09.006>.
- [49] Durst J, Simon C, Hasché F, Gasteiger H. Hydrogen oxidation and evolution reaction kinetics on carbon supported Pt, Ir, Rh, and Pd electrocatalysts in acidic media. *J Electrochem Soc* 2015;162:F190–203. <https://doi.org/10.1149/2.0981501jes>.
- [50] Gago S, Burggraf F, Wang L, Biermann K, Hosseini S, Gazdzicki P, et al. Zukunftspotenziale der Elektrolyse, 4.Stuttgarter EnergieSpeicherSymposium; 2015.
- [51] Ito H, Maeda T, Nakano A, Hasegawa Y, Yokoi N, Hwang C, et al. Effect of flow regime of circulating water on a proton exchange membrane electrolyzer. *Int J Hydrogen Energy* 2010;35:9550–60. <https://doi.org/10.1016/j.ijhydene.2010.06.103>.
- [52] Bernt M, Siebel A, Gasteiger HA. Analysis of voltage losses in pem water electrolyzers with low platinum group metal loadings. *J Electrochem Soc* 2018;304:1–14. <https://doi.org/10.1149/2.0641805jes>.
- [53] Vierrath S, Breitwieser M, Klingele M, Britton B, Holdcroft S, Zengerle R, et al. The reasons for the high power density of fuel cells fabricated with directly deposited membranes. *J Power Sources* 2016;326:170–5. <https://doi.org/10.1016/j.jpowsour.2016.06.132>.
- [54] Breitwieser M, Klose C, Klingele M, Hartmann A, Erben J, Cho H, et al. Simple fabrication of 12 µm thin nanocomposite fuel cell membranes by direct electrospinning and printing. *J Power Sources* 2017;337:137–44. <https://doi.org/10.1016/j.jpowsour.2016.10.094>.
- [55] Ito H, Miyazaki N, Ishida M, Nakano A. Cross-permeation and consumption of hydrogen during proton exchange membrane electrolysis. *Int J Hydrogen Energy* 2016;41:20439–46. <https://doi.org/10.1016/j.ijhydene.2016.08.119>.
- [56] Chandresis M, Médeau V, Guillet N, Chelghoum S, Thoby D, Fouda-Onana F. Membrane degradation in pem water electrolyzer: numerical modeling and experimental evidence of the influence of temperature and current density. *Int J Hydrogen Energy* 2015;40:1353–66. <https://doi.org/10.1016/j.ijhydene.2014.11.111>.
- [57] Mahabunphachai S, Cora O, Koc M. Effect of manufacturing processes on formability and surface topography of proton exchange membrane fuel cell metallic bipolar plates. *J Power Sources* 2010;195:5269–77. <https://doi.org/10.1016/j.jpowsour.2010.03.018>.
- [58] Trinke P, Bensmann B, Hanke-Rauschenbach R. Experimental evidence of increasing oxygen crossover with increasing current density during pem water electrolysis. *Electrochem Commun* 2017;82:98–102. <https://doi.org/10.1016/j.elecom.2017.07.018>.
- [59] GmbH SV. Drying by adsorption. 2017 URL: <<https://silica.berlin/en/air-and-gas-drying.html>>, [accessed June 27, 2018].
- [60] Dowson M, Grogan M, Birks T, Harrison D, Craig S. Streamlined life cycle assessment of transparent silica aerogel made by supercritical drying. *Appl Energy* 2011;97:396–404.
- [61] Ayers K, Anderson E, Capuano C, Carter B, Dalton L, Hanlon G, et al. Research advances towards low cost, high efficiency pem electrolysis. *ECS Trans* 2010;33:3–15. <https://doi.org/10.1149/1.3484496>.
- [62] Siemens AG. Sylizer 200 - Mit Hochdruck effizient im Megawattbereich; 2017.
- [63] H-TEC Systems. Datasheet Series ME 100/350 PEM Electrolyser; 2017.
- [64] Proton OnSite. Technical Specifications: M Series Hydrogen Generation Systems; 2017.
- [65] Valente A, Iribarren D, Dufour J. Life cycle assessment of hydrogen energy systems: a review of methodological choices. *The International Journal of Life Cycle Assessment* 22; 2016.
- [66] Valente A, Iribarren D, Dufour J. Harmonising the cumulative energy demand of renewable hydrogen for robust comparative life-cycle studies. *J Cleaner Prod* 175; 2018.
- [67] Repenning J, Emele L, Blanck R, Böttcher H, Dehoust G, Förster H, et al. Klimaschutzszenario 2050. Tech. rep. Öko-Institut e.V. and Fraunhofer ISI; 2015.
- [68] Kuhn P. Iteratives Modell zur Optimierung von Speicherausbau und -betrieb in einem Stromsystem mit zunehmend fluktuierender Erzeugung [Ph.D. thesis]. Technische Universität München, München; 2013.
- [69] Kirchner A, Kemmler A, Wunsch M, der Maur AA, Ess F, Koziol S, et al. Klimapfade für deutschland. Tech. rep. Prognos, BCG; 2018.
- [70] Bründlinger T, König JE, Frank O, Gründig D, Jugel C, Kraft P, et al. dena-Leitstudie Integrierte Energiewende: Impulse für die Gestaltung des Energiesystems bis 2050. Tech. rep. Deutsche Energie-Agentur GmbH (dena); 2018.
- [71] Dorfner J, Dorfner M, Candas S, Müller S, Özşahin Y, Zipperle T, et al. urbs v0.7.3. Tech. rep., TUM; 2017. doi:<https://doi.org/10.5281/zenodo.1228851>.
- [72] infas, DLR, Mobilität in Deutschland 2008, Tabellenband. Tech. rep., Bundesministerium für Verkehr, Bau und Stadtentwicklung; 2008.
- [73] Felgenhauer M, Hamacher T. State-of-the-art of commercial electrolyzers and on-site hydrogen generation for logistic vehicles in south carolina. *Int J Hydrogen Energy* 2015;40(5):2084–90. <https://doi.org/10.1016/j.ijhydene.2014.12.043>.
- [74] Matthes FC, Flachsbarth F, Loreck C, Hermann H, Falkenberg H, Cook V. ZUKUNFT STROMSYSTEM II – Regionalisierung der erneuerbaren Stromerzeugung vom Ziel her denken. Tech. rep. Umweltbundesamt; 2018.
- [75] Lütkehus I, Salecker H, Adlunger K. Potential der Windenergie an Land. Tech. rep. Umweltbundesamt; 2013.
- [76] Janker KA. Creation and evaluation of a database of renewable production time series and other data for energy system modelling [Ph.D. thesis]. München: Technische Universität München; 2015.
- [77] Bareiß K, Schönleber K, Hamacher T. Szenarien für den Strommix zukünftiger, flexibler Verbraucher am Beispiel von P2X-Technologien. Tech. rep. TUM - Lehrstuhl für Erneuerbare und Nachhaltige Energiesysteme; 2018.
- [78] Huelsmann F, Mottschall M, Hacker F, Kasten P. Konventionelle und alternative Fahrzeugtechnologien bei Pkw und schweren Nutzfahrzeugen – Potenziale zur Minderung des Energieverbrauchs bis 2050. Tech. rep. Öko-Institute e.V.; 2014.
- [79] Gniffke P. Nationale Trendtabellen für die deutsche Berichterstattung atmosphärischer Emissionen. Tech. rep., Umweltbundesamt, 2017. URL:https://www.umweltbundesamt.de/sites/default/files/medien/361/dokumente/2017_01_23_em_entwicklung_in_d_trendtabelle_thg_v1.0.xlsx, [accessed June 27, 2018].
- [80] Burkhardt J, Patyk A, Tanguy P, Retzke C. Hydrogen mobility from wind energy – a life cycle assessment focusing on the fuel supply. *Appl Energy* 2016;181:54–64. <https://doi.org/10.1016/j.apenergy.2016.07.104>.
- [81] Eriksson M, Ahlgren S. Lcas for petrol and diesel - a literature review. Tech. rep. Swedish University of Agricultural Science Department of Energy and Technology; 2013.
- [82] Comission E. Methodology for establishing the eu list of critical raw materials – guidelines. Tech. rep. European Comission; 2017. <https://doi.org/10.2873/769526>.
- [83] Sustainability D. TNO, British Geological Survey, Bureau de Recherches Géologiques et Minières, Study on the review of the list of critical raw materials, Tech. rep., European Comission; 2017. doi:<https://doi.org/10.2873/876644>.
- [84] Hagelüken C, Buchert M, Stahl H. Substantial outflows of platinum group metals identified - spent autocatalysts are systematically withdrawn from the european market. *World Metall - ERZMETALL* 2003;56:529–40.

5.2 Proton Exchange Membrane Water Electrolysis at High Current Densities: Investigation of Thermal Limitations

This section contains the study "Proton Exchange Membrane Water Electrolysis at High Current Densities: Investigation of Thermal Limitations" [117]. The article was submitted in September 2019 and published in December 2019 (online) / January 2020 (print) in the *International Journal of Hydrogen Energy* after peer-review process. The publisher Elsevier grants permission to reuse this article in this thesis.

The permanent web link to this article is <https://doi.org/10.1016/j.ijhydene.2019.11.144> .

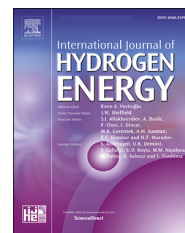
One possibility to address the problem of limited iridium availability for large scale PEMWE installation in the future is the operation at significantly higher current densities as today's state-of-the-art (which is $\approx 1.5 \text{ A/cm}^2$ [11]). To maintain high efficiency at high current densities, also the cell voltage needs to stay reasonably low (for reference: 1.79 V correspond to $\eta_{\text{LHV}} = 70 \%$). This is feasible by reducing ohmic losses in the cell when using significantly thinner membranes. In this study we show that it is technically possible to reduce the membrane thickness from 178 μm (Nafion[®] 117) down to 30 μm (Nafion[®] XL), integrate such thin MEAs into cell hardware (5 cm^2 laboratory cell; see figure 23, panel a)) and reach very high current densities. With MEAs based on Nafion[®] XL and current commercial standard catalysts and standard catalyst loadings (Anode: Elyst Ir75 0480 by Umicore, Germany with 75 wt% iridium content, loading: $1.24 \pm 0.01 \text{ mg}_{\text{Ir}}/\text{cm}^2$; Cathode: 46.7 wt% Pt/C TEC10V50E by Tanaka, Japan on Vulcan XC72 carbon, loading: $0.33 \pm 0.10 \text{ mg}_{\text{Pt}}/\text{cm}^2$) it is possible to run the cell at up to 25 A/cm^2 at corresponding cell voltages of $\approx 3 \text{ V}$. Though this high cell voltage is not suitable for long term service, the configuration allows operation at still very high current densities of 10 A/cm^2 and moderate cell voltages of 2.05 V (electric efficiency $\eta_{\text{LHV}} = 61 \%$). However, operation at high current densities around 10 A/cm^2 is associated with high heat production in the cell from the remaining irreversible losses. To analyze the temperature evolution in the MEA during high current density operation, a one dimensional model of in-cell heat transport from MEA to flow field channels is built and validated by in-situ temperature measurements inside the MEA. This is done by integrating thin bare wire thermocouples into MEAs based on Nafion[®] 117. The experiments show temperature differences from MEA to channel of up to 9.9 K at heat production rates of 7.8 W/cm^2 at low water flow rates of 2 $\text{ml}/(\text{min cm}^2)$ in the anode side flow field only and up to 2.4 K at heat production rates of 7.9 W/cm^2 at high water flow rates of 40 $\text{ml}/(\text{min cm}^2)$ in both anode and cathode side flow fields. At high heat production rates, the model overpredicts the MEA temperature by about 50 %. However, the model is suitable for estimating the maximum MEA temperature at a certain cooling water flow rate or for calculating the minimum water flow demand for sufficient cooling of the cell. This means that for continuous operation of our Nafion[®] XL based MEA at 80 °C and 10 A/cm^2 at an efficiency $\eta_{\text{LHV}} = 61 \%$, a minimum anode side water flow of 25 $\text{ml}/(\text{min cm}^2)$ would be necessary. If water flow is present on anode and cathode side of the cell, 10 $\text{ml}/(\text{min cm}^2)$ are enough to keep the MEA below a critical temperature of 90 °C.

Author Contributions

M.M. conceived and developed the idea. M.M., M.B. and J.S. fabricated electrodes and MEAs and performed electrochemical tests. M.M. developed the heat transfer model and the temperature sensor integration into the MEA. M.M. performed the analysis of the experimental data and wrote the manuscript. All authors discussed the results and revised the manuscript.

Available online at www.sciencedirect.com

ScienceDirect

journal homepage: www.elsevier.com/locate/ije

Proton exchange membrane water electrolysis at high current densities: Investigation of thermal limitations

Maximilian Möckl^{a,*}, Maximilian Bernt^a, Jonas Schröter^a,
Andreas Jossen^b

^a ZAE Bayern, Electrochemical Energy Storage, Walther-Meißner-Str. 6, 85748, Garching, Germany

^b Technical University of Munich, Department of Electrical and Computer Engineering, Chair of Electrical Energy Storage Technology, Karlstraße 45, 80333, Munich, Germany

HIGHLIGHTS

- In-situ measurements of membrane electrode assembly temperature in PEMWE cell.
- High current density experiments with thin membranes up to 25 A/cm².
- Analytic 1D model for in cell heat transport.
- Calculation of cooling flow demand dependent on cell heat production.

ARTICLE INFO

Article history:

Received 26 September 2019

Received in revised form

14 November 2019

Accepted 18 November 2019

Available online 18 December 2019

Keywords:

Proton exchange membrane water electrolysis (PEMWE)

High current density operation

Thermal limitation

Heat transport

ABSTRACT

In this work the thermal limitations of high current density proton exchange membrane water electrolysis are investigated by the use of a one dimensional model. The model encompasses in-cell heat transport from the membrane electrode assembly to the flow field channels. It is validated by in-situ temperature measurements using thin bare wire thermocouples integrated into the membrane electrode assemblies based on Nafion® 117 membranes in a 5 cm² cell setup. Heat conductivities of the porous transport layers, titanium sinter metal and carbon paper, between membrane electrode assembly and flow fields are measured in the relevant operating temperature range of 40 °C – 90 °C for application in the model. Additionally, high current density experiments up to 25 A/cm² are conducted with Nafion® 117, Nafion® 212 and Nafion® XL based membrane electrode assemblies. Experimental results are in agreement with the heat transport model. It is shown that for anode-only water circulation, water flows around 25 ml/(min cm²) are necessary for an effective heat removal in steady state operation at 10 A/cm², 80 °C water inlet temperature and 90 °C maximum membrane electrode assembly temperature. The measured cell voltage at this current density is 2,05 V which corresponds to a cell efficiency of 61 % based on lower heating value. Operation at these high current densities results in three to ten-fold higher power density compared to current state of the art proton exchange membrane water electrolyzers. This would drastically lower the material usage and the capital expenditures for the electrolysis cell stack.

© 2019 Hydrogen Energy Publications LLC. Published by Elsevier Ltd. All rights reserved.

* Corresponding author.

E-mail address: maximilian.moeckl@zae-bayern.de (M. Möckl).

<https://doi.org/10.1016/j.ijhydene.2019.11.144>

0360-3199/© 2019 Hydrogen Energy Publications LLC. Published by Elsevier Ltd. All rights reserved.

Introduction

Hydrogen production by proton exchange membrane water electrolysis (PEMWE) driven by renewable energy could be an environmental friendly alternative to fossil fuel based hydrogen production in a future energy system [1]. PEMWE has several advantages compared to alkaline and solid oxid electrolysis: It features high dynamic range and fast load change capability [2]. Furthermore, it can run in differential pressure mode. High purity hydrogen can be produced at the cathode at elevated pressure while the anode for the water splitting and oxygen evolution is kept close to atmospheric pressure [3]. This operation mode, together with a constant water transport due to electroosmosis from anode to cathode, allows for a simplified system layout where pure water is circulated at the anode side only at low pressures using mainly plastic piping and metal free components like water tanks or other parts of the system [4] to maintain high water quality. At the cathode side stainless steel fittings and piping can be used at the cell outlet to withstand high production pressures up to several 10 bar or even more than 100 bar [5] without the risk of contaminating the system with metal ions [6]. Nevertheless, one of the most outstanding features is the high current density that can be reached with PEMWE systems. Several publications report values up to 4 A/cm² [7,8], 10 A/cm² [9] or even 20 A/cm² [10]. The possibility to go up to high current densities while maintaining reasonably high efficiency potentially opens the field for appreciable reductions in material usage of the cell stack. This would lower the environmental footprint [1] and enables cost reduction of the PEMWE system [11] which is desirable for the facilitation of a large scale implementation of this technology.

However, high current density and consequential high power density goes along with an increase of voltage losses resulting in a significant heat production in the cell. The question then arises up to which cell heat production rate a safe operation without overheating of the cell or stack and the membrane electrode assembly is possible. In this context, Frensch et al. [12] point out, that elevated operation temperatures can intensify degradation effects. Especially the minimum flow requirements for the water circulation in the flow fields for the handling of a certain heat dissipation in the cell is of interest for PEMWE cell stack and system architecture. To reveal the influence of heat production rate on MEA temperature, a direct measurement with an integrated sensor seems the best option. In the closely linked field of proton exchange membrane fuel cells (PEMFC) several publications address the topic of MEA temperature measurement with sensors: He et al. [13] integrated a thin film type sensor inside two Nafion® 112 membranes to measure the MEA temperature in real-time at 0,2 V and 0,19 A/cm². Another design was proposed by Ali et al. [14] with thin film thermocouples deposited on Kapton foil on top of the MEA in a polybenzimidazole-based high temperature proton exchange membrane unit cell. Also flexible micro sensors manufactured on thin stainless-steel substrates have been used by Lee et al. [15]. Finally, thin wire thermocouples were used for temperature measurements in PEMFCs by several authors [16–20]. This concept seems to be a viable option also for PEMWE cells. Nevertheless, in the field of PEMWE the publications that deal with the thermal behaviour of the cell or stack during

operation are mainly simulation based: Grigoriev et al. [21] made a detailed mathematical model of a PEMWE cell to find optimum values for critical operating parameters. Besides several other findings they identified a cell temperature increase from inlet to outlet of 3 K to be optimal in terms of heat removal by water flow. Olesen et al. [22] used a 3D PEM electrolysis cell model to analyse different flow field designs at current densities up to 5 A/cm². They found high in-plane temperature differences in the membrane up to 20,2 K. Another modelling approach, which also incorporates in cell heat transport, was done by Aubras et al. [23] to examine the impact of two-phase-flow on PEMWE behaviour. Furthermore, Ojong et al. [24] used a semi-empirical fully-coupled performance model of a PEMWE cell to determine the effect of operating temperature and pressure, inlet water flowrate and porous transport layer (PTL) thickness on mass transport limitations at high current densities up to 5 A/cm². Garcia-Valverde et al. [25] proposed a lumped thermal capacitance model of a PEMWE stack for analyzing the temperature evolution during operation. They also measured the stack bulk temperatures and compared them to their model results for transient operation modes, but did not analyse the internal temperature distribution in the cell. A similar approach with modeling and experimental validation was published by Agbli et al. [26] focusing on the dynamic temperature trend in PEMWE stack and water tank during operation. Finally, Bock et al. [27] made a detailed finite elements 2D heat conduction model of PEMWE and anion exchange membrane water electrolyser cells and used measured values for the thermal conductivity of several different PTLs to calculate the MEA temperature and the temperature distribution in the cell. Convective heat transfer from the surface of the PTLs to the channels was not considered. They report temperature differences from the bipolar plate to the center of the MEA from 7 K to 17 K. However, to our knowledge there is no publication with a direct in-situ and operando measurement of the MEA temperature in a PEMWE cell. To close this gap and to be able to validate theoretical models we developed a specialized MEA with integrated temperature sensor based on a thin bare wire type K thermocouple and compared the measured data with a simple analytical 1D model. This model incorporates also the convective heat transfer from the PTL surfaces to the water flow in the channels and will be described in the following.

Thermal cell model

Heat production rate

For the water splitting reaction at standard conditions a total energy amount of $\Delta H_{298}^0 = 286$ kJ/mol is necessary of which a minimum amount of $\Delta G_{298}^0 = 237$ kJ/mol has to be delivered in form of electric energy. By application of the Faraday constant the reaction enthalpy and Gibbs free energy can be related to a certain cell voltage:

$$E_{\min} = \frac{\Delta G_{298}^0}{2 \cdot F} = 1,23\text{V} \quad (1)$$

$$E_{\text{th}} = \frac{\Delta H_{298}^0}{2 \cdot F} = 1,48\text{V} \quad (2)$$

The corresponding minimum cell voltage (equation (1)) for

the start of the reaction is 1,23 V, whereas at least 1,48 V (equation (2)) are necessary to deliver the total reaction enthalpy. At operation between 1,23 V and 1,48 V the reaction includes ambient heat to fulfill the total energy amount. Only if the cell runs at voltages exceeding 1,48 V, also called thermoneutral voltage E_{tn} , excess energy is set free in form of heat. As indicated above the values of ΔH and ΔG depend on the state of pressure and temperature. Nevertheless, at ambient pressure and moderate temperatures below 100 °C the differences are small [28]. Therefore, only the standard condition values are used for further calculations. The heat production $\dot{\omega}$ in a PEMWE cell thus depends on the difference of the actual cell voltage E_{cell} to the thermoneutral voltage E_{tn} and on the current density i at which the device is running:

$$\dot{\omega} = (E_{cell} - E_{tn}) \cdot i \quad (3)$$

Thermal balance

To establish the thermal balance of the PEMWE cell, all heat and mass in- and outflows crossing the cell system boundary have to be taken into account. Fig. 1 shows a graphic representation of the cell and the flows crossing the system boundary. Three main assumptions are made:

1. Adiabatic boundary condition: This assumption does not hold for small single cells but is getting more realistic for large active area format stacks with lower surface to volume ratio.
2. Negligible water consumption compared to water inflow: Under typical operating conditions the total water inflow is at least by a factor of ten higher than the water

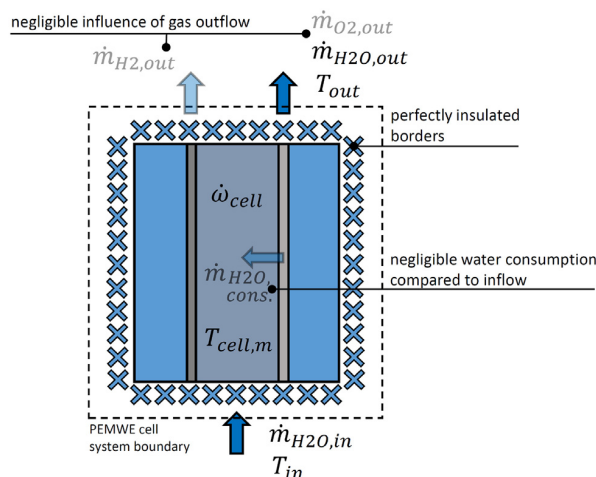


Fig. 1 – Simplified PEMWE cell domain for establishing the overall thermal balance for calculation of the outflow temperature and mean cell temperature in dependence of the water flow. The water consumption is usually small compared to the total water flow and is therefore neglected. Water inflow and outflow thus are assumed to be equal. Furthermore, also the gas outflow of hydrogen and oxygen is neglected and the cell is assumed to have adiabatic borders.

consumption in the reaction. Thus, the inlet and outlet water mass flows are assumed to be equal.

3. Negligible influence of gas outflow: The gas outflow also transports a certain amount of heat out of the cell. But due to the fact that the gas density is about a factor of thousand lower compared to liquid water, the gas bound heat transport is disregarded in the calculation.

This reduces the thermal balance of the cell to:

$$\dot{\omega} = \dot{m}_{H_2O} \cdot c_{p,H_2O} \cdot (T_{out} - T_{in}) \quad (4)$$

For a fixed inlet temperature T_{in} and a defined water mass flow \dot{m}_{H_2O} the outlet temperature T_{out} can be calculated based on the actual heat production rate $\dot{\omega}$ and the specific water heat capacity c_{p,H_2O} . Finally, also the cell mean temperature can be calculated:

$$T_m = \frac{1}{2} (T_{out} + T_{in}) = \frac{\dot{\omega}}{2 \dot{m}_{H_2O} c_{p,H_2O}} + T_{in} \quad (5)$$

Heat transport model - MEA to channel

However, the thermal balance of the cell just gives an integral information about the outlet or mean cell temperature and not about the internal temperature distribution. Fig. 2 shows a closeup cross section of the internal structure of the PEMWE cell used for the analysis in this study. The 5 cm² active area cell design is the same as described in Ref. [29]. The MEA is placed between the porous transport layers, a carbon paper at the cathode side (Toray TGP-H-120T without micro porous layer, PTFE content of 20 wt%, uncompressed thickness of 370 μm and compressed thickness of 280 μm) and a titanium sinter at the anode side (Mott Corporation, 50 % porosity and thickness of 280 μm). On both sides the serpentine type flow fields with channels of 1 mm width and depth and 0,7 mm wide lands and single channel lengths (= straight part between sharp 180° deflections at the bottom and top) of 22 mm complete the cell unit. According to the analysis done by Bernt et al. [29] applying proper cell compression and using gold coated flow fields produces about 10 mΩ cm² of electric contact resistance at the interfaces of the MEA and flow fields to the porous transport layers (PTL). Hence, in a simple approach there is 2,5 mΩ cm² of contact resistance at each of the in total four contact surfaces of the two PTLs. Another 2 mΩ cm² arises by the bulk resistance of the carbon PTL [29]. The electric resistance of the remaining parts, titanium sinter and the flow fields, is negligible small. Using a Nafion 212 based MEA at an exemplaric current density of 3 A/cm² and 80 °C cell temperature, Bernt et al. report a cell voltage of 1,72 V [29]. At this particular operating point 85 % of the heat is produced inside the MEA, another 6 % at the interfaces of the MEA to the PTLs, and 9 % outside the MEA in the carbon PTL and at the interfaces of PTLs to the flow fields. Based on these numbers (91 % of the heat production takes place inside or at the surface of the MEA) an important simplification of the heat transport model can be done by assuming the full heat production to occur inside the MEA.

As it is visible in Fig. 2, the flow fields are in direct contact to the PTLs only at the top of the lands which is about 40 % of the total flow field area. In order to use a 1D approach for the heat

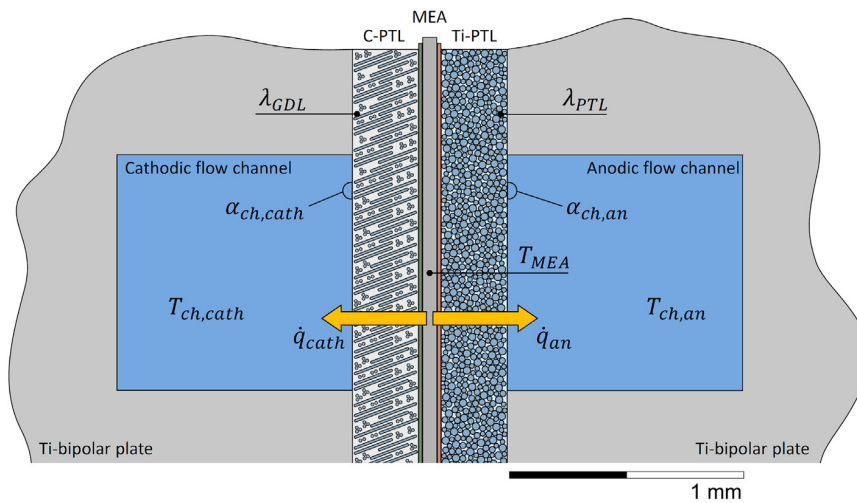


Fig. 2 – Cross sectional closeup view of membrane electrode assembly in the cell setup. All relevant parameters for modelling the through plane heat transport from MEA to the channels are depicted.

transport modelling, it is assumed that the land area has the same total heat transfer coefficient from MEA to channel as the channel area itself. This simplification can be justified by the relatively short ways the heat has to be conducted in the titanium land to reach the channel. At an exemplary heat conduction distance of 0,3 mm and a thermal conductivity of the titanium of about 16 W/(mK) the conduction heat transport coefficient would be high in the region of 50 kW/m². Thus, the titanium land acts similar to a cooling fin which adds only a small thermal resistance on the way from PTL to channel. However, a correct calculation of the heat transport through the solid titanium land would need a 2D model similar to the analysis done by Bock et al. [27].

In our modelling approach to reach the channels the heat produced in the MEA needs to cross the PTLs first and couple into the water flow at the interface of PTL to channel. Both processes have a certain heat transport coefficient or thermal resistance. Their calculation is described in the following.

Heat transport inside the PTL

Although the PTLs are porous and a complex two-phase-flow of water and gases takes place in their void volume, the main heat transport mode is via solid phase heat conduction. Thus, the PTLs are considered as being “dry” in terms of their thermal conductivity. For typical conditions the water flow crossing the MEA and the PTLs from anode to cathode via electroosmosis is about six times of the water consumption with electroosmotic drag coefficients around 3 mol H₂O/molH⁺ at 80 °C and fully water saturated Nafion® type membrane [30]. At the same time the molar gas flux of the hydrogen evolved at the cathode is equal to the molar flux of the water consumption whereas the oxygen molar gas flux evolved at the anode is only half the value of the water consumption molar flux. However, looking at the volumetric flow rates at atmospheric pressure the hydrogen gas flow is about 1570 times the volumetric water consumption rate and the oxygen gas flow is still 790 times the volumetric water consumption rate. Therefore, inside the void fraction of the PTLs comparing

the flow rates of gases and water cross flow results in a volumetric share during operation of less than 1 % water and more than 99 % gas at both cathode and anode side. Table 1 contains the dry thermal conductivities λ of both the un-compressed carbon paper (C-PTL) and the titanium sinter (Ti-PTL) for three temperatures within the typical operating range of PEMWE cells:

The materials were measured at ZAE Bayern, division Energy Efficiency, in Würzburg (Germany) using a Netzsch LFA 467 HyperFlash light flash system. As the PTLs are thin plates with an edge-length of about 80 times their thickness d , the stationary heat transport coefficient U_p in W/(m²K) can be calculated with equation (6):

$$U_p = \frac{\lambda}{d} \quad (6)$$

Table 2 contains the calculated heat transport coefficients for the two PTL materials. In the case of the carbon paper the compression of about 25 % in the cell during operation may have an influence on the thermal conductivity of the bulk material. Nevertheless, the effect was assumed to be small and was disregarded in the calculation. Thus, for the carbon paper the dry and uncompressed values for λ were used with the compressed thickness of 280 μ m for d .

The fluid and gas phase convective transport crossing the PTLs is relatively small. For an exemplaric operating point at 65 °C PTL mean temperature, a temperature difference of 10 K across the PTLs and 3 A/cm², the maximum transferable heat fluxes via product gases outflow and electroosmotic water crossflow are listed in Table 3 and compared with the solid phase conduction heat flux.

Table 1 – Measured thermal conductivities of applied PTL materials at 40 °C, 65 °C and 90 °C in dry state.

T (°C)	λ C-PTL (W/mK)	λ Ti-PTL (W/mK)
40	1,66	8,61
65	1,72	8,72
90	1,80	8,72

Table 2 – Calculated heat transport coefficients of applied PTL materials at 40 °C, 65 °C and 90 °C in dry state.

T (°C)	U_p C-PTL (W/m ² K)	U_p Ti-PTL (W/m ² K)
40	5930	30750
65	6140	31140
90	6430	31140

The solid phase conduction heat fluxes are several orders of magnitude higher than the maximum transferable convective heat fluxes of the produced gases and the water crossflow by electroosmosis. Hence, only the solid phase conduction is used to model the heat transport across the PTLs.

Convective heat transfer from PTL to channel

After crossing the PTLs the further heat transport takes place in form of a convective transfer from the PTL surfaces to the water flow in the channels on anode and cathode side of the cell unit. With the product gas bubbles entering as well, a complex two-phase-flow takes place in the channels. However, due to the fact that the water flow is externally controlled, the water flow rate does not change with the rising gas fraction in the channels. Thus, it is assumed that the convective heat transfer coefficient for a certain flow regime and water flow rate without gas bubbles represents a minimum value. The real heat transfer coefficients considering two phase flow with bubbles should be higher due to more pronounced turbulence in the flow at a given externally controlled water flow rate. Nevertheless, for simplification of the model the heat transfer coefficients are calculated using correlations for single phase water flow.

In the channels turbulent or laminar flow can be present. Using the dimensionless Reynolds number, which represents the ratio of inertia forces to friction forces in the flowing medium, a distinction of the flow regime can be done [31]. At Reynolds numbers below the critical value of 2300 the flow is considered laminar, above this value the flow regime is getting more and more turbulent [31]. The parameters for calculation of the Reynolds number are the mean flow velocity u , the hydraulic diameter D_h of the channel and the kinematic viscosity ν of the medium:

$$Re = \frac{uD_h}{\nu} \quad (7)$$

In the serpentine flow field channels at Reynolds numbers below 2300, laminar flow is present. The following correlation by Stephan [32] is used here for the calculation of the dimensionless heat transfer coefficient, the Nusselt number Nu :

$$Nu = \frac{3,657}{\tanh\left(2,264 \tilde{L}^{\frac{1}{3}} + 1,7 \tilde{L}^{\frac{2}{3}}\right)} + \frac{0,0499}{\tilde{L}} \cdot \tanh \tilde{L} \quad (8)$$

$1 \cdot 10^{-4} < \tilde{L} < 10$

According to Ref. [32] \tilde{L} is used as a dimensionless coordinate and is defined by equation (9) using the single channel length L , the hydraulic diameter of the channel D_h and the dimensionless Reynolds and Prandtl numbers:

$$\tilde{L} = \frac{L}{D_h Re Pr} \quad (9)$$

As described in Ref. [31] the Prandtl number Pr is the ratio of momentum, characterized by the kinematic viscosity ν , and the thermal diffusivity a :

$$Pr = \frac{\nu}{a} \quad (10)$$

At flow rates higher than 2 ml/(min cm²), hydrodynamic entrance has to be considered. This is done by applying following additional correlation by Stephan [32] to correct the Nusselt number obtained by equation (8):

$$Nu_h = \frac{Nu}{\tanh\left[2,432 \left(\frac{L}{D_h Re}\right)^{\frac{1}{6}}\right]} \quad (11)$$

Increasing the water flow rate to values over 10 ml/(min cm²) at temperatures around 80 °C leads to Reynolds numbers exceeding the critical value of 2300 for the specific channel dimensions of the analyzed cells flow field. Starting from these flow rates, the Gnielinski correlation [33] for turbulent flow with combined (thermal and hydrodynamical) entrance is used to calculate the dimensionless heat transfer coefficient:

$$Nu = \frac{\xi (Re - 1000) Pr}{1 + 12,7 \sqrt{\frac{\xi}{8}} \left(Pr^{\frac{2}{3}} - 1\right)} \left[1 + \left(\frac{D_h}{L}\right)^{\frac{2}{3}}\right] \quad (12)$$

$0,5 < Pr < 500, 2300 < Re < 10^6$

The friction factor ξ for smooth tubes is calculated by the Filonienko relationship [34]:

$$\xi = (1,82 \log Re - 1,64)^{-2} \quad (13)$$

After obtaining the dimensionless Nusselt numbers from both correlations 8 and 12 the convective heat transfer coefficients α can be computed by using the thermal conductivity λ of water at the local conditions (pressure and temperature) and the hydraulic diameter of the channel D_h :

$$\alpha = \frac{Nu \lambda}{D_h} \quad (14)$$

At a reference temperature of 80 °C and exemplary flow rates

Table 3 – Maximum transferable convective heat fluxes by product gas outflow and electroosmotic water crossflow at 65 °C PTL mean temperature, 10 K temperature difference and 3 A/cm² compared with solid phase conduction heat fluxes in applied PTL materials at same conditions.

Heat flux inside/by	(W/m ²)
H ₂ -gas-flow	45
O ₂ -gas-flow	23
EO-water-flow	703
C-PTL	61400
Ti-PTL	311400

of 2 ml/(min cm²) (laminar) and 40 ml/(min cm²) (turbulent) the resulting convective heat transfer coefficients are 3800 W/(m²K) calculated with correlation 8, 4200 W/(m²K) with additional hydrodynamic entrance correction factor 11 and 35200 W/(m²K) with correlation 12. In the special case of no active water circulation at the cathode side, the water flow in the cathode flow field is caused solely by water transported via electroosmosis from anode to cathode. For a current density of 3 A/cm² the flow rate due to electroosmosis in the cathode flow field is 0,01 ml/(min cm²). Thus, the convective heat transfer coefficient calculated by equation (8) is considerably lower than with active water flow and reaches values around 2500 W/(m²K).

MEA temperature calculation

Based on both above described heat transfer mechanisms the resulting sum heat transfer coefficients for each side can be calculated by:

$$U_{an} = \left(\frac{1}{U_{PTL,an}} + \frac{1}{\alpha_{ch,an}} \right)^{-1}$$

$$U_{cath} = \left(\frac{1}{U_{PTL,cath}} + \frac{1}{\alpha_{ch,cath}} \right)^{-1} \quad (15)$$

Finally, it is assumed that the water flow in both anode and cathode channels has the same temperature. This should be also true in the case of no active water circulation at the cathode side: Due to the fact that in a cell stack the anode flow field of the neighbouring cell with active water flow is situated directly at the opposite side of the cathode flow field, also the cathode flow field gets cooled from the water flow in the neighbouring cell. Therefore, the calculation of the MEA temperature is reduced to the following:

$$T_{MEA} = \frac{\dot{\omega} + T_{ch} \cdot (U_{an} + U_{cath})}{U_{an} + U_{cath}} \quad (16)$$

In the 1D model the channel temperatures are set equal to the mean water temperature in the cell computed by equation (5) for calculation of the mean MEA temperature. However, for the calculation of the maximum MEA temperature the outlet temperature from equation (4) is used. In the special case of the comparison of experimental and model values, the channel temperature is set to the flow field temperature measured by a sensor in the titanium flow field plates 2 mm behind the channels (experimental setup is described into detail in the following section). In the model all material values influencing the transfer coefficients are evaluated at the cell mean temperature obtained by equation (5). Again, in the case of the comparison of experimentally measured MEA temperatures with model results the measured flow field temperature is used as the reference for the material values.

Experimental setup

MEA preparation

All tests were performed with 5 cm² active area MEAs prepared by a decal transfer method. As cathode catalyst for the

hydrogen evolution reaction platinum nanoparticles supported on highly disperse carbon (46,7 wt% Pt/C TEC10V50E by Tanaka, Japan on Vulcan XC72 carbon) was used. For the anode side oxygen evolution reaction an IrO₂ based catalyst (Elyst Ir75 0480 by Umicore, Germany with 75 wt% Iridium content) on a TiO₂ support was employed. Both catalysts were prepared as inks by mixing catalyst powder, analytic grade isopropanol and ultrapure water with Nafion® ionomer solution (20 wt% of ionomer content, type D2021 by IonPower, USA) on a roller mill with 5 mm zirconia grinding balls for an entire day. Subsequently the inks were coated on low adhesive PTFE foil (50 μm by Angst+Pfister, Germany) by the use of a Mayer-rod coating machine. The decals (= electrode on PTFE foil) were then hotpressed on the different membrane materials using always the same parameters (3 min at 155 °C and 2,5 MPa). The applied membranes were Nafion® 117 (180 μm thickness), Nafion® 212 (50 μm thickness) and reinforced Nafion® XL (30 μm thickness). To evaluate the catalyst loading the PTFE decals were measured before and after hotpressing with a microbalance (Mettler Toledo, Germany). For all MEAs the anode catalyst loading was 1,24 ± 0,01 mg_{Ir}/cm² with an ionomer content of 11,6 wt% relative to the total electrode. All cathodes had loadings of 0,33 ± 0,10 mg_{Pt}/cm² with an ionomer to carbon ratio of 0,6/1.

Thermocouple integration in MEA

In order to measure the temperature inside the MEA during electrolysis, a thin sensor was integrated in a specialized setup presented in Fig. 3. A type K fine gage bare wire thermocouple (Omega Engineering, USA) with a nominal wire thickness of 75 μm and a junction thickness of 190 μm was used as the sensor element.

To protect the thermocouple from the harsh environment inside the MEA with pH values near 0 and to minimize influence on the thermoelectric potential by parasitic currents from the electrodes or by potential shift due to proton reduction on the metal surfaces, it needs to be electrically insulated by a durable material. This was achieved by placing the thermocouple in a PTFE micro tube with 300 μm inner diameter and wall thickness of 150 μm (Conrad Electronic, Germany). As depicted, the MEA was composed by two half MEAs consisting of anode and cathode, each hotpressed on an individual Nafion® 117 membrane. During cell assembly the shielded sensor was placed in the middle of the active area of the cell between cathodic and anodic half-MEA. Due to the relatively large dimensions of the sensor element, it was not possible to use thinner membranes. Earlier tests with thinner thermocouples have all been unsuccessful because of the susceptibility to mechanical failure. However, the final setup was robust and stable and could be used during the several days long test campaign without deterioration. As shown in equation (16) the temperature of the MEA should depend on the heat transfer coefficients on anode and cathode side outside of the MEA and on the heat production rate inside the MEA. Thus, in a first approximation for any cell-MEA combination at same heat production rates and heat transfer coefficients also the same temperature should be measured in the MEA. Operation at high cell voltage and lower current

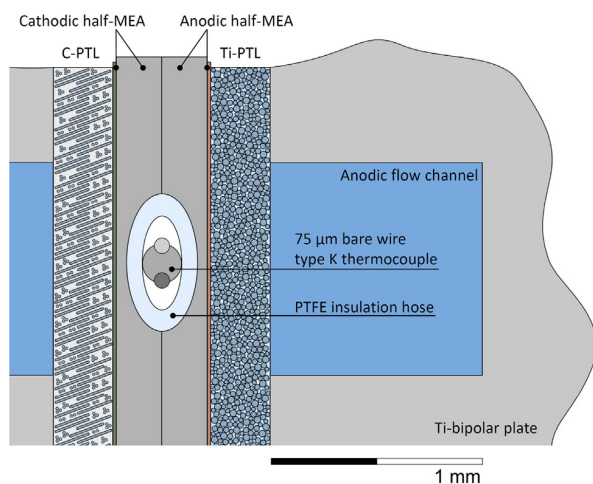


Fig. 3 – Cross sectional closeup view of 75 μm thin bare wire type K thermocouple integrated in MEA. The MEA is formed by two half MEAs based on two Nafion® 117 membranes with single electrodes laminated on only one side each. To prevent influence on the thermoelectric voltage during cell operation (potential shift by proton reduction on metal surface or by parasitic current from electrodes), the thermocouple is shielded by a PTFE insulation hose.

density should thermally resemble high current density operation at lower cell voltage, as long as the heat production rates are equal in both cases. This makes it possible to use thicker membranes with higher ohmic losses and consequently steeper polarization curves for the specialized temperature measurement setup instead of very thin MEAs with low losses and flat polarization curves.

Test procedures

MEA temperature measurements

The MEA temperature measurements were done at two different cooling water flow modes: A laminar low flow mode with 2 ml/(min cm^2) at the anode side only and a turbulent high flow mode at 40 ml/(min cm^2) on both sides of the cell. The high flow mode measurements were performed on a fully automated teststation with water recirculation pumps for high water flows up to 2 l/min (HoribaFuelcon, Germany). In contrast, the low flow mode measurements were performed on another fully automated test station (Greenlight Innovation, Canada) with direct preheated feed water injection (no water recirculation) by a precise HPLC pump to achieve a constant laminary flow in the flowfield without pressure spikes. In both cases the endplates of the cell were heated by cartridge heaters to 80 °C and also the water inlet temperature was set to 80 °C. The flow field temperature was measured by a PT100 sensor placed in a drilled hole in the titanium flow field block 2 mm behind the channels. The MEA temperature sensor signal was processed by a handheld digital thermometer (CHY Firemate, Taiwan) in order to have a floating measurement circuit. After reaching steady state conditions the zero current temperature was measured. Then the current

density was ramped up in steps of 1 A/ cm^2 up to a cell voltage threshold of 3,5 V. Every current density level was held for 5 min and the resulting temperatures in MEA and flow field were recorded. Both anode and cathode side were kept at atmospheric pressure during the whole test (besides a small dynamic overpressure at the cell inlet due to high water flow during high flow mode as mentioned in the following section).

High current density tests

The high current density tests were performed on the same test station as the high flow mode MEA temperature measurements with water flows of 40 ml/(min cm^2) on anode and cathode side. The water inlet temperature was set to 80 °C and endplates were heated by cartridge heaters also to 80 °C to achieve isothermal starting conditions. To maintain a high water quality throughout the whole experiments the water was pumped through deionizer cartridges (Leyco, Germany) before entering the cell. Both anode and cathode side were not statically pressurized. However, due to the high water flow rate a small overpressure of about 75 mbar is present at the inlet of the cell at zero current. After heating up the cell to steady state thermal conditions each cell was tested for a short circuit fault by applying 1 V and checking the current response. With no short circuit present the system was switched to current control mode and polarization curves were recorded by ramping up the current starting from 20 mA/ cm^2 to 1 A/ cm^2 in five smaller steps and thenceforth in steps of 1 A/ cm^2 up to a cell voltage threshold of 3,1 V. All steps were held for at least 15 s.

Results and discussion

Fig. 4 shows the measured temperature difference (continuous lines) between MEA and flow field/channel and the correspondent model results (dotted lines) for the same conditions as in the experiment for the two different flow regimes in the cell. The maximum heat production rate in the test was 7,8 W/ cm^2 during low flow measurement (green lines, triangle symbols) with anode side only circulation at 2ml/(min cm^2) and 7,9 W/ cm^2 during high flow measurement (blue lines, dot symbols) with water circulation on both sides at 40 ml/(min cm^2). Both measured curves show an equal trend: As expected the temperature differences rise with increasing cell heat production up to 9,9 K (low flow) and 2,4 K (high flow) in a relatively linear course. Only above a heat production rate of 4,3 W/ cm^2 there is a deviation of the linear behaviour with smaller increase in temperature difference. The model results show a very linear behaviour with maximum temperature differences of 13,8 K (low flow) and 3,6 K (high flow). However, the relative differences between experiment and model results are comparatively high, especially at higher heat production rates. For the low flow measurement the deviation is between 32 % and 45 % and for the high flow measurement between 16 % and 50 % in relation to the measured values. The model therefore very likely overestimates the MEA temperature. Possible reasons for the deviation and the non-linear behaviour at higher heat production rates could be an interaction between gas production and heat transport from the PTL surfaces to the channel. With more gas present, the

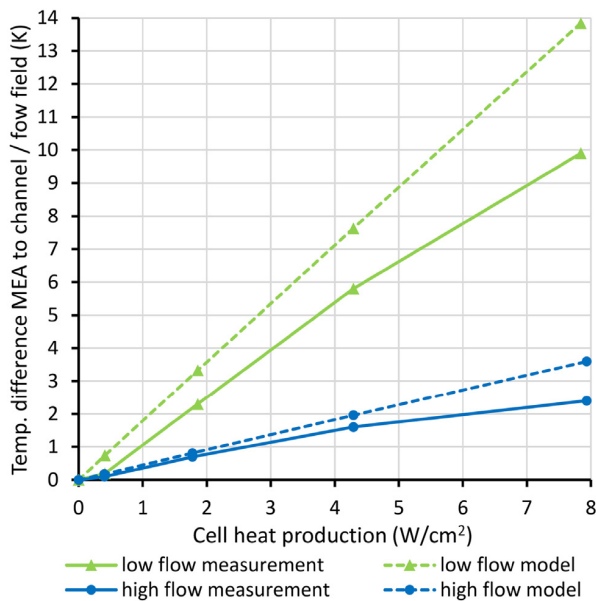


Fig. 4 – Comparison of modeled (dotted line) and measured (continuous line) temperature rise over cell heat production for low flow (green) with 2 ml/(min cm²) anode side circulation only and high flow (blue) with 40 ml/(min cm²) anode and cathode side circulation. (For interpretation of the references to colour in this figure legend, the reader is referred to the Web version of this article.)

convective heat transfer coefficient could be enhanced due to higher turbulence in the channels. This would as well be an explanation for the higher initial model to measurement difference in the laminar low flow experiment compared to the high flow experiment: The laminar flow convective heat transport coefficients are about a magnitude lower than the heat transport coefficients during fully turbulent flow. Thus, even a rather small perturbation of the laminar flow should result in elevated convective heat transport coefficients compared to the undisturbed case with no gas bubbles present. Also measurement errors could play a role in the origin of the differences between model and experiment. As it is visible in Fig. 4 the sensor inside the PTFE micro tubing is still quite large compared to the MEA thickness (approximately 400 μm in wet state) which could result in inhomogeneities or attenuation of the current density in the proximity of the sensor and thus also in differences of the local heat production rate compared to the undisturbed MEA area without sensor element. Nevertheless, experimental and model results are still of the same magnitude. This makes it possible to use the model as a tool to estimate the maximum expectable temperatures in a MEA during high current density operation.

The polarization curves obtained in the high current density tests with different membrane types are depicted in Fig. 5. The high operating temperature of 80 °C allows for an overall high efficiency of the cells, as membrane resistance is lowered and also activation losses are reduced [35]. It is clearly visible that the ohmic losses are strongly reduced by using thinner membranes which allows for a significant increase in current

density. The 180 μm thick Nafion® 117 based MEA (diamond symbols) shows the steepest polarization curve. At a cell voltage of about 2,02 V, which corresponds to a cell efficiency of about 62 % (LHV), the cell reaches a current density of 3 A/cm². At the upper cell voltage limit in the test (3,1 V) a maximum current density of 7 A/cm² is achieved. By changing the membrane type from 180 μm Nafion® 117 to 50 μm Nafion® 212 the cell resistance, evaluated in the linear region of the polarization curve between 3 A/cm² and 4 A/cm², is reduced by 103 m Ω cm². This MEA (triangle symbols) reaches 7 A/cm² at 2,04 V and 18 A/cm² at the upper voltage limit. The third MEA (dot symbols) with the thin reinforced Nafion® XL membrane (30 μm dry thickness) yields another 14 m Ω cm² of reduction in cell resistance and has the lowest losses and reaches 10 A/cm² at 2,05 V and 25 A/cm² close to the upper voltage limit at 2,9 V. The electric power density at this point is 72,5 W/cm² at an electric cell efficiency of 43 % (LHV). Taking 2 V as the upper operation limit with still reasonable cell efficiency greater 60 % (LHV) and because of increasing degradation effects for higher voltages, the current density could be doubled with the Nafion® 212 membrane and even more than tripled with the Nafion® XL membrane compared to Nafion® 117 which in turn offers the possibility to use only a third of active cell area to achieve the same hydrogen output. Sufficient stability of the cell and all of its materials provided, also the region above 2 V at high current densities around 15 A/cm² could be used for short time overload operation, which would especially be interesting for the coupling to intermittent renewable energies like wind turbines or photovoltaics where high peak powers occur for only short times [36,37].

However, the thinner membranes can also cause problems like higher cross permeation of product gases [38] or

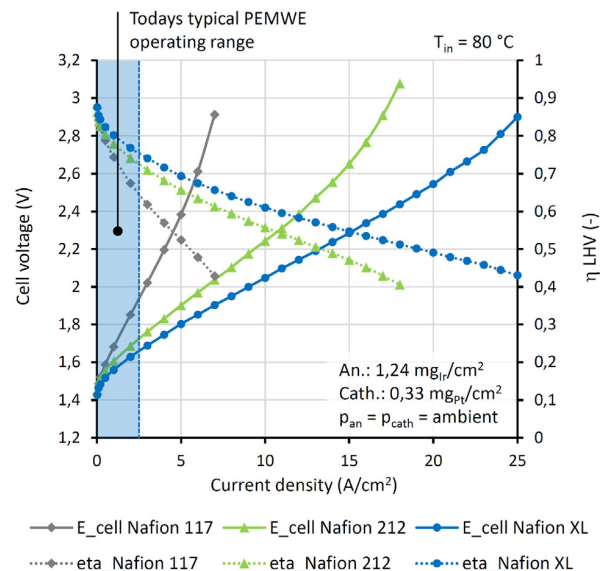


Fig. 5 – Cell polarization curves and corresponding cell efficiencies (LHV) for high current density tests with Nafion® 117, Nafion® 212 and Nafion® XL based MEAs. Water inlet and cell endplate temperature 80 °C, ambient pressure at cathode and anode side, water flows of 40 ml/(min cm²) on anode and cathode side.

insufficient mechanical stability [39]. Furthermore, the temperature inside the MEA should not overshoot a certain limit for the membrane material at the high current densities achieved. According to Barclay-Satterfield et al. [40] the elastic modulus of Nafion® membranes decreases significantly with rising temperatures: In a dry state the elastic modulus at 90 °C is only about a fourth of the value at room temperature and is further reduced to 1% at 110 °C. Therefore 90 °C is taken as the upper operation limit of the MEA temperature in this analysis.

Fig. 6 shows the area specific heat production rate (calculated by equation (3)) during the high current density tests. It can be noticed that at today's typical maximum current densities (marked region) below 2,5 A/cm² [28] the heat production is low and reaches a maximum of about 1 W/cm² with Nafion® 117. With higher current densities also the heat production rate increases significantly in a nonlinear way: At 10 A/cm² the rate is 5,7 W/cm² with the Nafion® XL based MEA and 7,6 W/cm² with the MEA based on Nafion® 212. The highest heat production rate of 35,5 W/cm² is reached at a current density of 25 A/cm² with the Nafion® XL based MEA. Next to the heat production rate curves the maximum MEA temperatures obtained by the model are noted for several current density points for each MEA type. With the high water flows of 40 ml/(min cm²) present on both sides of the cell, the MEA temperature stays below 81 °C in the current density range below 3 A/cm² for all membrane types. The temperature

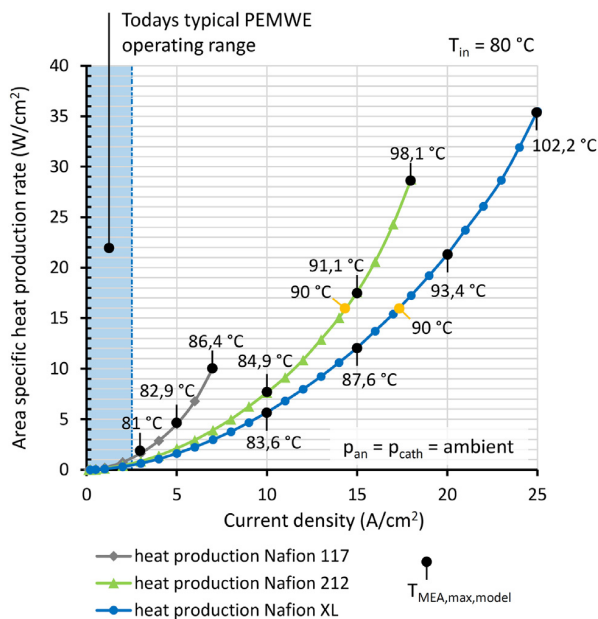


Fig. 6 – Area specific heat production rate and model results for maximum MEA Temperature during high current density tests with Nafion® 117, Nafion® 212 and Nafion® XL based MEAs. Water inlet and cell endplate temperature 80 °C, ambient pressure at cathode and anode side, water flows of 40 ml/(min cm²) on anode and cathode side. The 90 °C limit for the MEA temperature is marked yellow with diagonal marker lines. (For interpretation of the references to colour in this figure legend, the reader is referred to the Web version of this article.)

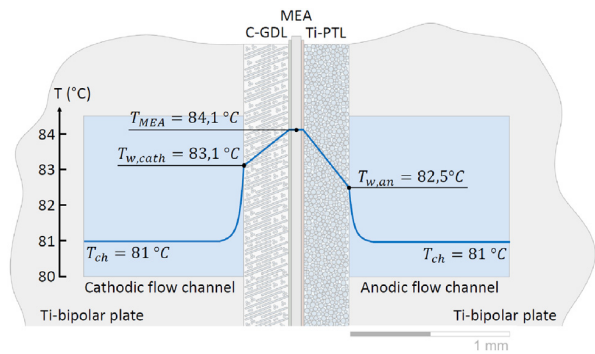


Fig. 7 – Model results for temperature profile MEA to channel at 5,7 W/cm² cell heat production and anode side circulation only at 40 ml/(min cm²). Inlet temperature is set to 80 °C. The corresponding current density would be 10 A/cm² with MEA based on Nafion® XL.

in the Nafion® 117 MEA is quickly rising with increased current density but does not reach the limit of 90 °C. Both Nafion® 212 and Nafion® XL based MEAs show a slower increase in temperature. The limiting temperature of 90 °C is reached at an area specific heat production rate of 15,9 W/cm². This corresponds to 14,5 A/cm² of current density for the Nafion® 212 based MEA and 17,5 A/cm² for the Nafion® XL based MEA. The calculated maximum temperature of 102,2 °C of the Nafion® XL based MEA is probably unrealistic as the boiling point of water should already be reached at the present atmospheric pressure conditions which identifies a limitation of the model. However, maximum current densities around 10 A/cm² should be realistic to achieve in future systems as the cell voltage is not too high (2,05 V) and the maximum MEA temperature can be kept fairly below the limit also at high operating temperatures of 80 °C.

For the exemplary current density of 10 A/cm² the calculated temperature profiles (mean values) in the cell are presented in Fig. 7 for anode side only water circulation with 40 ml/(min cm²) and in Fig. 8 for water circulation on both sides

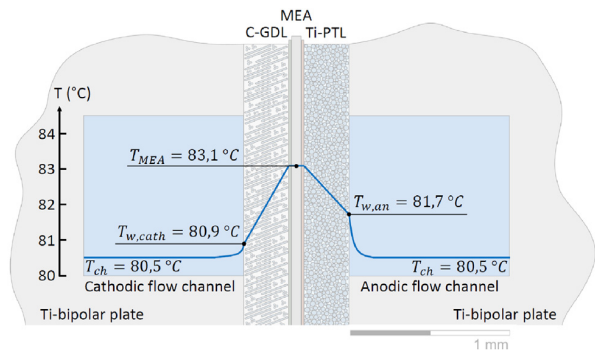


Fig. 8 – Model results for temperature profile MEA to channel at 5,7 W/cm² cell heat production and circulation both anode and cathode side at 40 ml/(min cm²). Inlet temperature is set to 80 °C. The corresponding current density would be 10 A/cm² with MEA based on Nafion® XL.

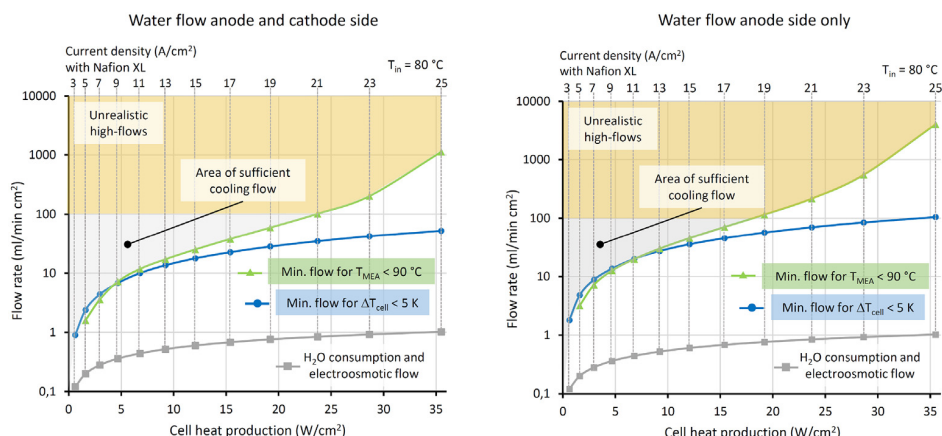


Fig. 9 – Minimum necessary circulation flow over cell heat production with water circulation at anode and cathode side (left) and water circulation at anode side only (right). The green line (triangle symbols) marks the minimum flow necessary for MEA temperature less than 90 °C. The blue line (dot symbols) marks the minimum flow necessary for cell inlet to outlet temperature difference less than 5 K. Flows above 100 ml/(min cm²) are considered unrealistic due to high flow velocity in the channels and subsequently high pressure drop in the flow fields. (For interpretation of the references to colour in this figure legend, the reader is referred to the Web version of this article.)

with 40 ml/(min cm²). Between the two operating modes the main differences are the lowered temperature level of the cell (channel temperature 0,5 K cooler) and the steeper temperature gradient in the cathode carbon paper PTL due to the higher convective heat transfer coefficient at the interface between PTL to channel during water circulation at both sides. Thus, during anode side circulation only the mean MEA temperature is 1 K higher than with circulation on both sides at the given conditions. This difference has to be considered especially during PEM electrolysis system development for choosing the right flow rate suitable for the selected system design (single or both sides water circulation).

In order to summarize the findings of this study, Fig. 9 shows the necessary minimum flow rates for safe operation within the thermal limits of a high current density PEMWE cell or stack with MEAs based on Nafion® XL at a water inlet temperature of 80 °C. The grey line (square symbols) marks the necessary flowrate to compensate the water consumption at the anode and the electroosmotic flow from anode to cathode. The blue line (dot symbols) is the necessary minimum flow rate to keep the temperature difference of cell inlet to cell outlet lower than 5 K, under the premise that all heat generated is transported out of the cell only by the cooling water. Finally, the green line (triangle symbols) marks the minimum flowrate to keep the maximum MEA temperature below 90 °C. Flowrates exceeding 100 ml/(min cm²) (yellow marked area) are considered unrealistic because of high flow velocity in the channels and subsequently high pressure drop over the flowfield. With water flow on both sides, the 5 K inlet to outlet temperature difference criterion is decisive up to a cell heat production of about 5 W/cm² or a current density of 9 A/cm² with a MEA based on Nafion® XL. For higher heat production rates and current densities the minimum flow rate requirement for a limited maximum MEA temperature below 90 °C becomes the leading criterion. For anode side only water

flow the crossing point of both criteria is shifted towards higher heat production rates and higher current densities. At first sight this behaviour seems unexpected: For the same water flow rate in the case of anode side only water flow the MEA temperature is higher than for the anode and cathode side water flow case as shown in Figs. 7 and 8. This would actually shift the crossing point towards lower current densities. However, for anode side only water flow the minimum flow rate for keeping the cell inlet to outlet temperature difference lower than a certain value always needs to be twice the flow rate which would be necessary for anode and cathode side water flow. Because this second effect outweighs the first, in total the crossing point is shifted towards higher current densities.

Conclusion

In this study we investigated the thermal limitation of high current density operation of PEMWE cells. In order to reveal the behaviour of in-cell heat transport from MEA to flow field channels we built a simple cell thermal balance model and a 1D internal heat transport model. Furthermore, we conducted in-situ measurements of the MEA temperature during cell operation. We measured temperature differences from MEA to channel of up to 9,9 K at heat production rates of 7,8 W/cm² at low water flow rates of 2 ml/(min cm²) in the anode side flow field only and up to 2,4 K at heat production rates of 7,9 W/cm² at high water flow rates of 40 ml/(min cm²) in both anode and cathode side flow fields. Though the model overpredicts the MEA temperature by up to 50 % at high heat production rates, both model and measurements show similar trend in temperature difference over heat production rate. Thus, the model is suitable as a tool to estimate the upper limit of the maximum MEA temperature and the cooling flow

needed at high current density operation of PEMWE cells and stacks. For three different MEA types based on Nafion® 117, Nafion® 212 and Nafion® XL membranes high current density tests were performed up to 25 A/cm². The heat production rate is nonlinear increasing with current density which limits the upper steady state operation point. At a cell inlet temperature of 80 °C with a Nafion® XL based MEA, operation around 10 A/cm² and 60 % efficiency (LHV) is possible at water flow rates of 25 ml/(min cm²) for anode side only circulation and 10 ml/(min cm²) at anode and cathode side circulation to remove the heat with less than 5 K temperature difference between cell inlet and outlet and to keep the MEA temperature below 90 °C. This allows for a reduction in active cell area to only one-third compared to a Nafion® 117 based MEA. Higher current densities are feasible (e.g. for short time overload operation), but require very high water flow rates.

Acknowledgements

The authors gratefully acknowledge funding by the Bavarian Ministry of Economic Affairs, Regional Development and Energy within the project ZAE-ST. We thank Frank Hemberger (ZAE Bayern, Würzburg) for the heat conductivity measurements and Matthias Rzepka as well as Franz Spingler for valuable discussions and reviewing the paper.

REFERENCES

- [1] Bareiß K, de la Rua C, Möckl M, Hamacher T. Life cycle assessment of hydrogen from proton exchange membrane water electrolysis in future energy systems. *Appl Energy* 2019;237:862–72. <https://doi.org/10.1016/j.apenergy.2019.01.001>.
- [2] Schiebahn S, Grube T, Robinius M, Tietze V, Kumar B, Stolten D. Power to gas: technological overview, systems analysis and economic assessment for a case study in Germany. *Int J Hydrogen Energy* 2015;40:4285–94. <https://doi.org/10.1016/j.ijhydene.2015.01.123>.
- [3] Sartory M, Wallnöfer-Ogris E, Salman P, Fellinger T, Justl M, Trattner A, Klell M. Theoretical and experimental analysis of an asymmetric high pressure pem water electrolyser up to 155 bar. *Int J Hydrogen Energy* 2017;42:30493–508. <https://doi.org/10.1016/j.ijhydene.2017.10.112>.
- [4] Sun S, Shao Z, Yu H, Li G, Yi B. Investigations on degradation of the long-term proton exchange membrane water electrolysis stack. *J Power Sources* 2014;267:515–20. <https://doi.org/10.1016/j.jpowsour.2014.05.117>.
- [5] Grigoriev SA, Porembskiy VI, Korobtsev SV, Fateev VN, Aupretre F, Millet P. High-pressure pem water electrolysis and corresponding safety issues. *Int J Hydrogen Energy* 2011;36:2721–8. <https://doi.org/10.1016/j.ijhydene.2010.03.058>.
- [6] Li N, Araya SS, Kaer SK. Long-term contamination effect of iron ions on cell performance degradation of proton exchange membrane water electrolyser. *J Power Sources* 2019;434:226755. <https://doi.org/10.1016/j.jpowsour.2019.226755>.
- [7] Siracusano S, Oldani C, Assunta Navarra M, Tonella S, Mazzapodia L, Briguglio N, Arico AS. Chemically stabilised extruded and recast short side chain aquivon proton exchange membranes for high current density operation in water electrolysis. *J Membr Sci* 2019;578:136–48. <https://doi.org/10.1016/j.memsci.2019.02.021>.
- [8] Lettenmeier P, Wang R, Abouatallah R, Helmly S, Morawietz T, Hiesgen R, Kolb S, Burggraf F, Kallo J, Gago AS, Friedrich KA. Durable membrane electrode assemblies for proton exchange membrane electrolyzer systems operating at high current densities. *Electrochim Acta* 2016;210:502–11. <https://doi.org/10.1016/j.electacta.2016.04.164>.
- [9] Villagra A, Millet P. An analysis of pem water electrolysis cells operating at elevated current densities. *Int J Hydrogen Energy* 2019;44:9708–17. <https://doi.org/10.1016/j.ijhydene.2018.11.179>.
- [10] Lewinski KA, van der Vliet D, Luopa SM. Nstf advances for pem electrolysis. *ECS Transactions* 2015;69:893–917. <https://doi.org/10.1149/06917.0893ecst>.
- [11] Schmidt O, Gambhir A, Staffell I, Hawkes A, Nelson J, Few S. Future cost and performance of water electrolysis: an expert elicitation study. *Int J Hydrogen Energy* 2017;42:30470–92. <https://doi.org/10.1016/j.ijhydene.2017.10.045>.
- [12] Frensch SH, Fouda-Onana F, Serre G, Thoby D, Araya SS, Kær SK. Influence of the operation mode on pem water electrolysis degradation. *Int J Hydrogen Energy* 2019;44:29889–98. <https://doi.org/10.1016/j.ijhydene.2019.09.169>.
- [13] He S, Mench MM, Tadigadapa S. Thin film temperature sensor for real-time measurement of electrolyte temperature in a polymer electrolyte fuel cell. *Sens Actuators A Phys* 2006;2:170–7. <https://doi.org/10.1016/j.sna.2005.05.021>.
- [14] Ali ST, Lebak J, Nielsen LP, Mathiasen C, Møller P, Kær SK. Thin film thermocouples for in situ membrane electrode assembly temperature measurements in a polybenzimidazole-based high temperature proton exchange membrane unit cell. *J Power Sources* 2010;195:4835–41. <https://doi.org/10.1016/j.jpowsour.2010.02.018>.
- [15] Lee C-Y, Weng F-B, Cheng C-H, Shiu H-R, Jung S-P, Chang W-C, Chan P-C, Chen W-T, Lee C-J. Use of flexible micro-temperature sensor to determine temperature in situ and to simulate a proton exchange membrane fuel cell. *J Power Sources* 2011;196:228–34. <https://doi.org/10.1016/j.jpowsour.2010.06.051>.
- [16] Vie PJS, Kjelstrup S. Thermal conductivities from temperature profiles in the polymer electrolyte fuel cell. *Electrochim Acta* 2004;49:1069–77. <https://doi.org/10.1016/j.electacta.2003.10.018>.
- [17] Wilkinson M, Blanco M, Gu E, Martin JJ, Wilkinson DP, Zhang JJ, Wang H. In situ experimental technique for measurement of temperature and current distribution in proton exchange membrane fuel cells. *Electrochim Solid State Lett* 2006;9:A507–11. <https://doi.org/10.1149/1.2338769>.
- [18] Wen C-Y, Huang G-W. Application of a thermally conductive pyrolytic graphite sheet to thermal management of a pem fuel cell. *J Power Sources* 2008;178:132–40. <https://doi.org/10.1016/j.jpowsour.2007.12.040>.
- [19] Lee S-K, Ito K, Ohshima T, Noda S, Sasaki K. In situ measurement of temperature distribution across a proton exchange membrane fuel cell. *Electrochim Solid State Lett* 2009;12:B126–30. <https://doi.org/10.1149/1.3152331>.
- [20] Zhang G, Guo L, Ma L, Liu H. Simultaneous measurement of current and temperature distributions in a proton exchange membrane fuel cell. *J Power Sources* 2010;195:3597–604. <https://doi.org/10.1016/j.jpowsour.2009.12.016>.
- [21] Grigoriev SA, Kalinnikov AA, Millet P, Porembsky VI, Fateev VN. Mathematical modeling of high-pressure pem water electrolysis. *J Appl Electrochem* 2010;40:921–32. <https://doi.org/10.1007/s10800-009-0031-z>.

- [22] Olesen AC, Frensch SH, Kær SK. Towards uniformly distributed heat, mass and charge: a flow field design study for high pressure and high current density operation of pem electrolysis cells. *Electrochim Acta* 2019;293:476–95. <https://doi.org/10.1016/j.electacta.2018.10.008>.
- [23] Aubras F, Deseure J, Kadjo JJA, Dedigama I, Majasan J, Grondin-Perez B, Chabriat JP, Brett DJL. Two-dimensional model of low-pressure pem electrolyser: two-phase flow regime, electrochemical modelling and experimental validation. *Int J Hydrogen Energy* 2017;42:26203–16. <https://doi.org/10.1016/j.ijhydene.2017.08.211>.
- [24] Ojong ET, Kwan JTH, Nouri-Khorasani A, Bonakdarpour A, Wilkinson DP, Smolinka T. Development of an experimentally validated semi-empirical fully-coupled performance model of a pem electrolysis cell with a 3-d structured porous transport layer. *Int J Hydrogen Energy* 2017;42:25831–47. <https://doi.org/10.1016/j.ijhydene.2017.08.183>.
- [25] García-Valverde R, Espinosa N, Urbina A. Simple pem water electrolyser model and experimental validation. *Int J Hydrogen Energy* 2012;37:1927–38. <https://doi.org/10.1016/j.ijhydene.2011.09.027>.
- [26] Agbli KS, Péra MC, Hissel D, Rallières O, Turpin C, Doumbia I. Multiphysics simulation of a pem electrolyser: energetic macroscopic representation approach. *Int J Hydrogen Energy* 2011;36:1382–98. <https://doi.org/10.1016/j.ijhydene.2010.10.069>.
- [27] Bock R, Karoliussen H, Seland F, Pollet BG, Thomassen MS, Holdcroft S, Burheim OS. Measuring the thermal conductivity of membrane and porous transport layer in proton and anion exchange membrane water electrolyzers for temperature distribution modeling - corrected proof. *Int J Hydrogen Energy* 2019;xx. <https://doi.org/10.1016/j.ijhydene.2019.01.013>. xxx–xxx.
- [28] Buttler A, Spliethoff H. Current status of water electrolysis for energy storage, grid balancing and sector coupling via power-to-gas and power-to-liquids: a review. *Renew Sustain Energy Rev* 2018;82:2440–54. <https://doi.org/10.1016/j.rser.2017.09.003>.
- [29] Bernt M, Gasteiger HA. Influence of ionomer content in irO₂/tio₂ electrodes on pem water electrolyzer performance. *J Electrochem Soc* 2016;163:F3179–89. <https://doi.org/10.1149/2.0231611jes>.
- [30] Luo Z, Chang Z, Zhang Y, Liu Z, Li J. Electro-osmotic drag coefficient and proton conductivity in nafion membrane for pemfc. *Int J Hydrogen Energy* 2010;35:3120–4. <https://doi.org/10.1016/j.ijhydene.2009.09.013>.
- [31] Incropera FP, Dewitt DP, Bergman TL, Lavine A. *Fundamentals of heat and mass transfer*. Hoboken: John Wiley and Sons; 2007.
- [32] Stephan P, Stephan K, Wärmeübertragung, Grote K-H, Bender B, Göhlich D, editors. *Dubbel Taschenbuch für den Maschinenbau*. Berlin: Springer; 2018. D36. Ch. D11.
- [33] Gnielinski V. New equations for heat and mass transfer in the turbulent pipe and channel flow. *Int Chem Eng* 1976;16:359–68.
- [34] Filonienko GK. Friction factor for turbulent pipe flow. *Teplotoenergetika* 1954;1(4):40–4.
- [35] Abdin Z, Webb CJ, Gray EM. Modelling and simulation of a proton exchange membrane (pem) electrolyser cell. *Int J Hydrogen Energy* 2015;40:13243–57. <https://doi.org/10.1016/j.ijhydene.2015.07.129>.
- [36] Zhao L, Brouwer J. Dynamic operation and feasibility study of a self-sustainable hydrogen fueling station using renewable energy sources. *Int J Hydrogen Energy* 2015;40:3822–37. <https://doi.org/10.1016/j.ijhydene.2015.01.044>.
- [37] Kopp M, Coleman D, Stiller C, Scheffer K, Aichinger J, Scheppat B. Energiepark mainz: technical and economical analysis of the worldwide largest power-to-gas plant with pem electrolysis. *Int J Hydrogen Energy* 2017;42:13311–20. <https://doi.org/10.1016/j.ijhydene.2016.12.145>.
- [38] Bessarabov D, Millet P. Chapter 5 - gas permeation in pem water electrolyzers. *Hydrogen Energy and Fuel Cells Primers* 2018:117–58. <https://doi.org/10.1016/B978-0-12-811145-1.00006-X>.
- [39] Stucki S, Scherer GG, Schlagowski S, Fischer E. Pem water electrolyzers: evidence for membrane failure in 100 kw demonstration plants. *J Appl Electrochem* 1998;28:1041–9. <https://doi.org/10.1023/A:1003477305336>.
- [40] Barclay-Satterfield M, Majsztzik PW, Ota H, Benziger JB, Bocarsly AB. Mechanical properties of nafion and titania/nafion composite membranes for polymer electrolyte membrane fuel cells. *J Polym Sci B Polym Phys* 2006;44:2327–45. <https://doi.org/10.1002/polb.20857>.

5.3 Analysis of Gas Permeation Phenomena in a PEM Water Electrolyzer Operated at High Pressure and High Current Density

In the following, the article "Analysis of Gas Permeation Phenomena in a PEM Water Electrolyzer Operated at High Pressure and High Current Density" [118] is presented. After submission in April 2020 and the peer-review process, the article was published in August 2020 in *The Journal of the Electrochemical Society*. The article is under open access, distributed under the terms of the Creative Commons Attribution 4.0 License (CC BY). The permanent web link is <https://doi.org/10.1149/1945-7111/abaa68>.

As described in the previous section 5.2, the use of thin membranes reduces ohmic losses in PEMWE cells and thus enables high current density operation at high electric efficiency. In this context, thin membranes are one major part of the solution for the problem of extensive material consumption (especially iridium) which comes along with a multi-GW/year installation of PEMWE systems for future large scale green hydrogen production. However, when using thin membranes also the permeation losses in the cell increase. This is especially critical for the hydrogen which permeates from cathode to anode and which is not recombined to water at the anode catalyst layer during PEMWE operation. Thus, the permeated hydrogen persists in the anode side product gas stream and forms a flammable gas mixture at concentrations above $\approx 4\%$ H_2 in O_2 . In order to investigate the occurring hydrogen permeation at high current density operation and high pressure differences when using thin membranes, in this study experiments with MEAs based on Nafion[®] 117 (178 μm dry thickness) and Nafion[®] 212 (51 μm dry thickness) at 80 °C cell temperature are conducted using a 5 cm^2 PEMWE cell (see figure 23, panel a)) in a fully automated test station coupled to an on-line mass spectrometer gas analyzer. To validate the setup, a first set of permeation measurements without PEMWE operation (no current flow) at different hydrogen pressures is conducted. The results show a linear dependency of the permeation rate on the H_2 partial pressure at the cathode and are in good agreement to an established electrochemical permeation measurement technique where the losses by permeation are compensated by hydrogen production (PEMWE) or electrochemically driven hydrogen transport against the pressure gradient (hydrogen pump). The observed hydrogen permeation rates are 0.31 $\text{mA}/(\text{cm}^2 \text{ bar})$ for Nafion[®] 117 and 1.10 $\text{mA}/(\text{cm}^2 \text{ bar})$ for Nafion[®] 212. In a second step, permeation measurements during PEMWE operation are conducted with MEAs at hydrogen partial pressures between 1 bar and 30 bar and operation up to 5 A/cm^2 with Nafion[®] 117 and up to 6 A/cm^2 with Nafion[®] 212. In agreement with literature data, a significant increase of the permeation rates with current density is observed, most pronounced for low pressures. Furthermore, an increase of the cathode ionomer content from standard 0.6/1 ionomer to carbon (I/C) ratio up to 1.2/1, which goes along with a diminution of the void fraction of the electrode, increases the H_2 permeation especially at high current densities. However, using cathodes with low I/C = 0.6/1 limits the permeation increase with current density at 30 bar cathode pressure to $\approx 16\%$ at 5 A/cm^2 . Using the results from the permeation measurements allows for a calculation of the total cell efficiency, the product of electric and faradaic efficiency, in dependence of the current density. For total cell efficiencies higher than 70 %, the operating range for Nafion[®] 117 is from 0.07 to 1.4 A/cm^2 for Nafion[®] 117 based MEAs and 0.23 to 3.1 A/cm^2 with Nafion[®] 212. The corresponding dynamic stack power range is 0.11 to 2.5 W/cm^2 (dynamic load spread factor of ≈ 23) for Nafion[®] 117 and ≈ 0.36 to 5.5 W/cm^2 (dynamic load spread factor of ≈ 15) for Nafion[®] 212.

Author Contributions

M.B., J.S. and H.G. conceived and developed the idea. M.B. and J.S. fabricated electrodes and MEAs and performed electrochemical tests. M.B., J.S. and M.M. set up the gas analysis system. M.B. and J.S. performed the analysis of the experimental data and wrote the manuscript. All authors discussed the results and revised the manuscript.



Analysis of Gas Permeation Phenomena in a PEM Water Electrolyzer Operated at High Pressure and High Current Density

M. Bernt,^{1,2,*} J. Schröter,^{1,2,=} M. Möckl,¹ and H. A. Gasteiger^{2,**}

¹Bayerisches Zentrum für angewandte Energieforschung, 85748 Garching, Germany

²Chair of Technical Electrochemistry, Department of Chemistry and Catalysis Research Center, Technische Universität München, 85748 Garching, Germany

In this study, on-line mass spectrometry is used to determine hydrogen permeation during proton exchange membrane water electrolyzer (PEM-WE) operation for a wide range of current densities (0–6 A cm⁻²) and operating pressures (1–30 bar, differential pressure). H₂ permeation measurements with a permeation cell setup, i.e., without applying a current, show a linear correlation between permeation rate and H₂ partial pressure, indicating diffusion as the main crossover mechanism. Measurements with full membrane electrode assemblies (MEAs) during PEM-WE operation reveal a significant increase of the gas permeation rate at high current densities, by up to ≈20-fold at 1 bar H₂ and up to ≈1.2-fold at 30 bar H₂ (Nafion[®] 212 or Nafion[®] 117 membrane; Ir-black (anode) and Pt/C (cathode)). Recently, H₂ super-saturation of the ionomer phase in the cathode catalyst layer was shown to be the reason for this increase, and we discuss the impact of this effect for different electrode compositions and operating conditions. Finally, the determined H₂ permeation rates and electrolyzer performance are used to discuss the overall PEM-WE efficiency for different membrane thicknesses and it is shown that the formation of an explosive gas mixture in the anode at low current densities requires additional mitigation strategies.

© 2020 The Author(s). Published on behalf of The Electrochemical Society by IOP Publishing Limited. This is an open access article distributed under the terms of the Creative Commons Attribution 4.0 License (CC BY, <http://creativecommons.org/licenses/by/4.0/>), which permits unrestricted reuse of the work in any medium, provided the original work is properly cited. [DOI: 10.1149/1945-7111/abaa68]



Manuscript submitted April 25, 2020; revised manuscript received June 30, 2020. Published August 7, 2020. This was paper 1598 presented at the Cancun, Mexico, Meeting of the Society, September 30-October 4, 2018.

PEM water electrolysis (PEM-WE) could become a key component in a future energy scenario based on renewable energy sources by providing electrolytic hydrogen for energy storage as well as for industrial processes and the mobility sector. Currently, only a small share of the global hydrogen demand is served by PEM-WE due to the relatively high costs associated with this technology.^{1,2} The overall H₂ generation costs depend on the operating costs which are governed by the electricity price and the investment costs for the PEM-WE system. While electricity prices from renewable energies have dropped significantly in recent years, with on-shore wind electricity at ≈0.06 US\$/kWh in 2017,^{3,4} corresponding to electricity costs of ≈3 US\$/kg_{H2} at 70% efficiency (based on the lower heating value), reducing the investment costs for the PEM-WE stack still presents a major challenge. Apart from reducing material costs for stack components,⁵ increasing the current density can be a way to lower costs by reducing the total cell area required to achieve a given hydrogen production rate. Recent publications show that current densities of 5 A cm⁻² and above are feasible,^{6–8} which is significantly higher than typical values for state-of-the-art systems (1–2 A cm⁻²).⁹ However, ohmic losses, which are mostly attributed to the membrane resistance, increase with current density and, consequently, thinner membranes have to be used to retain a high efficiency resulting in low operating costs (cf Results and Discussion section for detailed analysis). On the other hand, thinner membranes typically exhibit an increased gas crossover which presents a big challenge for PEM-WE applications, since H₂ is often produced at elevated pressures,¹⁰ generally between 20 – 50 bar.^{5,9} However, since H₂ is usually stored and distributed as a compressed gas or in the liquefied form,¹¹ PEM-WE operation at elevated H₂ pressure is beneficial to reduce overall system cost.^{9,10} Permeation of H₂ from the cathode through the membrane to the anode compartment not only reduces the faradaic efficiency of the electrolyzer, but can also lead to the formation of explosive gas mixtures in the anode compartment (the lower explosion limit for H₂ in O₂ is ≈4%),¹² since H₂ does not oxidize on the iridium oxide based anode catalysts.¹³ O₂ crossover is less critical, since O₂ is usually produced

at ambient pressure and permeation rates are lower than for H₂¹⁴; furthermore, O₂ can reduce to H₂O on the cathode catalyst, so that the accumulation of O₂ in the cathode compartment is minimal.¹⁵

In state-of-the-art PEM-WEs, perfluorosulfonic acid (PFSA) membranes such as Nafion[®] are used because they are mechanically robust and generally provide a good compromise between ohmic resistance and low gas permeability. Gas permeation rates for Nafion[®] membranes as a function of temperature, relative humidity, and differential pressure have been studied extensively in the literature using ex situ measurement techniques.^{16–22} However, recent studies show that permeation rates are different when measured under actual PEM-WE operating conditions and that they exhibit a significant dependence on current density.^{15,23–25} This phenomenon has been ascribed to a more complex water transport within the membrane during operation,²⁵ generally to a local pressure increase in the catalyst layer or to H₂ super-saturation.²⁴ Additionally, the influence of structural properties of the catalyst layer and the porous transport layer (PTL) as well as the impact of different cell hardware (applying, e.g., different compressive forces on the membrane electrode assembly (MEA)) is not fully understood yet^{24,26} and further research is required to clarify how these factors influence gas permeation.

In this study, we use on-line mass spectrometry to determine H₂ permeation rates during PEM-WE operation for a wide range of current densities (0–6 A cm⁻²) and operating pressures (1–30 bar, differential pressure) for MEAs with Nafion[®] 117 (thickness ≈178 μm) and Nafion[®] 212 (thickness ≈51 μm) membranes. Based on these results, the overall efficiency and the operating range of MEAs with different membrane thicknesses is discussed.

Experimental

Membrane electrode assembly (MEA) preparation and cell assembly.—The 5 cm² active area MEAs used in this study were prepared by a decal transfer method that has been described previously.⁷ Iridium black (Heraeus Metal Processing, Ltd., Ireland) was used as catalyst for the oxygen evolution reaction (OER) on the anode with loadings of 0.9 ± 0.3 mg_{Ir} cm⁻², while platinum supported on Vulcan XC72 carbon (45.8 wt% Pt/C; TEC10V50E from Tanaka, Japan) with loadings of 0.3 ± 0.1 mg_{Pt} cm⁻² was used as a cathode catalyst for the hydrogen evolution reaction (HER). The catalyst inks were prepared with catalyst powder, solvent (2-propanol purity ≥99.9% from Sigma Aldrich,

⁼These authors contributed equally to this work: M. Bernt and J. Schröter.

*Electrochemical Society Student Member.

**Electrochemical Society Fellow.

[†]E-mail: maximilian.bernt@tum.de

Germany), and Nafion[®] ionomer solution (20 wt% ionomer; D2021 from IonPower, USA). ZrO₂ grinding balls (5 mm diameter) were added for the 24 h mixing procedure on a roller mill. The ink was coated onto a 50 μm thick PTFE foil (from Angst+Pfister, Germany) using a Mayer-rod coating machine. To fabricate the 5 cm² active area MEAs, the electrodes were cut to size and then hot-pressed onto Nafion[®] 117/212 membranes (178 μm/51 μm thick; from Quintech, Germany) for 3 min at 155 °C at a pressure of 2.5 MPa. The electrode loadings were calculated from the weight difference of the PTFE decal before and after the transfer step, measured with a microbalance ($\pm 15 \mu\text{g}$; XPE105DR from Mettler Toledo, Germany). The ionomer content was fixed at 8.9 wt% for the anode while an ionomer to carbon (I/C) mass ratio between 0.6/1–1.2/1 was used for the cathode electrodes.

As porous transport layers (PTLs), sintered titanium (Ti) (from Mott Corporation, USA) with a porosity of $\approx 50\%$ and a thickness of $280 \pm 10 \mu\text{m}$ on the anode and carbon fiber paper (TGP-H-120 from Toray, no MPL) with a thickness of $370 \pm 10 \mu\text{m}$ on the cathode were used. A 10 μm PTFE sub-gasket was used to prevent the MEA from being cut by the sharp edges of the Ti PTL. The cell was sealed with two $310 \pm 10 \mu\text{m}$ thick PTFE gaskets to achieve a $\approx 25\%$ compression of the carbon PTL (corresponding to a compression of $\approx 1.7 \text{ MPa}$), whereby the Ti PTL is assumed to be incompressible.

Electrochemical characterization.—All tests were performed on a Greenlight E40 Electrolyzer Test Station equipped with a potentiostat and a booster (Reference 3000 and 30 °A booster, Gamry). The absolute pressure on the cathode was varied between 1.47 and 30.47 bar_a, while the anode was kept at ambient pressure. Taking into account the vapor pressure of water at 80 °C (0.47 bar) this translates into H₂ partial pressures between 1–30 bar on the cathode. Note that in the following, all pressure values refer to the H₂ partial pressure and not to the total pressure in the cathode compartment. Cell and reactant inlet temperatures were set to 80 °C and DI water was supplied at a flow rate of 10 ml min^{-1} to the anode. Hydrogen was supplied to the cathode and oxygen to the anode at flow rates between 50 and 200 ml min^{-1} (note that all gas flow rates are referenced to standard conditions of 0 °C and 1.013 bar). A $\approx 2 \text{ h}$ lasting cell-warmup and a conditioning procedure were performed before the measurements. During the conditioning, the current density was ramped to 1 A cm^{-2} over 200 s and held for 30 min. Three polarization curves with current densities starting from 0.01 and increasing to 6 A cm^{-2} were recorded afterwards. Each current density step was held for 5 min followed by an AC impedance measurement in a range of 20 kHz–10 Hz to determine the high frequency resistance (HFR). During the H₂ permeation rate measurements the current density was varied between 0–6 A cm⁻² with hold times from 90–180 min for each current step. Additional polarization curves were recorded following the permeation measurement at each H₂ pressure step as well as at the end of test.

Hydrogen permeation rate.—The test setup used in this work to determine the H₂ permeation rates is based on the analysis of the H₂ volume fraction (on a dry basis) in the O₂ exhaust of the anode, using a mass spectrometer (cf Fig. 1). A defined flow of dry H₂ gas can be supplied to the cathode inlet of the electrolyzer cell, while defined flows of H₂O and O₂ gas can be supplied to the anode inlet. The product gas at the anode outlet of the cell is typically a mixture of H₂O, O₂, and H₂ that permeates from the cathode compartment through the membrane into the anode compartment. Water is then separated from the product gas by a heat exchanger and a water separator unit implemented in the test station (E40 from Greenlight, Canada), as shown in Fig. 1). The dry product gas, consisting of a mixture of O₂ and H₂ is then analyzed by a quadrupole mass spectrometer (CirrusTM3 from MKS). Thorium filaments are used to ensure a sufficient filament lifetime in the highly corrosive O₂ environment. The capillary which supplies the gas to be analyzed to the mass spectrometer requires a minimum flow of 20 ml min^{-1} .

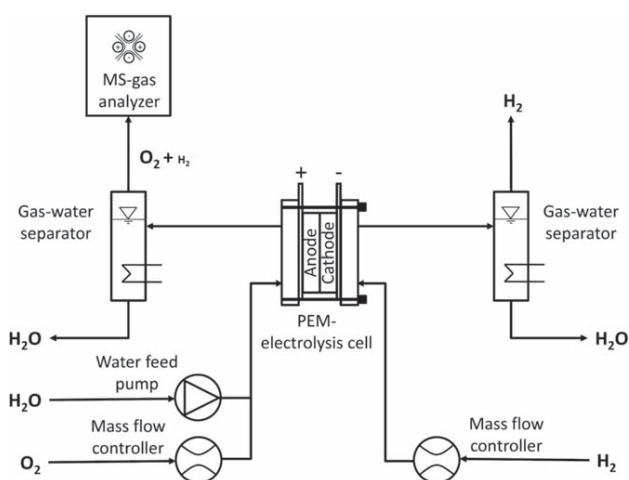


Figure 1. Schematic flow diagram of the test setup used for gas permeation measurements via mass spectrometry. Dry H₂ gas can be supplied to the cathode, while H₂O and O₂ can be supplied to the anode. Water is separated from the product gases at the cell outlet by a heat exchanger and a water separator. The dry product gas on the anode (a mixture of O₂ and H₂) is analyzed by a mass spectrometer. Measurements are performed at a temperature of 80 °C and at H₂ partial pressures of 1–30 bar, while the anode is being kept at ambient pressure.

Consequently, if the O₂ production rate during electrolyzer operation is too low (i.e., at low current densities) or for the permeation cell measurements (cf Fig. 2) where no O₂ is produced at all, additional O₂ gas needs to be supplied in order to ensure sufficient gas flow to the capillary. The amount of O₂ supplied to the anode inlet (cf Fig. 1) is regulated by a mass flow controller to achieve a total gas flow at the anode outlet of at least 50 ml min^{-1} . Furthermore, this additional O₂ flow prevents the formation of explosive gas mixtures in the anode gas stream (lower explosion limit for H₂ in O₂: $\approx 4\%$ ¹²). Of course, the additional O₂ flow needs to be considered when calculating the actual H₂ in O₂ content that would be obtained in a PEM-WE (i.e., in the absence of adding O₂ to the anode inlet) that is shown in Fig. 8.

During the measurements, the anode compartment is kept at ambient pressure, while the H₂ partial pressure on the cathode is varied between 1–30 bar. The pressure in the cathode compartment is controlled by a back pressure regulator which requires a continuous gas flow to maintain a constant pressure. Hence, an additional H₂ gas flow of 50 ml min^{-1} is supplied to the cathode inlet during all measurements in order to ensure a sufficient gas flow even at low current densities (i.e., at low H₂ production rates) and during the permeation cell measurements (cf Fig. 2). A more detailed description of the MEAs and the transport processes taking place in the cell can be found in the following sections for the respective test setups.

Theory of Gas Permeation

In this section, the mass transport mechanisms which are responsible for H₂ gas permeation in a PEM-WE, namely diffusive and convective transport are discussed briefly. For a more detailed discussion of crossover mechanisms we refer to Ref. 27.

Diffusion.—In general, diffusion of H₂ from the cathode to the anode can occur through the polymer phase as well as the liquid phase in ionomeric membranes.²⁰ For Nafion[®] membranes the contribution of diffusion through the polymer phase is very small and it is generally assumed that diffusion through the liquid phase is the dominating mechanism²¹; a quantitative separation of the permeation of various gases through a Nafion[®] membrane was also given by Mittelsteadt and Liu.²⁰ The diffusive H₂ flux according to Fick's law can be expressed as

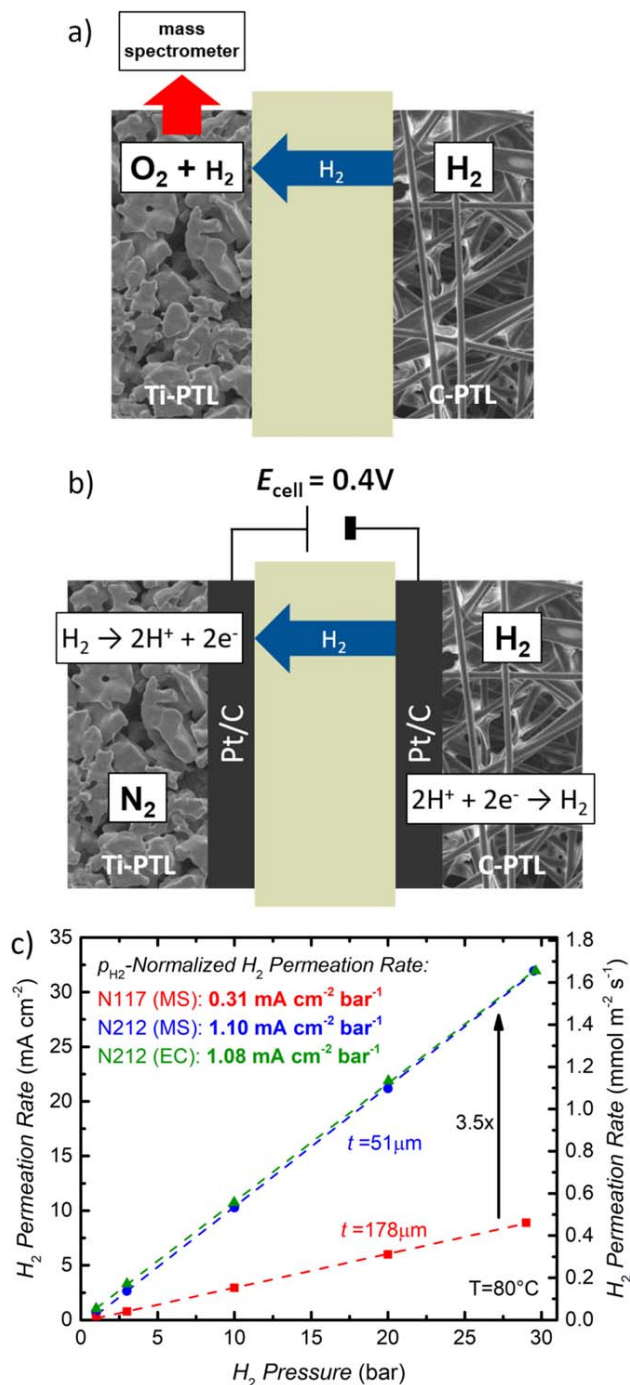


Figure 2. (a) Sketch of the here developed test setup to measure H₂ permeation rates by quantifying the H₂ content in the O₂-rich anode gas using a mass spectrometer. For this, H₂ is supplied to the cathode (50 ml min⁻¹), while the anode is supplied with H₂O (10 ml min⁻¹) and O₂ (50 ml min⁻¹ for $p_{\text{H}_2} \leq 10$ bar and 100 ml min⁻¹ for $p_{\text{H}_2} > 10$ bar). (b) Sketch of the test setup used for conventional electrochemical H₂ permeation rate measurements. H₂ (50 ml min⁻¹) is supplied to the cathode, while the anode is supplied with H₂O (50 ml min⁻¹) and N₂ (50 ml min⁻¹); the limiting current density obtained at a potential of 0.4 V represents the H₂ permeation current. (c) H₂ permeation rate as a function of H₂ partial pressure on the cathode for a Nafion[®] 117 membrane (red) and a Nafion[®] 212 membrane (blue) determined with the test setup shown in Fig. 2a. The H₂ permeation rate for a Nafion[®] 212 membrane determined with the electrochemical measurement method presented in Fig. 2b is shown for comparison (green). The H₂ partial pressure normalized H₂ permeation rate (in units of mA cm⁻² bar⁻¹) was determined by a linear regression of the measured permeation rates (dashed lines).

$$N_{\text{H}_2}^{\text{diff}} = D_{\text{H}_2}^{\text{eff}} \cdot \frac{\Delta c_{\text{H}_2}}{t_{\text{memb}}} \quad [1]$$

Here, Δc_{H_2} represents the H₂ concentration gradient between anode and cathode. Assuming a negligible H₂ concentration in the anode compartment compared to that in the cathode compartment, Δc_{H_2} is directly proportional to the partial pressure of H₂ in the cathode compartment. $D_{\text{H}_2}^{\text{eff}}$ is the effective diffusion coefficient of the membrane which is a function of porosity and tortuosity,²⁷ i.e., of the water content of the membrane, while t_{memb} represents the membrane thickness. Assuming a constant water content of the membrane, the diffusive H₂ flux is expected to scale linearly with the H₂ partial pressure on the cathode of the electrolyzer.

Convection.—Convective transport of H₂ dissolved in liquid water due to a net water transport through the membrane is another possible mechanism of H₂ crossover and can be described as²⁷

$$N_{\text{H}_2}^{\text{conv}} = v_{\text{H}_2\text{O}} \cdot c_{\text{H}_2} \quad [2]$$

where $v_{\text{H}_2\text{O}}$ is the velocity of water moving through the membrane and c_{H_2} is the concentration of dissolved H₂ in the water phase. Differential pressure operation is a possible reason for a net water transport and, consequently, a convective H₂ flux from cathode to anode. Here, the total pressure difference between cathode and anode, ΔP , would be directly proportional to the H₂ permeation rate according to Darcy's law²⁷

$$N_{\text{H}_2}^{\text{diff-press}} = D_{\text{H}_2}^{\text{diff-press}} \cdot \frac{p_{\text{H}_2,\text{cath}} \cdot \Delta P}{t_{\text{memb}}} \quad [3]$$

where $p_{\text{H}_2,\text{cath}}$ is the H₂ partial pressure on the cathode, t_{memb} the membrane thickness, and $D_{\text{H}_2}^{\text{diff-press}}$ a transport coefficient which depends on the permeability of the membrane, the solubility of H₂ in water, and the dynamic viscosity. If the pressure in the anode compartment is much smaller than in the cathode compartment, the partial pressure of H₂, $p_{\text{H}_2,\text{cath}}$, equals approximately the total pressure difference, ΔP , and the convective H₂ permeation should scale quadratically with $p_{\text{H}_2,\text{cath}}$.

Electro-osmotic drag of water is another possible source of convective H₂ transport. Here, water is transported from anode to cathode, at a rate which is directly proportional to the amount of protons transported, i.e., to the current density.²⁷

$$N_{\text{H}_2}^{\text{drag}} = D_{\text{H}_2}^{\text{drag}} \cdot p_{\text{H}_2,\text{an}} \cdot i \quad [4]$$

Here, i is the current density and $p_{\text{H}_2,\text{an}}$ the H₂ partial pressure on the anode while $D_{\text{H}_2}^{\text{drag}}$ is a transport coefficient which depends on the solubility of H₂ in water and the electro-osmotic drag coefficient that describes the ratio of the number of water molecules dragged along per proton. Since convective transport of H₂ due to the electro-osmotic drag would occur from anode to cathode, it would actually lead to a lower overall H₂ crossover flux from cathode to anode and would only affect it during electrolyzer operation, i.e., when a current is drawn.

Note that in the following, the term “permeation” is used to describe the measured H₂ crossover from cathode to anode, even though, strictly speaking, the term permeation would only apply to a partial gradient driven transport (Eq. 1) and not to the convective transport processes. Furthermore, H₂ permeation rates are referenced to the dry thickness of the membranes.

Results and Discussion

H₂ permeation rates using permeation cell measurements.—First, to validate the H₂ permeation measurement method based on the quantification of the H₂ concentration in the O₂ exit stream of the anode compartment of a PEM-WE by mass spectrometric analysis,

the H₂ permeation rates through Nafion® membranes are measured as a function of the H₂ partial pressure. The thus determined H₂ permeation rates are then compared with those determined by the well-established electrochemical method to quantify H₂ permeabilities, which is based on the electrooxidation of H₂ that is permeating through an MEA with the same membrane from a H₂-filled compartment into a N₂-filled compartment of a fuel cell or electrolyzer cell.^{18,21}

For the here used H₂ permeation measurement method that is based on quantifying the H₂ concentration in the O₂-containing anode compartment, a Nafion® membrane is assembled between the PTLs (Ti sinter on anode and carbon paper on cathode) in the cell hardware (cf Fig. 2a). A mixture of O₂ (50 ml min⁻¹ for $p_{\text{H}_2} \leq 10$ bar and 100 ml min⁻¹ for $p_{\text{H}_2} > 10$ bar) and H₂O (10 ml min⁻¹) is supplied to the anode inlet in order to ensure sufficient humidification of the membrane as well as a sufficient gas flow to the mass spectrometer (see Experimental section). On the cathode, H₂ gas is supplied at a flow rate of 50 ml min⁻¹ and the H₂ partial pressure is varied from 1–30 bar while the anode is kept at ambient pressure. A hold time of 15 min is applied for each pressure step to give the system enough time to stabilize and to obtain a constant signal in the mass spectrometer. Each pressure step is measured twice (once while increasing the pressure and once while decreasing the pressure), and the deviation between the obtained values was always $<0.4 \text{ mA cm}^{-2}$ ($\approx 0.02 \text{ mmol m}^{-2} \text{ s}^{-1}$). The averaged H₂ permeation rates calculated from the mass spectrometer (MS) data are shown in Fig. 2c as a function of H₂ partial pressure for a Nafion® 117 (referenced to a dry thickness of $\approx 178 \mu\text{m}$) and a Nafion® 212 (referenced to a dry thickness of $\approx 51 \mu\text{m}$) membrane. For both Nafion® 117 (red symbols/line in Fig. 2c) and Nafion® 212 (blue symbols/line in Fig. 2c), the permeation rate increases linearly with H₂ partial pressure. Furthermore, the H₂ partial pressure normalized permeation rate (i.e., the slope of the lines in Fig. 2c) of the thin Nafion® 212 membrane ($1.10 \text{ mA cm}^{-2} \text{ bar}^{-1}$) is a factor ≈ 3.5 higher compared to the Nafion® 117 membrane ($0.31 \text{ mA cm}^{-2} \text{ bar}^{-1}$), exactly matching the inverse of the thickness ratio between the two membranes ($178 \mu\text{m}/51 \mu\text{m} \approx 3.5$). Both findings indicate that diffusion-driven H₂ permeation according to Eq. 1 is the dominating process, since the H₂ diffusion rate is directly proportional to the H₂ partial pressure and to the inverse of the membrane thickness (cf Eq. 1). If convective transport due to the pressure difference between anode and cathode were to have a significant influence, a quadratic dependency on H₂ pressure would be expected (cf Eq. 3), which clearly is not observed in these measurements.

To validate the H₂ permeation rates obtained by quantifying the concentration of crossover H₂ in O₂ with the mass spectrometer setup (cf Fig. 2a), we will now compare them with the results from an electrochemical measurement technique frequently used to determine H₂ permeation rates.^{18,21} The setup for this measurement is described in Fig. 2b. An MEA is fabricated with a Nafion® 212 membrane and carbon supported platinum (Pt/C) electrodes ($\approx 0.3 \text{ mg}_{\text{Pt}} \text{ cm}^{-2}$) with a standard ionomer/carbon mass ratio of 0.6/1 on both sides of the MEA. This MEA is then assembled between the Ti sinter and the carbon paper PTLs in the same electrolyzer cell hardware, and N₂ gas (50 ml min⁻¹) along with water (5 ml min⁻¹) are supplied to the anode compartment while H₂ (50 ml min⁻¹) is supplied to the cathode compartment. A positive potential of 0.4 V is applied to the anode and, consequently, H₂ permeating through the membrane to the anode is oxidized to protons at the Pt catalyst (note that the counter reaction in the H₂ compartment is the H₂ evolution reaction), whereby the measured limiting current density represents the rate of H₂ permeation through the membrane. This measurement was performed for H₂ partial pressures from 1–30 bar and the results are shown by the green symbols/line in Fig. 2c. The results fit perfectly with the H₂ permeation rate obtained for a Nafion® 212 membrane with the mass spectrometer setup (cf Fig. 2a). On account of this excellent agreement between these two methods, we consider our test setup based on a mass spectrometer to analyze the H₂ content in the O₂-rich anode gas suitable for H₂ permeation

measurements during operation of a PEM-WE which will be discussed in the next section.

H₂ permeation rates during PEM-WE operation.—To determine the H₂ permeation rate during electrolyzer operation, i.e., as a function of the applied current density, the setup shown in Fig. 3a is used. MEAs are fabricated based on either a Nafion® 212 or a Nafion® 117 membrane. The anode electrode consists of Ir-black ($0.9 \pm 0.3 \text{ mg}_{\text{Ir}} \text{ cm}^{-2}$), while a Pt/C cathode ($0.3 \pm 0.1 \text{ mg}_{\text{Pt}} \text{ cm}^{-2}$) with a standard ionomer/carbon mass ratio of 0.6/1 is used. The MEAs are assembled between Ti sinter (anode) and carbon paper (cathode) PTLs in the cell hardware. After a conditioning procedure described in the Experimental section, H₂ permeation rates are measured for different current densities up to 5 A cm^{-2} for the Nafion® 117 membrane and up to 6 A cm^{-2} for the Nafion® 212 membrane. The maximum current density is determined by an upper potential limit of 2.4 V. Permeation rates at a current density of zero are recorded while a potential of 1.3 V is applied to the iridium anode. At this potential, the surface of the iridium catalyst is oxidized and, consequently, exhibits a very low HOR activity.¹³ This is crucial, since H₂ oxidation on the anode would reduce the amount of H₂ detected at the anode outlet by the MS and, therefore, would lead to an underestimation of the H₂ permeation rate. The current measured during the potential hold at 1.3 V is $<1 \text{ mA cm}^{-2}$ ($<0.05 \text{ mmol m}^{-2} \text{ s}^{-1}$), proving that the HOR activity of the iridium catalyst is negligible, which is a prerequisite for the here used H₂ permeation rate measurements. Furthermore, the potential hold at 1.3 V ensures that the anode catalyst is never exposed to a reducing atmosphere. This is important since it was shown that frequent cycling between a reducing and an oxidizing atmosphere on the anode can lead to a significant alteration of the catalyst properties, which could also influence H₂ permeation measurements.²⁸

The obtained H₂ permeation rates for H₂ partial pressures between 1 – 30 bar as a function of current density are shown in Fig. 3b for a Nafion® 117 membrane and in Fig. 3c for a Nafion® 212 membrane. Full symbols along with full lines represent the data measured while increasing the current density, whereas open symbols along with dotted lines show the data obtained while decreasing the current density. The error bars represent an overall error of the H₂ permeation measurement based on the accuracy of the mass spectrometer, fluctuations of the operating conditions, as well as uncertainties related to the active area in the cell (a detailed explanation can be found in the Appendix). Brown crosses give the H₂ permeation rates measured with the permeation cell setup shown in Fig. 2a. It can be observed that these values very closely match the H₂ permeation rates for the Nafion® 212 membrane measured for the setup shown in Fig. 3a during the potential hold at 1.3 V (cf Fig. 3c, comparing the brown crosses and the symbols at 0 A cm^{-2}), while they are up to $\approx 15\%$ lower for the Nafion® 117 membrane (cf Fig. 3b). A possible explanation for this deviation is an insufficient humidification of the membrane in the permeation cell test setup shown in Fig. 2a, where the membrane was equilibrated with liquid water by supplying $5 \text{ ml}_{\text{H}_2\text{O}} \text{ min}^{-1}$ to the anode for ≈ 2 h. However, studies on the water uptake of Nafion® membranes show that an equilibration time of up to 150 h. can be required for a Nafion® 117 membrane at $80 \text{ }^\circ\text{C}$.²⁹ For the measurements performed with the test setup shown in Fig. 3a, on the other hand, conditioning of the MEA included a current hold at 1 A cm^{-2} as well as several polarization curves. This not only results in a longer overall conditioning time, but also the transport of water from anode to cathode due to the electro-osmotic drag during electrolyzer operation is expected to lead to a faster equilibration of the membrane. Since in general a longer equilibration time is expected for a thicker membrane, this could explain why a difference in H₂ permeation rates at 0 A cm^{-2} is observed for the Nafion® 117 membrane ($\approx 15\%$, cf Fig. 3b), but not for the Nafion® 212 membrane (cf Fig. 3c).

From Figs. 3b and 3c it can be observed that the H₂ permeation rate increases with the current density for both membranes. With both membranes, there is a hysteresis in the H₂ permeation rates, with the values being lower while increasing the current density

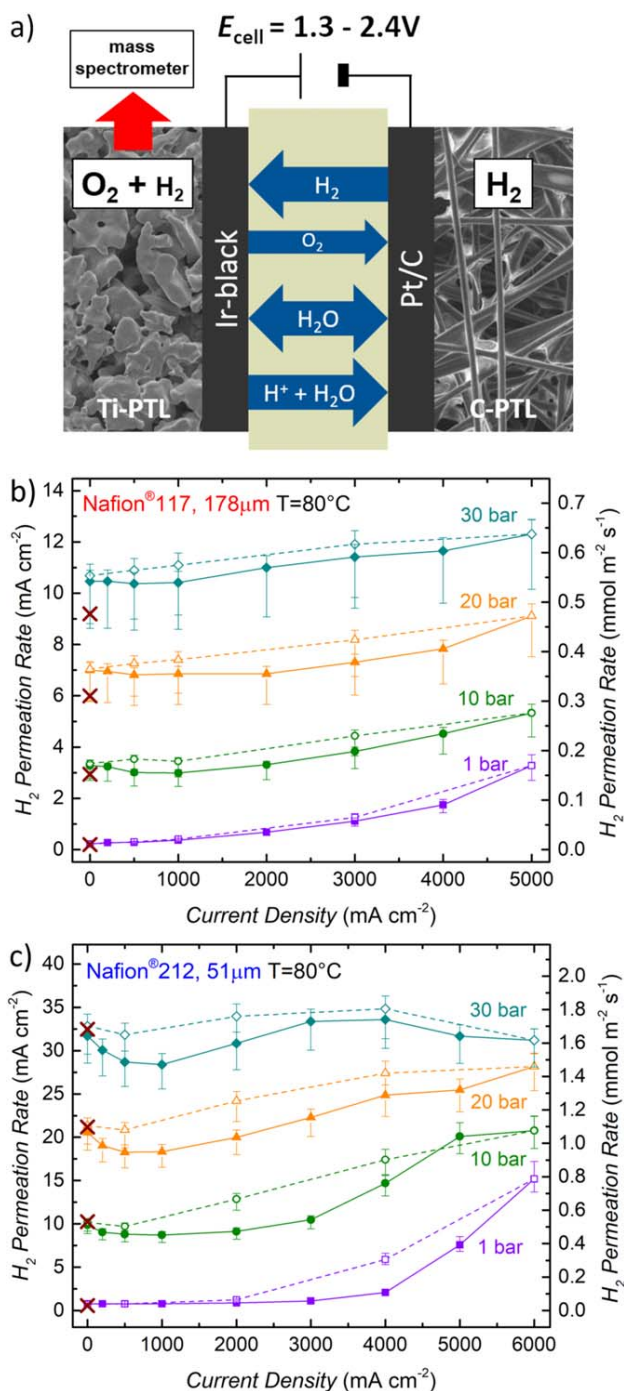


Figure 3. (a) Sketch of the test setup used for H_2 permeation measurements with a mass spectrometer during PEM-WE operation. For this, H_2 is supplied to the cathode (50 ml min^{-1}), while the anode is supplied with H_2O (10 ml min^{-1}) and O_2 (50 ml min^{-1} for $p_{\text{H}_2} \leq 10 \text{ bar}$ and 100 ml min^{-1} for $p_{\text{H}_2} > 10 \text{ bar}$). (b) H_2 permeation rate as a function of current density for different H_2 partial pressures measured with a Nafion[®] 117 membrane at 80°C . (c) H_2 permeation rate as a function of current density for different H_2 partial pressures measured with a Nafion[®] 212 membrane at 80°C . Full symbols along with full lines in (b) and (c) represent the data measured while increasing the current density, whereas open symbols along with dotted lines show the data obtained while decreasing the current density. The electrodes of the MEA consist of iridium black ($0.9 \pm 0.3 \text{ mg}_{\text{Ir}} \text{ cm}^{-2}$) on the anode and of Pt/C ($0.3 \pm 0.1 \text{ mg}_{\text{Pt}} \text{ cm}^{-2}$) with a standard ionomer/carbon mass ratio of 0.6/1 on the cathode. Brown crosses give the H_2 permeation rates measured with the permeation cell setup shown in Fig. 2a, i.e., for the membrane without electrodes.

(solid symbols/lines) compared to when subsequently decreasing the current density. A possible explanation for this phenomenon is that even though a hold time of 90–180 min was applied at each measurement point, the H_2 permeation rate was still not completely constant (i.e., it was still slowly increasing with time), especially for the measurements taken while increasing the current density.

The relative increase of the H_2 permeation rate with current density is most pronounced for small H_2 partial pressures. For an MEA with the Nafion[®] 117 membrane, the H_2 permeation rate at a pressure of 1 bar reaches a value of 3.3 mA cm^{-2} at a current density of 5 A cm^{-2} , which is ≈ 15 times higher than the expected value at this H_2 partial pressure that is measured at 0 A cm^{-2} . A similar increase is observed for the Nafion[®] 212 membrane, where a value of 15.2 mA cm^{-2} is reached at a current density of 6 A cm^{-2} , ≈ 20 times higher than the value obtained at 0 A cm^{-2} . For higher operating pressures, the relative increase is smaller, with only $\approx 16\%$ at 5 A cm^{-2} and 30 bar for the Nafion[®] 117 membrane, while the permeation rate can be considered essentially independent of current density (within the range of the measurement error) for the Nafion[®] 212 membrane at 30 bar. The observed increase of permeation rate with current density has been shown frequently in the literature,^{23,24,30} albeit to different extents, which indicates a strong influence of the measurement method and/or the cell setup (cell hardware, PTL, MEA, etc.) on this phenomenon.²⁶ Possible reasons for this current dependency will be discussed briefly in terms of the simple models for H_2 transport through the membrane presented in the Theory section. Diffusive flux of H_2 according to Eq. 1 only depends on the H_2 concentration gradient between cathode and anode, ΔC_{H_2} , the membrane thickness, t_{memb} , and the effective diffusion coefficient, $D_{\text{H}_2}^{\text{eff}}$, i.e., it should not directly depend on the current density. However, if one of the above mentioned parameters were to be affected by the current density, this would indeed lead to a current density dependence of the H_2 permeation rate. For example, there are in principle two possibilities to increase the effective H_2 concentration at/near the membrane/cathode interface with increasing current densities, which have been discussed in the literature^{14,23–25}: either an increase in the local H_2 partial pressure at the membrane/cathode interface due to limited removal rates of the evolved H_2 or H_2 super-saturation in the ionomer phase at high H_2 production rates (i.e., at high current densities). An increased H_2 concentration in the ionomer phase at/near the membrane/cathode interface either by an increased p_{H_2} or by H_2 super-saturation would directly translate into an increase of the diffusive H_2 flow. With regards to the H_2 diffusion coefficient, $D_{\text{H}_2}^{\text{eff}}$, there are two possible effects which must be considered: (i) $D_{\text{H}_2}^{\text{eff}}$ is expected to increase with temperature, so that a local temperature increase at the MEA due to the high amount of heat produced at high current densities could lead to an increase of the H_2 permeation rate; (ii) a change in the water content of the membrane with current density could also affect $D_{\text{H}_2}^{\text{eff}}$. Due to the electro-osmotic drag water is transported from anode to cathode, which could lead to a more homogeneous water distribution across the membrane at high current densities. However, this may be negatively affected by differential pressure operation and the corresponding hydraulic water transport from cathode to anode. For the conceivable variations in MEA temperature and membrane water content, one would expect, however, that the variation of $D_{\text{H}_2}^{\text{eff}}$ could not account for the above described more than 10-fold increase in the H_2 permeation rate.

Convective transport due to a total pressure difference between cathode and anode was shown to be insignificant by the permeation cell measurements presented in the previous section. There, the permeation rate was found to be perfectly first order with respect to p_{H_2} (cf Fig. 2c), as predicted in the absence of a total pressure difference driven flux (as discussed in the Theory section). Another possible effect on H_2 permeation could be the convective flux of water due to the electro-osmotic drag that is a function of current density. However, since the electro-osmotic drag of protons goes from the anode to the cathode, dragging along H_2O and thus H_2 dissolved in H_2O , it would lead to a lowering of the overall H_2

permeation rate from cathode to anode with increasing current density, i.e., the opposite of what we observe. Hence, the effect of the electro-osmotic drag is either negligible or is compensated by other effects which lead to an increase of H_2 permeation rate with current density.

In recent studies, Trinke et al. suggested that H_2 super-saturation in the ionomer phase of the cathode catalyst layer is the main reason for the increase of the H_2 permeation rate with current density, and that the extent of this increase depends on the mass transport properties of the cathode catalyst layer.³¹ The authors changed the ionomer content in the cathode and, consequently, the void volume fraction of the catalyst layer; they found that with increasing ionomer content the mass transport overpotential increased similar to what was shown previously by Rheinländer et al.³² Additionally, they observed a stronger increase of the H_2 permeation rate with current density for a higher ionomer content.³¹ While they ascribed this to an increasing degree of H_2 super-saturation in the ionomer phase with current density, a partial pressure build-up at/near the membrane/cathode interface could also explain this phenomenon. A similar behavior was observed in the present study when the ionomer/carbon (I/C) mass ratio in the cathode electrode was increased from its standard value of 0.6/1 to higher values of 1.2/1 (cf Fig. 4). By increasing the cathode I/C ratio, the volume fraction of ionomer in the cathode catalyst layer increases while its void volume fraction decreases, as is shown in Fig. 4a. Here, the catalyst volume fraction (V_{cat} ; gray bars) is determined from the measured catalyst loading (L_{cat}), the average density of the 45.8 wt% Pt/C catalyst ($\rho_{cat} \approx 3.1 \text{ g cm}^{-3}$), and the measured cathode layer thickness (t_{cath}), as outlined in detail in Ref. 7 For the calculation of the ionomer volume fraction (V_{ion} , brown bars), swelling of the ionomer due to water uptake is accounted for by considering a water content of $\lambda = 21$ (λ being the moles of water per mole of sulfonic acid group) for the applied operating conditions (liquid water at 80 °C),^{29,33} which leads to a $\approx 80\%$ volume increase of the ionomer compared to the dry ionomer (for details, see Ref. 7). The void volume fraction (V_{void}) then equates to $V_{void} = 100\% - V_{cat} - V_{ion}$, which becomes rather small at an I/C mass ratio of 1.2/1 (white bars in Fig. 4a).

This low void volume fraction and the high ionomer volume fraction in cathode electrodes with high I/C ratios has two possible consequences: (i) a low V_{void} will likely impede the removal of the evolved H_2 gas, which would lead to a partial pressure build-up at the membrane/cathode interface and thus to an increase of the H_2 concentration in the ionomer phase (as predicted by Henry's law), which in turn would increase the H_2 permeation rate acc. to Eq. 1; and/or (ii) a high V_{ion} might lead to a restricted transfer of the evolved H_2 from the catalyst surface into the open pore volume, which could lead to H_2 super-saturation in the ionomer phase, which in turn again would increase the H_2 permeation rate. While Trinke et al. suggest that H_2 super-saturation is responsible for the increase of the H_2 permeation rate with current density,³¹ a local H_2 pressure build-up was also suggested to cause this effect. Both phenomena would lead to an increase in the H_2 permeation rate with increasing current density, which would be expected to be increasingly more pronounced with increasing I/C ratio of the cathode electrode. This is indeed observed for the H_2 permeation rate vs current density recorded at 10 bar H_2 shown in Fig. 4b: between 0 $A \text{ cm}^{-2}$ and 4 $A \text{ cm}^{-2}$, the H_2 permeation rate increases by a factor of ≈ 1.4 , ≈ 2.5 , and ≈ 3.3 for cathode electrode I/C ratios of 0.6/1 (green symbols/lines), 0.9/1 (purple symbols/lines), and 1.2/1 (dark red symbols/lines), respectively. If this were simply due to a local H_2 partial pressure build-up at the membrane/cathode interface ($p_{H_2,local(i)}$), $p_{H_2,local(i)}$ at 4 $A \text{ cm}^{-2}$ over that at 0 $A \text{ cm}^{-2}$ would have to increase by the same factor. As $p_{H_2,local}$ at 0 $A \text{ cm}^{-2}$ must correspond to the H_2 partial pressure in the cathode compartment ($p_{H_2,cathode}$), the H_2 partial pressure difference between the cathode compartment and the membrane/cathode interface at a given current density ($\Delta p_{cathode(i)}$) would then correspond to $p_{H_2,local(i)} - p_{H_2,cathode}$.

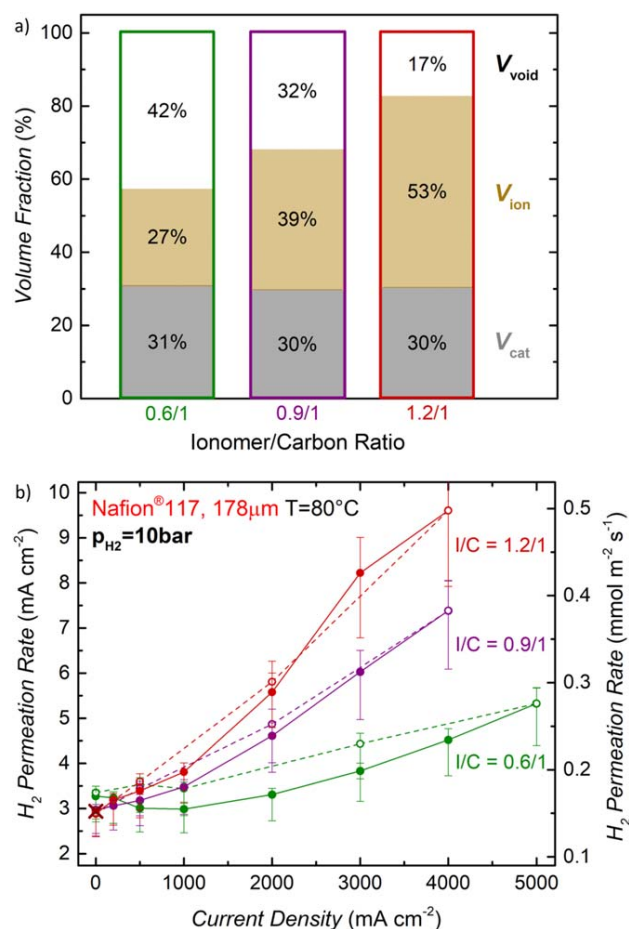


Figure 4. (a) Cathode catalyst layer volume fractions for three different ionomer to carbon (I/C) ratios (by mass). V_{cat} represents the volume fraction of the Pt/C catalyst, V_{ion} the volume fraction of ionomer equilibrated with liquid water at 80 °C, and V_{void} the remaining electrode void volume. These were determined by measuring the thickness and the areal weight of the cathode catalyst layers (see text and reference⁷). (b) H_2 permeation rate as a function of current density for cathode electrodes with different I/C ratios measured with a Nafion[®] 117 membrane at 80 °C and a H_2 partial pressure of 10 bar. Full symbols along with full lines represent the data measured while increasing the current density, whereas open symbols along with dotted lines show the data obtained while decreasing the current; the MEAs are composed of iridium black ($0.9 \pm 0.3 \text{ mg}_{Ir} \text{ cm}^{-2}$) on the anode and of Pt/C ($0.3 \pm 0.1 \text{ mg}_{Pt} \text{ cm}^{-2}$) on the cathode. The brown cross marks the H_2 permeation rate measured with the permeation cell setup shown in Fig. 2a, i.e., for the membrane without electrodes and without applied current.

Based on this, the increase of the H_2 permeation rate between 0 $A \text{ cm}^{-2}$ and a given current density would be proportional to $\Delta p_{cathode(i)}/p_{H_2,cathode}$, which for the observed increase of the H_2 permeation rate between 0 and 4 $A \text{ cm}^{-2}$ at 10 bar (see above) would amount to $\Delta p_{cathode(i)} \approx 4 \text{ bar}$, $\approx 15 \text{ bar}$, and $\approx 23 \text{ bar}$, for the cathode electrode I/C ratios of 0.6/1, 0.9/1, and 1.2/1, respectively.

Assuming that $\Delta p_{cathode(i)}$ produced by a hindered H_2 transport through the void volume of the cathode electrode for a given cathode electrode I/C ratio (i.e., for a given V_{void}) were independent of the total H_2 pressure in the cathode compartment ($p_{H_2,cathode}$), the relative increase of the H_2 permeation rate between 0 $A \text{ cm}^{-2}$ and a given current density would again be expected to be proportional to $\Delta p_{cathode(i)}/p_{H_2,cathode}$, so that it should diminish as $p_{H_2,cathode}$ increases. This would be consistent with the observations shown in Fig. 3b and 3c, where the relative current density dependence of the H_2 permeation rate diminishes with increasing $p_{H_2,cathode}$. While this local H_2 pressure build-up seems to be a reasonable explanation for

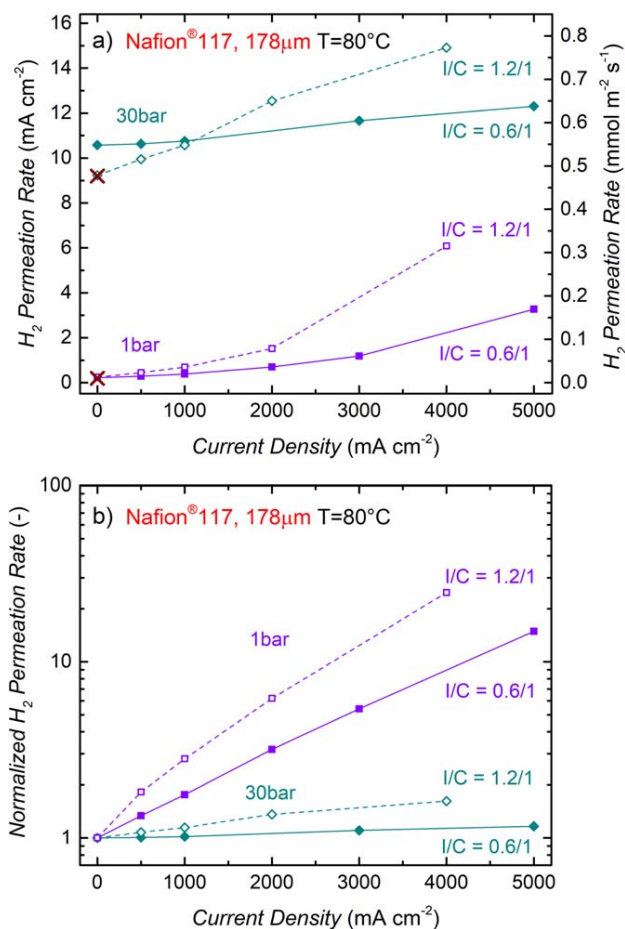


Figure 5. (a) H₂ permeation rate vs current density for cathode electrodes with a standard I/C ratio of 0.6/1 (solid symbols/lines) and a high I/C ratio of 1.2/1 (open symbols, dotted lines) measured with a Nafion® 117 membrane at 80 °C and H₂ partial pressures of either 1 bar (purple) or 30 bar (turquoise). Here, the average value of the data points measured while increasing and decreasing the current is shown. Brown crosses give the H₂ permeation rates measured with the permeation cell setup shown in Fig. 2a, i.e., for the membrane without electrodes and without applied current. (b) H₂ permeation rates for the same cathode electrodes and operating pressures as in a) normalized by the permeation rates obtained at zero current. The MEAs are composed of iridium black ($0.9 \pm 0.3 \text{ mg}_{\text{Ir}} \text{ cm}^{-2}$) on the anode and of Pt/C ($0.3 \pm 0.1 \text{ mg}_{\text{Pt}} \text{ cm}^{-2}$) on the cathode.

the increase of the H₂ permeation rate with current density, the effect of H₂ super-saturation is another possible explanation.

In terms of the practical application of PEM-WEs, a substantial increase of the H₂ permeation rate with current density could be problematic, since it would result in a lower faradaic efficiency and could lead to the formation of a sufficiently high H₂ concentration in the anode gas even at high current densities, possibly exceeding the explosive limit. To illustrate the extent of an increasing H₂ permeation rate with current density, the H₂ permeation rates determined for Nafion® 117 MEAs with either the standard cathode electrode I/C ratio of 0.6/1 (solid symbols/lines) or with the highest here examined I/C ratio of 1.2/1 (open symbols, dotted lines) are plotted in Fig. 5a for two different H₂ pressures in the cathode compartment ($p_{\text{H}_2, \text{cathode}}$): (i) for a H₂ partial pressure of 1 bar (purple symbols/lines), where the strongest increase of the H₂ permeation rate with current density is observed, and (ii) at an application-relevant PEM-WE operating pressure of 30 bar (turquoise symbols/lines). As expected, the increase of the H₂ permeation rate with current density is more pronounced for cathode electrodes with the high I/C ratio of 1.2/1 compared to the standard

I/C ratio of 0.6/1, both for 1 bar as well as for 30 bar. This clearly demonstrates the importance of designing cathode electrodes with an as low as possible I/C ratio, whereby for the standard cathode electrode I/C ratio of 0.6/1e proton conduction related voltage losses at 80 °C are $< 10 \text{ mV}$ at 3 A cm^{-2} .⁷ The relative H₂ permeation rate at $p_{\text{H}_2, \text{cathode}} = 1 \text{ bar}$ shown in Fig. 5b increases rather dramatically from 0 to 4 A cm^{-2} , namely by a factor of ≈ 9 (cathode I/C of 0.6/1) and ≈ 25 (cathode I/C of 1.2/1), consistent with the strong current density dependence of the H₂ permeation rate at 1 bar reported in the literature.^{24,30} While a similarly high factor at $p_{\text{H}_2, \text{cathode}} = 30 \text{ bar}$ would lead to very poor if not unacceptable faradaic efficiencies, the relative increase of the H₂ permeation rate at 30 bar is fortunately quite small, corresponding to a factor of only ≈ 1.1 (cathode I/C of 0.6/1) and ≈ 1.6 (cathode I/C of 1.2/1). This shows that at realistic PEM-WE operating conditions (i.e., at a H₂ pressure of 30 bar) and for a cathode electrode which is optimized with regards to its mass transport properties (i.e., with regards to its I/C ratio), the increase of the H₂ permeation rate with current density is almost negligible. In the following section, we will discuss the impact of the measured H₂ permeation rates on the efficiency and the operating range of a PEM-WE.

PEM-WE efficiency and operating range.—In this section, the measured H₂ permeation rates will be used to discuss the overall efficiency and the feasible operating range of a PEM-WE for the membranes with different dry thicknesses investigated in this study (Nafion® 117 and Nafion® 212 with $\approx 178 \mu\text{m}$ and $\approx 51 \mu\text{m}$, respectively). In today's PEM-WEs, relatively thick membranes (e.g., Nafion® 117) are used, because they are mechanically robust and provide a good compromise between ohmic resistance and low gas permeability.³⁴ However, thinner membranes offer a high potential for reduction of H₂ generation costs,¹ as will be illustrated in the following.

Figure 6a shows a PEM-WE polarization curve of an MEA with a Nafion® 117 membrane at a temperature of 80 °C and a H₂ partial pressure of 30 bar in the cathode compartment (the anode compartment is kept at ambient pressure), which today would be operated at a maximum current density of $1 - 2 \text{ A cm}^{-2}$ in a commercial electrolyzer.⁹ In general, increasing the current density can be a way to lower H₂ generation costs by reducing the total cell area required to achieve a given target H₂ production rate, i.e., lowering the capital expenditures. However, at higher current densities the cell voltage increases significantly due to the high ohmic resistance of the thick proton-conducting membrane, leading to a lower efficiency. This is illustrated by the following voltage loss analysis, that was performed analogous to how it was done in our previous work.⁷ Briefly, the overpotential for the OER (ΔE_{OER}) was determined by a Tafel analysis, based on a Tafel slope of $\approx 45 \text{ mV dec}^{-1}$ (determined in the $10 - 100 \text{ mA cm}^{-2}$ region) and a mass activity of $\approx 63 \text{ A g}_{\text{Ir}}^{-1}$ (determined at an iR-free cell voltage of 1.5 V) and is represented by the purple shaded areas in Fig. 6. Due to the fast kinetics of the HER, the resulting HER overpotential (ΔE_{HER}) is negligible as shown in our previous studies.^{7,35} The overpotential due to ohmic losses (ΔE_{ohmic}) was determined by multiplying the ohmic resistance with the current density ($\Delta E_{\text{ohmic}} = i \cdot R_{\Omega}$) and is illustrated by the orange shaded areas in Fig. 6. The ohmic resistance (R_{Ω}) represents the sum of the ionic resistance of the membrane (R_{memb}) and the electrical resistance (R_{el}) and is obtained by extracting the high frequency resistance (HFR) from the measured impedance spectra. The remaining overpotential ($\Delta E_{\text{transport}}$), i.e., the difference between the measured cell voltage (E_{cell}) and the sum of the reversible cell voltage (E_{rev}), the OER overpotentials (ΔE_{OER}), and ohmic losses (ΔE_{ohmic}), is attributed to transport phenomena ($\Delta E_{\text{transport}} = E_{\text{cell}} - (E_{\text{rev}} + \Delta E_{\text{OER}} + \Delta E_{\text{ohmic}})$). This includes voltage losses due to proton transport in the catalyst layers ($R_{\text{HT,an}}^{\text{eff}}$, $R_{\text{HT,cath}}^{\text{eff}}$) as well as mass transport losses (ΔE_{mt})⁷ and is represented by the green shaded areas in Fig. 6.

This analysis of the various voltage loss contributions shows that at the highest current density of 5 A cm^{-2} $\approx 64\%$ of the total voltage

loss are due to ohmic losses (ΔE_{ohmic}) that are mostly due to the proton conduction resistance of the thick Nafion[®] 117 membrane (see orange shaded area in Fig. 6a). Since the electrical resistance represents only a small fraction of the ohmic resistance ($\approx 12 \text{ m}\Omega\text{cm}^2$ for the setup used in this study⁷), reducing the ionic membrane resistance offers the largest leverage to improve high current density performance. Figure 6b shows the result of reducing the membrane thickness by a factor of ≈ 3.5 by using a Nafion[®] 212 (51 μm dry thickness) instead of the Nafion[®] 117 (178 μm dry thickness). With the thinner membrane, the ΔE_{ohmic} contribution at the highest current density of 5 A cm^{-2} is lowered by a factor of ≈ 2 , now accounting for only $\approx 44\%$ of the total voltage loss. Simultaneously, at the frequently used voltage efficiency target of 70% based on the lower heating value (LHV) of H_2 (corresponding to $\approx 1.79 \text{ V}$), the current density increases from 1.6 A cm^{-2} to 3.5 A cm^{-2} (see red and blue dashed lines in Fig. 6), i.e., by a factor of ≈ 2.3 for the MEA with the thinner Nafion[®] 212 membrane. This increase of the stack's H_2 output translates directly into a stack cost reduction by a factor of ≈ 2.3 while the same voltage efficiency is retained. From this example, it becomes clear that minimizing the membrane thickness offers great potential for cost reduction.

While the voltage efficiency of a thin Nafion[®] 212 membrane is quite superior, it obviously exhibits a higher H_2 permeation rate which results in a lower faradaic efficiency, especially if the electrolyzer is operated at elevated pressure. In general, however, pressurized electrolysis is beneficial compared to ambient pressure operation, because it reduces the energy demand for subsequent mechanical compression as well as the effort for gas drying due to the lower water content at higher pressure.^{1,36} Typical operating pressures of commercial PEM-WEs are in a range of 20–50 bar,^{9,37} and a H_2 partial pressure of 30 bar is chosen here for the following analysis. The overall efficiency taking into account the voltage efficiency as well as the faradaic efficiency is presented in Fig. 7a for MEAs based on a Nafion[®] 117 membrane (red lines in Fig. 7a) and a Nafion[®] 212 membrane (blue lines). The voltage efficiency based on the LHV of H_2 , η_{voltage} , can be calculated by dividing the reaction enthalpy for water in its gaseous state, ΔH^0 (-242 kJ mol^{-1} , corresponding to an LHV-equivalent voltage of 1.25 V) by the actual electrical energy input determined from the operating cell potential, E_{cell} :

$$\eta_{\text{voltage}} = \left| \frac{-\Delta H^0}{2 \cdot F \cdot E_{\text{cell}}} \right| \quad [5]$$

The dashed lines in Fig. 7a show the voltage efficiency, η_{voltage} , at a H_2 partial pressure of 30 bar, at ambient anode compartment pressure, and at a temperature of $80 \text{ }^\circ\text{C}$, as determined from the measured polarization curves in Fig. 6 in combination with Eq. 5. Obviously, the MEA with the thin Nafion[®] 212 membrane (blue line) exhibits a higher voltage efficiency than that with the thick Nafion[®] 117 membrane, especially at high current densities, due to the lower ohmic resistance as already discussed in Fig. 6.

On the other hand, the faradaic efficiency can be calculated as

$$\eta_{\text{faradaic}} = \frac{i_{\text{cell}} - i_{\text{H}_2} - i_{\text{O}_2}}{i_{\text{cell}}} \quad [6]$$

where i_{cell} is the current density at which the cell is operated—corresponding to a certain theoretical H_2 production rate—and i_{H_2} and i_{O_2} are the H_2 and the O_2 permeation current densities in units of mA cm^{-2} . Let us first estimate the relative contribution of i_{O_2} compared to i_{H_2} for the here considered PEM-WE operation with $p_{\text{H}_2} \approx 30 \text{ bar}$ in the cathode compartment and with ambient pressure in the anode compartment (corresponding to $p_{\text{O}_2} \approx 0.5 \text{ bar}$ at $80 \text{ }^\circ\text{C}$), first looking into the case where no electrolysis current is applied: even though i_{O_2} in PFSA membranes is very similar to i_{H_2} at equal partial pressures of O_2 and H_2 (note: while the O_2 permeability is ≈ 2 times lower than that of H_2 ,¹⁴ each mol of O_2 consumes two moles of H_2 upon its reaction to H_2O on the cathode catalyst), the ≈ 60 -fold

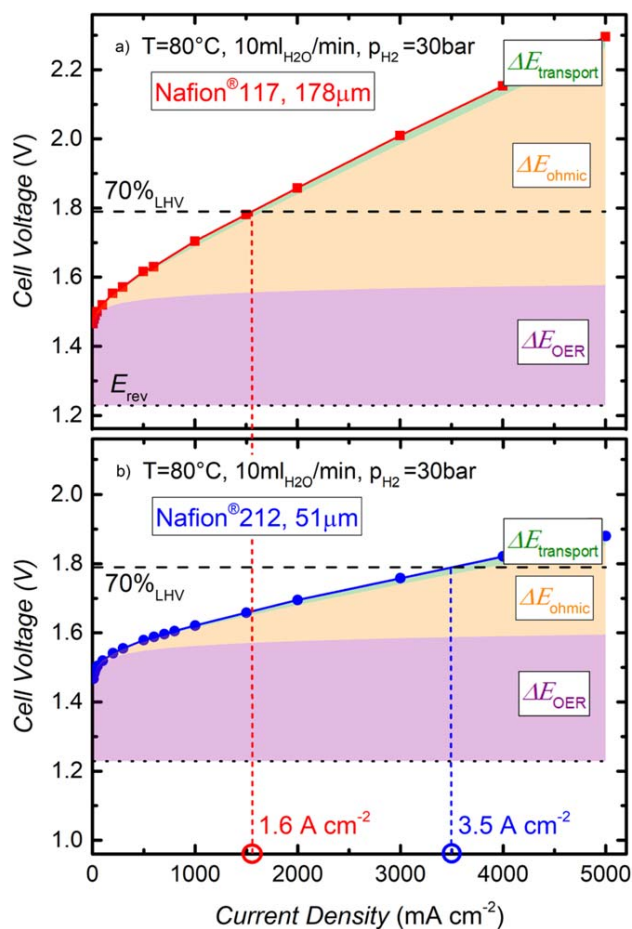


Figure 6. PEM-WE single-cell (5 cm^2) polarization curves at a temperature of $80 \text{ }^\circ\text{C}$ and a H_2 partial pressure of 30 bar (the anode compartment is kept at ambient pressure) obtained for MEAs with thick vs thin membranes: (a) with a Nafion[®] 117 (178 μm dry thickness; red solid line); (b) with Nafion[®] 212 (51 μm dry thickness; blue solid line). The electrodes of the MEA consist of iridium black ($0.9 \pm 0.3 \text{ mg}_{\text{Ir}} \text{ cm}^{-2}$) on the anode and of Pt/C ($0.3 \pm 0.1 \text{ mg}_{\text{Pt}} \text{ cm}^{-2}$) with a standard ionomer/carbon mass ratio of 0.6/1 on the cathode. The dotted black lines mark the reversible cell voltage at these conditions (1.23 V), while the purple shaded areas represent the OER kinetic overpotential losses (ΔE_{OER}), the orange shaded areas mark the ohmic potential losses (ΔE_{ohmic}), and the green shaded areas represent the overpotentials due to proton conduction resistances in the electrodes and mass transport resistances of the evolved gases ($\Delta E_{\text{transport}}$). The dashed black lines represent a voltage efficiency of 70% based on the lower heating value (LHV) of H_2 , and the current density at which this voltage efficiency is reached is marked for the Nafion[®] 117 membrane (red) and for the Nafion[®] 212 membrane (blue) in Fig. 6b (note that the voltage efficiency discussed here does not include the faradaic efficiency which is discussed in the following).

higher partial pressure of H_2 compared to O_2 equates to a ≈ 60 -fold lower i_{O_2} compared to i_{H_2} . Therefore, under these pressure conditions and at 0 A cm^{-2} , i_{O_2} is negligible compared to i_{H_2} . On the other hand, under PEM-WE operation at ambient anode compartment pressure, the O_2 permeation rate was found to increase by a factor of ≈ 17 between 0 and 2 A cm^{-2} ¹⁵ (analogous to what is observed for the H_2 permeation rate; cf Fig. 5b), so that on the basis of this report the ratio of i_{H_2} over i_{O_2} is projected to change to $\approx 3/1$ at 2 A cm^{-2} . While this would not be entirely negligible anymore, the contribution of i_{O_2} to the overall faradaic efficiency at $>1 \text{ A cm}^{-2}$ can nevertheless be neglected, since the faradaic efficiency is well above 95% at current densities of $>1 \text{ A cm}^{-2}$. Therefore, we have neglected i_{O_2} in the following calculation of the faradaic efficiency that is based only on the current dependent H_2 permeation rates

taken from Fig. 3 (using the average value of the measurements taken at increasing and decreasing current density), and which is represented by the dotted lines in Fig. 7a. As expected, the faradaic efficiency is higher for the MEA with the thick membrane, especially at $<0.5 \text{ A cm}^{-2}$, where the H_2 production rate is relatively low compared to the losses due to H_2 permeation; again, as argued above, the contribution of i_{O_2} to the faradaic efficiency is negligible at such low current densities for the here considered PEM-WE operation at a H_2 partial pressure of 30 bar and ambient pressure in the anode compartment.

The overall efficiency, taking into account voltage losses as well as losses due to H_2 permeation can now be calculated as

$$\eta_{\text{total}} = \eta_{\text{voltage}} \cdot \eta_{\text{faradaic}} \quad [7]$$

and is represented by the full lines in Fig. 7a. An optimum in total efficiency of 77% is achieved for the MEA based on a Nafion® 117 membrane at a current density of $\approx 0.3 \text{ A cm}^{-2}$. For the Nafion® 212 membrane, a maximum in efficiency of 75% is obtained at a significantly higher current density of $\approx 0.8 \text{ A cm}^{-2}$. In general, the MEA with the thick Nafion® 117 membrane shows a higher efficiency compared to the thin Nafion® 212 membrane at low current densities, where losses due to H_2 permeation are the dominating effect (as discussed above, the contribution by i_{O_2} is projected to be negligible at $<1 \text{ A cm}^{-2}$). At high current densities, on the other hand, ohmic losses are dominating the overall efficiency while faradaic losses are almost negligible. Consequently, the MEA with the thin Nafion® 212 membrane exhibits a higher efficiency at current densities above $\approx 0.7 \text{ A cm}^{-2}$. Considering that operation at high current densities is preferred to reduce the electrolyzer stack costs, a thin membrane would always be favorable in terms of efficiency.

However, besides of the maximum efficiency at a certain operating point, the dynamic operating range, i.e., the range of current densities over which an electrolyzer can be operated, is another important factor for the application of PEM-WEs, especially in the context of an increasing share of renewable energy sources and the resulting intermittent energy output. Defining a minimum total efficiency of 70% (LHV basis) as a target for PEM-WE operation, the MEA with the thick Nafion® 117 membrane could be operated in a range from $0.07 - 1.4 \text{ A cm}^{-2}$ (cf red dashed bar in Fig. 7b) and the MEA with the thin Nafion® 212 membrane in a range from $0.23 - 3.1 \text{ A cm}^{-2}$ (cf blue dashed bar in Fig. 7b). Translated into a dynamic stack power range ($P_{\text{stack}} = E_{\text{cell}} \times i_{\text{cell}}$), this corresponds to $\approx 0.11 - 2.5 \text{ W cm}^{-2}$ and $\approx 0.36 - 5.5 \text{ W cm}^{-2}$ for Nafion® 117 and Nafion® 212, respectively. This shows that when a minimum efficiency of 70% is the only criteria that is taken into account, a reasonably large dynamic stack power range with a factor of ≈ 23 (Nafion® 117) and ≈ 15 (Nafion® 212) can be achieved for both membranes.

For a practical application, however, the lower limit in current density at which an electrolyzer can be operated will not be defined solely by an efficiency requirement, but the H_2 concentration in the anode compartment as a result of the H_2 permeation through the membrane has also to be considered. Since the HOR activity of iridium-based catalysts is negligible in the relevant anode potentials,¹³ permeating H_2 will only be removed by the exiting anode gas, so that the H_2 volume fraction (x_{H_2}) in the O_2 -containing anode compartment can simply be calculated from the H_2 permeation rates (in terms of i_{H_2}) from Fig. 3 and the PEM-WE current (i_{cell}) under the assumption that a loss of O_2 on the anode due to permeation to the cathode is negligible:

$$x_{\text{H}_2} = i_{\text{H}_2} / (i_{\text{H}_2} + 0.5 \cdot i_{\text{cell}}) \quad [8]$$

Figure 8 shows the resulting values of x_{H_2} vs current density for different H_2 partial pressures for Nafion® 117 (Fig. 8a) and for Nafion® 212 (Fig. 8b). The lower explosive limit for H_2 in O_2 is $\approx 4\%$ ¹² but in a real system we assume that a safety factor of at least

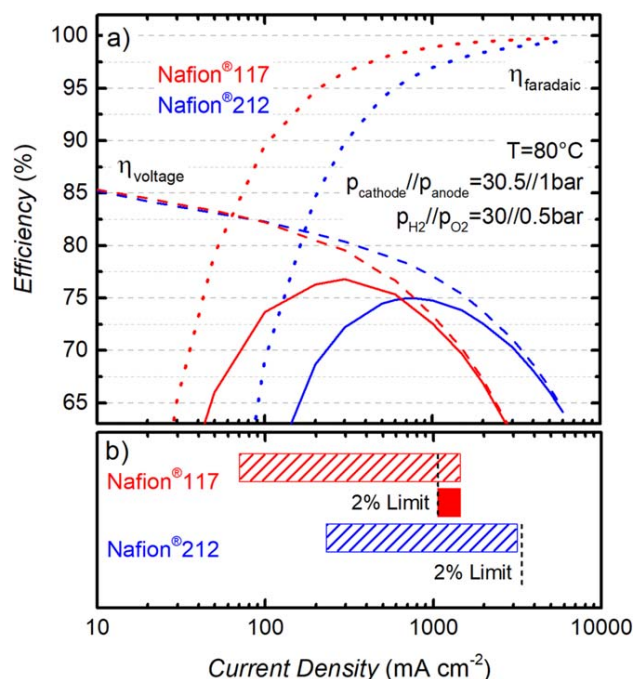


Figure 7. (a) Single-cell (5 cm^2) PEM-WE total efficiency vs current density for a Nafion® 117 (red) and a Nafion® 212 (blue) membrane at a temperature of $80 \text{ }^\circ\text{C}$, and a H_2 partial pressure of 30 bar while the anode compartment is kept at ambient pressure. Dashed lines give the voltage efficiency, η_{voltage} ; dotted lines give the faradaic efficiency, η_{faradaic} , and full lines give the total efficiency (see Eq. 7); note that the contribution of O_2 permeation to the faradaic efficiency has been neglected here (see text). (b) Operating range at a total efficiency of $\geq 70\%$ referenced to the LHV of H_2 (with 100% LHV corresponding to 1.25 V) for a Nafion® 117 (red dashed bar) and a Nafion® 212 (blue dashed bar) membrane. The vertical dashed black lines indicate the current density below which the H_2 in O_2 content in the anode compartment would exceed 2% (derived from Fig. 8). The MEAs are composed of iridium black ($0.9 \pm 0.3 \text{ mg}_{\text{Ir}} \text{ cm}^{-2}$) on the anode and of Pt/C ($0.3 \pm 0.1 \text{ mg}_{\text{Pt}} \text{ cm}^{-2}$) on the cathode.

two would be applied, which means that the H_2 in O_2 volume fraction should not exceed 2%, a value which is marked by the dashed red line in Fig. 8. At a H_2 partial pressure of 30 bar and a temperature of $80 \text{ }^\circ\text{C}$, this requirement would result in a lower limit for operation of 1.1 A cm^{-2} for the Nafion® 117 membrane (cf Fig. 8a), while safe operation would not be possible below 3.4 A cm^{-2} for the Nafion® 212 membrane (cf Fig. 8b). Taking into account the current density range imposed by the efficiency target of 70% LHV (cf Fig. 7) as well as the upper limit for x_{H_2} of 2%, the MEA with a Nafion® 117 membrane could only be operated in a very small window of current densities from $1.1 - 1.4 \text{ A cm}^{-2}$, while both criteria cannot be fulfilled simultaneously for the Nafion® 212 based MEA. Therefore, without additional mitigation strategies to lower the H_2 concentration in the anode compartment, the desired PEM-WE operating conditions of 30 bar and $80 \text{ }^\circ\text{C}$ with a reasonable dynamic range would not be possible with MEAs based on either of the two membranes.

On the materials level, this issue could be addressed by using membranes that have a higher proton conductivity to H_2 permeability ratio ($\sigma_{\text{H}^+}/P_{\text{H}_2}$ ratio) than PFSA membranes,³⁸ but so far alternative membrane materials such as hydrocarbon (HC) based membranes do not show a more than $\approx 1.5 - 2$ times higher $\sigma_{\text{H}^+}/P_{\text{H}_2}$ ratio than conventional PFSA membranes.^{38,39} While this would be a benefit, it would still not provide a sufficiently large dynamic power range; furthermore, the durability of HC based membranes still needs to be improved.³⁹ Therefore, other mitigation strategies have currently to be employed in order to prevent the formation of an explosive gas mixture at low current densities in a PEM-WE. A

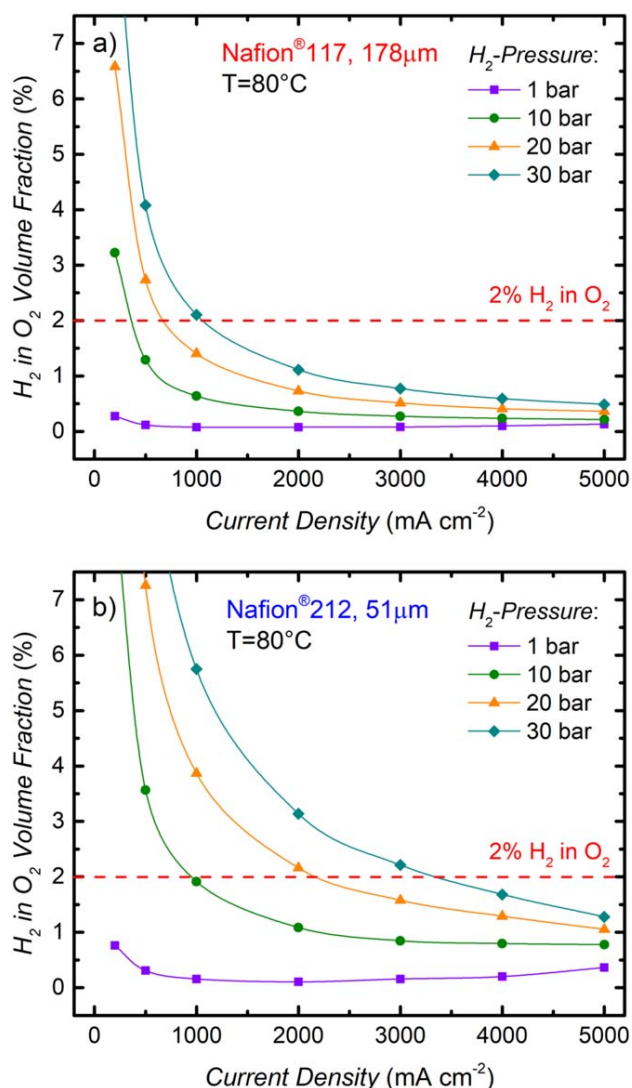


Figure 8. Volume fraction of H_2 (x_{H_2}) in the O_2 -containing anode gas vs current density for PEM-WE operation at different H_2 partial pressures and ambient pressure in the anode compartment at $80^\circ C$ based on the H_2 permeation rates in Fig. 3 (averaged over the values obtained with increasing and decreasing current density) and Eq. 8: (a) for an MEA with a Nafion[®] 117 membrane ($178 \mu m$ dry thickness); (b) for an MEA with a Nafion[®] 212 membrane ($51 \mu m$ dry thickness). The red dashed lines mark the volume fraction of 2% H_2 in O_2 which is considered as a safety limit in this work.

detailed analysis of different mitigation strategies for PEM-WE as well as for alkaline electrolysis can be found in a recent study by Trinke et al.²⁷ The simplest options are to reduce the operating temperature and/or the H_2 pressure in order to reduce H_2 permeation and to extend the operating range to lower current densities. However, lower temperatures result in higher kinetic overpotentials and lower proton conductivity, i.e., in a lower efficiency, while a lower H_2 output pressure translates into a higher energy demand for subsequent mechanical compression. Therefore, for electrolysis at higher pressures, the formation of an explosive gas mixture even at low current densities is generally prevented by the incorporation of a H_2/O_2 recombination catalyst to react the permeated H_2 to water. Typically, a platinum catalyst is used, which can be placed at several locations within the cell. In some instances, it is used in a gas recombiner positioned downstream of the anode gas outlet or it is deposited on the backside of the PTL.³⁰ However, the former approach still leaves the risk of a small volume of potentially

explosive gas within the catalyst layer, PTL, and flow-field. Another approach is the incorporation of a recombination catalyst into the membrane, either dispersed within a certain region of the membrane or introduced as an inter-layer, so that permeating H_2 and O_2 can recombine to water inside the membrane, which was shown to lead to a significant reduction of the H_2 in O_2 volume fraction in the anode compartment.^{40–42} Of course, a recombination catalyst will only reduce the risk of the formation of an explosive gas mixture but will not improve the faradaic efficiency. However, as the analysis in Fig. 7b shows, a sufficient dynamic operating range at a high efficiency of $\geq 70\%$ can be obtained despite of the faradaic losses. Consequently, the implementation of a recombination catalyst is currently the only approach to obtain a reasonable dynamic power operating range for a PEM-WE with PFSA membranes.

Conclusions

In this study, we measured H_2 permeation rates during PEM-WE operation at $80^\circ C$ and various H_2 partial pressures for MEAs with a Pt/C catalyst on the cathode, an Ir-black catalyst on the anode, and PFSA membranes with different thicknesses (Nafion[®] 212 with $\approx 51 \mu m$ and Nafion[®] 117 with $\approx 178 \mu m$ dry thickness). Based on these results, a detailed analysis of the efficiency as well as the possible operating range of PEM-WEs was presented.

First, in order to validate our test setup based on on-line mass spectrometry, measurements of the H_2 permeation rate as a function of H_2 partial pressure were performed in a permeation cell setup, i.e., without applying a current. A linear correlation of H_2 permeation rate and H_2 partial pressure was observed with rates of $0.31 \text{ mA cm}^{-2} \text{ bar}^{-1}$ for a Nafion[®] 117 and $1.10 \text{ mA cm}^{-2} \text{ bar}^{-1}$ for a Nafion[®] 212 membrane, indicating diffusion as the main crossover mechanism. A good correlation of the results with a well-established electrochemical measurement method was observed, confirming the validity of the results measured with the mass spectrometer.

In the second part, H_2 permeation rates for MEAs with Nafion[®] 117 and Nafion[®] 212 membranes were measured during PEM-WE operation at $80^\circ C$ for H_2 partial pressures between 1 – 30 bar. Consistent with the literature, a significant increase of the H_2 permeation rate with current density was observed. This effect increased with increasing ionomer to carbon (I/C) ratio of the cathode electrode, and the possible causes for this phenomenon were discussed. While the increase of the H_2 permeation rate is most pronounced for low H_2 partial pressures and high cathode I/C ratios, it can be reduced to a maximum of $\approx 16\%$ at 5 A cm^{-2} at a realistic operating pressure of 30 bar by optimizing the I/C ratio of the cathode electrode.

Finally, the impact of the measured H_2 permeation rates on the dynamic range of a PEM-WE operated at a H_2 partial pressure of 30 bar and an anode compartment pressure of 1 bar at $80^\circ C$ was discussed. The current density range over which a total efficiency (i.e., the product of cell voltage and faradaic efficiency) of $\geq 70\%$ w.r.t. the lower heating value (LHV) of H_2 could be achieved was $0.07 - 1.4 \text{ A cm}^{-2}$ for Nafion[®] 117 based MEAs and $0.23 - 3.1 \text{ A cm}^{-2}$ with Nafion[®] 212. This corresponds to a dynamic stack power range of $\approx 0.11 - 2.5 \text{ W cm}^{-2}$ (a factor of ≈ 23) for Nafion[®] 117 and of $\approx 0.36 - 5.5 \text{ W cm}^{-2}$ (a factor of ≈ 15) for Nafion[®] 212. To utilize this dynamic range, however, a mitigation strategy to avoid the formation of safety-critical H_2 concentrations in the anode gas are required, which currently consists of the application of a H_2/O_2 recombination catalyst to the membrane, the porous transport layer in the anode, to the stack hardware, or at the anode outlet.

Acknowledgments

This work was funded by the Bavarian Ministry of Economic Affairs and Media, Energy and Technology through the project ZAE-ST (storage technologies) as well as by the German Federal Ministry of Education and Research (BMBF) in the framework of the Kopernikus P2X project (funding number 03SFK2V0). We would like to thank Christian Gebauer (Heraeus Deutschland

GmbH & Co. KG) for providing catalyst material as well as Alexandra Weiß and Armin Siebel for the valuable discussions.

Appendix

Error calculation.—This section briefly explains the assumptions made to determine the measurement error of the H₂ permeation rate as displayed by the error bars in Fig. 3 and 4. Three main sources of measurement errors were considered to calculate the overall error of the H₂ permeation measurement: (i) For the mass spectrometer a total error $\sigma_{MS} = 3.2\%$ was determined based of the inaccuracy of the calibration curve and fluctuations of the measurement value over time; (ii) An overall error $\sigma_{TS} = 2.7\%$ was assumed for the components of the test station, i.e., for the inaccuracy of the gas flow determined by the mass flow controllers and the limited accuracy of temperature and pressure regulation; (iii) The largest error is related to an inaccuracy when determining the active area for H₂ permeation due to edge effects resulting from the assembly of the MEA along with gaskets and subgaskets in the cell hardware. A schematic drawing of the cell cross section is shown in Fig. A-1. The area of the electrodes, A_E , is 5 cm² and is taken into account to calculate the area specific current density. However, to determine the area specific H₂ permeation rate an area of 5.76 cm² was assumed (corresponding to the size of the window in the subgasket, A_{SG} , i.e., 24 × 24 mm) since H₂ permeation can in general occur through the entire subgasket window. If one assumes that the increase in H₂ permeation rate with current density is related to H₂ super saturation in the catalyst layer as discussed in the previous sections, this effect would of course only occur within the electrode area (5 cm²) and not at the edge between electrode and subgasket. Consequently, assuming an area of 5.76 cm² to determine the area specific H₂ permeation rate would lead to an underestimation of the real value, especially at high current densities where the effect of H₂ super saturation is most pronounced. The resulting error which is a function of the current density, i , can be calculated according to

$$\sigma_{AA,+}(i) = \frac{A_{SG} - A_E}{A_{SG}} \cdot \frac{n_{H_2}(i) - n_{H_2}(i=0)}{n_{H_2}(i)} \quad [A.1]$$

The first term in Eq. A.1 denotes the difference between the area of the subgasket window, A_{SG} , and the electrode area, A_E , normalized by A_{SG} . The second term accounts for the fraction of the H₂ permeation rate which is current dependent by subtracting the permeation rate at zero current, $n_{H_2}(i=0)$, from the permeation rate at a certain current density, $n_{H_2}(i)$, normalized by $n_{H_2}(i)$. For the measured permeation rates shown in Fig. 3 this yields an error of

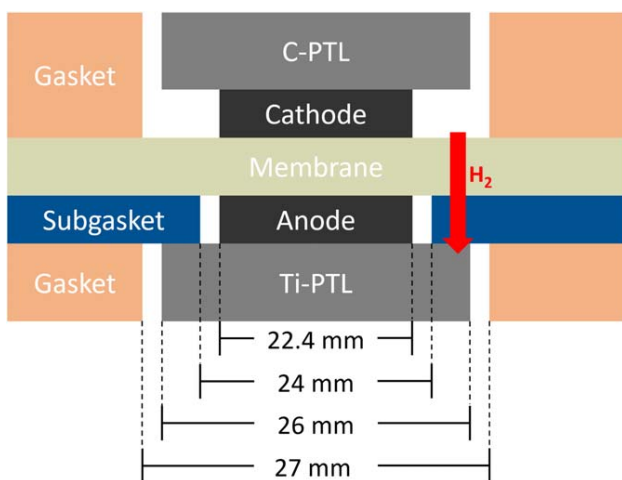


Figure A-1. Schematic drawing of the cell cross section between the flow fields. Edge lengths of the electrodes, subgasket windows, PTLs, and gasket windows are marked.

$\sigma_{AA,+}(i) = 0 - 11.9\%$ depending on current density and pressure. Since this effect would lead to an underestimation of the H₂ permeation rate, $\sigma_{AA,+}(i)$ will be considered to determine the error bars in positive direction in Figs. 3 and 4.

On the other hand, while the PTFE gaskets (thickness $\approx 300\ \mu\text{m}$) can be assumed as impermeable, the PTFE subgasket is only 10 μm thick and, hence, H₂ permeation through the subgasket is not negligible (cf red arrow in Fig. A-1). This additional permeation which is not accounted for in our measurement would lead to an overestimation of the area specific H₂ permeation rate. The permeation coefficient for PTFE is about ten times lower than for wet Nafion[®]21 and the resulting error can be calculated as

$$\sigma_{AA,-} = \frac{A_G - A_{SG}}{A_{SG}} \cdot \frac{t_{\text{memb}}}{10 \cdot t_{SG} + t_{\text{memb}}} \quad [A.2]$$

Here, A_G is the area of the gasket window (27 × 27 mm, cf Fig. A-1) and A_{SG} is the area of the subgasket window while t_{memb} is the membrane thickness and t_{SG} the thickness of the subgasket. This yields an error $\sigma_{AA,-} = 9.0\%$ for the Nafion[®] 212 membrane and an error $\sigma_{AA,-} = 17.0\%$ for the Nafion[®] 117 membrane which will be

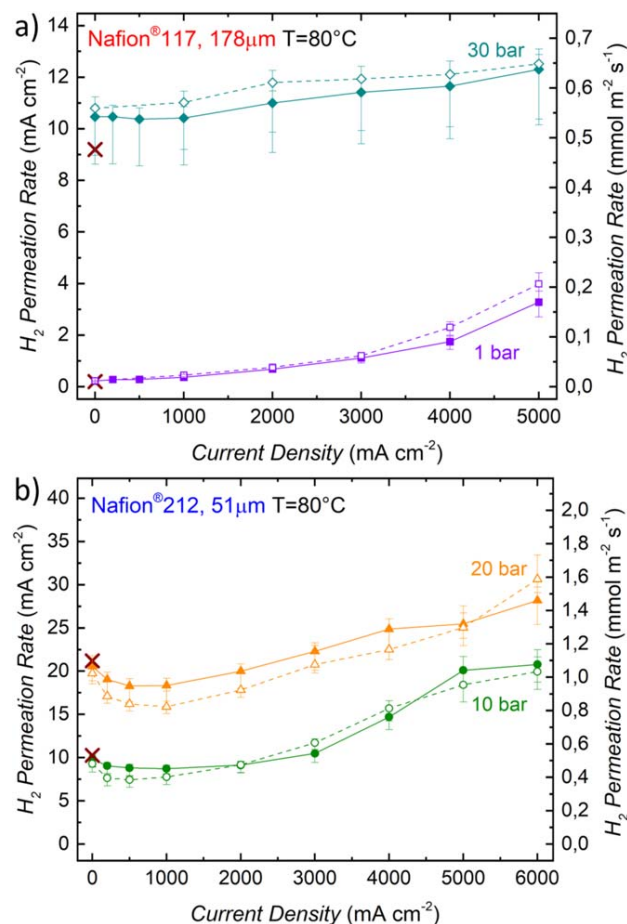


Figure A-2. (a) H₂ permeation rate as a function of current density for different H₂ partial pressures measured with a Nafion[®] 117 membrane at 80 °C. (b) H₂ permeation rate as a function of current density for different H₂ partial pressures measured with a Nafion[®] 212 membrane at 80 °C. Full symbols along with full lines in represent the original data (shown also in Fig. 3) measured while increasing the current density, whereas open symbols along with dotted lines show the data obtained in the repeat experiment. The electrodes of the MEA consist of iridium black ($0.9 \pm 0.3\ \text{mg}_{Ir}\ \text{cm}^{-2}$) on the anode and of Pt/C ($0.3 \pm 0.1\ \text{mg}_{Pt}\ \text{cm}^{-2}$) with a standard ionomer/carbon mass ratio of 0.6/1 on the cathode.

considered to determine the error bars in negative direction in Figs. 3 and 4.

The total error for the H₂ permeation rate is then determined according to

$$\sigma_{\text{total},\pm} = \sqrt{\sigma_{\text{MS}}^2 + \sigma_{\text{TS}}^2 + \sigma_{\text{AA},\pm}^2} \quad [\text{A.3}]$$

This yields total errors $\sigma_{\text{total},+} = 4.2 - 12.6\%$ and $\sigma_{\text{total},-} = 9.9/17.5\%$ (Nafion® 212 / Nafion® 117) for the H₂ permeation rates which is illustrated by the error bars in Fig. 3 and 4.

Repeat experiments.—In order to verify that the permeation rate values for different MEAs shown in Fig. 3a and 3b are reproducible, we did conduct a limited number of repeat experiments. The permeation rates obtained from the repeat measurements (open symbols and dashed lines) are compared to the original data (full symbols and full lines) in Fig. A-2.

ORCID

M. Bernt  <https://orcid.org/0000-0001-8448-5532>

J. Schröter  <https://orcid.org/0000-0001-7114-8502>

References

1. K. E. Ayers, E. B. Anderson, C. Capuano, B. Carter, L. Dalton, G. Hanlon, J. Manco, and M. Niedzwiecki, *ECS Trans.*, **33**, 3 (2010).
2. M. Carmo, D. L. Fritz, J. Mergel, and D. Stolten, *Int. J. Hydrogen Energy*, **38**, 4901 (2013).
3. IRENA, *Renewable Power Generation Costs in 2017*, International Renewable Energy Agency (2018).
4. Fraunhofer ISE, *Current and Future Cost of Photovoltaics. Long-term Scenarios for Market Development, System Prices and LCOE of Utility-Scale PV Systems*, Study on behalf of Agora Energiewende (2015).
5. K. Ayers, N. Danilovic, R. Ouimet, M. Carmo, B. Pivovar, and M. Bornstein, *Annual Review of Chemical and Biomolecular Engineering*, **10**, 219 (2019).
6. K. A. Lewinski, D. van der Vliet, and S. M. Luopa, *ECS Trans.*, **69**, 893 (2015).
7. M. Bernt and H. A. Gasteiger, *J. Electrochem. Soc.*, **163**, F3179 (2016).
8. M. Möckl, M. Bernt, J. Schröter, and A. Jossen, *Int. J. Hydrogen Energy*, **45**, 1417 (2020).
9. A. Buttler and H. Spliethoff, *Renew. Sustain. Energy Rev.*, **82**, 2440 (2018).
10. F. Marangio, M. Pagani, M. Santarelli, and M. Cali, *Int. J. Hydrogen Energy*, **36**, 7807 (2011).
11. A. Peschel, *Fuel Cells*, in press.
12. H. Janssen, J. C. Bringmann, B. Emonts, and V. Schroeder, *Int. J. Hydrogen Energy*, **29**, 759 (2004).
13. M. Schalenbach, M. Carmo, D. L. Fritz, J. Mergel, and D. Stolten, *Int. J. Hydrogen Energy*, **38**, 14921 (2013).
14. T. Sakai, H. Takenaka, N. Wakabayashi, Y. Kawami, and E. Torikai, *J. Electrochem. Soc.*, **132**, 1328 (1985).
15. P. Trinke, B. Benschmann, and R. Hanke-Rauschenbach, *Electrochem. Commun.*, **82**, 98 (2017).
16. M. Doyle and G. Rajendran, in *Handbook of Fuel Cells*, ed. W. Vielstich, A. Lamm, and H. A. Gasteiger (Wiley, New York: New York) p. 18 (2003).
17. F. Barbir, *Sol. Energy*, **78**, 661 (2005).
18. S. S. Kocha, J. Deliang Yang, and J. S. Yi, *AIChE J.*, **52**, 1916 (2006).
19. J. Zhang, H. A. Gasteiger, and W. Gu, *J. Electrochem. Soc.*, **160**, F616 (2013).
20. C. Mittelsteadt and H. Liu, in *Handbook of Fuel Cells*, ed. W. Vielstich, H. A. Gasteiger, and H. Yokokama (Wiley, New York: Chichester, UK) p. 345 (2009).
21. M. Schalenbach, T. Hoefner, P. Paciok, M. Carmo, W. Lueke, and D. Stolten, *The Journal of Physical Chemistry C*, **119**, 25145 (2015).
22. M. Schalenbach, M. A. Hoeh, J. T. Gostick, W. Lueke, and D. Stolten, *The Journal of Physical Chemistry C*, **119**, 25156 (2015).
23. H. Ito, N. Miyazaki, M. Ishida, and A. Nakano, *Int. J. Hydrogen Energy*, **41**, 20439 (2016).
24. P. Trinke, B. Benschmann, and R. Hanke-Rauschenbach, *Int. J. Hydrogen Energy*, **42**, 14355 (2017).
25. D. Bessarabov, A. Kruger, S. M. Luopa, J. Park, A. A. Molnar, and K. A. Lewinski, *ECS Trans.*, **75**, 1165 (2016).
26. M. Stähler, A. Stähler, F. Scheepers, M. Carmo, W. Lehnert, and D. Stolten, *Int. J. Hydrogen Energy*, **45**, 4008 (2020).
27. P. Trinke, P. Haug, J. Brauns, B. Benschmann, R. Hanke-Rauschenbach, and T. Turek, *J. Electrochem. Soc.*, **165**, F502 (2018).
28. A. Weiß, A. Siebel, M. Bernt, T.-H. Shen, V. Tileli, and H. A. Gasteiger, *J. Electrochem. Soc.*, **166**, F487 (2019).
29. G. Alberti, R. Narducci, and M. Sganappa, *J. Power Sources*, **178**, 575 (2008).
30. S. A. Grigoriev, P. Millet, S. V. Korobtsev, V. I. Porembskiy, M. Pepic, C. Etievant, C. Puyenchet, and V. N. Fateev, *Int. J. Hydrogen Energy*, **34**, 5986 (2009).
31. P. Trinke, G. P. Keeley, M. Carmo, B. Benschmann, and R. Hanke-Rauschenbach, *J. Electrochem. Soc.*, **166**, F465 (2019).
32. P. J. Rheinländer, P. Peitl, M. Bernt, and H. A. Gasteiger, *Meeting Abstracts, p. 1513, ECS Spring Meeting* (2017).
33. T. A. Zawodzinski, T. E. Springer, J. Davey, R. Jestel, C. Lopez, J. Valerio, and S. Gottesfeld, *J. Electrochem. Soc.*, **140**, 1981 (1993).
34. U. Babic, M. Suermann, F. N. Büchi, L. Gubler, and T. J. Schmidt, *J. Electrochem. Soc.*, **164**, F387 (2017).
35. M. Bernt, A. Siebel, and H. A. Gasteiger, *J. Electrochem. Soc.*, **165**, F305 (2018).
36. B. Benschmann, R. Hanke-Rauschenbach, G. Müller-Syring, M. Henel, and K. Sundmacher, *Appl. Energy*, **167**, 107 (2016).
37. D. Bessarabov, H. Wang, H. Li, and N. Zhao, *PEM Electrolysis for Hydrogen Production: Principles and Applications* (CRC Press, Boca Raton) (2016).
38. A. Daryaei et al., *ACS Applied Materials & Interfaces*, **9**, 20067 (2017).
39. A. Albert, T. Lochner, T. J. Schmidt, and L. Gubler, *ACS Applied Materials & Interfaces*, **8**, 15297 (2016).
40. C. Klose, P. Trinke, T. Böhm, B. Benschmann, S. Vierrath, R. Hanke-Rauschenbach, and S. Thiele, *J. Electrochem. Soc.*, **165**, F1271 (2018).
41. E. Price, *Johnson Matthey Technology Review*, **61**, 47 (2017).
42. D. Bessarabov, *ECS Trans.*, **85**, 17 (2018).

5.4 On the Limitations in Assessing Stability of Oxygen Evolution Catalysts Using Aqueous Model Electrochemical Cells

This section contains the study "On the Limitations in Assessing Stability of Oxygen Evolution Catalysts Using Aqueous Model Electrochemical Cells" [119]. The manuscript was submitted in December 2020 and published as an open access article (Creative Commons Attribution 4.0 License (CC BY)) in the peer-reviewed journal *Nature Communications* in April 2021. The permanent web link to the article is <https://doi.org/10.1038/s41467-021-22296-9>.

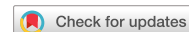
One important challenge for future large scale PEMWE systems is achieving long term stability of all parts to reach low maintenance cost. Especially the MEAs as the most critical part of the cell/stack need to be highly durable. However, as the trend for future systems is towards a lowered anode catalyst loading, in particular low anode catalyst degradation is of high importance for a reliable long term operation. So far, the durability of catalysts for OER has rarely been tested in real devices with MEAs, but mostly in model systems with aqueous electrolytes which try to mimic the operating conditions of PEMWE in many aspects such as potential range and pH. However, recent studies show that the stability of catalysts in real devices is several orders of magnitude higher than the results obtained with aqueous model systems (AMS). Thus, this gap in stability of the same catalysts tested in a real MEA versus tests in an AMS is addressed and explained by this study. To elucidate the gap between MEA and AMS based catalyst stability measurements, a well established method of ICP-MS coupled to a scanning flow cell (SFC-ICP-MS) for the aqueous tests and a newly developed galvanic-redeposition-free MEA-based setup, where the tapped water samples are tested for dissolved catalyst species also by ICP-MS, are used. The GR-free setup consists of a specialized cell (see figure 23, panel b)) and anode water cycle which are made almost entirely from plastics or glass. Only the electric conducting parts such as flow fields and porous transport layers/current collectors are made from titanium and have a noble metal coating of gold or platinum. A commercial IrO_x catalyst (Alfa Aesar) is applied as catalyst material for all measurements. The results from the GR-free MEA setup show a five orders of magnitude higher catalyst stability compared to the AMS setup. Several tests with the AMS show that neither catalyst loading, electrolyte flow rate and presence of Ir-species in the electrolyte have an influence on stability. Also a difference between electrode Nafion[®] ionomer contents can not explain the visible stability difference. However, higher electrolyte pH-value and longer operation time have a significant influence and improve the catalyst stability in AMS measurements. Vice versa, running the MEA setup with a diluted sulfuric acid (0.1 mol H₂SO₄) instead of water decreases the catalyst stability, with a catalyst half-life of \approx 150 years for an operation with pure DI water and only several days with acid. To rule out iridium deposition in the membrane, STEM-energy dispersive X-ray (EDX) analysis is performed on several MEAs after test and only small, insignificant amounts of iridium can be detected close to the anode catalyst layers. Thus, PEMWE systems operated with DI water show a high anode catalyst stability compared to AMS during uninterrupted operation. The main factors for the discrepancy are higher pH-values in MEAs than estimated and a stabilization effect with time during prolonged electrolysis.

Author Contributions

S.C. conceived and developed the idea and coordinated the work. J.K. and S.C. designed the experiments. J.K. prepared electrodes for aqueous measurements, performed dissolution measurements in aqueous electrolyte, liquid sample analysis, and data analysis. M.M. developed the GR-free MEA

setup, prepared MEAs, performed MEA measurements, and data analysis. K.S. performed H-cell measurements. M.B. performed STEM measurements. T.B. performed ultramicrotome thin-film cuts for STEM. The manuscript was written by J.K., M.M., D. E.-L., and S.C. with input and feedback from all authors. All authors contributed through scientific discussions and have given approval to the final version of the manuscript.

ARTICLE

<https://doi.org/10.1038/s41467-021-22296-9>

OPEN

On the limitations in assessing stability of oxygen evolution catalysts using aqueous model electrochemical cells

Julius Knöppel ^{1,2}✉, Maximilian Möckl³, Daniel Escalera-López¹, Kevin Stojanovski^{1,2}, Markus Bierling^{1,2}, Thomas Böhm^{1,2}, Simon Thiele ^{1,2}, Matthias Rzepka³ & Serhiy Cherevko ¹✉

Recent research indicates a severe discrepancy between oxygen evolution reaction catalysts dissolution in aqueous model systems and membrane electrode assemblies. This questions the relevance of the widespread aqueous testing for real world application. In this study, we aim to determine the processes responsible for the dissolution discrepancy. Experimental parameters known to diverge in both systems are individually tested for their influence on dissolution of an Ir-based catalyst. Ir dissolution is studied in an aqueous model system, a scanning flow cell coupled to an inductively coupled plasma mass spectrometer. Real dissolution rates of the Ir OER catalyst in membrane electrode assemblies are measured with a specifically developed, dedicated setup. Overestimated acidity in the anode catalyst layer and stabilization over time in real devices are proposed as main contributors to the dissolution discrepancy. The results shown here lead to clear guidelines for anode electrocatalyst testing parameters to resemble realistic electrolyzer operating conditions.

¹Forschungszentrum Jülich GmbH, Helmholtz Institute Erlangen-Nürnberg for Renewable Energy (IEK-11), Erlangen, Germany. ²Department of Chemical and Biological Engineering, Friedrich-Alexander-Universität Erlangen-Nürnberg, Erlangen, Germany. ³ZAE Bayern, Electrochemical Energy Storage, Garching, Germany. ✉email: j.knoepfel@fz-juelich.de; s.cherevko@fz-juelich.de

Global warming is driving the transition from fossil fuels to renewable energies. To support the transfer, economically promising alternatives to petrochemical processes for all sectors have to be established¹. Owing to its high energy density, low chemical complexity, and high efficiency, hydrogen is among the best candidates for energy storage and distribution^{2–4}. If hydrogen production from water electrolysis (WE) is fully supplied by renewable energy sources, greenhouse gas emissions can be reduced by 75%⁵. Therefore, research funding on upscaling WE technology is increasing^{6,7}. Currently, technologies, based on liquid alkaline and acidic solid electrolyte are equally considered. Classical alkaline electrolyzers lack the option of dynamic operation necessary for direct coupling to fluctuating energy sources, and solid electrolyte anion exchange membrane (AEM) electrolyzers are not at a technology readiness level suitable for upscaling^{8,9}. Acidic proton exchange membrane (PEM) electrolyzers consisting of membrane electrode assemblies (MEA), which lack these disadvantages, are the preferred system for upscaling in the short term¹⁰.

It is generally accepted that acidic conditions and high potentials at the anode side of PEM water electrolyzers (PEMWEs) where the oxygen evolution reaction (OER) takes place, demand for materials with high catalytic activity, and corrosion stability. Such criteria are only satisfied for electrocatalysts based on scarce noble metals such as iridium (Ir) and, to a lesser extent, ruthenium (Ru). Although their current implementation in PEMWEs is not hampered by their cost, upscaling fabrication of MEAs with these metals is expected to be a major cost driver at the GW scale^{11,12}. Therefore, a significant part of research activities on WE are focused on the reduction of noble metal content in PEMWE anodes^{13,14}.

For the state-of-the-art Ir catalysts, a cornerstone in fundamental research studies has been to maximize Ir utilization, specifically, to increase their OER mass activity whilst reducing noble metal content without a significant loss in activity^{15,16}. The use of high-surface-area catalyst supports^{17,18}, highly active perovskites^{19,20}, and multimetallic materials^{21,22} are employed to reduce the noble metal content. However, stability has to be monitored as a second major descriptor in electrocatalyst design and synthesis, as OER catalysis also triggers catalyst dissolution²³.

Activity and stability evaluations of newly developed catalysts are performed *ex situ* in the classical three-electrode electrochemical cell setup with acidic electrolyte to simulate the acidic pH environment of PEMWEs anodes in presence of Nafion^{24–26}. Current-potential profiles are recorded and analyzed for activity evaluation. For stability evaluations, however, more sophisticated

methods were developed, such as electrochemical quartz crystal microbalance²⁷, scanning flow cell (SFC) coupled to an inductively coupled plasma mass spectrometer (SFC-ICP-MS)^{28,29}, and post-analysis of electrolyte and catalyst layers^{30,31}. However, comparative data of catalyst stability in both systems show that degradation in aqueous systems does not represent the conditions in PEMWE^{32,33}.

Recent results from our group, based on aqueous SFC-ICP-MS measurements and end-of-life data from PEMWE, indicate an underestimation of the actual catalyst lifetime of several orders of magnitude, ranging from days in aqueous to years in MEA²⁸. In this work, the relevance of S-numbers, a new metric for OER catalyst lifetime estimation, measured in aqueous systems for real application based on end-of-life data of PEM electrolyzers, is discussed. As end-of-life data is rarely found for Ir-based electrolyzers, the data set of a system using RuO₂ as anode material published by Ayers *et al.*¹⁴ was compared with the same material measured in SFC-ICP-MS. It was found that the PEM electrolyzer outperforms the aqueous system by about three orders of magnitude, leading to a significant increase in the estimated lifetime of the electrolyzer in comparison to the same catalyst in the aqueous system. A similar concept, the activity-stability factor, was developed in parallel by Kim *et al.*³⁴.

In this work, we aim to reveal the experimental factors responsible for the observed OER catalyst dissolution differences between aqueous model systems (AMS) and PEMWEs. We evaluated how the parameters that diverge between the systems such as catalyst loading, mass transport conditions, Nafion binder content, and electrolyte pH influence Ir dissolution. Also, we aim to determine the real dissolution rates of MEAs for PEMWEs using a custom-made full cell setup devised to prevent galvanic precipitation of catalyst dissolved species under OER operation.

Results and discussion

Iridium OER catalyst dissolution: aqueous model versus MEA systems. The dissolution behavior of OER catalysts in AMS is already well studied^{28,35–37}. Utilizing online measurements, the dissolution behavior of OER catalysts under various electrochemical conditions has been shown. To put the results presented in this section into context, it is important to highlight the commonalities and differences between MEA and AMS. In AMS, the employed electrolyte, mostly an acid or base, is diluted by the reactant, deionized (DI) water. As schematically shown in Fig. 1a, the reaction products, H₂ at the cathode side and O₂ and protons at the anode side, as well as dissolution products, such as Ir³⁺,

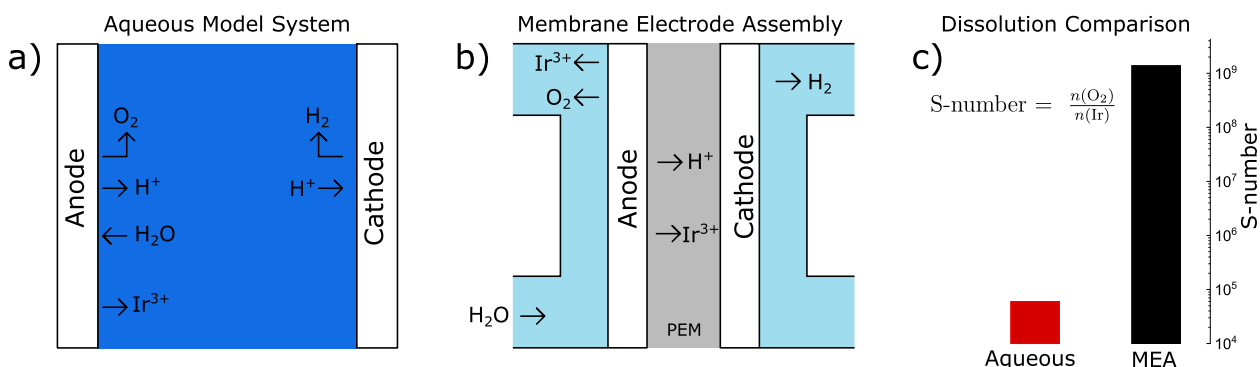


Fig. 1 Degradation processes of OER catalysts in aqueous and polymer electrolyte. **a** Schematic drawing of degradation processes in a classical aqueous electrolysis cell in aqueous electrolyte and **b** schematic drawing of degradation processes in MEA. **c** Dissolution stability of IrO_x under OER conditions in aqueous electrolyte, measured in SFC-ICP-MS, and polymer electrolyte, measured in a precipitation-free MEA device, expressed in the S-number metric. Measurements were carried out with a 5 min chronopotentiometry hold in aqueous electrolyte and over several days for MEA, typical timescales for the devices. Source data are provided in the source data file.

diffuse into the bulk. Hence, to measure dissolution, it is sufficient to take aliquots of electrolyte from the solution. Utilizing flow cells, which directly transport reaction products from the reaction site downstream (if coupled) to analytical techniques such as ICP-MS, the dissolution behavior can be directly correlated to the electrochemical operation^{28,34,38}.

To study the degradation behavior of MEA, a system with a much higher degree of complexity, long-term measurements, and end-of-life (EOL) data have been used thus far. Owing to the long lifetime of MEA electrolyzers, however, EOL data are scarce. Furthermore, measurements of dissolution products in MEA are more complicated than in AMS. As schematically shown in Fig. 1b, electrolyte and reactant are decoupled in MEA by placing the polymer electrolyte between the electrodes and circulating DI water as the reactant at the backside. Reaction products, H₂, and O₂ escape through porous transport layers at the respective electrodes, whereas H⁺ is transported through the PEM towards the reaction site at the cathode. In this system, dissolution products of OER catalysts have two ways to escape the anode catalyst layer: through the anode water cycle or the membrane towards the cathode side. Furthermore, galvanic replacement (GR) of dissolution products with stainless steel tubes, often employed in MEA test setups, can lead to an underestimation of dissolution³⁹.

Hence, to reliably determine dissolution in MEA and realistically compare results with AMS, several factors have to be controlled. The water level in the anode compartment and the water flow at the cathode outlet through electroosmotic drag have to be monitored at all times^{40,41}. Furthermore, the amount of iridium depositing in the membrane has to be estimated. Also, GR should be excluded as a measurement factor.

For such purpose, a dedicated MEA setup without metallic parts in the anode water cycle was developed and employed in this study. Cell components involved in electronic conduction, namely titanium flowfields and current collectors, are coated with gold or platinum to prevent GR. Samples are taken from the anode water cycle and the cathode outlet and analyzed separately by ICP-MS. The setup and flow scheme is shown in supplementary note 1. Water balance calculations, necessary to determine the amount of dissolved iridium, are shown in supplementary note 2.

To compare the dissolution stability of OER catalysts between MEA and AMS, a commercially available IrO_x catalyst is measured in the aforementioned dedicated MEA system as well as in an SFC-ICP-MS setup operated with 0.1 M H₂SO₄. Figure 1c shows dissolution stability in both systems, displayed in the S-number metric, a dimensionless descriptor that compares the amount of oxygen evolved, calculated from the measured current density at an estimated 100% faradaic efficiency towards OER, with the amount of iridium dissolved ($S\text{-number} = \frac{n(\text{O}_2)}{n(\text{Ir})}$)²⁸. S-numbers were calculated from constant current measurements of 5 minutes in AMS and several days in the MEA. Electrochemical data and dissolution data for MEA experiments are available in supplementary note 3. Electrochemical data, dissolution data, and the integration areas for determining S-numbers in SFC-ICP-MS are shown in Fig. 2. Both timescales are representative of the respective system.

The S-number of IrO_x in the SFC-ICP-MS is 6×10^4 . Although with the used H₂SO₄ electrolyte, a stronger adsorption of anions on the surface is anticipated⁴², the measured S-number is comparable to literature values measured in the non-coordinating HClO₄, which range between 10^4 and 10^5 ^{28,43–45}. Thus, although the influence of the electrolyte anion cannot be fully ruled out, its role in the stability of IrO_x is minor. Remarkably, the observed S-number of IrO_x in the MEA system

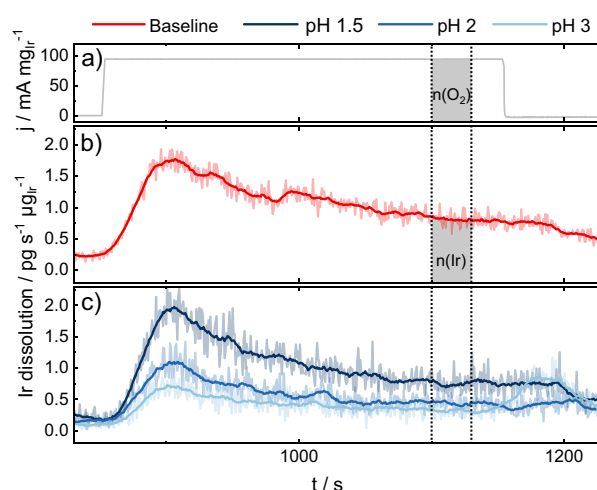


Fig. 2 Dissolution profiles of IrO_x catalyst spots in SFC-ICP-MS

measurements. **a** Applied current step and **b**, **c** resulting dissolution of **b** a baseline measurement at standard conditions (10 μg_{Ir}, cm⁻² catalyst loading, 200 μl min⁻¹ flow rate, fresh electrolyte, 33 wt% Nafion in the catalyst layer and 0.1 M H₂SO₄ (pH = 1)) and **c** with a variation of electrolyte pH. The integration area for the calculation of S-numbers is highlighted by vertical dashed lines. Source data are provided in the source data file.

exceeds the one observed in aqueous systems by almost five orders of magnitude. Further experiments in AMS were undertaken to unravel the reasons for this behavior.

Evaluation of model aqueous OER stability parameters. We evaluated several parameters that generally differ in both systems to determine the origin of the dissolution discrepancy between AMS and MEA. (a) catalyst loading; (b) electrolyte flow rate; (c) presence of electrochemically dissolved iridium species; (d) Nafion content in the catalyst layer; and (e) pH were individually varied during testing in the AMS (SFC-ICP-MS). All experiments were carried out with the same IrO_x catalyst powder as in previously shown MEA experiments.

Dissolution profiles of baseline measurement of IrO_x catalyst powder spots at a current step of 100 mA mg_{Ir}⁻¹ (Fig. 2a) are displayed in Fig. 2b. The full measurement protocol is shown in supplementary note 4. Representative electrochemical and dissolution data for all experiments are shown in supplementary note 5.

The corresponding S-numbers for all experiments, determined at a 30 s steady-state interval at the end of the current step²⁸, as shown in Fig. 2a and b) are displayed in Fig. 3. All error bars are acquired from at least three independent measurements. The baseline measurement is hereby displayed in Fig. 3a).

Our first study focused on differences in catalyst loading. Although Ir loading in aqueous studies rarely exceeds 10 μg_{Ir}, cm⁻², loading in MEA is typically ~1–2 mg_{Ir}, cm⁻²²⁴⁶. S-numbers of catalyst spots with different loading is shown in Fig. 3b, where loading is varied between 10 μg_{Ir}, cm⁻² and 250 μg_{Ir}, cm⁻². The obtained S-number values are comparable and in the same order of magnitude. Hence, we can exclude the influence of loading on the dissolution discrepancy.

The second study was different SFC operating flow rates. Given the flow rate uncertainty in PEMWE MEA systems, contrasting with its precise control in our SFC-ICP-MS setup, we evaluated the impact of SFC flow rate by variations within one order of magnitude. The flow rate of electrolyte to the ICP-MS was here varied between 66 μl min⁻¹ and 740 μl min⁻¹. S-numbers for these experiments are virtually equivalent as shown in Fig. 3c. As

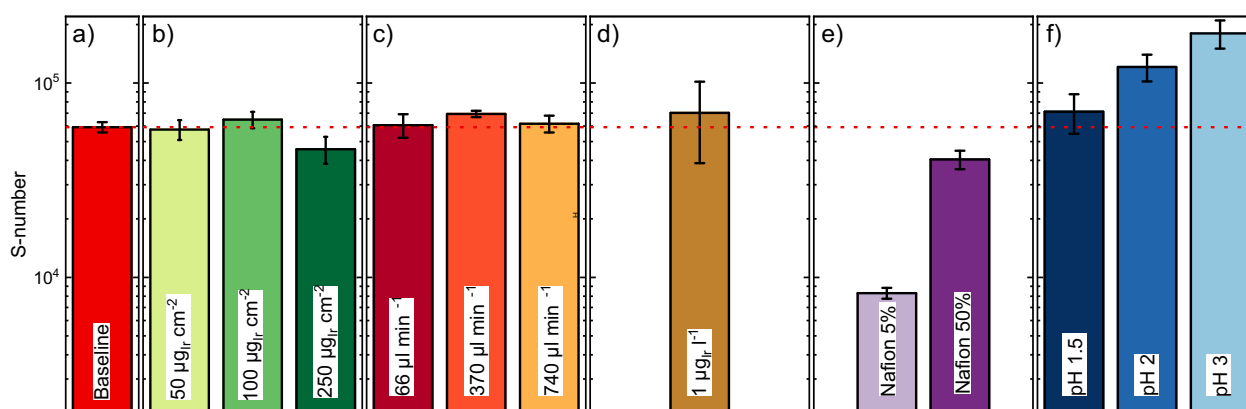


Fig. 3 S-numbers of IrO_x catalyst spots with varied conditions, measured in SFC-ICP-MS. **a** Baseline measurement. **b** Variation of loading. **c** Variation of flow rate. **d** Addition of pre-dissolved iridium in the electrolyte. **e** Variation of Nafion content in the catalyst layer. **f** Variation of pH. Red, dashed line: baseline measurement ($10 \mu\text{g}_{\text{Ir}} \text{cm}^{-2}$ catalyst loading, $200 \mu\text{l min}^{-1}$ flow rate, fresh electrolyte, 33 wt% Nafion in the catalyst layer and $0.1 \text{ M H}_2\text{SO}_4$ ($\text{pH} = 1$)), displayed for ease of comparison between **b** and **f**. Error bars were calculated as the standard deviation of at least three independent measurements. Source data are provided in the source data file.

the flow rate effectively dictates the mass transport rate of dissolved species from the electrode interface to the bulk electrolyte, a possible Ir redeposition mechanism should be affected by it as well. Based on the results obtained, these mass transport phenomena do not seem to play a key role in the AMS-MEA catalyst stability differences.

The third parameter variation tackled the dissolution–redeposition equilibrium of Ir-dissolved species, which can occur during MEA water circulation owing to low flow rates and slow mass transport in thick catalyst layers. To simulate such conditions in AMS, and enable a potential dissolution–redeposition mechanism, electrochemically dissolved iridium has to be present in the electrolyte in relevant concentrations. Therefore, Ir was electrochemically dissolved from polycrystalline iridium^{37,47} (see the experimental section for further details) and then intentionally incorporated into the acidic electrolyte used. The iridium concentration in the electrolyte is determined by ICP-MS and adjusted accordingly. Figure 3d shows the S-number of IrO_x spots measured with $1 \mu\text{g}_{\text{Ir}} \text{l}^{-1}$ dissolved iridium in the electrolyte. This value is similar to a recent publication, where Ir concentrations in MEAs were measured³⁹. Also, it is in the same order of magnitude as the concentrations measured in our MEA study (see supplementary note 3). As observed with the previous parameters, S-number values are comparable to the baseline experiment. Hence, equilibrium states between dissolution and redeposition are unlikely to largely contribute to the Ir dissolution discrepancy.

The fourth evaluated parameter is the influence of Nafion content in the catalyst layer on Ir dissolution. Unlike OER rotating disk electrode experiments, where no Nafion is required, it acts as a catalyst layer binder in SFC-ICP-MS to avoid particle detachment. Figure 3e shows the S-numbers of IrO_x spots with different Nafion contents, varied here between 5 and 50 wt% vs. the total catalyst content. Interestingly, the dissolution rate of catalysts spots with 5 wt% Nafion in the catalyst layer is significantly larger from the other Nafion contents. Indeed, the stability differs from baseline measurements by an order of magnitude, with an S-number of 8×10^3 . We hypothesize that, at lower Nafion contents, dissolved iridium mass transport from the catalyst layer to the electrolyte bulk might be more efficient. A local saturation might hereby inhibit dissolution. As baseline measurements have a Nafion content of 33 wt%, whereas MEA electrodes were produced with 9 wt% Nafion content in this study, Nafion content will have a role in stability observations.

However, different constraints have to be met for measurements in both systems. In SFC-ICP-MS, Nafion predominantly acts as a binder in the catalyst layer to avoid particle detachment. On the other hand, in the more complex MEA system, Nafion has not only an influence on the integrity of the catalyst layer, but also on features such as contact resistance with the porous transport layers (PTL). As Nafion contents employed in this study rather open the gap between AMS and MEA instead of closing it, this rather leads to an underestimation than an overestimation of the stability discrepancy.

The fifth study carried out is the variation of the working electrolyte pH value, varied here between 1 and 3 (experimental dissolution profiles shown in Fig. 2c). To ensure a similar ionic strength, a sulfate salt was added to electrolytes with $\text{pH} > 1$. The resulting S-numbers, shown in Fig. 3f, significantly differ from each other. Although the S-number metric obtained for pH 1.5 is still similar to the reference measurement (pH 1), a significant difference is observed for pH 2 and 3. Such difference in stability is a factor of three: for pH 1, S-number = 6×10^4 whilst for pH = 3, S-number = 1.8×10^5 . It should be noted that local pH at the electrode under OER conditions might be lower owing to the worsened buffer capacity of electrolytes with higher pH⁴⁸.

MEA environments for PEMWE are, according to the literature, highly acidic owing to the use of Nafion^{49,50}. The observations, made here in AMS, however, indicate, that the activity of protons in MEA electrolysis might be lower than generally accepted. Further experiments in MEA systems have to be conducted to unravel the magnitude of the differences.

Impact of pH in PEMWE operation: catalyst and MEA stability.

As shown in a previous section, of all parameters evaluated in our study of model aqueous systems, pH is the only one with a relevant impact on stability towards closing the gap. Hence, measurements of IrO_x in MEA were conducted with $0.1 \text{ M H}_2\text{SO}_4$ in the anode water cycle to investigate the influence of low pH environments on dissolution. The operational principles in both systems are schematically shown in Fig. 4a for MEA operated with DI water and in Fig. 4b) for the MEA operated with acid. S-numbers from liquid samples collected after 2 h operation are displayed in Fig. 4c). Strikingly, the S-number of the conventional system exceeds the one from the acid operated by more than two orders of magnitude. In comparison to AMS, which operates with

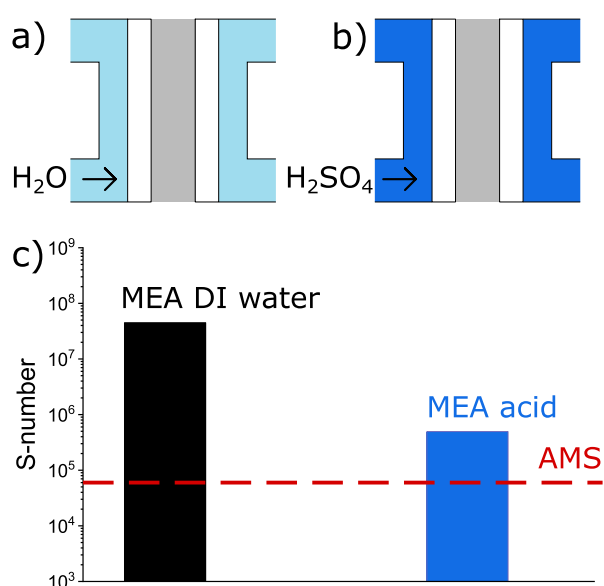


Fig. 4 Comparison of stability in different systems. **a** Working principle of an MEA operated with DI water. **b** Working principle of an MEA operated with 0.1 M H₂SO₄. **c** S-numbers of MEAs operated with DI water and 0.1 M H₂SO₄ after 2 h of measurement. The red, dashed line in **c** indicates the S-number of the AMS system. Source data are provided in the source data file.

S-numbers around 6×10^4 , the stability difference to the acidic operated MEA virtually vanishes. Its impact can be easily grasped when calculating catalyst half-life estimated from S-numbers²⁸. For a DI water-fed MEA system, its value is ca. 150 years, whereas for an acidified MEA it is just several days.

Post mortem scanning transmission electron microscopy (STEM) cross-section micrographs of the MEA after 48 h of continuous operation at $2 \text{ A mg}_{\text{Ir}}^{-1}$, shown in supplementary note 7, reinforce the stark degradation differences found from liquid sample analysis. Although the anode catalyst layer of the DI water-operated MEA is virtually intact and iridium migration into the membrane is non-existent, the anode catalyst layer of the acidic operated MEA reveals exceptional signs of degradation. Indeed, Au particles, originating from the partly dissolved flowfield coating, of μm diameter form in the membrane close to the anode side. The cathode side of the conventional operated MEA only shows signals of Pt and C, whereas iridium was detected in the catalyst layer of the acidified MEA. Furthermore, the MEA polarization curves indicate a shift in pH (for full description, see supplementary note 8)⁵¹ and the anode flowfield and current collector displays stark signs of degradation after the experiment. (See supplementary note 9)

Impact of OER operating timescale in catalyst stability in AMS and MEA. The different timescales have to be taken into account when comparing AMS with MEA systems. For instance, the data shown in Fig. 1c were measured over minutes for AMS and days for MEA. Indeed, MEA systems have proven stable operation for thousands of hours on the laboratory scale⁵² and in industrial applications⁵³. Hence, we investigated if the short experimental timescale in AMSs can be extrapolated to PEMWE systems, or stabilization effects occur over large timescale operating conditions.

SFC-ICP-MS measurements cannot be carried out for several hours or even days. Thus, electrochemical measurements were

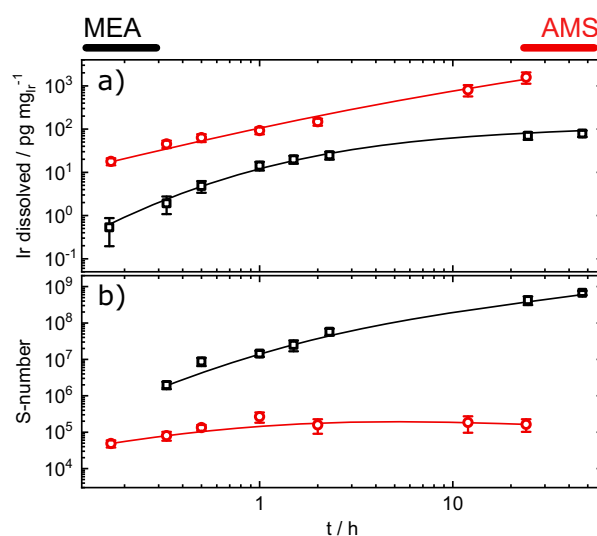


Fig. 5 Long-term stability of IrO_x in AMS and MEA environment.

a Loading-normalized total dissolved iridium amount at current densities of $0.2 \text{ A mg}_{\text{Ir}}^{-1}$ and $2 \text{ A mg}_{\text{Ir}}^{-1}$ in AMS and MEA, respectively; **b** S-numbers calculated from the amounts of dissolved iridium. Lines displayed for ease of interpretation. Error bars were calculated as the standard deviation of at least three independent measurements. Source data are provided in the source data file.

carried out in an H-cell configuration to represent an aqueous model system operated at longer timescales. A 0.1 M H₂SO₄ electrolyte with sample collection with sample collection from both compartments was used (see experimental). To have a side-by-side comparison, samples from the developed GR-free MEA system were taken from the anode water cycle and the cathode water outlet. Calculations for obtaining mass losses are shown in supplementary note 2.

Loading-normalized iridium dissolution for H-cell (IrO_x loading = $10 \mu\text{g}_{\text{Ir}} \text{ cm}^{-2}$) and MEA measurements (anode IrO_x loading = $1 \text{ mg}_{\text{Ir}} \text{ cm}^{-2}$) are displayed in Fig. 5a. Current densities were $0.2 \text{ A mg}_{\text{Ir}}^{-1}$ for AMS and $2 \text{ A mg}_{\text{Ir}}^{-1}$ for MEA. At the employed current density, the amount of dissolved iridium in the aqueous system rose almost constantly throughout the experiment after an early-stage stabilization. S-numbers (Fig. 5b) only stabilized marginally from values of 7×10^4 to 2×10^5 . In contrast, the iridium mass loss during DI water-operated MEA experiments stabilized rapidly after the start to an almost constant level. The S-numbers rose from an initial value of 10^7 in the first hours to a value of 10^8 and stabilize after the first day of the experiment at $\sim 10^9$ (compare supplementary information 2).

The results obtained in MEA are in heavy contrast with results previously shown by Babic et al.³⁹. In their experiment, the authors observed fluctuating or, after an initial increase, decreasing iridium concentrations in the electrolyte. Although a direct protocol comparison is not feasible, a similar decrease of iridium in the water feed was observed by Regmi et al.⁵⁴. Our results clearly show the advantage of the employed metal-free MEA setup, as the authors already pointed out a possible interference of GR in their results. Thus, in all studies concerning dissolution products of operational MEAs, GR should be taken into account, as otherwise, it might result in misleading conclusions.

Previous research would suggest a stabilization under long-term operation on iridium-based catalysts owing to crystallization³⁰. Indeed, both aqueous and MEA systems should eventually yield an equivalent degree of stabilization. For MEA

systems, such stabilization is reached at an earlier stage given the higher operating current density of $2 \text{ A mg}_{\text{Ir}}^{-1}$ inherent to the system compared with the current density of $0.2 \text{ A mg}_{\text{Ir}}^{-1}$ employed in our H-cell setup. Because of the low operational currents achieved in AMS, we cannot unambiguously prove such a stabilization effect. A method to circumvent such limitation, beyond the scope of this report, would be to perform studies on high-current density achieving gas diffusion electrode-type (GDE) reactors^{55–57}.

System breakdown of the dissolution discrepancy between AMS and MEA. A comparison of these results reveals the inherent differences between MEA and AMS. As shown in Fig. 6, the differences in S-numbers between AMS (1) and MEA decrease to less than one order of magnitude when circulating diluted acid through the MEA water feed (2). These differences cannot be related to a sole factor. Loading, flow rate, dissolved species, timescale or Nafion content, although not relevant factors in AMS, might play a role in MEA and have to be addressed in a follow-up study. However, the higher complexity of the MEA does not allow tangible conclusions on the main contributor. When operating an MEA with DI water on the same timescale (3), the S-number increases by two orders of magnitude, indicating a pH shift between AMS and MEA as a main contributor to the dissolution discrepancy. After 2 weeks of operation, the S-number of the MEA increased by more than one order of magnitude (4). At this timescale, based on lifetime calculations from the S-number, the catalyst in the aqueous system would already have been degraded completely. Hence, a stabilization on a larger timescale can be treated as the second main contributor to the dissolution discrepancy. As STEM-energy dispersive X-ray (EDX) only detects small amounts of iridium in the membrane close to the anode catalyst layer, iridium depositing in the membrane can be ruled out as a large contributor.

Given the aforementioned results, we should now address past preconceptions regarding local pH during PEMWE operation. PEMWE anodes are assumed to operate under highly acidic

conditions due to protons generated at the anode side during operation. However, literature is scarce regarding actual pH value estimation under PEMWE operation. An initial review by Carmo et al.¹⁰ tentatively estimated a pH 2 value, whereas later investigations reported pH values in the anode and cathode water cycle of an MEA setup in a range between 5.6 and 3.5⁵⁸. However, these results might not be representative for conditions in the anode catalyst layer as the local pH can decrease owing to proton generation in the water-splitting reaction. The results shown in this study indicate that proton activity in MEA environment is supposedly lower as estimated from the concentrations. Thus, it is likely, that the effective pH in MEA environment is less acidic as generally accepted in the literature.

These results indicate that future research should emphasize more on two aspects of MEA development: real conditions in the anode catalyst layer and effects in the catalyst/membrane interface.

Conclusions and outlook. In summary, we show that stability measurements performed in AMS have to be treated carefully regarding their relevance for long-term PEMWE applications. The main effects contributing to the dissolution discrepancy were identified as a discrepancy between estimated and real pH in MEA and stabilization occurring over time.

Based on this research, the community should critically evaluate the process of OER catalyst testing in AMS. Owing to faster degradation, AMS might serve as an ideal system for accelerated stress tests. For this purpose, GDE systems currently under development might help to study OER catalysts in model systems, which resemble the conditions in MEA much better.

However, those results should always be critically compared with experimental MEA data to extract representative conclusions. Furthermore, more focus should be put on the direct evaluation of catalysts under MEA device operation. In particular, a setup consisting of an MEA coupled to downstream analytics would allow a better understanding of dynamic operation conditions, relevant for coupling to renewable energies. We believe that the results shown here will provide improved

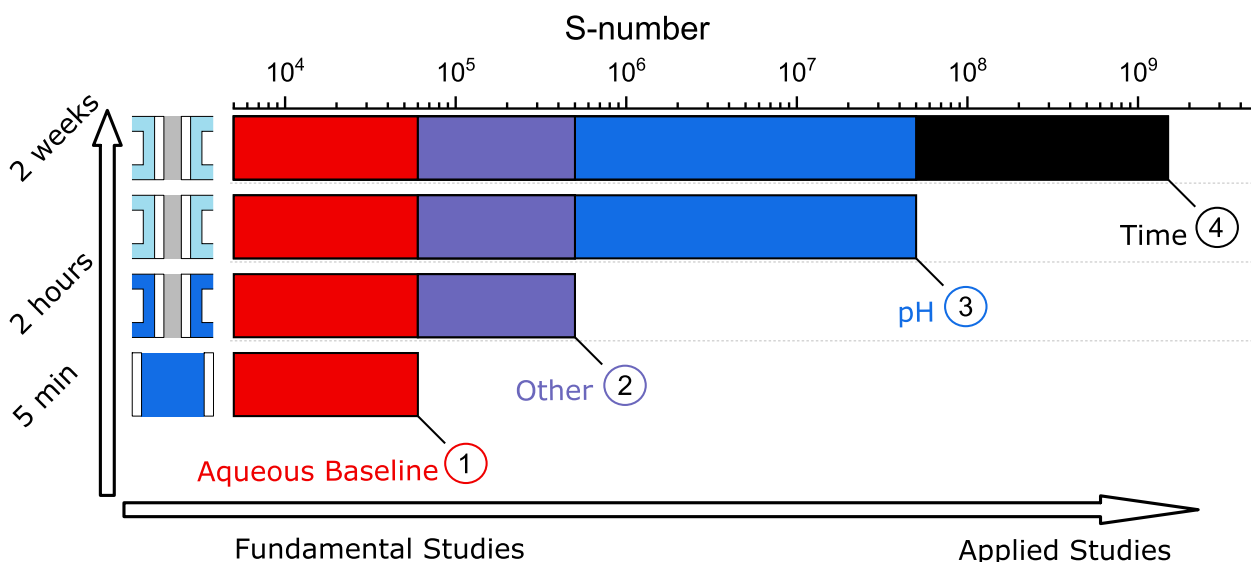


Fig. 6 Scheme on the proposed main contributors to the dissolution discrepancy. Schematic drawing of the factors contributing to the OER catalyst dissolution discrepancies between AMS and MEA. Measurements in AMS exhibit an S-number of 6×10^4 (1). The discrepancy to an MEA operated with acid (2), showing an S-number of 4×10^5 , cannot be pointed to a single factor. Various factors such as flow rate, Nafion content, and timescale have to be taken into account. The discrepancy of the MEA operated with acidic water feed to an MEA operated conventionally with DI water (3) of almost two orders of magnitude, however, is related to a pH shift in the system. With a longer operation time (4), additional stabilization effects in MEA take place. Source data are provided in the source data file.

guidelines for future catalyst development and testing to mimic realistic MEA operating conditions.

Methods

SFC-ICP-MS measurements

Electrode preparation. Electrodes were prepared by suspending commercial Alfa Aesar $\text{IrO}_x \cdot 2\text{H}_2\text{O}$ Premion catalyst powder in a mixture of 87.5% ultrapure water (Merck Milli-Q), 12.5% IPA, and Nafion® perfluorinated resin solution (Sigma Aldrich, 5 wt%). Standard inks had an iridium concentration of $663 \mu\text{g l}^{-1}$, a Nafion concentration of $332 \mu\text{g l}^{-1}$ and a volume of 1 ml in a 1.5 ml Eppendorf tube. Inks were sonicated for 10 min (4 s pulse, 2 s pause) and dropcasted as $0.2 \mu\text{l}$ on a freshly polished glassy carbon plate (SIGRADUR G, HTW). The quality and diameter of the dropcasted catalyst spots (O_2 of ca. 1.3 mm) was screened by employing Keyence VK-X250 profilometer.

For variations of loading and Nafion content, the concentration of iridium and Nafion in the ink was adjusted to the desired loading and concentration. An IPA: DI water ratio of 12.5:87.5, was employed in all IrO_x inks, accounting for the alcohol content in the Nafion solution.

Electrochemical measurements. Electrochemical measurements were carried out with an SFC-ICP-MS²⁹, with the modifications described in ref. 28 in Ar-saturated 0.1 M H_2SO_4 (Merck Suprapur) mixed with ultrapure water. The dropcasted spots, acting here as working electrodes, were located with a top view camera to enable vertical alignment with the SFC (O 2 mm). A graphite rod served as counter electrode, whereas a saturated Ag/AgCl electrode (Metrohm) was used as reference electrode. ICP-MS measurements were performed with a NexIon 300 spectrometer (Perkin Elmer), employing a flow rate of $208 \mu\text{l min}^{-1}$ for reference measurements. For the flow rate-dependence studies, flow rates were adjusted by tuning the speed of the ICP-MS peristaltic pump. Daily calibration of the ICP-MS was performed by freshly prepared standard solutions containing Ir (0.5 to $5 \mu\text{g l}^{-1}$), and Re ($10 \mu\text{g l}^{-1}$) as an internal standard. All current and dissolution rates shown in this report have been normalized to the nominal loading of the spots.

For the variation of dissolved iridium in the electrolyte, iridium was electrochemically dissolved in 0.1 M H_2SO_4 by 1000 cyclic voltammograms recorded in a potential range from 0.05 V_{RHE} –1.5 V_{RHE} ^{37,47}. The iridium concentration was then determined by ICP-MS. Electrolyte and standards were prepared from the electrolyte with dissolved iridium. A baseline measurement was taken before cell contact.

For the variation of pH, the electrolyte was set to the corresponding H_2SO_4 concentration. To ensure electronic conductivity of the electrolyte in measurements with a pH higher than 1, the total concentration of sulfate ions was set to 0.05 M with K_2SO_4 (99.999% purity, Sigma Aldrich).

H-cell measurements

Electrode preparation. Electrodes were prepared from Alfa Aesar $\text{IrO}_x \cdot 2\text{H}_2\text{O}$ Premion powder. Ink for electrodes was prepared with ultrapure water (Merck Milli-Q) at a concentration of $283 \mu\text{g l}^{-1}$ with a volume of 1 ml in an Eppendorf tube. The ink was sonicated for 15 min (4 s pulse, 2 s pause) and dropcasted as $10 \mu\text{l}$ on a freshly cleaned FTO plate, previously sonicated for 10 min sequentially in 2% Hellmanex III (Hellma Analytics) solution, DI water, and ethanol, respectively. The resulting dropcasted Ir catalyst exhibited a diameter of 6 mm and a loading of $10 \mu\text{g cm}^{-2}$.

Electrochemical measurements. Electrochemical bulk measurements were carried out in a homemade H-cell. Each compartment was filled with 28 ml 0.1 M H_2SO_4 (Merck Suprapur diluted with Merck Milli-Q) before the experiment. The working electrodes and reference electrodes (Basi, 3 M Ag/AgCl) were immersed in one compartment whereas the counter electrodes (glassy carbon, SIGRADUR G, HTW) were immersed in the other compartment. The compartments were covered with Parafilm to avoid evaporation of electrolytes. Convection in the system for equal distribution of dissolution product was enabled through Ar-purging of the anode compartments. Samples were taken by an automated liquid handler (Gilson GX-271). The electrochemical protocol (Gamry Interface1000 B) was started after the first sample was extracted. The total volume of electrolyte in both compartments was kept between the initial 28 ml and 24 ml at any time.

MEA measurements

MEA preparation. For the experiments with the PEMWE setup, square format 5 cm^2 active cell area MEAs were prepared by a decal transfer method. As catalyst for the OER at the anode side, the same Alfa Aesar $\text{IrO}_x \cdot 2\text{H}_2\text{O}$ Premion powder was applied as in the SFC and H-Cell experiments. The anode catalyst loading was $1.03 \pm 0.07 \text{ mg}_{\text{Ir}} \text{ cm}^{-2}$ for all tests. For the hydrogen evolution reaction at the cathode side, carbon-supported (Vulcan XC72) platinum nanoparticles catalyst (45.8 wt% Pt/C; TEC10V50E from Tanaka, Japan) with loadings of $0.30 \pm 0.14 \text{ mg}_{\text{Pt}} \text{ cm}^{-2}$ was used. To prepare the catalyst inks, catalyst powder, 2-propanol (purity $\geq 99.9\%$ from Sigma Aldrich, Germany), and Nafion® ionomer solution (20 wt% ionomer; D2021 from IonPower, USA) are mixed for 24 h using a roller mill and 5 mm zirconia grinding balls. The decals were coated with a Mayer-rod coating machine on $50 \mu\text{m}$ PTFE foil (from Angst+Pfister, Germany). Finally, MEAs were hot-pressed (3 min at 155°C , 2.5 MPa) using the decals and different

Nafion® membrane types 117 (180 μm thickness), 212 (50 μm thickness) and 211 (25 μm thickness). By evaluating the weight differences ($\pm 15 \mu\text{g}$; XPE105DR microbalance from Mettler Toledo, Germany) of the PTFE decals before and after hot pressing, the individual catalyst loadings of the MEAs were calculated. All anodes have an ionomer content of 9 wt%, whereas all cathodes have an ionomer to carbon mass ratio of 0.6/1.

MEA measurements. To prevent any precipitation of dissolved Iridium in the cell or in the test rig a special PEMWE setup was developed.

Cell. The cell uses a two-piece monopolar plate concept consisting of a metal flowfield sheet and a plastic body. The flowfield plates are made from 3 mm grade two titanium sheet with laser cut single serpentine channel (equal 1 mm land and 1 mm channel spacing). To prevent galvanic plating of iridium, the titanium flowfield plates are gold-coated (0.5 μm by physical vapor deposition and another 5 μm galvanic coating on top). Finally, the metal flowfield plates are inserted into a fitted plastic body made from polyoxymethylene (aqueous tests) or polytetrafluoroethylene (second design for aqueous and diluted sulfuric acid tests). The plastic body allows for media transport from the serpentine flowfield inside the cell without contact to metal surfaces to the in- and outlet fittings made from polypropylene (PP) at the face sides of the monopolar plates. At the anode side, an expanded titanium metal sheet (250 μm thickness, Sylatech, Germany) with 5 μm platinum coating is used as a porous transport layer between MEA and flowfield. The cathode side PTL is a carbon fiber paper (TGP-H-120 from Toray, Japan, no MPL) with a thickness of 370 μm .

Test rig. A fully automated test rig (E40 by Greenlight Innovation, Canada) equipped with a potentiostat and a booster (Reference 3000 and 30 A booster, Gamry, USA) was used as the basis for the integration of a metal-free anode water cycle and cathode exhaust water collector. Borosilicate glass bottles of 0.5 l to 1 l volume were used as the anode water cycle setup tank. A membrane pump (NF30 from KNF, Germany) and PE/PTFE tubes were used to feed the cell with water at a rate of $\sim 300 \text{ ml min}^{-1}$. To maintain an elevated temperature of $\sim 55\text{--}60^\circ\text{C}$ in the cell, the setup tank glass bottle is tempered by a heater plate (IKA, Germany). To initially clean the setup from ionic impurities a deionizer cartridge is used (Leyco-pure mixed bed resin from Leyco, Germany), which is bypassed during the actual dissolution experiment. The anode water samples were tapped from the cycle directly behind the cell. As there was no water cycling at the cathode side, the cathode water samples were taken from the PP cathode exhaust water collector bottle. Its reservoir volume was $\sim 10 \text{ ml}$ and was continuously flushed at the cathode water exhaust rate of $8.2 \pm 0.4 \text{ ml h}^{-1}$.

Measurement procedure. Before starting the dissolution tests, the anode water cycle is cleaned up at elevated temperature for at least 12 h by running the water through the deionizer cartridge to remove eventual ionic impurities released from the setup (feed water processed by ULTRA CLEAR® TP ultrapure water system from Evoqua, USA). After the cleaning period, the cartridge is bypassed and the first 10 ml water sample (standard volume for all samples) is tapped from the cycle without contact to the cell as a clean reference. In the next step, the cell is mounted and water is run through the cell for 10 min without current. At the end, again 10 ml water is tapped from the cycle. Subsequently, the current density was set to 0.2 A cm^{-2} for 10 min and another water sample was tapped. Thereafter, the current is set to 2 A cm^{-2} where it stays for the rest of the experiment. Anode water samples are tapped after holding intervals of 10 min, 30 min, 1 h, 1 h, and successive every 24 h. Cathode samples are taken for the first time 3 h after the start of the test and then also every 24 h. During the aqueous tests with fixed anode side water volume the tapped water, the consumed water, and the water lost to the cathode by electroosmosis is replaced by ultrapure feed water. In contrast, during the acidic tests and the aqueous tests with variable water volume, the tapped, consumed or electroosmotically transported electrolyte volume is not replaced and the initial volume of water or 0.1 M H_2SO_4 is gradually reduced. At the end of the dissolution test, both flowfields were purged with nitrogen and the cell was held for at least 12 h at 1.2 V cell voltage to avoid anode side catalyst reduction by permeating hydrogen from the cathode side or the membrane. In addition, for the last two tests with gradually reduced water/acid volume, polarization curves and electrical impedance spectroscopy were made to reveal the end-of life performance of the aged MEAs. The MEAs are extracted in a glove bag and stored under nitrogen until spectroscopic analysis/STEM graphs were made.

Scanning transmission electron microscopy

Sample preparation. Samples were embedded in Araldite 502 epoxy resin and cured overnight at 60°C . Ultrathin sections with a nominal thickness of 100 nm were cut with an RMC Boeckeler PowerTome using a Diatome ultra 45° diamond knife. The sections were collected on copper grids for subsequent imaging via scanning transmission electron microscopy.

Measurements. STEM micrographs were taken with a Zeiss Crossbeam 540 FIB-SEM with annular STEM with a detector accelerating voltage of 20 kV and probe current of 300 pA. High-angle annular dark-field was chosen as imaging mode,

owing to its high contrast between atoms with low atomic number Z (membrane: F, C,...) and a high atomic number (Ir, Au, Ti). The chemical composition was determined via EDX (X-Max 150 silicon drift detector, Oxford Instruments; Software: Aztec Version 3.3, Oxford instruments) with an accelerating voltage of 20 kV and a probe current of 300 pA.

STEM micrographs were post-processed with ImageJ. As the samples have an average thickness of 100 nm while the penetrating depth of the electron beam can be several micrometers, EDX analysis contains background elemental information like copper from the TEM-grid. For reasons of simplification, only elements of interest (Pt, Ir, Au, Ti, C, F, and O) are shown in the elemental point measurements.

Data availability

The authors declare that the main data supporting the findings of this study are available within the article and its Supplementary Information. Source data are provided with this paper. Extra data are available from the corresponding authors upon reasonable request. Source data are provided with this paper.

Received: 13 December 2020; Accepted: 9 March 2021;

Published online: 13 April 2021

References

- De Luna, P., et al. What would it take for renewably powered electrosynthesis to displace petrochemical processes? *Science* **364**, eaav3506 (2019).
- Bockris, J. O. A hydrogen economy. *Science* **176**, 1323 (1972).
- Staffell, I. et al. The role of hydrogen and fuel cells in the global energy system. *Energy Environ. Sci.* **12**, 463–491 (2019).
- Ardo, S. et al. Pathways to electrochemical solar-hydrogen technologies. *Energy Environ. Sci.* **11**, 2768–2783 (2018).
- Bareiß, K. et al. Life cycle assessment of hydrogen from proton exchange membrane water electrolysis in future energy systems. *Appl. Energy* **237**, 862–872 (2019).
- Kopernikus P2X Project funded by the German Ministry of Education and Research (BMBF). [<https://www.kopernikus-projekte.de/projekte/p2x>] 2020 [cited 2020 June 19th].
- Stockford, C. et al. H2FC SUPERGEN: An overview of the Hydrogen and Fuel Cell research across the UK. *Int. J. Hydrog. Energy* **40**, 5534–5543 (2015).
- Miller, H. A., et al. Green hydrogen from anion exchange membrane water electrolysis: a review of recent developments in critical materials and operating conditions. *Sustainable Energ. Fuels* <https://doi.org/10.1039/C9SE01240K> (2020).
- Abbasi, R. et al. A Roadmap to Low-Cost Hydrogen with Hydroxide Exchange Membrane Electrolyzers. *Adv. Mater.* **31**, e1805876 (2019).
- Carmo, M. et al. A comprehensive review on PEM water electrolysis. *Int. J. Hydrog. Energy* **38**, 4901–4934 (2013).
- Schmidt, O. et al. Future cost and performance of water electrolysis: An expert elicitation study. *Int. J. Hydrog. Energy* **42**, 30470–30492 (2017).
- Ayers, K. E. et al. Pathways to ultra-low platinum group metal catalyst loading in proton exchange membrane electrolyzers. *Catal. Today* **262**, 121–132 (2016).
- Bernt, M., Siebel, A. & Gasteiger, H. A. Analysis of voltage losses in PEM water electrolyzers with low platinum group metal loadings. *J. Electrochem. Soc.* **165**, F305–F314 (2018).
- Ayers, K. E., L. T. Dalton, and E. B. Anderson. Efficient generation of high energy density fuel from water. **41**, 27 (2012).
- Spoeri, C., et al. Experimental activity descriptors for iridium-based catalysts for the electrochemical oxygen evolution reaction (OER). *ACS Catal.* **10**, 14640–14648 (2020).
- Ledendecker, M., et al. Towards maximized utilization of iridium for the acidic oxygen evolution reaction. *Nano Res.* **12**, 2275–2280 (2019).
- Hufnagel, A. G. et al. Carbon-templated conductive oxide supports for oxygen evolution catalysis. *Nanoscale* **11**, 14285–14293 (2019).
- Böhm, D., et al. Efficient OER catalyst with low Ir volume density obtained by homogeneous deposition of iridium oxide nanoparticles on macroporous antimony-doped tin oxide support. *Adv. Funct. Mater.* **30**, 1906670 (2020).
- Seitz, L. C. et al. A highly active and stable IrOx/SrIrO3 catalyst for the oxygen evolution reaction. *Science* **353**, 1011–1014 (2016).
- Diaz-Morales, O. et al. Iridium-based double perovskites for efficient water oxidation in acid media. *Nat. Commun.* **7**, 12363 (2016).
- Nong, H. N. et al. Oxide-supported IrNiO(x) core-shell particles as efficient, cost-effective, and stable catalysts for electrochemical water splitting. *Angew. Chem. Int. Ed. Engl.* **54**, 2975–2979 (2015).
- Strickler, A. L., et al. Systematic investigation of iridium-based bimetallic thin film catalysts for the oxygen evolution reaction in acidic media. *ACS Appl. Mater. Interfaces* **37**, 34059–34066 (2019).
- Binninger, T. et al. Thermodynamic explanation of the universal correlation between oxygen evolution activity and corrosion of oxide catalysts. *Sci. Rep.* **5**, 12167 (2015).
- Schmidt, T. J. et al. Characterization of high-surface area electrocatalysts using a rotating disk electrode configuration. *J. Electrochem. Soc.* **145**, 2354–2358 (1998).
- Mayrhofer, K. J. J. et al. Measurement of oxygen reduction activities via the rotating disc electrode method: From Pt model surfaces to carbon-supported high surface area catalysts. *Electrochim. Acta* **53**, 3181–3188 (2008).
- Garsany, Y. et al. Experimental methods for quantifying the activity of platinum electrocatalysts for the oxygen reduction reaction. *Anal. Chem.* **82**, 6321–6328 (2010).
- Frydendal, R. et al. Benchmarking the stability of oxygen evolution reaction catalysts: the importance of monitoring mass losses. *ChemElectroChem* **1**, 2075–2081 (2014).
- Geiger, S. et al. The stability number as a metric for electrocatalyst stability benchmarking. *Nat. Catal.* **1**, 508–515 (2018).
- Klemm, S. O. et al. Coupling of a high throughput microelectrochemical cell with online multielemental trace analysis by ICP-MS. *Electrochem. Commun.* **13**, 1533–1535 (2011).
- Li, T. et al. Atomic-scale insights into surface species of electrocatalysts in three dimensions. *Nat. Catal.* **1**, 300–305 (2018).
- Cherevko, S. Stability and dissolution of electrocatalysts: building the bridge between model and “real world” systems. *Curr. Opin. Electrochem.* **8**, 118–125 (2018).
- Alia, S. M. et al. Activity and durability of iridium nanoparticles in the oxygen evolution reaction. *J. Electrochem. Soc.* **163**, F3105–F3112 (2016).
- Alia, S. M. & Anderson, G. C. Iridium oxygen evolution activity and durability baselines in rotating disk electrode half-cells. *J. Electrochem. Soc.* **166**, F282–F294 (2019).
- Kim, Y. T. et al. Balancing activity, stability and conductivity of nanoporous core-shell iridium/iridium oxide oxygen evolution catalysts. *Nat. Commun.* **8**, 1449 (2017).
- Cherevko, S. et al. Oxygen and hydrogen evolution reactions on Ru, RuO2, Ir, and IrO2 thin film electrodes in acidic and alkaline electrolytes: A comparative study on activity and stability. *Catal. Today* **262**, 170–180 (2016).
- Cherevko, S. et al. Oxygen evolution activity and stability of iridium in acidic media. Part 1. - metallic iridium. *J. Electroanal. Chem.* **773**, 69–78 (2016).
- Cherevko, S. et al. Oxygen evolution activity and stability of iridium in acidic media. Part 2. - electrochemically grown hydrous iridium oxide. *J. Electroanal. Chem.* **774**, 102–110 (2016).
- Siracusano, S. et al. New insights into the stability of a high performance nanostructured catalyst for sustainable water electrolysis. *Nano Energy* **40**, 618–632 (2017).
- Babic, U., et al. Understanding the effects of material properties and operating conditions on component aging in polymer electrolyte water electrolyzers. *J. Power Sources* **451**, 227778 (2020).
- Onda, K., et al. Performance analysis of polymer-electrolyte water electrolysis cell at a small-unit test cell and performance prediction of large stacked cell. *J. Electrochem. Soc.* **149**, A1069 (2002).
- Shin, H.-S. & Oh, B. S. Water transport according to temperature and current in PEM water electrolyzer. *Int. J. Hydrog. Energy* **45**, 56–63 (2020).
- Arminio-Ravelo, J. A., et al. Electrolyte effects on the electrocatalytic performance of iridium-based nanoparticles for oxygen evolution in rotating disc electrodes. *Chemphyschem* **20**, 2956–2963 (2020).
- Pham, C. V., et al. IrO2 coated TiO2 core-shell microparticles advance performance of low loading proton exchange membrane water electrolyzers. *Appl. Catal. B: Environ.* **269**, 118762 (2020).
- da Silva, G. C. et al. Dissolution stability: the major challenge in the regenerative fuel cells bifunctional catalysis. *J. Electrochem. Soc.* **165**, F1376–F1384 (2018).
- Silva, G. C. et al. Oxygen evolution reaction on tin oxides supported iridium catalysts: do we need dopants? *ChemElectroChem* **7**, 2330–2339 (2020).
- Rozain, C. et al. Influence of iridium oxide loadings on the performance of PEM water electrolysis cellsart II – advanced oxygen electrodes. *Appl. Catal. B: Environ.* **182**, 123–131 (2016).
- Pickup, P. G. & Birss, V. I. A model for anodic hydrous oxide growth at iridium. *J. Electroanal. Chem. Interf. Electrochem.* **220**, 83–100 (1987).
- Giordano, L. et al. pH dependence of OER activity of oxides: current and future perspectives. *Catal. Today* **262**, 2–10 (2016).
- Lædre, S. et al. Materials for proton exchange membrane water electrolyzer bipolar plates. *Int. J. Hydrog. Energy* **42**, 2713–2723 (2017).
- Hsueh, K.-L., et al. *Direct methanol fuel cells*. Electrochemical Technologies for Energy Storage and Conversion. 701–727 (2012).
- Naito, T., et al. Water electrolysis in saturated phosphate buffer at neutral pH. *ChemSusChem* **13**, 5921–5933 (2020).
- Rakousky, C. et al. The stability challenge on the pathway to high-current-density polymer electrolyte membrane water electrolyzers. *Electrochim. Acta* **278**, 324–331 (2018).

53. Kopp, M. et al. Energiepark Mainz: Technical and economic analysis of the worldwide largest Power-to-Gas plant with PEM electrolysis. *Int. J. Hydrog. Energy* **42**, 13311–13320 (2017).
54. Regmi, Y. N., et al. A low temperature unitized regenerative fuel cell realizing 60% round trip efficiency and 10 000 cycles of durability for energy storage applications. *Energy Environ. Sci.* <https://doi.org/10.1039/D0EE02970J> (2020).
55. Pinaud, B. A. et al. Key Considerations for High Current Fuel Cell Catalyst Testing in an Electrochemical Half-Cell. *J. Electrochem. Soc.* **164**, F321–F327 (2017).
56. Inaba, M. et al. Benchmarking high surface area electrocatalysts in a gas diffusion electrode: measurement of oxygen reduction activities under realistic conditions. *Energy Environ. Sci.* **11**, 988–994 (2018).
57. Ehelebe, K. et al. Evaluating Electrocatalysts at Relevant Currents in a Half-Cell: The Impact of Pt Loading on Oxygen Reduction Reaction. *J. Electrochem. Soc.* **166**, F1259–F1268 (2019).
58. Langemann, M. et al. Validation and characterization of suitable materials for bipolar plates in PEM water electrolysis. *Int. J. Hydrog. Energy* **40**, 11385–11391 (2015).

Acknowledgements

J.K., M.M., M.R., and S.C. acknowledge funding by the German Federal Ministry of Education and Research (BMBF) within the Kopernikus Project P2X under the grant number 03SFK211-2. D.E.-L. and S.C. acknowledge financial support from Deutsche Forschungsgemeinschaft DFG under project number CH 1763/3-1 and 1763/4-1. We thank the chair of Technical Electrochemistry at the Technical University of Munich for providing the MEA preparation equipment. We thank Carina Schramm for electrode preparation.

Author contributions

S.C. conceived and developed the idea and coordinated the work. J.K. and S.C. designed the experiments. J.K. prepared electrodes for aqueous measurements, performed dissolution measurements in aqueous electrolyte, liquid sample analysis, and data analysis. M.M. developed the GR-free MEA setup, prepared MEAs, performed MEA measurements, and data analysis. K.S. performed H-cell measurements. M.B. performed STEM measurements. T.B. performed ultramicrotome thin-film cuts for STEM. The manuscript was written by J.K., M.M., D. E.-L., and S.C. with input and feedback from all authors.

All authors contributed through scientific discussions and have given approval to the final version of the manuscript.

Funding

Open Access funding enabled and organized by Projekt DEAL.

Competing interests

The authors declare no competing interests.

Additional information

Supplementary information The online version contains supplementary material available at <https://doi.org/10.1038/s41467-021-22296-9>.

Correspondence and requests for materials should be addressed to J.K. or S.C.

Peer review information *Nature Communications* thanks the anonymous reviewers for their contributions to the peer review of this work. Peer review reports are available.

Reprints and permission information is available at <http://www.nature.com/reprints>

Publisher's note Springer Nature remains neutral with regard to jurisdictional claims in published maps and institutional affiliations.



Open Access This article is licensed under a Creative Commons Attribution 4.0 International License, which permits use, sharing, adaptation, distribution and reproduction in any medium or format, as long as you give appropriate credit to the original author(s) and the source, provide a link to the Creative Commons license, and indicate if changes were made. The images or other third party material in this article are included in the article's Creative Commons license, unless indicated otherwise in a credit line to the material. If material is not included in the article's Creative Commons license and your intended use is not permitted by statutory regulation or exceeds the permitted use, you will need to obtain permission directly from the copyright holder. To view a copy of this license, visit <http://creativecommons.org/licenses/by/4.0/>.

© The Author(s) 2021

5.5 Durability Testing of Low-Iridium PEM Water Electrolysis Membrane Electrode Assemblies

The article "Durability Testing of Low-Iridium PEM Water Electrolysis Membrane Electrode Assemblies" was submitted in February 2022 and published in June 2022 in the *The Journal of the Electrochemical Society* [120]. The article is under open access, distributed under the terms of the Creative Commons Attribution 4.0 License (CC BY). The permanent web link is: <https://doi.org/10.1149/1945-7111/ac6d14>.

In this study we investigate the durability of PEMWE MEAs with low-iridium loaded anodes compared to MEAs with a commercial benchmark anode catalyst. So far, there is no more active and equally stable material for the catalysis of OER than iridium. However, iridium is one of the scarcest elements on earth, its annual production (mining and recycling) is low at ≈ 7 t/y [61] and presumably can not be increased by several orders of magnitude. Thus, for a future multi-GW per year installation of PEMWE systems, the power specific iridium loading needs to be significantly reduced compared to current state-of-the-art systems. For reference, the current power specific iridium loading is at ≈ 0.75 g_{Ir}/kW_{70%(LHV)} (1.5 A/cm² at 1.79 V [11]) whereas at a projected future annual installation rate of > 100 GW/y, the power specific iridium loading needs to be as low as ≈ 0.01 g_{Ir}/kW_{70%(LHV)} [10] [70]. Besides using thin membranes for loss reduction and for reaching high current densities, the development and use of new or improved OER catalysts which enable low iridium loadings at comparable or better performance than benchmark catalysts is a key factor on reaching the set goal. One possible improvement strategy is a reduction of the iridium packing density from ≈ 2.3 g_{Ir}·cm⁻³ (Benchmark, Umicore Elyst Ir75 0480) to ≈ 0.5 g_{Ir}·cm⁻³ by using a titanium dioxide support of lower surface area. This enables the manufacturing of electrodes with reasonable thickness of ≈ 5 μm at loadings of ≈ 0.25 mg_{Ir}/cm² [121]. This new catalyst, which was developed within the Kopernikus P2X project and provided by the project partner Heraeus GmbH, allows for an 8-fold reduction in iridium loading while keeping similar to slightly better begin-of-life (BOL) performance compared to the Benchmark catalyst [70]. To test the long term durability of the new developed catalyst compared to the benchmark catalyst, 5 MEAs with each type of anode catalyst (P2X catalyst loading: 0.25 mg_{Ir}/cm²; Benchmark catalyst loading: 2 mg_{Ir}/cm²) based on Nafion[®] 117 membranes, are fabricated by the project partner Greenerity GmbH and integrated in an industrial short stack from H-TEC Systems GmbH (see figure 23, panel c)). During 3700 h, a typical operation of a PEMWE system in combination with intermittent renewable energies is simulated by applying a continuous current cycling to the stack between low (0.1 A/cm²), intermediate (1.75 A/cm²) and high current densities (2 A/cm²) with 10 min step holding time. Each week, all 10 cells in the stack are analyzed by polarization curves and electrochemical impedance spectroscopy. Furthermore, selected individual MEAs are analyzed by SEM at begin-of-life and after finishing the test to determine the thickness evolution of the membranes. Finally, the P2X and Benchmark catalysts are analyzed ex-situ by XPS in order to determine the iridium film thickness ratio on the non-conductive TiO₂ support particles of the catalysts. The main findings of the study are:

1. The begin-of-life performance of the new P2X catalyst is slightly better than the Benchmark with a 30-fold higher mass activity at 1.5 V iR-free cell voltage at 8-fold lower iridium loading.
2. A stabilization of the initial higher electrode degradation of both catalysts occurs after about 1000 h. An extrapolation of the catalyst mass activity data to the next logarithm-

mic time decade suggests only a moderate further increase in iR-free cell voltage at a rate of $\approx +1 \mu\text{V}/\text{h}$ for the P2X catalyst and $\approx +0.25 \mu\text{V}/\text{h}$ for the Benchmark catalyst which would be sufficiently low for industrial PEMWE applications with lifetimes in the 10^4 to 10^5 h region.

3. The measured HFR drops significantly during the test by $\approx 25 \%$ at a decreasing rate and shows a trend towards stabilization at the end of the test. The falling HFR seems partly caused by an increased membrane water content (which leads to higher conductivity and swelling of the membrane into the pores of the PTLs which reduces contact resistances and the effective membrane thickness) and partly by a membrane thinning visible at the MEA cross sections analyzed by SEM of $\approx 10 \%$. As the focus of the study was the long-term catalyst performance, the true reasons for the falling HFR need to be clarified in a follow-up study.
4. The mass activity ratio of P2X to benchmark catalyst levels out at $\approx 4-5$ at the end of the test and is thus of the same order of magnitude as the iridium thin film thickness ratio of the catalysts measured by XPS of $\approx 2-3$.

Author Contributions

H.G. proposed the stack test. The test procedure and protocol was developed by M.M., F.A., M.B., J.B., C.E., A.M. and H.G.. H.G. and M.M. coordinated the work. M.M. performed the electrochemical tests. M.K. and M.M. performed physical characterization (SEM and XPS). M.M., M.B., M.E. and M.K. analyzed the experimental data. M.M. wrote the manuscript with input from M.K. for the sections regarding the physical characterization. All authors discussed the results and revised the manuscript.



Durability Testing of Low-Iridium PEM Water Electrolysis Membrane Electrode Assemblies

Maximilian Möckl,^{1,2,z} Matthias F. Ernst,³ Matthias Kornherr,³ Frank Allebrod,⁴ Maximilian Bernt,^{2,3,a} Jan Byrknes,⁵ Christian Eickes,⁵ Christian Gebauer,⁶ Antonina Moskovtseva,⁴ and Hubert A. Gasteiger³

¹Technical University of Munich, School of Engineering and Design, Department of Energy and Process Engineering, Institute for Electrical Energy Storage Technology, 80333 Munich, Germany

²ZAE Bayern, Electrochemical Energy Storage, 85748 Garching, Germany

³Technical University of Munich, Department of Chemistry, Chair of Technical Electrochemistry, 85748 Garching, Germany

⁴H-TEC Systems GmbH, 86167 Augsburg, Germany

⁵Greenerity GmbH, Industriegebiet Süd E11, 63755 Alzenau, Germany

⁶Heraeus Deutschland GmbH & Co. KG, 63450 Hanau, Germany

Lowering the iridium loading at the anode of proton exchange membrane (PEM) water electrolyzers is crucial for the envisaged GW-scale deployment of PEM water electrolysis. Here, the durability of a novel iridium catalyst with a low iridium packing density, allowing for low iridium loadings without decreasing the electrode thickness, is being investigated in a 10-cell PEM water electrolyzer short stack. The anodes of the membrane electrode assemblies (MEAs) of the first five cells utilize a conventional iridium catalyst, at loadings that serve as benchmark for today's industry standard ($2 \text{ mg}_{\text{Ir}} \text{ cm}^{-2}$). The last five cells utilize the novel catalyst at 8-fold lower loadings ($0.25 \text{ mg}_{\text{Ir}} \text{ cm}^{-2}$). The MEAs are based on Nafion[®] 117 and are tested for 3700 h by load cycling between 0.2 and 2.0 A cm^{-2} , with weekly polarization curves and impedance diagnostics. For both catalysts, the performance degradation at low current densities is dominated by an increase of the overpotential for the oxygen evolution reaction (OER), whereby the OER mass activity of the novel catalyst remains ≈ 4 -fold higher after 3700 h. The temporal evolution of the OER mass activities of the two catalysts will be analyzed in order to assess the suitability of the novel catalyst for industrial application.

© 2022 The Author(s). Published on behalf of The Electrochemical Society by IOP Publishing Limited. This is an open access article distributed under the terms of the Creative Commons Attribution 4.0 License (CC BY, <http://creativecommons.org/licenses/by/4.0/>), which permits unrestricted reuse of the work in any medium, provided the original work is properly cited. [DOI: 10.1149/1945-7111/ac6d14]



Manuscript submitted February 17, 2022; revised manuscript received April 19, 2022. Published June 8, 2022. *This paper is part of the JES Focus Issue on Advanced Electrolysis for Renewable Energy Storage.*

A large-scale production of hydrogen by water electrolysis offers the possibility to store large amounts of electrical energy from fluctuating renewable sources. The chemically stored energy can then be transported and used flexibly in terms of time and space. Thus, an extensive defossilization of different sectors (mobility, industry, heat) could be achieved and possible supply gaps could be bridged more easily and cost-efficiently than with electrical storage alone.^{1–3}

Several water electrolysis technologies exist: The three most important are alkaline electrolysis (AEL), PEM (proton exchange membrane) water electrolysis (PEMWE), and solid oxide electrolysis (SOE). The AEL is a long established technology that has been implemented on the MW scale, with demonstrated electrolyzer lifetimes of ca. 100,000 h.⁴ Similar lifetimes have been achieved for PEMWE, which is already available on an industrial scale as well, but needs further development, especially with regard to mass production.⁴ On the other hand, the SOE technology is not yet commercialized on the MW scale and its lifetime is at least one order of magnitude lower compared to AEL and PEMWE,⁴ so that the latter two will likely be the most prominent technologies in the near future. However, PEMWE has several advantages: Hydrogen can be produced at elevated pressure (30 to 40 bar) with a highly dynamic power range directly from purified water, whereby the H₂ quality remains high even at higher pressures, and only few and simple purification steps are necessary to reach high purity.⁵ In addition, the current density at rated full-power is at $\approx 2 \text{ A cm}^{-2}$ for commercial PEMWEs and thus about four-fold higher than that of AELs ($\approx 0.5 \text{ A cm}^{-2}$), a difference which will very likely increase further in the future.⁴

In order to achieve a significant impact of renewable hydrogen, very large production capacities have to be installed in the coming decades. Bernt et al.⁶ estimated the necessary electrolysis power installation for a full defossilization of the mobility sector (i.e., a complete replacement of fossil transportation fuels) until the end of the 21st century to be in the range of $\approx 150 \text{ GW/year}$. Although most of the materials for the PEMWE are available in sufficient quantities even for such large scale-up rates, the resource constraints of the platinum group metals that are required for the PEMWE catalysts are very critical. At the cathode, typically platinum on a carbon support (at current loadings of ≈ 0.5 – $1.0 \text{ mg}_{\text{Pt}} \text{ cm}^{-2}$) is used to catalyze the hydrogen evolution reaction (HER), whereas at the anode iridium based catalysts (at current loadings of $\approx 2 \text{ mg}_{\text{Ir}} \text{ cm}^{-2}$) are used for the oxygen evolution reaction (OER).⁷ However, the currently high platinum loadings at the cathode are less of a concern, as they can be reduced by an order of magnitude without any performance losses, due to the fast kinetics of the HER in the acidic PEMWE environment.^{6,8–10} In contrast, the OER kinetics at the anode are very slow, so that any lowering of the iridium catalyst loading leads to decreasing efficiencies at the same current density, in the best case amounting to an additional kinetic overpotential at the anode of $\approx 50 \text{ mV}$ for a 10-fold reduction in iridium loading.^{6,11,12} In practice, with current iridium catalysts, the anode loadings cannot be reduced to below $\approx 0.5 \text{ mg}_{\text{Ir}} \text{ cm}^{-2}$, as this results in anode catalyst layers that are too thin to achieve a homogenous electrical contacting of the electrode. Lower loadings would require catalysts with a much reduced iridium packing density (in terms of $\text{g}_{\text{Ir}} \text{ cm}^{-3}$ electrode);^{6,11} these are difficult to achieve, since there are no electrically conductive support materials that are stable at the high anodic potentials of the PEMWE anode. Since there is currently no equally stable and active alternative for iridium as anode catalyst for a PEMWE,^{8,13,14} a strong increase in PEMWE deployment could lead to a shortage of iridium. According to a platinum group metal (PGM) market report,¹⁵ the iridium demand in 2018 was $\approx 6.8 \text{ t}$, reasonably consistent with the estimated iridium supply of $\approx 8.4 \text{ t}$ in

^aPresent address: Freudenberg FST GmbH, Bayerwaldstr. 3, 81737 München, Germany.

^zE-mail: maximilian.moeckl@zae-bayern.de

2018 (based on the South African production of ≈ 6.8 t and the South African share of the world-wide iridium production of $\approx 81\%$).¹⁶ For an electrolyzer efficiency of 70% referenced to the lower heating value (LHV; corresponding to a cell voltage of 1.79 V), current commercial PEMWEs yield a current density of ≈ 1.5 A cm⁻² and have an anode catalyst loading of ≈ 2 mg_{Ir} cm⁻², resulting in an iridium-specific power density of ≈ 0.75 g_{Ir}/kW. Thus, with the currently installed PEMWE technology, only ≈ 10 GW of newly installed PEMWE power per year would already require ≈ 7.5 t of iridium per year, which would essentially consume the entire world-wide iridium supply, and thus would not allow for the large-scale deployment of PEMWEs at the above mentioned rate required to defossilize the transport sector.

To overcome this obstacle, recent studies suggest the need for a substantial reduction of the anode iridium loading to at least 0.25–0.4 mg_{Ir} cm⁻²,^{8,17} or, more precisely, to loadings that are low enough to reach iridium-specific power densities of ≈ 0.01 g_{Ir}/kW at 70%_{LHV} that are estimated to be necessary for a large-scale PEMWE deployment.⁶ One option to reduce the iridium-specific power density at a given iridium loading is to reduce the non-kinetic performance losses of a PEMWE, so that higher current densities and thus higher power densities could be obtained at the same cell voltage and efficiency. By far the largest share of non-kinetic losses is currently caused by ohmic resistances due to proton conduction across the relatively thick membranes (≈ 180 μ m for Nafion[®] 117).¹⁸ If thinner membranes are used, a substantial fraction of these losses can be eliminated. Laboratory experiments with thinner membranes (conducted with conventional catalysts loadings and at 80 °C) reached current densities at an efficiency of 70%_{LHV} ranging from ≈ 3.3 A cm⁻² (90 μ m Aquivion[®] C98-09S)¹⁹ to 4.0 A cm⁻² (50 μ m Nafion[®] 212²⁰) all the way up to ≈ 4.8 A cm⁻² (30 μ m Nafion[®] XL²¹); this may be compared to ≈ 1.7 A cm⁻² for a ≈ 180 μ m thick Nafion[®] 117 membrane under the same conditions.^{12,18} Thus, reducing membrane thickness can result in an up to ≈ 3 -fold increase in current density at the same cell voltage/efficiency, corresponding to a ≈ 3 -fold increase in power density. However, when using thin membranes, the increasing product gas crossover must be taken into account. From a safety perspective, the hydrogen crossover from the cathode to the anode side is particularly important. The use of thin membranes can severely limit the minimum current density where the system can be operated safely without countermeasures.^{18,22,23} Possible mitigation strategies for excessive hydrogen crossover include the incorporation of chemical recombination catalysts into the membrane electrode assembly (MEA),^{24–27} or the integration of recombination catalysts either at some point in the O₂ outlet stream at the anode side of the electrolyzer or at the back side of the anode porous transport layer (PTL).²⁸

Based on the above discussion, simply using thinner membranes can increase the power density by ≈ 3 -fold, so that with a conventional iridium loading of 2 mg_{Ir} cm⁻², iridium-specific power densities of ≈ 0.25 g_{Ir}/kW at 70%_{LHV} should be reachable. As a matter of fact, this was demonstrated for an MEA based on a 50 μ m Nafion[®] 212 membrane with an anode iridium loading of ≈ 1.6 mg_{Ir} cm⁻² and a cathode platinum loading of ≈ 0.30 mg_{Pt} cm⁻², operated at 80 °C and ambient pressure.⁶ A further lowering of the iridium-specific power density, however, requires a reduction of the anode iridium loading. As shown in references⁶ and,²⁹ current commercial OER catalysts that are based on a thick, electrically conductive IrO₂ coating applied on a non-conductive TiO₂ support (for example Umicore Elyst Ir75 0480, further on referred to as 'Benchmark catalyst') are limited by the insufficient in-plane electrical conductivity and the inhomogeneity of the thin electrode layers that result at low iridium loadings of approximately < 0.5 mg_{Ir} cm⁻². This could be remedied by an electrically conductive support material on which the active iridium particles are finely dispersed, in analogy to the carbon supported platinum catalysts (Pt/C) that are used at the cathode (e.g., the thickness of an only ≈ 0.03 mg_{Pt} cm⁻² cathode electrode based on a ≈ 5 wt% Pt/C catalyst is ≈ 11 μ m).⁶ Possible candidates are

antimony-doped tin oxide (ATO),^{30,31} niobium-doped titanium oxide (NTO),^{32,33} or tungsten doped titanium oxide.³⁴ Nevertheless, the long-term stability of these support materials in the acidic environment of a PEMWE is still under investigation. Another approach toward low loadings is the use of iridium thin-films which can be coated directly on highly structured membranes³⁵ or on nano structures (e.g., whiskers) on the membrane surface.³⁶

Within the framework of the Kopernikus P2X project,³⁷ the partners Greenerity GmbH, Heraeus Deutschland GmbH & Co. KG and Technical University of Munich (TUM) investigated a catalyst concept that would allow for low iridium loadings without decreasing the electrode thickness, i.e. a concept that would offer a reduced iridium packing density in the electrode. It is based on utilizing a non-conductive TiO₂ support material coated with a thin layer of an amorphous, hydrous iridium oxide (a-IrO(OH)_x), as shown by Tovini et al. for the Benchmark catalyst,³⁸ but utilizing a low specific surface area TiO₂ support.³⁹ With this approach, a substantial reduction of the iridium packing density from ≈ 2.3 g_{Ir} cm⁻³ for the Benchmark catalyst to ≈ 0.5 g_{Ir} cm⁻³ for the newly designed catalyst is possible (further on referred to as "P2X" catalyst),³⁹ which now enables the preparation of sufficiently thick electrodes of, e.g., ≈ 5 μ m at iridium loadings of 0.25 mg_{Ir} cm⁻² (with the Benchmark catalyst, this loading would result in an electrode thickness of only ≈ 1 μ m, too thin for a well-performing electrode⁶). In addition to enabling thicker electrodes at low iridium loadings, this new P2X catalyst was shown to enable a ≈ 8 -fold reduction in iridium loading at even a ≈ 50 mV better begin-of-life (BOL) performance compared to the Benchmark catalyst.³⁹ Part of this better performance can be attributed to the higher intrinsic activity for the oxygen evolution reaction (OER) of the a-IrO(OH)_x coating of the P2X catalyst compared to the more crystalline and thus less OER active IrO₂ of the Benchmark catalyst.^{40,41} However, a platinum-coated PTL is required for the P2X catalyst, owing to the lower intrinsic conductivity of a-IrO(OH)_x compared to crystalline IrO₂.^{39,42} In combination with a 50 μ m thick Nafion[®] 212 membrane, the performance of MEAs with the P2X catalyst at a loading of 0.27 mg_{Ir} cm⁻² is projected to yield a current density of ≈ 4 A cm⁻² at 1.79 V (i.e., at an efficiency of 70%_{LHV}) when operated at 80 °C and ambient pressure,³⁹ which would correspond to an iridium-specific power density of ≈ 0.04 g_{Ir}/kW, within a factor of 4 of the above stated long-term target (in comparison, the projected value for the Benchmark catalyst under the same conditions is ≈ 0.4 g_{Ir}/kW³⁹).

Apart from the initial performance of a new catalyst, however, its long-term stability is another important factor for its use in actual applications. PEMWE systems should have a long service life, so that the at the moment still high investment costs of 1000 to 1400 \$/kW (with near-future projected costs for large scale production of ≈ 400 \$/kW⁴³) are as low as possible when translated into operating time, whereby commercial PEMWEs already have a lifetime of $\approx 100,000$ h.⁴ However, testing a new catalyst over such a long period is difficult to implement in practice, especially in the early stages of catalyst development. Yet, as will be shown, even shorter operating times of several thousand hours can provide a robust initial indication of catalyst durability, which is done most efficiently in a short stack configuration. Therefore, 5 MEAs each with the Benchmark and the P2X catalyst were tested at 60 °C and ambient pressure in a 10-cell PEMWE short stack with an active area of 30 cm² over a period of 3700 h, cycling the current density between 0.2, 1.0, and 2.0 A cm⁻². Every week, full polarization curves were recorded, together with acquiring the high frequency resistance (HFR) of each cell. This allowed to determine the cell voltage degradation rate as well as the iR-free cell voltage degradation rate as a function of current density. Furthermore, a Tafel analysis of the iR-free cell voltages at low current densities allowed for a quantification of the OER mass activity vs. time for the two different catalysts, providing further insights into the relative stability of the new P2X catalyst compared to the commercial Benchmark catalyst. Finally, the observed evolution of the HFR over time will be discussed.

Experimental

Membrane electrode assemblies (MEAs) and test stack.—30 cm² active area MEAs based on Nafion[®] 117 membranes were prepared by Greenerity GmbH according to the specifications of the used stack type ELS-30 with 10 cells from H-TEC Systems GmbH. A commercial carbon-supported platinum catalyst was used for the cathode electrodes with a loading of 0.3 mg_{Pt} cm⁻² for the HER. Two different catalysts were used on the anode side as described by Bernt et al.³⁹: i) a commercial Benchmark catalyst consisting of mostly crystalline IrO₂ deposited as thick film on a high surface area TiO₂ support (75wt% iridium; Elyst Ir75 0480 from Umicore, Germany); ii) the newly developed P2X catalyst based on hydrous iridium oxide deposited as thin film on a lower surface area TiO₂ support (49.2wt% iridium from Heraeus, Germany; note that the wt % iridium for this catalyst batch is slightly higher than that reported in reference³⁹). The Benchmark catalyst was applied at a loading of 2.0 mg_{Ir} cm⁻², resulting in an anode electrode thickness of ≈7.4 μm, while the P2X catalyst was applied at a loading of 0.25 mg_{Ir} cm⁻², resulting in an anode electrode thickness of ≈3.5 μm. The MEAs were assembled in a 10-cell short stack by H-TEC Systems in two groups. The first five cells contained the MEAs with the Benchmark catalyst and the last five cells the MEAs with the P2X catalyst. Platinized titanium PTLs were used on the anode side to prevent progressive passivation of the titanium in contact with the electrode and to ensure a low contact resistance.^{39,44} All 11 individual bipolar/monopolar plate potentials are accessible from the outside by fine pins, which allow monitoring of the individual cell voltages and of individual impedance spectra. The stack has a water inlet and water/O₂ outlet at the anode side and a single H₂/water outlet at the cathode side. Thus, water feed and flow field purging is possible at the anode side of the stack only. Although the outflowing water at the cathode side could in principle be tested for dissolved iridium species by ICP-MS as shown, e.g. by Knoeppel et al.,⁴⁵ the measurements however would be biased by the contact of the water to non-noble metal surfaces in the stack which would lead to galvanic redeposition of iridium species.⁴⁵

Short stack test station and operation.—A fully automated test station from Horiba-Fuelcon was used for conducting the short stack test. It is equipped with an impedance meter (True-Data-EIS from Sensotech, Germany) in combination with a multiplexer. This allows sequential impedance measurements to be made at any DC current within the range of the electrical power source on all 10 cells in the stack without changing the connections during the test. Furthermore, all individual cell potentials were recorded simultaneously during the whole test.

The temperature of the stack was controlled via the anode water circuit, whereby the water temperature at the inlet of the stack was kept at 60 °C. Higher operating temperatures around 80 °C would in principle be beneficial for an accelerated stress test, but the temperature in this study was limited to 60 °C based on the recommendation by the stack manufacturer. In order to achieve a relatively uniform temperature distribution in the stack and to avoid excessive in-plane temperature differences across the flow fields (with a maximum temperature difference between inlet and outlet of ≈5 K at 2.0 A cm⁻²), the water flow rate was set to 3.3 ml/(min cm²).²¹ To ensure continuously high water quality, only highly purified make-up water was used (water processed by ULTRA CLEAR[®] TP ultrapure water system from Evoqua, USA). Additionally, a two stage cleanup system was installed in the anode water recirculation loop, comprising a larger deionization vessel (5 L resin volume) behind the main feed water pump and a second smaller cartridge (250 ml resin volume) close to the stack, both filled with mixed bed resin (Leycopure from Leyco, Germany). The second cartridge and all further tubing and fittings on the remaining water path to the stack were made from plastics (SAN, PP or PTFE) to prevent metal ion leaching into the feed water, and thus possible ionic contamination of the MEAs.^{46,47}

X-ray photoelectron spectroscopy.—To investigate the near-surface chemical state and composition of the P2X and the Benchmark catalyst, X-ray photoelectron spectroscopy (XPS) was performed using an Axis Supra System (Kratos, UK). XPS spectra were recorded with a monochromatic Al K α source (1486.6 eV) at a pass energy of 40 eV, using a step size of 0.05 eV and a dwell time of 1000 ms. XPS samples were prepared by finely dispersing the catalyst powders in a mixture of 2-propanol (purity ≥ 99.8%, from Sigma Aldrich, Germany) and ultrapure water (Milli-Q[®] IQ 7005 water purification system from Merck, Germany), and then drop-casting the resulting ink on a non-conductive Gylon[®] substrate (type 3545, from Garlock, USA). Infrared radiation was used to evaporate the solvent. Before insertion into the ultra-high vacuum chamber for analysis, the samples were dried at 50 °C under vacuum overnight. The samples were analyzed without sputter cleaning, and the C 1s line of adventitious carbon at 284.6 eV was used to correct the binding energies of all recorded spectra. Data treatment was carried out using the program CasaXPS with application of a Shirley background.

MEA cross sections and scanning electron microscopy.—Cross Sections from a pristine Benchmark and P2X MEA sample as well as a Benchmark and a P2X MEA harvested after the durability test from the short stack were investigated via scanning electron microscopy (SEM). For this, small snippets cut from the active area of the MEAs were sandwiched between copper tape and polished with a cryo cross Section polisher (IB-19520CCP from JEOL, Japan) at -80 °C and at an acceleration voltage of 6 kV, followed by a fine-mode step at 4 kV. Afterwards, the cross Sections were examined with a scanning electron microscope (JSM-IT200 from JEOL, Japan) in order to evaluate the membrane thicknesses at BOL and EOT.

Electrochemical measurement procedures and test sequences.—The stack test was started by a warm-up phase of several hours without applying a current and with water circulation only in order to reach a steady water inlet temperature of 60 °C and to heat up the stack. The water inlet temperature was kept constant, and cathode and anode side were kept at ambient pressure during the whole durability test. After a subsequent conditioning for 20 min at 0.1 A cm⁻², the first galvanostatically controlled BOL polarization curves for all 10 cells of the short stack were recorded, stepwise changing the current from 33 mA cm⁻² to 2.2 A cm⁻² (11 steps) and allowing for an equilibration time of 10 min at each current density. At 0.2, 1.0, and 2.0 A cm⁻², galvanostatically controlled AC impedance spectra for each cell were recorded at 15 frequencies, ranging from 15 kHz to 150 mHz. The perturbation current amplitude was 0.5 A (≡0.017 A cm⁻²) at 0.2 A cm⁻², and 5.0 A (≡0.17 A cm⁻²) at 1.0 A cm⁻² and 2.0 A cm⁻² in order to maintain a linear system response at a reasonable signal to noise ratio. The high frequency resistance (HFR) for each cell in the stack was obtained at a fixed frequency of 6.9 kHz, which consistently represents the first measuring point after the real axis intercept in the Nyquist plot.

After BOL characterization, the stack was subjected to a durability protocol that consisted of repeatedly cycling the current density between three levels for 10 minutes each, namely 0.1, 1.75, and 2.0 A cm⁻². This protocol emulates an intermittent operation without any shut-down phases, i.e., avoiding periods at open-circuit-voltage (OCV) in order to prevent catalyst dissolution by repeated reduction/oxidation events.⁴⁸ After each 7 day period of continuous current cycling (i.e., after every 168 h or after every set of 336 current cycles), another set of polarization curves and impedance spectra was recorded according to the above mentioned scheme. This procedure was continued over ≈3700 h.

At several points during the ≈3700 h durability test, certain events that are not part of the above durability test sequence (system maintenance, external errors by auxiliary equipment, etc.; see Table 1) forced a short shut-down of the test station. The first

Table I. List of events that required a temporary shut-down of the test station during the ≈ 3700 h durability test. The right-hand column shows the time during the durability test at which a given event occurred.

Event type	Occurrence (h)
exhaust line blocked	350
water supply system maintenance	1180, 2380, 3220
critical software updates	1270, 1370, 2040, 3530
maintenance of security relevant system components	3050

polarization curve directly after such an event was always recorded, but was not used in the regression analysis of the degradation rate and of the OER mass activity evolution, due to the observed transient performance increase after each of the shut-down and start-up cycles. This is caused by a change in the catalyst surface properties of the iridium of the OER catalyst (reduction to hydrous iridium oxide during the OCV period upon shut-down, and re-oxidation to iridium oxide after start-up), which was shown to temporarily affect its OER activity.⁴⁸ However, all of these thus biased performance data are depicted as red symbols in the presented performance/OER mass activity versus time plots (Figs. 3, 4, 6 and 7).

Results and Discussion

XPS based estimation of the relative iridium utilization of the catalysts.—X-ray photoelectron spectroscopy (XPS) measurements were carried out to estimate the ratio of the active (hydrous) iridium oxide film thickness on the TiO₂ support between the P2X and the Benchmark catalyst.

Considering that only the outermost surface of the (hydrous) iridium oxide film is catalytically active for the OER, and assuming a (hydrous) iridium oxide film thickness (t_{film}) of more than a few monolayers, the ratio of t_{film} of the Benchmark catalyst over that of the P2X catalyst ($t_{\text{film}}(\text{Benchmark})/t_{\text{film}}(\text{P2X})$) would correspond to the ratio of the iridium utilization (u_{Ir}) of the P2X catalyst over that of the Benchmark catalyst ($u_{\text{Ir}}(\text{P2X})/u_{\text{Ir}}(\text{Benchmark})$). On the basis of the known iridium content of the catalysts, of the specific surface areas of the TiO₂ supports (estimated to be $\approx 100 \text{ m}^2 \text{ g}^{-1}$ for the Benchmark catalyst and $\approx 50 \text{ m}^2 \text{ g}^{-1}$ for the P2X catalyst), and assuming the deposition of a homogeneous (hydrous) iridium oxide film, Bernt et al. estimated that $t_{\text{film}}(\text{Benchmark})/t_{\text{film}}(\text{P2X}) \approx 6 \text{ nm}/2 \text{ nm} \approx 3.0/1$,³⁹ which in turn suggests that the iridium utilization of the P2X catalyst should be ≈ 3 -fold higher for the P2X catalyst (i.e., $u_{\text{Ir}}(\text{P2X})/u_{\text{Ir}}(\text{Benchmark}) \approx 3.0/1$). In this case, if the surface-normalized, so-called specific OER activity of the two catalysts were to be the same, the P2X catalyst would be expected to have a ≈ 3 -fold higher mass activity for the oxygen evolution reaction (OER). However, since the specific OER activity of hydrous iridium oxide (as is the case for the P2X catalyst) is ≈ 10 -fold higher than that of iridium oxide (as is the case for the Benchmark catalyst),^{40,41} the beginning-of-life OER mass activity of the P2X catalyst should be ≈ 30 -fold higher than that of the Benchmark catalyst, which is in reasonably good agreement with the experimentally observed ≈ 37 -fold higher OER mass activity.³⁹

Alternatively to the approach taken by Bernt et al.,³⁹ the relative thickness of the (hydrous) iridium oxide films between the Benchmark and the P2X catalyst can also be estimated by the following XPS analysis of the Ir 4p_{3/2} and the Ti 2p intensities (here taken as the sum of Ti 2p_{1/2} and Ti 2p_{3/2}) of the (hydrous) iridium oxide film and the TiO₂ support, respectively. Qualitatively, it is obvious already from the XPS data shown in Fig. 1, that the ratio of the Ir 4p_{3/2} over the Ti 2p intensities (i.e., of the areas under the two spectral features) is much smaller for the P2X compared to the Benchmark catalyst, indicating a substantially thinner (hydrous) iridium oxide film thickness.

In order to quantify this observed difference, the following considerations and approximations are taken: (i) both XPS features

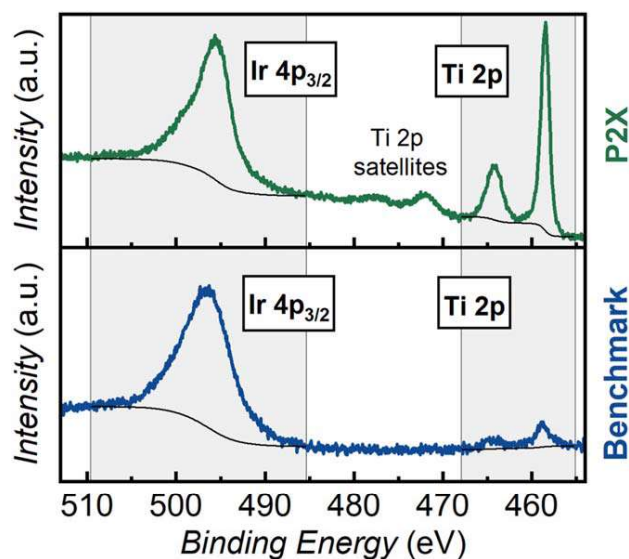


Figure 1. X-ray photoelectron spectra of the P2X (green line) and of the Benchmark (blue line) catalyst samples. Ir 4p_{3/2} signals of the (hydrous) iridium oxide films and Ti 2p signals of the TiO₂ supports are recorded with a step size of 0.05 eV. The thin black line represents the Shirley background that was subtracted to obtain the peak areas given in Table II.

occur in a rather narrow binding energy range (≈ 455 – 505 eV), so that the kinetic energy of the photoelectrons is also very similar (≈ 982 – 1032 eV); (ii) for such a narrow kinetic energy range, the inelastic mean free path (λ) of the Ir 4p_{3/2} and the Ti 2p photoelectrons is essentially identical (≈ 3.0 nm based on Shea and Dench;⁴⁹) (iii) for essentially identical λ values, the instrumental sensitivity factor ratio of the Ir 4p_{3/2} and the Ti 2p features corresponds to the ratio of their Scofield cross-sections; (iv) the radius of the TiO₂ particles is at least 2-fold larger than λ (for the estimated $100 \text{ m}^2 \text{ g}^{-1}$ BET TiO₂ support of the Benchmark catalyst, $r_{\text{TiO}_2} \approx 7 \text{ nm}$;³⁹) and, v) the (hydrous) iridium oxide film homogeneously covers the TiO₂ support. For a hypothetical planar geometry, the (hydrous) iridium oxide film thickness (t_{film}) on the TiO₂ support could then be calculated based on the following equation (equation (1) in reference,⁵⁰ corrected, however, for the wrong sign in the original publication):

$$t_{\text{film}} = \lambda \cdot \cos(\theta) \cdot \ln \left(1 + \frac{(I_{\text{Ir } 4p_{3/2}})/(S_{\text{Ir } 4p_{3/2}})}{(I_{\text{Ti } 2p})/(S_{\text{Ti } 2p})} \right) \quad [1]$$

Here, $I_{\text{Ir } 4p_{3/2}}$ and $I_{\text{Ti } 2p}$ are the experimentally measured peak intensities for a given catalyst, $S_{\text{Ir } 4p_{3/2}}$ and $S_{\text{Ti } 2p}$ are the Scofield cross-sections,⁵¹ and θ is the angle between the surface normal of a planar sample and the photoelectron analyzer (for a planar sample, $\theta = 0^\circ$ in the XPS system used here). For the non-planar samples used here, θ is not anymore constant, but assuming that the size and the morphology of the Benchmark and the P2X catalyst are similar, the spatial variation of θ should also be similar, so that the ratio of

t_{film} of the Benchmark catalyst over that of the P2X catalyst can be estimated as:

$$t_{\text{film (Benchmark)}}/t_{\text{film (P2X)}} \approx \frac{\ln\left(1 + \frac{(I_{\text{Ir } 4p_{3/2}}/s_{\text{Ir } 4p_{3/2}})}{(I_{\text{Ti } 2p}/s_{\text{Ti } 2p})}\right)_{\text{Benchmark}}}{\ln\left(1 + \frac{(I_{\text{Ir } 4p_{3/2}}/s_{\text{Ir } 4p_{3/2}})}{(I_{\text{Ti } 2p}/s_{\text{Ti } 2p})}\right)_{\text{P2X}}} \quad [2]$$

Based on the data tabulated in Table II, this yields a (hydrous) iridium film thickness ratio of $t_{\text{film (Benchmark)}}/t_{\text{film (P2X)}} \approx 2.1/1$. This is clearly smaller than the film thickness ratio of ≈ 3 that was estimated by Bernt et al.³⁹ by assuming that the BET surface area of the TiO₂ support of the Benchmark catalyst would be $\approx 100 \text{ m}^2 \text{ g}^{-1}$. While the latter assumption is reasonable, the actual TiO₂ BET cannot be determined, but if the true value were $\approx 67 \text{ m}^2 \text{ g}^{-1}$, the iridium utilization ratio obtained via the BET-based estimate and via our XPS analysis would be identical. Owing to the uncertainty in the TiO₂ BET estimate, we consider the XPS-based iridium utilization ratio of ≈ 2.1 to be the more reliable value.

MEA performance and long-term performance degradation.—

For a first overview of the performance of the new P2X anode catalyst compared to the Benchmark anode catalyst over the course of the long-term performance test, Fig. 2 shows a comparison of the averaged polarization curves for both MEA types at beginning-of-life (BOL; squares), after 890 h (circles) as well as at the end-of-test (EOT) after 3700 h (triangles). Figures 2a and b show the polarization curves and the HFR values at 60 °C and ambient pressure, averaged over the five MEAs with the Benchmark anode catalyst at a loading of $2.0 \text{ mg}_{\text{Ir}} \text{ cm}^{-2}$ (error bars represent the standard deviation), while Figs. 2c and d show the analogous data for the P2X catalyst at a loading of $0.25 \text{ mg}_{\text{Ir}} \text{ cm}^{-2}$. The solid lines in Figs. 2a and c represent the measured cell voltages (E_{cell}) and the dashed lines the iR-free cell voltage ($E_{\text{iR-free}}$), corresponding to E_{cell} corrected by the HFR ($E_{\text{iR-free}} = E_{\text{cell}} - i \cdot \text{HFR}$). The HFR values were obtained from the electrical impedance spectra recorded at three current densities (0.2, 1.0, and 2.0 A cm^{-2}) and were used for the iR-correction of several current densities, as marked by the gray shaded areas in Fig. 2.

A first inspection of the data in Figs. 2a and c reveals the good reproducibility of the cell voltage performance of each set of five MEAs, expressed by the small error bars: The maximum variation occurs at the highest current density of 2.2 A cm^{-2} , with less than $\pm 22 \text{ mV}$ at BOL and less than $\pm 16 \text{ mV}$ at EOT. A closer look at the BOL polarization curves (squares) reveals a $\approx 20 \text{ mV}$ lower cell voltage (solid lines) and iR-free cell voltage (dashed lines) of the P2X catalyst MEAs compared to the Benchmark catalyst MEAs over the whole current density range, with the HFR values of both MEA types being identical ($\approx 185 \text{ m}\Omega \text{ cm}^2$). Thus, the higher initial performance of the P2X catalyst at an 8-fold lower iridium loading, as reported by Bernt et al.¹¹ for 5 cm^2 active area single-cell measurements, can also be observed for the measurements in a 30 cm^2 active area 10-cell short stack shown here. Calculating the iridium-specific power density at a cell voltage efficiency of 70%_{LHV} ($\equiv 1.79 \text{ V}$), the P2X catalyst MEAs reach a value of $0.11 \text{ g}_{\text{Ir}}/\text{kW}$, which is ≈ 10 -fold lower than the $1.0 \text{ g}_{\text{Ir}}/\text{kW}$ obtained for the Benchmark MEAs.

Looking at the temporal evolution of the iR-free cell voltage (dashed lines in Figs. 2a and c), which allows for a closer inspection of the evolution of the anode catalyst activity, two aspects stand out: first, for both catalyst types, the iR-free cell voltage performance and thus the catalyst activity decreases (visible by the up-shift of the iR-free polarization curves) and second, this performance decay is clearly most pronounced during the first 890 h (circles) compared to the following 2810 h until EOT. Over the first 890 h, the Benchmark catalyst MEAs show an average $E_{\text{iR-free}}$ increase at 1 A cm^{-2} of $\approx 50 \text{ mV}$, whereas the average $E_{\text{iR-free}}$ of the P2X catalyst MEAs is slightly higher, amounting to $\approx 70 \text{ mV}$. In contrast, for the following 2810 h there is no change visible for the Benchmark catalyst MEAs and a less than $\approx 15 \text{ mV}$ increase for the P2X catalyst MEAs. In fact, the iR-free EOT performance of both MEA types is approximately the same, with the iR-free cell voltage of the P2X catalyst MEAs at 2.2 A cm^{-2} being only $\approx 12 \text{ mV}$ higher than that of the Benchmark catalyst MEAs, even though the former have an 8-fold lower iridium loading.

When again considering the non-corrected cell voltages (solid lines in Figs. 2a and c), a further effect becomes apparent for both MEA types. The slope of the E_{cell} vs. current density curves at current densities greater than 0.5 A cm^{-2} clearly decreases with time, which is caused by a decreasing HFR, as shown in Figs. 2b and d. The overall HFR decrease over the 3700 h of testing is $\approx 25\%$ on average, but slightly more pronounced for the Benchmark catalyst MEAs (from 186 to $134 \text{ m}\Omega \text{ cm}^2$) than for the P2X catalyst MEAs (from 184 to $145 \text{ m}\Omega \text{ cm}^2$). This leads to the phenomenon that at high current densities, the HFR drop for the Benchmark MEAs is strong enough to overcompensate the catalyst activity decay, resulting in a slightly higher current density of 1.18 A cm^{-2} at EOT at the 70%_{LHV} efficiency benchmark (i.e., at 1.79 V) compared to BOL, whereas the current density of the P2X catalyst MEAs at the same voltage decreases slightly to 1.04 A cm^{-2} at EOT. When evaluating the iridium-specific power densities at 70%_{LHV} for the two MEA types at EOT, there still remains a ≈ 7 -fold advantage of the P2X compared to the Benchmark catalyst MEAs ($0.13 \text{ g}_{\text{Ir}}/\text{kW}$ for the former and $0.95 \text{ g}_{\text{Ir}}/\text{kW}$, respectively). At the highest current density of 2.2 A cm^{-2} , also the P2X catalyst MEAs show slightly higher EOT performance compared to BOL, due to the HFR decrease outweighing the catalyst activity decay.

To better quantify the above observations and to gain more insights into the MEA performance degradation mechanisms, we will next discuss the degradation rates at different current densities. Due to the weekly recording of polarization curves and impedance spectra, a closer look at the MEA performance degradation is possible. Figure 3 shows the temporal evolution of the mean cell voltages (E_{cell}) for both the Benchmark catalyst MEAs (Figs. 3a) and the P2X catalyst MEAs (Fig. 3b) at three current densities, corresponding to the low, mid, and high power density regime (0.2 A cm^{-2} (squares), 1.0 A cm^{-2} (circles), and 2.0 A cm^{-2} (triangles)). As mentioned before, all red marked symbols represent biased polarization curves due to preceding shut-down events (listed in Table I). Looking at the evolution of E_{cell} over time reveals two clearly distinguishable time-dependent phenomena at 0.2 and 1.0 A cm^{-2} : in the time period from BOL up to $\approx 1000 \text{ h}$, the cell voltage shows an initially rather fast increase that gradually levels off, whereas in the subsequent time period, from $\approx 1000 \text{ h}$ onwards,

Table II. Summary of the analysis of the Ti 2p (sum of Ti 2p_{1/2} + Ti 2p_{3/2}) and of the Ir 4p_{3/2} XPS features obtained for the P2X and the Benchmark catalyst. The Shirley background corrected areal intensities ($I_{\text{Ti } 2p}$ and $I_{\text{Ir } 4p_{3/2}}$) are determined from Fig. 1 and the Scofield cross-sections ($s_{\text{Ti } 2p}$ and $s_{\text{Ir } 4p_{3/2}}$) are taken from reference 51.

Catalyst	XPS features	Areal Intensity I	Scofield cross-section s
P2X	Ti 2p _{1/2} + Ti 2p _{3/2}	2776	7.91
	Ir 4p _{3/2}	5747	5.59
Benchmark	Ti 2p _{1/2} + Ti 2p _{3/2}	616	7.91
	Ir 4p _{3/2}	7592	5.59

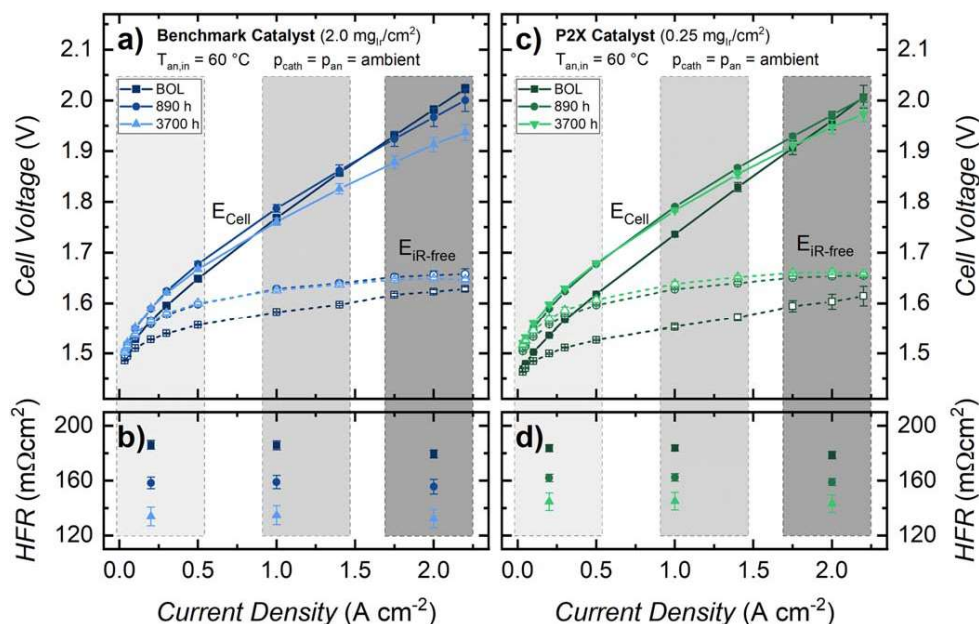


Figure 2. Averaged polarization curves of 30 cm² active area Nafion[®] 117 based MEAs (from 5 MEAs each, with error bars representing the standard deviation) at BOL (squares) as well as after 890 h (circles) and 3700 h (triangles) of the load cycling durability test (switched every 10 min between 0.1, 1.75, and 2.0 A cm⁻²), recorded with a 10-cell short stack at ambient pressure and 60 °C anode water inlet temperature (3.3 ml_{H₂O}/(min cm²)): (a) of the MEAs with the Benchmark anode catalyst at a loading of 2.0 mg_{Ir} cm⁻²; (c) of the MEAs with the P2X anode catalyst at a loading of 0.25 mg_{Ir} cm⁻². The same Pt/C based cathode catalyst is used for both MEA types at a loading of 0.3 mg_{Pt} cm⁻². The solid lines show the measured cell voltages (E_{cell}), while the dashed lines represent the iR-free cell voltage corrected by the HFR ($E_{\text{iR-free}}$). b) & d) Averaged HFR values and standard deviation for the two sets of MEAs, determined from impedance measurements for all cells at three different current densities (0.2, 1.0, and 2.0 A cm⁻²). The iR-correction is done by using the same HFR value for several current densities, as marked by the gray shaded areas in the figure.

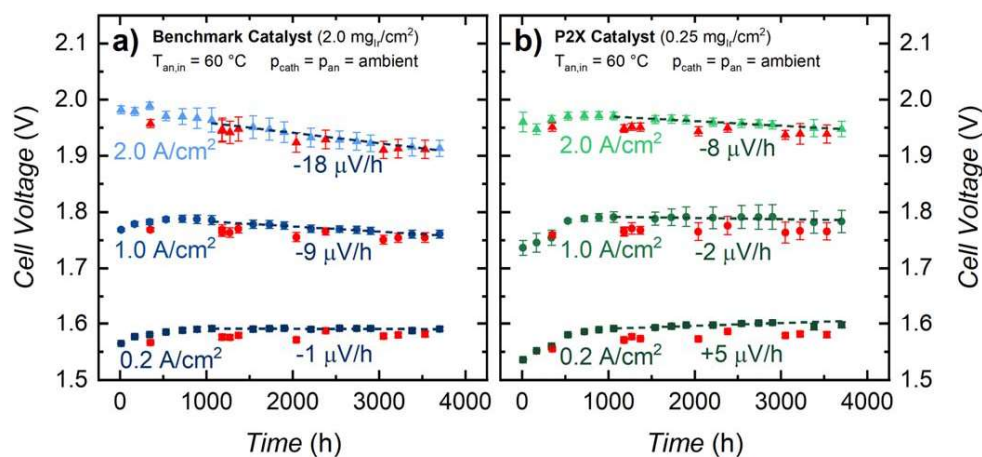


Figure 3. Temporal evolution of the mean cell voltage during prolonged load cycling (switched every 10 min between 0.1, 1.75, and 2.0 A cm⁻²) of a 10-cell short stack at 60 °C anode water inlet temperature and ambient pressure: a) average and standard deviation of E_{cell} of the five Benchmark catalyst MEAs (2.0 mg_{Ir} cm⁻²); b) average and standard deviation of E_{cell} of the five P2X catalyst MEAs (0.25 mg_{Ir} cm⁻²). The E_{cell} values are taken from weekly performed polarization curves at the current densities of 0.2 A cm⁻² (squares), 1.0 A cm⁻² (circles), and 2.0 A cm⁻² (triangles). The average cell voltage degradation rates are evaluated between 1000 h and 3700 h for each current density by means of a linear regression fit (dashed black lines). All red marked symbols show values from polarization curves which were recorded directly after a shut-down event of the test station, and thus are excluded from the regression analysis (a complete list of shut-down events is given in Table 1).

the evolution of E_{cell} with time is rather linear. The increase of E_{cell} during the first ≈ 1000 h is more prominent for the P2X catalyst than for the Benchmark catalyst, consistent with the results shown in Figs. 2a and c (i.e., comparing the performance at BOL and after 890 h). From ≈ 1000 h onwards, the cell voltages remain almost constant at the low current density of 0.2 A cm⁻² (reflected in low rates of voltage change of -1 and $+5$ $\mu\text{V/h}$ for the Benchmark and the P2X catalyst MEAs, respectively), and even show a clearly decreasing trend at the high current density of 2.0 A cm⁻² (with -18

and -8 $\mu\text{V/h}$ for the Benchmark and the P2X catalyst MEAs, respectively), which can be attributed to the decrease of the HFR with time (see 2b and (d)) that positively affects the cell voltage. Overall, the degradation rates evaluated between 1000 and 3700 h are consistently lower (or more negative) for the Benchmark catalyst MEAs compared to the P2X catalyst MEAs.

Comparing our data with long-term test results from other groups reveals a similar behavior, with a stabilization of the cell voltage at around 1000 h, following an initial phase with higher degradation

rates. Siracusano et al.⁵² report an initial degradation rate of $\approx 90 \mu\text{V/h}$ during a 1000 h steady-state test at a rather high current density of 3.0 A cm^{-2} , which attenuated to $33 \mu\text{V/h}$ during the last 300 h, and they attribute this rather slow stabilization to mass transfer resistances or to a change of the oxidation state of the anode catalyst surface. However, their MEAs feature an IrRuOx catalyst at the anode side and are based on thinner, $90 \mu\text{m}$ Aquivion® membranes, which renders a quantitative comparison with our data in Fig. 3 difficult. Also Danilovic et al.⁵³ show averaged cell voltage data for a long-term electrolysis test (60,000 h) of two different industrial stack design evolution levels, whereby the cell voltage change rates are highest during the first 1000 h. However, there are also results in the literature where such an initial increase or nonlinear change is not immediately visible. In a publication by Rakousky et al.,⁴⁴ the cell voltage evolution is shown during galvanostatic operation at 2.0 A cm^{-2} for 400 h, using a platinumized anode PTL. The cell voltage remains at a stable level while the HFR shows a gradual decrease of the ohmic cell resistance by $\approx 10\%$, which the authors attribute to a reduced contact resistance between the PTLs and the electrodes, caused by a gradual membrane creep into the pores of the PTLs. Since the change in ohmic resistances (e. g., contact resistances and membrane resistances) over the course of a durability test can mask the effect of catalyst degradation on the cell voltage evolution, a better understanding on the long-term stability of different catalysts can be obtained by analyzing the iR-free cell voltage evolution.

Using the cell voltages and the HFR values from the regularly performed polarization curves and impedance measurements, a closer look at the electrode aging can be taken by evaluating the temporal evolution of the iR-free cell voltage. Figures 4a and b thus show the mean iR-free cell voltage for the Benchmark and the P2X catalyst MEAs, respectively, determined at three current densities (0.2, 1.0, and 2.0 A cm^{-2}). Again, measurement points that were recorded directly after shut-down events of the test station are marked in red and are not used for the analysis. For both MEA types, the electrode aging is most pronounced during the first 1000 h. The average performance decay in this initial time period at the three different current densities ranges between $\approx 30\text{-}50 \text{ mV}$ for the Benchmark catalyst MEAs, while it is somewhat larger for the P2X catalyst MEAs ($\approx 60\text{-}80 \text{ mV}$). Interestingly, however, the iR-free cell voltages at the three different current densities are essentially identical after 1000 h, which is due to the initially $\approx 25\text{-}30 \text{ mV}$ superior performance of the P2X catalyst MEAs (despite its 8-fold lower iridium loading), owing to the substantially

higher intrinsic OER activity of the P2X catalyst compared to the Benchmark catalyst.

Following the stabilization of the iR-free cell voltages after the first 1000 h, both MEA types show only single-digit $\mu\text{V/h}$ changes of the iR-free voltage, when determined by a linear regression analysis between 1000 h and the EOT at 3700 h. At 0.2 A cm^{-2} , the mean iR-free cell voltage of the Benchmark catalyst MEAs is increasing at a rate of $+1 \mu\text{V/h}$, whereas that of the P2X catalyst MEAs shows a clearly higher increase of $+6 \mu\text{V/h}$, pointing toward a faster decay of the OER activity of the P2X catalyst compared to the Benchmark catalyst. At the higher current densities of 1.0 and 2.0 A cm^{-2} , the degradation rates should in principle be equal or higher (i.e., more positive), since any possible mass transport related resistances in the electrodes would be expected to become more prominent at higher current densities. Surprisingly, however, the $\mu\text{V/h}$ changes of the iR-free cell voltage at 2.0 A cm^{-2} are lower, namely $-1 \mu\text{V/h}$ for the Benchmark catalyst MEAs (i.e., $2 \mu\text{V/h}$ lower than at 0.2 A cm^{-2}) and $+1 \mu\text{V/h}$ for the P2X catalyst MEAs (i.e., $5 \mu\text{V/h}$ lower than at 0.2 A cm^{-2}). This, we believe, must be due to small errors in the quantification of the absolute values of the HFR, as is illustrated by the following analysis: Assuming that the degradation rates of the iR-free cell voltage of the P2X catalyst MEAs at 2.0 A cm^{-2} were to be at least the same as that at 0.2 A cm^{-2} (i.e., $+6 \mu\text{V/h}$), its iR-free cell voltage at 2.0 A cm^{-2} and 3700 h would have to be at least $\approx 14 \text{ mV}$ higher (from $\Delta 5 \mu\text{V/h} \cdot 2700 \text{ h} \approx \Delta 14 \text{ mV}$), which would be obtained if the HFR measured at 3700 h were to be $\approx 7 \text{ m}\Omega \text{ cm}^2$ higher (from $7 \text{ m}\Omega \text{ cm}^2 \cdot 2.0 \text{ A cm}^{-2} \approx 14 \text{ mV}$), which amounts to a difference of only $\approx 5\%$ of the measured HFR between 870-3700 h ($\approx 160\text{-}145 \text{ m}\Omega \text{ cm}^2$, see Fig. 2(c)). As this corresponds to the expected accuracy of our HFR measurements, one must conclude that the iR-free cell voltage change rates at 2.0 A cm^{-2} cannot be determined reliably to better than approximately $\pm 5 \mu\text{V/h}$. On the other hand, for the analysis of current densities of 0.2 A cm^{-2} or below, the absolute error in determining the iR-free cell voltage is an order of magnitude lower and, in addition, it can be assumed that any mass transport effects are also negligible at such low current densities, so that an analysis at 0.2 A cm^{-2} or below should allow for a rather accurate quantification of any changes of the OER catalyst activity over time. Therefore, we will next examine the OER mass activity evolution of the two types of anode catalyst by conducting a Tafel analysis in the low current density region.

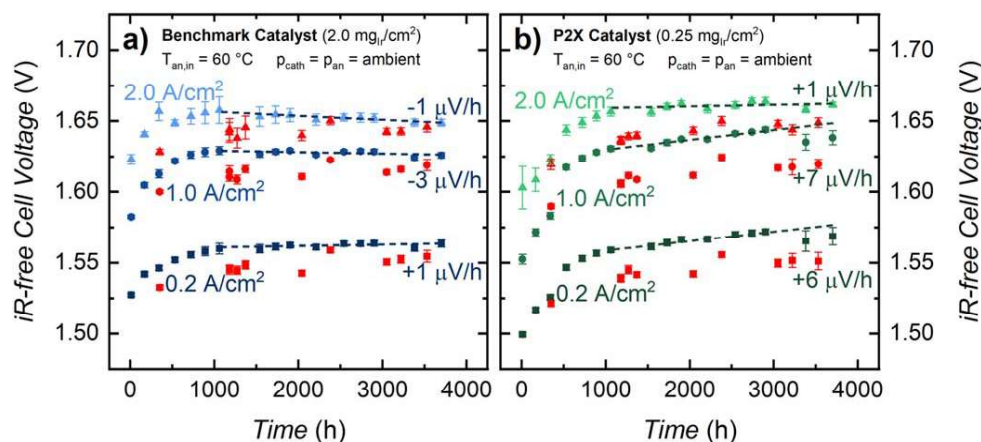


Figure 4. Temporal evolution of the mean iR-free cell voltage during prolonged load cycling (switched every 10 min between 0.1, 1.75, and 2.0 A cm^{-2}) of a 10-cell short stack at $60 \text{ }^\circ\text{C}$ anode water inlet temperature and ambient pressure: (a) average and standard deviation of $E_{\text{iR-free}}$ of the five benchmark catalyst MEAs (2.0 mgIr cm^{-2}); (b) average and standard deviation of $E_{\text{iR-free}}$ of the five P2X catalyst MEAs ($0.25 \text{ mgIr cm}^{-2}$). The $E_{\text{iR-free}}$ values are taken from weekly performed polarization curves and impedance measurements at the current densities of 0.2 A cm^{-2} (squares), 1.0 A cm^{-2} (circles), and 2.0 A cm^{-2} (triangles). The average iR-free cell voltage degradation rates are evaluated between 1000 h and 3700 h for each current density by means of a linear regression fit (dashed black lines). All red marked symbols show values from polarization curves which were recorded directly after a shut-down event of the test station, and thus are excluded from the regression analysis (a complete list of shut-down events is given in Table I).

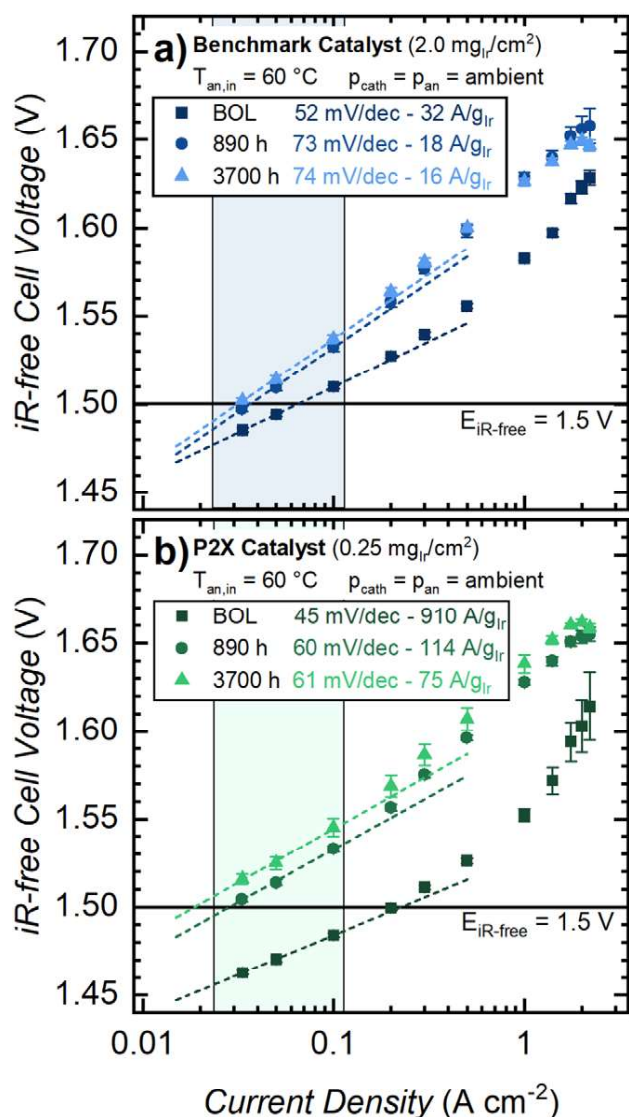


Figure 5. Tafel plot of the iR -free cell voltage vs. the logarithm of the current density for the two different MEA types at BOL (squares) as well as after 890 h (circles) and 3700 h (triangles) of the load cycling durability test, recorded at ambient pressure and $60\ ^\circ C$ anode side water inlet temperature (same data as the dashed lines in Figs. 2a and c): (a) of the Benchmark anode catalyst (at $2.0\ mg_{Ir}\ cm^{-2}$); (b) of the P2X anode catalyst (at $0.25\ mg_{Ir}\ cm^{-2}$). A linear regression fit between 33 and $100\ mA\ cm^{-2}$ is used to obtain the Tafel slopes (dashed lines). Additionally, the OER mass activities of the catalysts at $E_{iR-free} = 1.5\ V$ are determined by the value of the respective fitted Tafel line at $E_{iR-free} = 1.5\ V$. OER mass activity values at $E_{iR-free} = 1.5\ V$ and Tafel slopes are given in the legend inside the figure.

OER mass activity evolution of the benchmark and the P2X catalyst.—To gain better insight into the change of the OER kinetics of both catalysts, Figs. 5a and b show the averaged Tafel plots (i.e., $E_{iR-free}$ vs. the logarithm of the current density) at ambient pressure and at $60\ ^\circ C$ anode water inlet temperature of the five Benchmark and the five P2X catalyst MEAs, respectively, recorded at BOL (squares) as well as after 890 h (circles) and 3700 h (triangles) of the durability test (same data as shown by the dashed lines in Figs. 2a and c). A linear regression fit of the data between 33 and $100\ mA\ cm^{-2}$ is used to obtain the Tafel slopes (dashed lines in Fig. 5). Considering the negligible overpotential for the hydrogen evolution reaction (HER) at the here used cathode loadings of $0.3\ mg_{Pt}\ cm^{-2}$ ($\eta_{HER} \ll 5\ mV$ at $1\ A\ cm^{-2}$)²⁶ and the expected

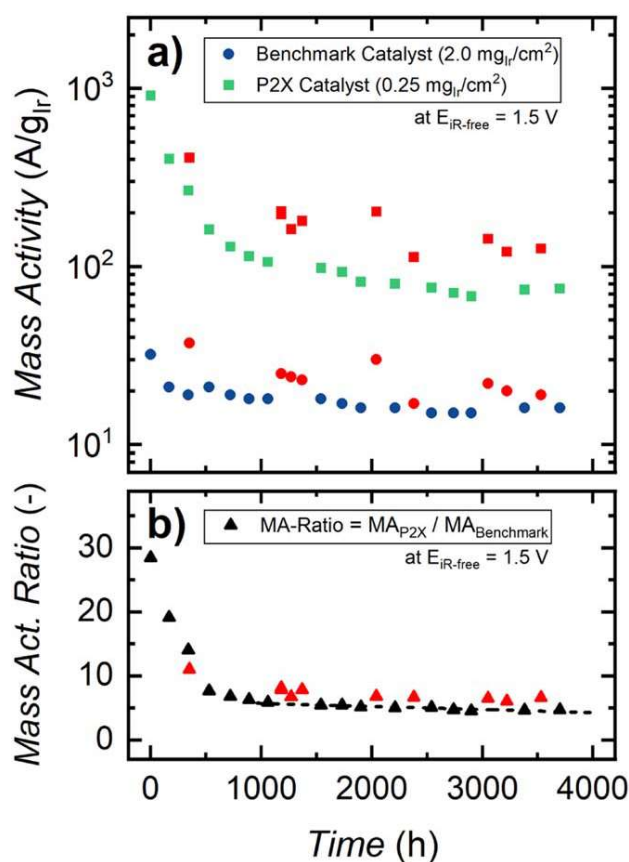


Figure 6. a) Temporal evolution of mean OER mass activity at $1.5\ V$ iR -free cell voltage (ambient pressure, $60\ ^\circ C$ anode water inlet temperature) for the Benchmark catalyst MEAs (circles, $2.0\ mg_{Ir}\ cm^{-2}$) and for the P2X catalyst MEAs (squares, $0.25\ mg_{Ir}\ cm^{-2}$). b) Temporal evolution of the OER mass activity ratio between the P2X catalyst and the Benchmark catalyst MEAs. All red marked symbols show values from polarization curves, which were recorded directly after a shut-down event of the test station (for a complete list of shut-down events see Table 1).

negligible mass transport resistances at low current densities, the fitted Tafel lines should very closely represent the OER activity of the two catalysts. Consequently, the OER mass activities of the catalysts at an iR -free cell voltage of $1.5\ V$ are determined from current density values of the fitted Tafel lines at $E_{iR-free} = 1.5\ V$, normalized by the anode catalyst loading.

In line with the results presented in the previous figures, two major findings stand out: At first, the P2X catalyst exhibits a ≈ 30 -fold higher initial mass activity at $E_{iR-free} = 1.5\ V$ of $910\ A/g_{Ir}$ compared to $32\ A/g_{Ir}$ for the Benchmark catalyst (see legends in Figs. 5a and b). This is due to the fact that the former consists mostly of the more OER active hydrous iridium oxide, while the latter consists of less OER active iridium oxide³⁹ (note that the pristine Benchmark catalyst was shown to consist of a $\approx 50/50$ mixture of crystalline and amorphous IrO_2 .³⁸) The higher OER mass activity of the P2X catalyst is also reflected in its rather low initial Tafel slope of $45\ mV/dec$ (see legends in Figs. 5a and b) that is typical for hydrous iridium oxide based OER catalysts³⁹, while the higher Tafel slope of $52\ mV/dec$ obtained for the Benchmark catalyst is typical for iridium oxide based OER catalysts.^{6,48} Second, both catalysts show a decline in OER mass activity and an increase in Tafel slope over the course of the prolonged cycling test. The OER mass activity decline is clearly more pronounced for the P2X catalyst than for the Benchmark catalyst, with the P2X catalyst's OER mass activity decreasing by a factor of ≈ 12 to $75\ A/g_{Ir}$ after 3700 h, in contrast to only a factor of ≈ 2 in case of the Benchmark catalyst, namely to

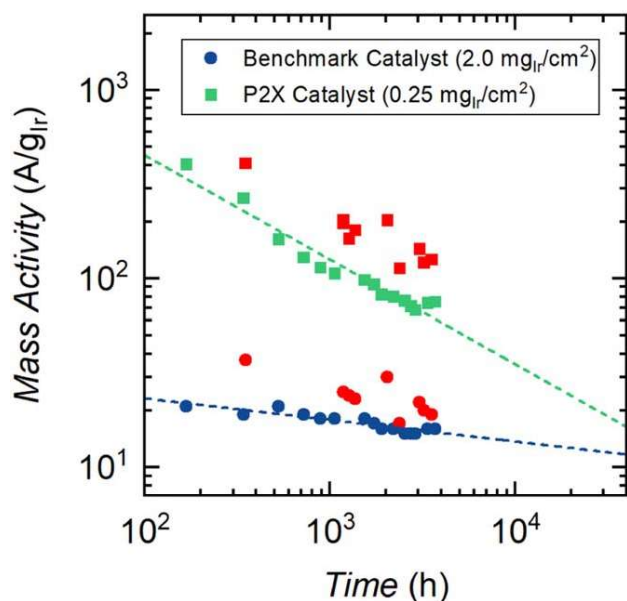


Figure 7. Double logarithmic plot of the mean OER mass activities at 1.5 V iR -free cell voltage (recorded at ambient pressure, 60 °C anode water inlet temperature; same data as in Fig. 6) for the Benchmark catalyst MEAs (blue circles, 2.0 $\text{mg}_{\text{Ir}} \text{cm}^{-2}$) and for the P2X catalyst MEAs (green squares, 0.25 $\text{mg}_{\text{Ir}} \text{cm}^{-2}$). The dashed lines are linear regression fits of the logarithm of the OER mass activities ($i_m^{*(1.5V)}$, in units of A/g_{Ir}) versus the logarithm of time (t , in units of h): $\log(i_m^{*(1.5V)}) = (-0.114 \pm 0.015) \cdot \log(t) + (1.593 \pm 0.046)$ for the Benchmark catalyst MEAs and $\log(i_m^{*(1.5V)}) = (-0.553 \pm 0.037) \cdot \log(t) + (3.760 \pm 0.117)$ for the P2X catalyst MEAs (excluding the data taken directly after a shut-down, marked in red).

16 A/g_{Ir} after 3700 h. At the same time, the Tafel slope of the P2X catalyst increases from 45 to 61 mV/dec , suggesting a gradual transformation of the hydrous iridium oxide into iridium oxide³⁹. An increase in Tafel slope is also observed for the Benchmark catalyst, namely from 52 to 72 mV/dec , which may be indicative of the gradual transformation of the initially partially amorphous iridium oxide into predominantly crystalline iridium oxide over extended times at high anodic potentials.^{54,55}

In order to obtain a better resolution of the time evolution of the OER mass activities, the weekly recorded polarization curves were also subjected to the same type of Tafel analysis. The results are shown in Fig. 6, whereby the red marked symbols represent the measurements that directly followed a system shut-down event (as mentioned above, the OER activity of the anode catalysts increases after system shut-downs during which the anode got exposed to crossover hydrogen, an effect that had been discussed previously⁴⁸). Figure 6a shows the temporal evolution of the OER mass activity for the P2X catalyst (squares) and the Benchmark catalyst (circles), while Fig. 6b shows the evolution of the ratio of the OER mass activities of the P2X catalyst over that of the Benchmark catalyst.

As expected based on the literature,^{40,41} the P2X catalyst based on hydrous iridium oxide is significantly more active at BOL than the Benchmark catalyst (≈ 30 -fold, as shown in Fig. 6b) that is based on a mixture of amorphous and crystalline iridium oxide³⁸. The temporal evolution of the OER mass activity reflects the above observed relatively fast rise in cell voltage and iR -free cell voltage over the first 1000 h (see Figs. 3 and 4, respectively), with both catalysts showing a relatively fast initial drop in the OER mass activity over the first 1000 h (see Fig. 6a), whereby the OER activity of the P2X catalyst drops much more rapidly, so that its OER mass activity benefit over the Benchmark catalyst shrinks to ≈ 6 -fold after 1000 h (see Fig. 6b). This initially fast decay, however, is followed by a rather slow decrease over the remaining 2700 h until EOT, at

which point the OER mass activity benefit of the P2X catalyst seems to stabilize at a factor of ≈ 4 . Considering that the OER activity is highest for hydrous iridium oxide and lowest for crystalline iridium oxide,⁴⁰ we believe that the rather fast OER mass activity decay of the P2X catalyst in the first 1000 h observed here is due to a gradual conversion of the hydrous iridium oxide phase at the high anode potential during electrolysis to an amorphous iridium oxide phase, which over longer times becomes more crystalline.^{54,55} On the other hand, the Benchmark catalyst that starts out with a roughly 50/50 mixture of amorphous and crystalline iridium oxide,³⁸ experiences a much slower OER activity decay, presumably due to an intrinsically slower conversion of amorphous to crystalline iridium oxide. Over much longer times than the 3700 h examined here, we would thus expect that the intrinsic OER activities of the two catalysts should become identical, which in terms of OER mass activity would imply that the P2X catalyst should retain a long-term OER mass activity benefit over the Benchmark catalyst by a factor that corresponds to the iridium utilization ratio, namely ≈ 2.1 (see Section 3.1).

Zero-order estimate of the longer-term catalyst-specific degradation rates.—While it would be desirable to test the performance of the P2X anode catalyst and to compare it to the performance of the Benchmark catalyst over much longer times, this is unfortunately not practical. However, in the following we will attempt to project the decay of the catalytic activity of the two catalysts on the basis of the OER mass activity data shown in Fig. 6. As described above, the OER mass activity at a low iR -free cell voltage (here 1.5 V) is a good quantitative descriptor for catalyst performance, since it is determined at very low current densities (i.e., between 33–100 mA cm^{-2} , see Fig. 5), where other voltage losses (e.g., due to mass transport resistances) and correction errors (e.g., due to imperfect HFR correction) have only minimal influence. Therefore, we need to emphasize that the thus projected voltage losses are only those that can be ascribed to OER mass activity losses and that possible additional voltage losses due to other aging mechanisms are not included (e.g., buildup of interfacial contact resistances, changes in mass transport resistances, membrane/ionomer degradation, etc.).

In order to project the catalyst mass activity losses over time, its functional dependence on time would have to be known. As the latter is not directly evident in Fig. 6, we have replotted the OER mass activity data from Fig. 6 in terms of the logarithm of the mass activity versus the logarithm of time in Fig. 7. Here, the data at BOL (nominally after 1 hour) are excluded, because the stack had been preconditioned at the manufacturer's site over the course of several tens of hours at different operating conditions, so that the mass activity values directly at the start of our experiment (BOL) do not represent the initial state of the catalyst. For the mass activities obtained from the second polarization curve after ≈ 200 h (first point shown in Fig. 7) and for any later measurements, however, this uncertainty in time is negligible. Surprisingly, the logarithm of the mass activity versus the logarithm of time follows a perfectly linear relationship for both catalysts between ≈ 200 –3700 h, marked by the dashed linear regression lines in Fig. 7 (note that the red data points that represent data taken directly after a shut-down event were excluded from the fit). While the fundamental mechanistic reason for this empirically observed relationship is unclear, it does hold over about 1.3 decades in time, so that it should serve as a reasonable zero-order estimate for projecting the drop in mass activity over another decade of time, i.e., from the end-of-test at ≈ 3700 h to $\approx 40,000$ h. The measured values for the OER mass activity at an iR -free cell voltage of 1.5 V after 3700 h ($i_m^{*(1.5V)}(3700 \text{ h})$) are 15.3 A/g_{Ir} for the Benchmark catalyst and 61 A/g_{Ir} for the P2X catalyst, whereas the extrapolated values for $i_m^{*(1.5V)}(40,000 \text{ h})$ are $11.7 \pm 0.4 \text{ A/g}_{\text{Ir}}$ for the Benchmark catalyst and $16.4 \pm 1.5 \text{ A/g}_{\text{Ir}}$ for the P2X catalyst (marked by the dashed lines in Fig. 7; the fitting Eqs. are given in the Fig. caption; the uncertainties of the extrapolated mass activities are calculated by using the standard errors of the slopes of the fits which are ± 0.015 for the Benchmark catalyst and ± 0.037 for the P2X

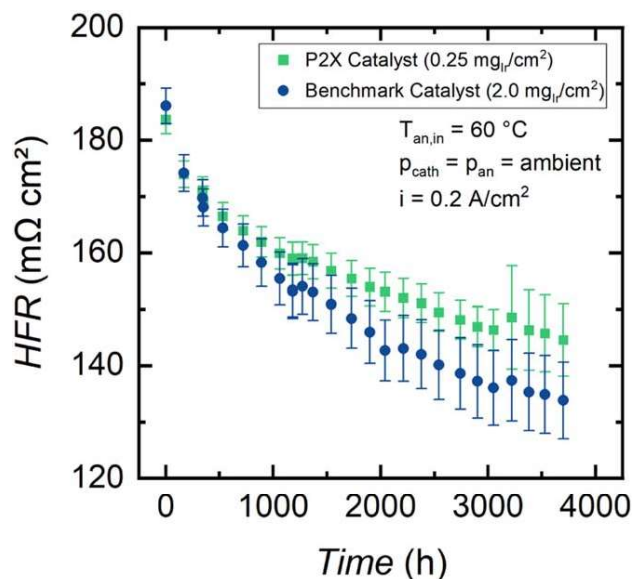


Figure 8. Temporal evolution of the HFR acquired at 0.2 A cm^{-2} and averaged for each type of MEA, namely for the five Benchmark catalyst MEAs (blue dots) and for the five P2X MEAs (green squares), with the error bars corresponding to the standard deviation for each MEA type. The data were acquired during prolonged load cycling test (switched every 10 min between 0.1 A cm^{-2} , 1.75 A cm^{-2} and 2.0 A cm^{-2}) at $60 \text{ }^\circ\text{C}$ anode water inlet temperature and ambient pressure.

catalyst, in such a way, that a minimum-maximum corridor for the extrapolation from 3700 h onwards is set). These extrapolated values including the propagated uncertainties would give a mass activity ratio of about 1.4 ± 0.1 at 40,000 h. While this is somewhat less than the ratio of 2.1 that we estimated as the final ratio by our XPS-based analysis of the iridium film thickness ratio (Section 3.1), it is nevertheless reasonably close considering that the estimate involves an extrapolation over an order of magnitude in time.

Assuming that this projection of the time dependence of the OER mass activity is valid, one can then estimate the kinetic voltage loss that is solely due to the OER mass activity loss. For this, we assume that the OER kinetics are described by simple Tafel kinetics (as suggested by Fig. 5), that the overpotential for the HER is negligible,⁶ and that the ohmic losses due to membrane and contact resistances are properly accounted for by the HFR. In this case, the iR-free cell voltage ($E_{\text{iR-free}}$) in the absence of other mass-transport related losses can be described by the following equation that is a modification of the equation that was derived by Neyerlin et al. for the iR-free cell voltage in PEM fuel cells (see equation (11) in reference⁵⁶):

$$E_{\text{iR-free}} = 1.5 \text{ V} + \frac{2.303 \cdot R \cdot T}{\alpha_a \cdot F} \cdot \log \left(\frac{i + i_x}{L_{\text{Ir,el}} \cdot i_m^{*(1.5\text{V})} \cdot 10^{-3} \cdot f(p_{\text{O}_2}, p_{\text{H}_2}) \cdot f(T)} \right) \quad [3]$$

Here, 1.5 V represents the iR-free cell voltage at which the OER mass activity ($i_m^{*(1.5\text{V})}$, in units of A/gIr) is specified, α_a denotes the anodic transfer coefficient, and the prefactor $\frac{2.303 \cdot R \cdot T}{\alpha_a \cdot F}$ before the logarithm term is the Tafel slope TS in (mV/dec). Within the logarithm, i denotes the current density and i_x the current density lost by gas crossover (both in units of A cm^{-2}), $L_{\text{Ir,el}}$ is the OER catalyst loading (in units of mgIr cm^{-2}), 10^{-3} is a unit conversion factor, and the last two factors, $f(p_{\text{O}_2}, p_{\text{H}_2})$ and $f(T)$, are gas partial pressure and cell temperature dependent terms (for details, see Eq. 11 in reference⁵⁶). Based on the projected loss in OER mass activity

between end-of-test (3700 h) and 40,000 h (see Fig. 7 and above discussion), one can use Eq. 3 to project the kinetic voltage loss that is solely due to the OER mass activity loss, assuming that the Tafel slope does not change significantly over that time (a reasonable assumption based on the negligible change of the Tafel slope between 890 and 3700 h, see Fig. 5), thus using the Tafel slope values determined at 3700 h (given in Fig. 5) as an estimate:

$$\Delta E_{\text{iR-free}} (3700 \text{ h} \rightarrow 40,000 \text{ h}) = TS_{3700 \text{ h}} \cdot \log \left(\frac{i_m^{*(1.5\text{V})} (3700 \text{ h})}{i_m^{*(1.5\text{V})} (40,000 \text{ h})} \right) \quad [4]$$

Inserting the above extrapolated mass activity values into Eq. (4), the iR-free voltage of the Benchmark catalyst MEAs would be projected to increase by 9 mV between 3700 and 40,000 h, equating to a projected average degradation rate of $\approx +0.25 \mu\text{V/h}$ between 3700 and 40,000 h. In contrast, an increase of 35 mV between 3700 and 40,000 h (or $\approx +1.0 \mu\text{V/h}$) would be projected for the P2X catalyst. An interesting corollary of Eq. 4 can be drawn for the case when the performance loss of a PEMWE is governed by a loss in OER mass activity that follows the behavior shown here (i.e., $\log(i_m^{*(1.5\text{V})}) \propto \log(t)$), the expected loss in iR-free cell voltage of the PEMWE would be proportional to the logarithm of time (i.e., $E_{\text{iR-free}} \propto \log(t)$).

For the projected degradation rates (albeit with a high degree of uncertainty), the new P2X catalyst seems to be a promising approach to significantly lower the iridium-specific power density over time scales that are relevant for industrial electrolysis applications. There is, however, a note of caution with regards to the above lifetime extrapolation for the $\text{IrO}_2/\text{TiO}_2$ core-shell type catalysts used here. This has to do with the fact that a loss of iridium by dissolution would not be expected to affect the OER mass activity of the catalysts until the IrO_2 shell would be depleted to an extent that the IrO_2 coverage of the TiO_2 core would become incomplete. At that point, the OER mass activity decrease would be expected to accelerate, which we did not observe during our 3700 h test. For the Benchmark catalyst, the thickness of the IrO_2 shell was estimated to ≈ 10 monolayers,³⁸ so that one might expect this effect to become visible after an iridium loss of on the order of $\approx 80\%$ (assuming that an average of two monolayers would still form a complete shell); for the P2X catalyst with an IrO_2 shell thickness of ≈ 5 monolayers based on our XPS analysis, this effect might become visible after an iridium loss of on the order of $\approx 60\%$. Unfortunately, we did not perform any measurements to determine whether there might be a significant loss of iridium from the anode electrode, which would limit the validity of our lifetime estimation of the catalyst. For follow-up studies, we therefore will use extended diagnostic methods to quantify a possible loss of iridium from the anodes during operation.

Finally, we should mention again that this zero-order estimate of the long-term catalyst-specific degradation rates cannot be used for a complete MEA or even cell/stack lifetime estimation, as several other degradation mechanisms may occur (ionomer, membrane, interfacial contact resistances, etc.), which we did not investigate in this study.

Analysis of the HFR decrease over time.—Finally, we want to take a closer look at the decrease of the HFR that is observed over the course of the short stack durability test. Figure 8 shows the averaged HFR values acquired at 0.2 A cm^{-2} of the five individual cells during the complete 3700 h test period for both the Benchmark (blue dots) and the P2X MEAs (green squares). Both MEA types show a similar behavior: After a rather fast decrease of the HFR from its initial value of $\approx 185 \text{ m}\Omega \text{ cm}^2$ to $\approx 165 \text{ m}\Omega \text{ cm}^2$ after 500 h, the HFR continues to decrease more gradually until the EOT after 3700 h. At EOT, the average HFR of the Benchmark catalyst MEAs has decreased by $\approx 52 \text{ m}\Omega \text{ cm}^2$ compared to BOL, which is slightly more than the decrease of $\approx 39 \text{ m}\Omega \text{ cm}^2$ observed for the P2X MEAs; however, considering the rather large standard deviation of

the HFR for each MEA type, this difference is likely not significant. The overall mean HFR at EOT for all 10 cells is $\approx 140 \text{ m}\Omega \text{ cm}^2$, corresponding to a $\approx 45 \text{ m}\Omega \text{ cm}^2$ or $\approx 25\%$ decrease compared to BOL.

In general, a gradual decrease of the HFR during extended PEMWE has been observed by other researchers^{44,52,57}. In principle, the decrease of the HFR over time can have three different reasons, namely: (i) a gradual increase of the water content of the membrane over time,^{58,59} which increases the intrinsic conductivity of the ionomer⁶⁰; (ii) a gradual intrusion of the membrane into the pores of the PTL, which decreases the effective membrane thickness^{61,62}; and, (iii) a thinning of the membrane due to ionomer chemical degradation.^{52,63,64} In this context, we want to note that also membrane degradation can limit the PEMWE MEA lifetime. Typically, a 10% loss in fluoride inventory is considered a failure criterion for Nafion[®] membranes.⁶⁵ As the aim of our study was to conduct a comparison of the durability of the Benchmark and the P2X catalyst, a detailed analysis of the HFR decrease over time was not in our focus. Post-mortem SEM cross-sectional analysis suggested a minor thinning of the membranes over the course of the durability test (on the order of $\approx 10\%$), but there was no indication of any loss of mechanical integrity of the membrane that could possibly affect the OER mass activity data.

Conclusions

To validate the durability of a novel low-iridium OER catalyst, we cycled five MEAs with the new low-iridium-loading catalyst at $0.25 \text{ mg}_{\text{Ir}} \text{ cm}^{-2}$ and another five MEAs with a Benchmark OER catalyst at $2 \text{ mg}_{\text{Ir}} \text{ cm}^{-2}$ together in a 10-cell industrial short stack from H-TEC Systems between 0.1 A cm^{-2} , 1.75 A cm^{-2} and 2.0 A cm^{-2} for 10 min each during 3700 h. Polarization curves and impedance spectra were recorded weekly for every cell in the stack, which allowed for a thorough Tafel-analysis at low current densities and evaluation of the mass-activities of the two different OER catalysts as a function of time over the course of the test campaign. The new catalyst with a significantly lowered iridium packing density shows a 30-fold higher BOL mass-activity at 1.5 V iR-free cell voltage compared to the Benchmark catalyst. Both types of MEAs show an initially faster increase in iR-free cell voltage during the first $\approx 1000 \text{ h}$ which is significantly less pronounced for the rest of the test. The mass activity ratio between the low-iridium loaded catalyst and the Benchmark catalyst decreases during the test and gradually levels out to a value of ≈ 4 between 1000 and 3700 h. We attribute the rise in iR-free cell voltage visible for both catalyst types (more pronounced for the at beginning-of-life more amorphous novel low-iridium-catalyst and less pronounced for the more crystalline Benchmark catalyst) not to a loss of active material, but to a gradual change in the oxidation state of the surface layer of the catalyst particles from a more active, amorphous hydrous iridium oxide in the beginning to a less active, crystalline IrO_2 during operation. The extrapolated long term degradation rate for the low loading catalyst anodes is higher ($\approx +1.0 \mu\text{V/h}$) than for the benchmark catalyst anodes ($\approx +0.25 \mu\text{V/h}$), but still acceptable low for an industrial application with an additional iR-free cell voltage increase of only $\approx 35 \text{ mV}$ starting from 3700 h onwards to a projected 40,000 h stack lifetime.

Acknowledgments

This work was funded by the German Federal Ministry of Education and Research (BMBF) within the project Kopernikus P2X (funding numbers: 03SFK2I1-2 (ZAE Bayern), 03SFK2V0-2 (Technical University of Munich, Chair of Technical Electrochemistry), 03SFK2R1-2 (H-TEC Systems GmbH), 03SFK2S0-2 (Greenery GmbH), 03SFK2K1-2 (Heraeus Deutschland GmbH & Co. KG)). The authors gratefully acknowledge Paulette Loichet (Technical University of Munich) and Simon Qian (Technical University of Munich) for valuable discussions and

their support on the recording and analysis of the XPS spectra as well as Matthias Rzepka (ZAE Bayern) for valuable discussions.

ORCID

Maximilian Möckl  <https://orcid.org/0000-0002-1937-9669>

Matthias F. Ernst  <https://orcid.org/0000-0003-2670-3516>

Matthias Kornherr  <https://orcid.org/0000-0002-0201-7506>

Hubert A. Gasteiger  <https://orcid.org/0000-0001-8199-8703>

References

- L. Barreto, A. Makihiro, and K. Riahi, "The hydrogen economy in the 21st century: a sustainable development scenario." *International Journal of Hydrogen Energy*, **28**, 267 (2003).
- M. A. Pellow, C. J. M. Emmott, C. J. Barnhart, and S. M. Benson, "Hydrogen or batteries for grid storage? a net energy analysis." *Energy Environ. Sci.*, **8**, 1938 (2015).
- B. Emonts, M. Reuß, P. Stenzel, L. Welder, F. Knicker, T. Grube, K. Görner, M. Robinus, and D. Stolten, "Flexible sector coupling with hydrogen: A climate-friendly fuel supply for road transport." *International Journal of Hydrogen Energy*, **44**, 12918 (2019).
- A. Buttler and H. Spliethoff, "Current status of water electrolysis for energy storage, grid balancing and sector coupling via power-to-gas and power-to-liquids: A review." *Renew. Sustain. Energy Rev.*, **82**, 2440 (2018).
- T. Bacquart et al., "Hydrogen fuel quality from two main production processes: Steam methane reforming and proton exchange membrane water electrolysis." *Journal of Power Sources*, **444**, 227170 (2019).
- M. Bernt, A. Siebel, and H. A. Gasteiger, "Analysis of voltage losses in pem water electrolyzers with low platinum group metal loadings." *J. Electrochem. Soc.*, **165**, F305 (2018).
- M. Carmo, D. L. Fritz, J. Mergel, and D. Stolten, "A comprehensive review on pem water electrolysis." *International Journal of Hydrogen Energy*, **38**, 4901 (2013).
- K. Ayers, N. Danilovic, R. Ouimet, M. Carmo, B. Pivovar, and M. Bornstein, "Perspectives on low-temperature electrolysis and potential for renewable hydrogen at scale." *Annual Review of Chemical and Biomolecular Engineering*, **10**, 219 (2019).
- J. Durst, A. Siebel, C. Simon, F. Hasché, J. Herranz, and H. A. Gasteiger, "New insights into the electrochemical hydrogen oxidation and evolution reaction mechanism." *Energy Environ. Sci.*, **7**, 2255 (2014).
- J. Durst, C. Simon, F. Hasché, and H. A. Gasteiger, "Hydrogen oxidation and evolution reaction kinetics on carbon supported pt, ir, rh, and pd electrocatalysts in acidic media." *J. Electrochem. Soc.*, **162**, F190 (2015).
- M. Bernt, A. Hartig-Weiss, M. F. Tovini, H. A. El-Sayed, C. Schramm, J. Schröter, C. Gebauer, and H. A. Gasteiger, "Current challenges in catalyst development for pem water electrolyzers." *Chemie Ingenieur Technik*, **92**, 31 (2020).
- C. K. Mittelsteadt, "PEM electrolysis: Ready for impact." *ECS Trans.*, **69**, 205 (2015).
- S. Trasatti, "Electrocatalysis by oxides—attempt at a unifying approach." *Journal of Electroanalytical Chemistry and Interfacial Electrochemistry*, **111**, 125 (1980).
- M. A. Hubert et al., "Acidic oxygen evolution reaction activity–stability relationships in ru-based pyrochlores." *ACS Catal.*, **10**, 12182 (2020).
- A. Cowley et al., *Pgm Market Report February 2020, Johnson Matthey PLC—Downloaded at 04.02.2022* (2020), <https://matthey.com/-/media/files/press-releases/pgm-market-report-february-2020.pdf>.
- F. Price, *The Platinum Standard 2021, Heraeus and SFA Oxford Ltd—Downloaded at 04.02.2022* (2021), https://www.heraeus.com/media/media/hpm/doc_hpm-precious_metal_update/The_Platinum_Standard_2021.pdf.
- U. Babic, M. Suermann, F. N. Büchi, L. Gubler, and T. J. Schmidt, "Review—identifying critical gaps for polymer electrolyte water electrolysis development." *J. Electrochem. Soc.*, **164**, F387 (2017).
- M. Bernt, J. Schröter, M. Möckl, and H. A. Gasteiger, "Analysis of gas permeation phenomena in a PEM water electrolyzer operated at high pressure and high current density." *J. Electrochem. Soc.*, **167**, 124502 (2020).
- S. Siracusano, C. Oldani, M. Assunta Navarra, S. Tonella, L. Mazzapodia, N. Briguglio, and A. Arico, "Chemically stabilised extruded and recast short side chain aquivion proton exchange membranes for high current density operation in water electrolysis." *Journal of Membrane Science*, **578**, 136 (2019).
- M. Bernt and H. A. Gasteiger, "Influence of ionomer content in iro2/tio2 electrodes on pem water electrolyzer performance." *J. Electrochem. Soc.*, **163**, F3179 (2016).
- M. Möckl, M. Bernt, J. Schröter, and A. Jossen, "Proton exchange membrane water electrolysis at high current densities: Investigation of thermal limitations." *International Journal of Hydrogen Energy*, **45**, 1417 (2020).
- M. Schalenbach, M. Carmo, D. L. Fritz, J. Mergel, and D. Stolten, "Pressurized pem water electrolysis: Efficiency and gas crossover." *International Journal of Hydrogen Energy*, **38**, 14921 (2013).
- P. Trinke, B. Bensmann, and R. Hanke-Rauschenbach, "Current density effect on hydrogen permeation in pem water electrolyzers." *International Journal of Hydrogen Energy*, **42**, 14355 (2017).
- C. Klose, P. Trinke, T. Böhm, B. Bensmann, S. Vierrath, R. Hanke-Rauschenbach, and S. Thiele, "Membrane interlayer with pt recombination particles for reduction of the anodic hydrogen content in PEM water electrolysis." *J. Electrochem. Soc.*, **165**, F1271 (2018).

25. S. Garbe, U. Babic, E. Nilsson, T. J. Schmidt, and L. Gubler, "Communication-protected thin membranes for gas crossover suppression in polymer electrolyte water electrolysis." *J. Electrochem. Soc.*, **166**, F873 (2019).
26. F. Pantò, S. Siracusano, N. Briguglio, and A. S. Aricò, "Durability of a recombination catalyst-based membrane-electrode assembly for electrolysis operation at high current density." *Applied Energy*, **279**, 115809 (2020).
27. A. Stähler, M. Stähler, F. Scheepers, W. Lehnert, and M. Carmo, "Scalable implementation of recombination catalyst layers to mitigate gas crossover in PEM water electrolyzers." *J. Electrochem. Soc.*, **169**, 034522 (2022).
28. S. Grigoriev, P. Millet, S. Korobtsev, V. Porembskiy, M. Pepic, C. Etievant, C. Puyenche, and V. Fateev, "Hydrogen safety aspects related to high-pressure polymer electrolyte membrane water electrolysis." *International Journal of Hydrogen Energy*, **34**, 5986 (2009).
29. P. Mazúr, J. Polonský, M. Paidar, and K. Bouzek, "Non-conductive tio₂ as the anode catalyst support for pem water electrolysis." *International Journal of Hydrogen Energy*, **37**, 12081 (2012).
30. V. K. Puthiyapura, M. Mamlouk, S. Pasupathi, B. G. Pollet, and K. Scott, "Physical and electrochemical evaluation of ato supported iro₂ catalyst for proton exchange membrane water electrolyser." *Journal of Power Sources*, **269**, 451 (2014).
31. D. Böhm, M. Beetz, M. Schuster, K. Peters, A. G. Hufnagel, M. Döblinger, B. Böller, T. Bein, and D. Fattakhova-Rohlfing, "Efficient oer catalyst with low ir volume density obtained by homogeneous deposition of iridium oxide nanoparticles on macroporous antimony-doped tin oxide support." *Adv. Funct. Mater.*, **30**, 1906670 (2020).
32. C. Hao, H. Lv, C. Mi, Y. Song, and J. Ma, "Investigation of mesoporous niobium-doped tio₂ as an oxygen evolution catalyst support in an spe water electrolyzer." *ACS Sustainable Chemistry & Engineering*, **4**, 746 (2016).
33. A. G. Hufnagel, S. Häringer, M. Beetz, B. Böller, D. Fattakhova-Rohlfing, and T. Bein, "Carbon-templated conductive oxide supports for oxygen evolution catalysis." *Nanoscale*, **11**, 14285 (2019).
34. H. Xu, B. Rasimick, R. Stone, S. Zhao, and L. Yan, "High-performance, long-lifetime catalysts for proton exchange membrane electrolysis." *Annual Progress Report, Giner Inc.*, **II.B.2**, 1 (2017), https://www.hydrogen.energy.gov/pdfs/progress17/ii_b_2_xu_2017.pdf.
35. T. Hrbeč, P. Kůš, Y. Yakovlev, J. Nováková, Y. Lobko, I. Khalakhan, V. Matolín, and I. Matolínová, "Sputter-etching treatment of proton-exchange membranes: Completely dry thin-film approach to low-loading catalyst-coated membranes for water electrolysis." *International Journal of Hydrogen Energy*, **45**, 20776 (2020).
36. K. Lewinski, D. van der Vliet, and S. Luopa, "Nstf advances for pem electrolysis." *ECS Trans.*, **69**, 893 (2015).
37. Kopernikus p2x project funded by the german ministry of education and research, (BMBF) - accessed at 16.02.2022 (2022). <https://www.kopernikus-projekte.de/projekte/p2x>.
38. M. F. Tovini, A. M. Damjanovic, H. A. El-Sayed, J. Speder, C. Eickes, J.-P. Suchsland, A. Ghielmi, and H. A. Gasteiger, "Degradation mechanism of an IrO₂ anode co-catalyst for cell voltage reversal mitigation under transient operation conditions of a PEM fuel cell." *J. Electrochem. Soc.*, **168**, 064521 (2021).
39. M. Bernt, C. Schramm, J. Schröter, C. Gebauer, J. Byrknes, C. Eickes, and H. A. Gasteiger, "Effect of the irox conductivity on the anode electrode / porous transport layer interfacial resistance in pem water electrolyzers." *J. Electrochem. Soc.*, **168**, 084513 (2021).
40. T. Reier, D. Teschner, T. Lunkenbein, A. Bergmann, S. Selve, R. Kraehnert, R. Schlögl, and P. Strasser, "Electrocatalytic oxygen evolution on iridium oxide: Uncovering catalyst-substrate interactions and active iridium oxide species." *J. Electrochem. Soc.*, **161**, F876 (2014).
41. S. Geiger, O. Kasian, B. R. Shrestha, A. M. Mingers, K. J. J. Mayrhofer, and S. Cherevko, "Activity and stability of electrochemically and thermally treated iridium for the oxygen evolution reaction." *J. Electrochem. Soc.*, **163**, F3132 (2016).
42. D. Böhm, M. Beetz, C. Gebauer, M. Bernt, J. Schröter, M. Kornherr, F. Zoller, T. Bein, and D. Fattakhova-Rohlfing, "Highly conductive titania supported iridium oxide nanoparticles with low overall iridium density as oer catalyst for large-scale pem electrolysis." *Applied Materials Today*, **24**, 101134 (2021).
43. K. Ayers, N. Danilovic, K. Harrison, and H. Xu, "Pem electrolysis, a forerunner for clean hydrogen." *The Electrochemical Society Interface*, **30**, 67 (2021).
44. C. Rakousky, U. Reimer, K. Wippermann, M. Carmo, W. Lueke, and D. Stolten, "An analysis of degradation phenomena in polymer electrolyte membrane water electrolysis." *Journal of Power Sources*, **326**, 120 (2016).
45. J. Knöppel, M. Möckl, D. Escalera-Lopez, K. Stojanovski, M. Bierling, T. Böhm, S. Thiele, R. Matthias, and S. Cherevko, "On the limitations in assessing stability of oxygen evolution catalysts using aqueous model electrochemical cells." *Nat. Commun.*, **12**, 2231 (2021).
46. T. Okada, "Effect of ionic contaminants." *Handbook of Fuel Cells*, **3**, 627 (2003).
47. N. Li, S. S. Araya, X. Cui, and S. K. Kær, "The effects of cationic impurities on the performance of proton exchange membrane water electrolyzer." *Journal of Power Sources*, **473**, 228617 (2020).
48. A. Weiß, A. Siebel, M. Bernt, T.-H. Shen, V. Tileli, and H. A. Gasteiger, "Impact of intermittent operation on lifetime and performance of a PEM water electrolyzer." *J. Electrochem. Soc.*, **166**, F487 (2019).
49. M. P. Seah and W. A. Dench, "Quantitative electron spectroscopy of surfaces: A standard data base for electron inelastic mean free paths in solids." *Surface and Interface Analysis*, **1**, 2 (1979).
50. P. J. Cumpson, "The thickogram: a method for easy film thickness measurement in XPS." *Surface and Interface Analysis*, **29**, 403 (2000).
51. J. H. Scofield, "Hartree-slater subshell photoionization cross-sections at 1254 and 1487 ev." *J. Electron Spectrosc. Relat. Phenom.*, **8**, 129 (1976).
52. S. Siracusano, S. Trocino, N. Briguglio, F. Pantò, and A. S. Aricò, "Analysis of performance degradation during steady-state and load-thermal cycles of proton exchange membrane water electrolysis cells." *Journal of Power Sources*, **468**, 228390 (2020).
53. N. Danilovic, K. E. Ayers, C. Capuano, J. N. Renner, L. Wiles, and M. Pertoso, *plenary challenges in going from laboratory to megawatt scale PEM electrolysis*, *ECS Transactions*, **75**, 395 (2016).
54. H. G. Sanchez-Casaloungue, M. L. Ng, S. Kaya, D. Friebe, H. Ogasawara, and A. Nilsson, "In-situ observation of surface species on iridium oxide nanoparticles during the oxygen evolution reaction." *Angew. Chem. Int. Ed.*, **53**, 7169 (2014).
55. M. Fujita, I. Arima, H. Goto, S. Konaka, and T. Tada, "The relationship between activity and durability of surface area and catalyst loading of IrO_x anode catalyst in proton exchange membrane water electrolysis (PEMWE), ECS Meeting Abstracts MA2020-02."2466 (2020).
56. K. C. Neyerlin, W. Gu, J. Jorne, and H. A. Gasteiger, "Determination of catalyst unique parameters for the oxygen reduction reaction in a PEMFC." *J. Electrochem. Soc.*, **153**, A1955 (2006).
57. S. Siracusano, N. Van Dijk, R. Backhouse, L. Merlo, V. Baglio, and A. Aricò, "Degradation issues of pem electrolysis meas." *Renewable Energy*, **123**, 52 (2018).
58. G. Alberti, R. Narducci, and M. Sganappa, "Effects of hydrothermal/thermal treatments on the water-uptake of nafion membranes and relations with changes of conformation, counter-elastic force and tensile modulus of the matrix." *Journal of Power Sources*, **178**, 575 (2008).
59. G. Alberti and R. Narducci, "Evolution of permanent deformations (or memory) in nafion 117 membranes with changes in temperature, relative humidity and time, and its importance in the development of medium temperature pemfcs." *Fuel Cells*, **9**, 410 (2009).
60. T. E. Springer, T. A. Zawodzinski, and S. Gottesfeld, "Polymer electrolyte fuel cell model." *J. Electrochem. Soc.*, **138**, 2334 (1991).
61. T. Schuler, R. D. Bruycker, T. J. Schmidt, and F. N. Büchi, "Polymer electrolyte water electrolysis: Correlating porous transport layer structural properties and performance: Part i. tomographic analysis of morphology and topology." *J. Electrochem. Soc.*, **166**, F270 (2019).
62. T. Schuler, T. J. Schmidt, and F. N. Büchi, "Polymer electrolyte water electrolysis: Correlating performance and porous transport layer structure: Part II. electrochemical performance analysis." *J. Electrochem. Soc.*, **166**, F555 (2019).
63. F. Fouda-Onana, M. Chandesris, V. Médeau, S. Chelghoum, D. Thoby, and N. Guillet, "Investigation on the degradation of meas for pem water electrolyzers part i: Effects of testing conditions on mea performances and membrane properties." *International Journal of Hydrogen Energy*, **41**, 16627 (2016).
64. P. Marocco, K. Sundseth, T. Aarhaug, A. Lanzini, M. Santarelli, A. O. Barnett, and M. Thomassen, "Online measurements of fluoride ions in proton exchange membrane water electrolysis through ion chromatography." *Journal of Power Sources*, **483**, 229179 (1919).
65. A. Laconti, H. Liu, C. Mittelsteadt, and R. McDonald, *Polymer electrolyte membrane degradation mechanisms in fuel cells—findings over the past 30 years and comparison with electrolyzers*, *ECS Transactions*, **1**, 199 (2006).

6 Conclusion

The aim of this work was to investigate the possibilities of improving PEMWE at cell level in such a way that it can be deployed on a large scale in the future with very high installation rates of around ≈ 100 GW/year. Two key measures were identified: 1) The use of thin membranes, which greatly reduce ohmic losses in the cell and enable up to 3-fold higher current and power densities while maintaining high voltage efficiency of 70 % (LHV). This can save critical materials and cost. 2) The use of improved OER catalysts with about 10 to 20-fold lower iridium loading to achieve, together with the use of thin membranes, a low power-specific iridium loading of about ≈ 0.01 g_{Ir}/kW_{70%LHV} to avoid an iridium shortage at the aforementioned deployment rates. Several questions arise from these two central measures with regard to practicality, which were investigated in a total of five publications.

In the study presented in section 5.1, a life cycle analysis of hydrogen production with PEMWE in future energy systems was performed. It was shown that using only wind power and photovoltaics for the electricity supply of the electrolysis process, a strong reduction of greenhouse gas emissions by about 2/3 compared to the reference process of steam reforming of natural gas is possible. Since the LCA was prepared using static databases, as is common practice, the future greenhouse gas emissions for hydrogen production with PEMWE are very likely to still be significantly lower than the calculated values. A higher current density also reduces the material consumption for the PEMWE cell stack. However, the savings in greenhouse gas emissions due to the reduction in material use are very small compared to the greenhouse gas emissions due to electricity supply, even in the purely renewable scenario.

In the second study (section 5.2), it was shown that the use of thin membranes down to 30 μ m dry thickness (Nafion XL) in PEMWE cells is possible in principle and extremely high current densities up to 25 A/cm² can be achieved. However, high cell voltages close to 3 V and thus very low voltage efficiency around 40 % and presumably high degradation limit the operation at these extreme values. In addition, the high heat production in the cell at high current densities can lead to cooling problems. However, a model of heat transport in PEMWE cells from MEA to flow fields, verified with in-situ measurements of the MEA temperature, shows that operation with over 60 % (LHV) voltage efficiency up to 10 A/cm² seems possible using Nafion XL as membrane material with a still modest cooling water flow of 25 ml/(min cm²).

The hydrogen permeation already discussed in the theory section could show an increase with current density. This could lower the Faraday efficiency as well as raise the minimum current density for falling below the 2 % hydrogen in oxygen limit on the anode side. Therefore, hydrogen permeation in PEMWE cells was measured in the third study (section 5.3) for Nafion[®] 117 and Nafion[®] 212 at cathode pressures ranging from 1 bar to 30 bar and temperatures from 40 °C up to 80 °C. Using in-line mass spectrometry, a strong dependence of the permeation rate on the current density was found, especially for low cathode pressures, even at usual I/C ratios of 0.6 of the cathode. However, the increase is significantly less pronounced for operation at elevated cathode pressures. For example, for Nafion[®] 117, a 15-fold increase at 1 bar cathode pressure from 0 A/cm² to 5 A/cm² and of only 16 % at 30 bar cathode pressure between 0 A/cm² and 4 A/cm² could be determined. Higher I/C ratios further increase the hydrogen permeation rates. The results show that safe operation with thin membranes at high cell efficiencies greater 70 % (LHV) and moderate hydrogen pressures up to 30 bar on the cathode side is only possible using a recombination catalyst.

In order to reach high deployment rates for PEMWE systems, CAPEX and OPEX needs to be as

low as possible. An important influence in OPEX is the stability of the PEMWE stack and its most sensitive part, the MEA. Especially the anode side OER catalysts need to be durable under harsh operating conditions. However, the stability of OER catalysts is usually tested in aqueous model systems e.g. via current cycling in an RDE setup. The measured stabilities in AMS are unrealistic when compared to long term test results in real devices. Therefore, it is important to elucidate the differences between OER catalyst stability in AMS and in MEAs in real PEMWE devices. In the fourth study contained in this thesis (section 5.4), plausible OER catalyst dissolution rates were for the first time measured during operation in a real PEMWE MEA and compared to measurements obtained in AMS. In order to do so, a dedicated, galvanic redeposition-free PEMWE cell and test rig was developed. The results show, that the OER catalyst dissolution during uninterrupted operation of a PEMWE cell is comparably low, resulting in a calculated catalyst half life of ≈ 150 years for pure hydrous IrO_x at today's standard catalyst loadings of $\approx 1 \text{ mg}_{\text{Ir}}/\text{cm}^2$. The high differences in stability between AMS and MEA measurements of $\approx 10^4$ - 10^5 can be attributed mainly to a difference in estimated and real pH value in the MEA and to a stabilization effect occurring over time. Hence, for a realistic direct measurement of the stability of new or improved OER catalysts, especially at low PGM loading, it is important to use MEA-based systems instead of AMS.

The last study of this thesis (section 5.5) was dedicated to the long term testing of low iridium loaded MEAs with a focus on catalyst durability. Here, 5 MEAs with a benchmark OER catalyst at a loading of $2 \text{ mg}_{\text{Ir}}/\text{cm}^2$ and 5 additional MEAs with a newly developed low iridium packing density low-Ir OER catalyst at $0.25 \text{ mg}_{\text{Ir}}/\text{cm}^2$ were tested in an industrial short stack with 30 cm^2 active area for 3700 h. A current cycling profile with low, intermediate and high current density steps was used, which simulated the operation during coupling to intermittent renewable energies. Weekly diagnosis of all cells in the stack via polarization curves and EIS revealed two main degradation effects: The cells show an initially stronger increase in iR-free cell voltage up to 1000 h, which is leveling out slowly during the following 2700 h of testing. This effect seems to be caused by electrode aging and is more pronounced for the low-iridium loaded MEAs. However, the extrapolated rate is low enough to allow for an operation of the low-iridium loaded MEAs up to about 40.000 h at only moderate iR-free cell voltage increases of $\approx +1 \mu\text{V}/\text{h}$, compared to $\approx +0.25 \mu\text{V}/\text{h}$ for the benchmark catalyst MEAs. Furthermore, a drop in HFR of all cells by about 25 % from begin to the end of the testing is visible. This seems partly to be attributed to a change in water content of the membranes during prolonged electrolysis but also to a thinning of $\approx 10 \%$ of the membranes which has been quantified also by SEM graphs of MEA cross sections for begin of life and end of test samples for both catalyst types. As membrane degradation can also drastically limit the PEMWE lifetime, this effect needs to be further investigated in a dedicated follow-up study.

Summarizing the main results of this work, it is possible to reach low enough power specific iridium loadings of PEMWE cells to allow for a large scale implementation of this technology in the near future (≈ 10 to 20 years). Thin membranes and low-loaded catalysts are the keys to achieve low power specific iridium loading and allow for a significant reduction in CAPEX due to high current density operation. The stability of iridium based OER catalysts, also at low catalyst loadings of $0.25 \text{ mg}_{\text{Ir}}/\text{cm}^2$, was found to be high enough for long-term operation when using adequate operational strategies with mainly uninterrupted operation and minimized shut-down-start-up cycles. However, several unsolved issues were identified, which have to be tackled in the future. The use of thin membranes has many benefits, but calls for the integration of a recombination catalyst in the MEA or the PEMWE cell to allow safe operation over a wide current density range. Furthermore,

possible membrane thinning needs to be adequately detected and the underlying mechanisms have to be explained in order to be able to find solutions to mitigate this detrimental effect which could drastically curtail PEMWE stack lifetime.

References

- [1] *World Energy Outlook 2019*. IEA, 2019. 1
- [2] Umweltbundesamt. Endenergieverbrauch und -intensität für Raumwärme - Private Haushalte. https://www.umweltbundesamt.de/sites/default/files/medien/384/bilder/dateien/4_abb_eev-intensitaet-raumwaerme-ph-2020-07-01.pdf, 2020. Accessed: 21-June-2022. 1
- [3] Klimaschutzportal. Wie viel Kerosin verbrauchen deutsche Fluggesellschaften in einem Jahr? <https://www.klimaschutz-portal.aero/faq/wie-viel-kerosin-verbrauchen-deutsche-fluggesellschaften-in-einem-jahr/>, 2019. Accessed: 21-June-2022. 1
- [4] *The Paris Agreement*. UNFCCC, 2015. 1
- [5] Johan Rockström, Owen Gaffney, Joeri Rogelj, Malte Meinshausen, Nebojsa Nakicenovic, and Hans Joachim Schellnhuber. A roadmap for rapid decarbonization. *Science*, 355(6331):1269–1271, 2017. 1
- [6] Peter Van den Bossche, Frédéric Vergels, Joeri Van Mierlo, Julien Matheys, and Wout Van Autenboer. Subat: An assessment of sustainable battery technology. *Journal of Power Sources*, 162(2):913–919, 2006. 1
- [7] Michael A. Semeraro. Renewable energy transport via hydrogen pipelines and hvdc transmission lines. *Energy Strategy Reviews*, 35:100658, 2021. 1
- [8] Joakim Andersson and Stefan Grönkvist. Large-scale storage of hydrogen. *International Journal of Hydrogen Energy*, 44(23):11901–11919, 2019. 1
- [9] Ayeon Kim, Heehyang Kim, Hyunjun Lee, Boreum Lee, and Hankwon Lim. Comparative economic optimization for an overseas hydrogen supply chain using mixed-integer linear programming. *ACS Sustainable Chemistry & Engineering*, 9(42):14249–14262, 2021. 1
- [10] M. Bernt, A. Siebel, and H. A. Gasteiger. Analysis of voltage losses in pem water electrolyzers with low platinum group metal loadings. *Journal of The Electrochemical Society*, 165(5):F305–F314, 2018. 2, 3, 6, 13, 14, 16, 20, 94
- [11] A. Buttler and H. Spliethoff. Current status of water electrolysis for energy storage, grid balancing and sector coupling via power-to-gas and power-to-liquids: A review. *Renewable and Sustainable Energy Reviews*, 82:2440–2454, 2018. 2, 5, 6, 13, 23, 33, 56, 94
- [12] O. Schmidt, A. Gambhir, I. Staffell, A. Hawkes, J. Nelson, and S. Few. Future cost and performance of water electrolysis: An expert elicitation study. *International Journal of Hydrogen Energy*, 42:30470–30492, 2017. 2, 15, 16, 24
- [13] Thomas Bacquart, Karine Arrhenius, Stefan Persijn, Andrés Rojo, Fabien Auprêtre, Bruno Gozlan, Niamh Moore, Abigail Morris, Andreas Fischer, Arul Murugan, Sam Bartlett, Guillaume Doucet, François Laridant, Eric Gernot, Teresa E. Fernández, Concepción Gómez, Martine Carré, Guy De Reals, and Frederique Haloua. Hydrogen fuel quality from two main production processes: Steam methane reforming and proton exchange membrane water electrolysis. *Journal of Power Sources*, 444:227170, 2019. 2

- [14] M. Kopp, D. Coleman, C. Stiller, K. Scheffer, J. Aichinger, and B. Scheppat. Energiepark mainz: Technical and economical analysis of the worldwide largest power-to-gas plant with pem electrolysis. *International Journal of Hydrogen Energy*, 42:13311–13320, 2017. 2, 7, 23
- [15] Hiroshi Ito, Tetsuhiko Maeda, Akihiro Nakano, and Hiroyasu Takenaka. Properties of nafion membranes under pem water electrolysis conditions. *International Journal of Hydrogen Energy*, 36(17):10527–10540, 2011. 5, 8, 9
- [16] M. Bernt and H. A. Gasteiger. Influence of ionomer content in iro₂/tio₂ electrodes on pem water electrolyzer performance. *Journal of The Electrochemical Society*, 163(11):F3179–F3189, 2016. 5, 13, 14, 18, 20, 21, 35
- [17] D. Bessarabov, P. Millet, and B.G. Pollet. *PEM Water Electrolysis*. Hydrogen and Fuel Cells Primers. Elsevier Science, 2018. 5
- [18] Tuan Linh Doan, Han Eol Lee, Syed Shabbar Hassan Shah, MinJoong Kim, Chang-Hee Kim, Hyun-Seok Cho, and Taekeun Kim. A review of the porous transport layer in polymer electrolyte membrane water electrolysis. *International Journal of Energy Research*, 45(10):14207–14220, 2021. 6
- [19] N.P. Finkelstein and R.D. Hancock. A new approach to the chemistry of gold. *Gold Bulletin*, 7(3):72–77, 1974. 6
- [20] K. Bareiß, C. de la Rúa, M. Möckl, and T. Hamacher. Life cycle assessment of hydrogen from proton exchange membrane water electrolysis in future energy systems. *Applied Energy*, 237:862–872, 2019. 7, 16, 43
- [21] S. Sun, Z. Shao, H. Yu, G. Li, and B. Yi. Investigations on degradation of the long-term proton exchange membrane water electrolysis stack. *Journal of Power Sources*, 267:515–520, 2014. 6
- [22] Na Li, Samuel Simon Araya, Xiaoti Cui, and Søren Knudsen Kær. The effects of cationic impurities on the performance of proton exchange membrane water electrolyzer. *Journal of Power Sources*, 473:228617, 2020. 6
- [23] T. Okada. Effect of ionic contaminants. *Handbook of Fuel Cells*, 3:627, 2003. 6
- [24] Aldo Saul Gago, Philipp Lettenmeier, Svenja Stiber, Asif Syed Ansar, Li Wang, and Kaspar Andreas Friedrich. Cost-effective pem electrolysis: The quest to achieve superior efficiencies with reduced investment. *ECS Transactions*, 85(13):3–13, 2018. 6
- [25] B. Smitha, S. Sridhar, and A.A. Khan. Solid polymer electrolyte membranes for fuel cell applications—a review. *Journal of Membrane Science*, 259(1):10–26, 2005. 8
- [26] Albert Albert, Alejandro O Barnett, Magnus S Thomassen, Thomas J Schmidt, and Lorenz Gubler. Radiation-grafted polymer electrolyte membranes for water electrolysis cells: Evaluation of key membrane properties. *ACS applied materials & interfaces*, 7(40):22203–22212, October 2015. 8
- [27] Frank A. de Bruijn, Robert C. Makkus, Ronald K.A.M. Mallant, and Gaby J.M. Janssen. Chapter five - materials for state-of-the-art pem fuel cells, and their suitability for operation above 100 °c. In T.S. Zhao, K.-D. Kreuer, and Trung Van Nguyen, editors, *Advances in Fuel Cell*, volume 1 of *Advances in Fuel Cells*, pages 235–336. Elsevier Science, 2007. 8

- [28] M. Barclay-Satterfield, P.W. Majsztrik, H. Ota, J.B. Benziger, and A.B. Bocarsly. Mechanical properties of nafion and titania/nafion composite membranes for polymer electrolyte membrane fuel cells. *Journal of Polymer Science: Part B: Polymer Physics*, 44:2327–2345, 2006. 8
- [29] Stefano Giancola, Marta Zatoń, Álvaro Reyes-Carmona, Marc Dupont, Anna Donnadio, Sara Cavaliere, Jacques Rozière, and Deborah J. Jones. Composite short side chain pfsa membranes for pem water electrolysis. *Journal of Membrane Science*, 570-571:69–76, 2019. 8
- [30] C. K. Mittelsteadt and H. Liu. *Conductivity, permeability, and ohmic shorting of ionomeric membranes*. Wiley, 2010. 8, 10
- [31] Maximilian Philipp Bernt. *Analysis of Voltage Losses and Degradation Phenomena in PEM Water Electrolyzers*. Dissertation, Technische Universität München, München, 2019. 8, 9
- [32] James T. Hinatsu, Minoru Mizuhata, and Hiroyasu Takenaka. Water uptake of perfluoro-sulfonic acid membranes from liquid water and water vapor. *Journal of The Electrochemical Society*, 141(6):1493–1498, 1994. 8
- [33] K. Broka and P. Ekdunge. Oxygen and hydrogen permeation properties and water uptake of nafion® 117 membrane and recast film for pem fuel cell. *Journal of Applied Electrochemistry*, 27:117–123, 1997. 8
- [34] Felix N. Buechi and Guenther G. Scherer. Investigation of the transversal water profile in nafion membranes in polymer electrolyte fuel cells. *Journal of The Electrochemical Society*, 148(3):A183, 2001. 8
- [35] Thomas A. Zawodzinski, Charles Derouin, Susan Radzinski, Ruth J. Sherman, Van T. Smith, Thomas E. Springer, and Shimshon Gottesfeld. Water uptake by and transport through nafion® 117 membranes. *Journal of The Electrochemical Society*, 140(4):1041–1047, 1993. 8
- [36] Ugljesa Babic, Michel Suermann, Felix N. Büchi, Lorenz Gubler, and Thomas J. Schmidt. Review — identifying critical gaps for polymer electrolyte water electrolysis development. *Journal of The Electrochemical Society*, 164(4):F387–F399, 2017. 8, 13
- [37] T.D. Gierke and W.Y. Hsu. Perfluorinated ion exchange membranes. In A. Eisenberg and H.L. Yeager, editors, *ACS Symposium Series*, volume 180, pages 283–307. ACS, 1982. 9
- [38] T. E. Springer, T. A. Zawodzinski, and S. Gottesfeld. Polymer electrolyte fuel cell model. *Journal of The Electrochemical Society*, 138(8):2334–2342, 1991. 9
- [39] H Janssen, J.C Bringmann, B Emonts, and V Schroeder. Safety-related studies on hydrogen production in high-pressure electrolyzers. *International Journal of Hydrogen Energy*, 29(7):759–770, 2004. 9
- [40] Maximilian Schalenbach, Marcelo Carmo, David L. Fritz, Jürgen Mergel, and Detlef Stolten. Pressurized pem water electrolysis: Efficiency and gas crossover. *International Journal of Hydrogen Energy*, 38(35):14921–14933, 2013. 9

- [41] Z. Luo, Z. Chang, Y. Zhang, Z. Liu, and J. Li. Electro-osmotic drag coefficient and proton conductivity in nafion membrane for pemfc. *International Journal of Hydrogen Energy*, 35:3120–3124, 2010. 10, 11
- [42] Michael Suermann. *Pressurized Polymer Electrolyte Water Electrolysis: Electrochemical Characterization and Energetic Evaluation, PhD Thesis*. ETH Zürich, 2017. 10, 11, 15
- [43] R. Sander. Compilation of henry’s law constants (version 4.0) for water as solvent. *Atmospheric Chemistry and Physics*, 15(8):4399–4981, 2015. 12
- [44] C. Klose, P. Trinke, T. Böhm, B. Bensmann, S. Vierrath, R. Hanke-Rauschenbach, and S. Thiele. Membrane interlayer with pt recombination particles for reduction of the anodic hydrogen content in PEM water electrolysis. *Journal of The Electrochemical Society*, 165(16):F1271–F1277, 2018. 12
- [45] Steffen Garbe, Ugljesa Babic, Elisabeth Nilsson, Thomas J. Schmidt, and Lorenz Gubler. Communication—pt-doped thin membranes for gas crossover suppression in polymer electrolyte water electrolysis. *Journal of The Electrochemical Society*, 166(13):F873–F875, 2019. 12
- [46] Fabiola Pantò, Stefania Siracusano, Nicola Briguglio, and Antonino Salvatore Aricò. Durability of a recombination catalyst-based membrane-electrode assembly for electrolysis operation at high current density. *Applied Energy*, 279:115809, 2020. 12
- [47] S.A. Grigoriev, P. Millet, S.V. Korobtsev, V.I. Porembskiy, M. Pepic, C. Etievant, C. Puyenchet, and V.N. Fateev. Hydrogen safety aspects related to high-pressure polymer electrolyte membrane water electrolysis. *International Journal of Hydrogen Energy*, 34(14):5986–5991, 2009. 12
- [48] Emile Tabu Ojong, Jason Tai Hong Kwan, Amin Nouri-Khorasani, Arman Bonakdarpour, David P. Wilkinson, and Tom Smolinka. Development of an experimentally validated semi-empirical fully-coupled performance model of a pem electrolysis cell with a 3-d structured porous transport layer. *International Journal of Hydrogen Energy*, 42(41):25831–25847, 2017. 13, 14
- [49] Xingwen Yu and Siyu Ye. Recent advances in activity and durability enhancement of pt/c catalytic cathode in pemfc: Part i. physico-chemical and electronic interaction between pt and carbon support, and activity enhancement of pt/c catalyst. *Journal of Power Sources*, 172(1):133–144, 2007. 13
- [50] Marcelo Carmo, David L. Fritz, Jürgen Mergel, and Detlef Stolten. A comprehensive review on pem water electrolysis. *International Journal of Hydrogen Energy*, 38(12):4901–4934, 2013. 13, 33
- [51] Katherine Ayers, Nemanja Danilovic, Ryan Ouimet, Marcelo Carmo, Bryan Pivovar, and Marius Bornstein. Perspectives on low-temperature electrolysis and potential for renewable hydrogen at scale. *Annual Review of Chemical and Biomolecular Engineering*, 10(1):219–239, 2019. 13
- [52] J. Durst, A. Siebel, C. Simon, F. Hasché, J. Herranz, and H. A. Gasteiger. New insights into the electrochemical hydrogen oxidation and evolution reaction mechanism. *Energy Environ. Sci.*, 7:2255–2260, 2014. 13, 18

- [53] Julien Durst, Christoph Simon, Frédéric Hasché, and Hubert A. Gasteiger. Hydrogen oxidation and evolution reaction kinetics on carbon supported pt, ir, rh, and pd electrocatalysts in acidic media. *Journal of The Electrochemical Society*, 162(1):F190–F203, 2015. 13, 18
- [54] Jordi Ampurdanés, Muralidhar Chourashiya, and Atsushi Urakawa. Cobalt oxide-based materials as non-pgm catalyst for her in pem electrolysis and in situ xas characterization of its functional state. *Catalysis Today*, 336:161–168, 2019. 13
- [55] Tachmajal Corrales-Sánchez, Jordi Ampurdanés, and Atsushi Urakawa. Mos₂-based materials as alternative cathode catalyst for pem electrolysis. *International Journal of Hydrogen Energy*, 39(35):20837–20843, 2014. 13
- [56] Hoyoung Kim, Eunkyong Hwang, Hyanjoo Park, Byung-Seok Lee, Jong Hyun Jang, Hyoung-Juhn Kim, Sang Hyun Ahn, and Soo-Kil Kim. Non-precious metal electrocatalysts for hydrogen production in proton exchange membrane water electrolyzer. *Applied Catalysis B: Environmental*, 206:608–616, 2017. 13
- [57] Peter K. R. Holzapfel, Melanie Bühler, Daniel Escalera-López, Markus Bierling, Florian D. Speck, Karl J. J. Mayrhofer, Serhiy Cherevko, Chuyen V. Pham, and Simon Thiele. Fabrication of a robust pem water electrolyzer based on non-noble metal cathode catalyst: [mo₃s₁₃]₂-clusters anchored to n-doped carbon nanotubes. *Small*, 16(37):2003161, 2020. 13
- [58] Sergio Trasatti. Electrocatalysis by oxides — attempt at a unifying approach. *Journal of Electroanalytical Chemistry and Interfacial Electrochemistry*, 111(1):125–131, 1980. 13
- [59] 26 - cobalt, rhodium and iridium. In N.N. GREENWOOD and A. EARNSHAW, editors, *Chemistry of the Elements (Second Edition)*, pages 1113–1143. Butterworth-Heinemann, Oxford, second edition edition, 1997. 13
- [60] Alison Cowley, Lucy Bloxham, Stewart Brown, Laura Cole, Mikio Fujita, Nicolas Girardot, Jason Jiang, Rupen Raithatha, Margery Ryan, Elaine Shao, and Fei Xiaoyan. Pgm market report february 2020. *Johnson Matthey PLC*, 2020. 13
- [61] Ruthenium and iridium market analysis, may 2020. *SFA (Oxford)*, May 2020. 13, 94
- [62] Petr Mazúr, Jakub Polonský, Martin Paidar, and Karel Bouzek. Non-conductive tio₂ as the anode catalyst support for pem water electrolysis. *International Journal of Hydrogen Energy*, 37(17):12081–12088, 2012. 13
- [63] Vinod Kumar Puthiyapura, Mohammed Mamlouk, Sivakumar Pasupathi, Bruno G. Pollet, and Keith Scott. Physical and electrochemical evaluation of ato supported iro₂ catalyst for proton exchange membrane water electrolyser. *Journal of Power Sources*, 269:451–460, 2014. 14
- [64] Daniel Böhm, Michael Beetz, Maximilian Schuster, Kristina Peters, Alexander G. Hufnagel, Markus Döblinger, Bernhard Böller, Thomas Bein, and Dina Fattakhova-Rohlfing. Efficient oer catalyst with low ir volume density obtained by homogeneous deposition of iridium oxide nanoparticles on macroporous antimony-doped tin oxide support. *Advanced Functional Materials*, 30(1):1906670, 2020. 14

- [65] Chuanpu Hao, Hong Lv, Cangen Mi, Yukun Song, and Jianxin Ma. Investigation of mesoporous niobium-doped tio₂ as an oxygen evolution catalyst support in an spe water electrolyzer. *ACS Sustainable Chemistry & Engineering*, 4(3):746–756, 2016. 14
- [66] Alexander G. Hufnagel, Sebastian Häringer, Michael Beetz, Bernhard Böller, Dina Fattakhova-Rohlfing, and Thomas Bein. Carbon-templated conductive oxide supports for oxygen evolution catalysis. *Nanoscale*, 11:14285–14293, 2019. 14
- [67] Hui Xu, Brian Rasimick, Robert Stone, Shuai Zhao, and Litao Yan. High-performance, long-lifetime catalysts for proton exchange membrane electrolysis. *Annual Progress Report, Giner Inc.*, 2017. 14
- [68] Tomáš Hrbek, Peter Kúš, Yurii Yakovlev, Jaroslava Nováková, Yevheniia Lobko, Ivan Khalakhan, Vladimír Matolín, and Iva Matolínová. Sputter-etching treatment of proton-exchange membranes: Completely dry thin-film approach to low-loading catalyst-coated membranes for water electrolysis. *International Journal of Hydrogen Energy*, 45(41):20776–20786, 2020. 14
- [69] K.A. Lewinski, D. van der Vliet, and S.M. Luopa. Nstf advances for pem electrolysis. *ECS Transactions*, 69:893–917, 2015. 14
- [70] Maximilian Bernt, Alexandra Hartig-Weiß, Mohammad Fathi Tovini, Hany A. El-Sayed, Carina Schramm, Jonas Schröter, Christian Gebauer, and Hubert A. Gasteiger. Current challenges in catalyst development for pem water electrolyzers. *Chemie Ingenieur Technik*, 92(1-2):31–39, 2020. 14, 94
- [71] Elena Borgardt, Olha Panchenko, Franz Josef Hackemüller, Jürgen Giffin, Martin Bram, Martin Müller, Werner Lehnert, and Detlef Stolten. Mechanical characterization and durability of sintered porous transport layers for polymer electrolyte membrane electrolysis. *Journal of Power Sources*, 374:84–91, 2018. 14
- [72] Robert Bock, Håvard Karoliussen, Frode Seland, Bruno G. Pollet, Magnus Skinlo Thomassen, Steven Holdcroft, and Odne S. Burheim. Measuring the thermal conductivity of membrane and porous transport layer in proton and anion exchange membrane water electrolyzers for temperature distribution modeling. *International Journal of Hydrogen Energy*, 45(2):1236–1254, 2020. 14
- [73] Julian Parra-Restrepo, Rémi Bligny, Jérôme Dillet, Sophie Didierjean, Didier Stemmelen, Christian Moyne, Alain Degiovanni, and Gaël Maranzana. Influence of the porous transport layer properties on the mass and charge transfer in a segmented pem electrolyzer. *International Journal of Hydrogen Energy*, 45(15):8094–8106, 2020. 14, 15
- [74] Paul C. Okonkwo and Clement Otor. A review of gas diffusion layer properties and water management in proton exchange membrane fuel cell system. *International Journal of Energy Research*, 45(3):3780–3800, 2021. 14
- [75] Sehkyu Park and Branko N. Popov. Effect of hydrophobicity and pore geometry in cathode gdl on pem fuel cell performance. *Electrochimica Acta*, 54(12):3473–3479, 2009. 14
- [76] Zhenye Kang, Shaun M. Alia, James L. Young, and Guido Bender. Effects of various parameters of different porous transport layers in proton exchange membrane water electrolysis. *Electrochimica Acta*, 354:136641, 2020. 14

- [77] C.K. Mittelsteadt and H. Liu. 23 - conductivity, permeability, and ohmic shorting of ionomeric membranes. In W. Vielstich, H.A. Gasteiger, and H. Yokokawa, editors, *Handbook of Fuel Cells - Fundamentals, Technology and Applications*, volume 5: Advances in Electrocatalysis, Materials, Diagnostics and Durability, pages 345–358. John Wiley and Sons, New York, 2009. 14
- [78] K Kinoshita. *Carbon: electrochemical and physicochemical properties*. John Wiley and Sons, 1 1988. 14
- [79] Hiroshi Ito. 8 - current collectors (gdls) and materials. In Dmitri Bessarabov, Haijiang Wang, Hui Li, and Nana Zhao, editors, *PEM Electrolysis for Hydrogen Production*, pages 147–156. CRC Press, 2015. 14
- [80] Jingke Mo, Zhenye Kang, Gaoqiang Yang, Scott T. Retterer, David A. Cullen, Todd J. Toops, Johney B. Green, and Feng-Yuan Zhang. Thin liquid/gas diffusion layers for high-efficiency hydrogen production from water splitting. *Applied Energy*, 177:817–822, 2016. 14
- [81] Jingke Mo, Ryan R. Dehoff, William H. Peter, Todd J. Toops, Johney B. Green, and Feng-Yuan Zhang. Additive manufacturing of liquid/gas diffusion layers for low-cost and high-efficiency hydrogen production. *International Journal of Hydrogen Energy*, 41(4):3128–3135, 2016. 14
- [82] Zhenye Kang, Jingke Mo, Gaoqiang Yang, Scott T. Retterer, David A. Cullen, Todd J. Toops, Johney B. Green Jr, Matthew M. Mench, and Feng-Yuan Zhang. Investigation of thin/well-tunable liquid/gas diffusion layers exhibiting superior multifunctional performance in low-temperature electrolytic water splitting. *Energy Environ. Sci.*, 10:166–175, 2017. 14
- [83] Zhenye Kang, Shule Yu, Gaoqiang Yang, Yifan Li, Guido Bender, Bryan S. Pivovar, Johney B. Green, and Feng-Yuan Zhang. Performance improvement of proton exchange membrane electrolyzer cells by introducing in-plane transport enhancement layers. *Electrochimica Acta*, 316:43–51, 2019. 14
- [84] S.A. Grigoriev, P. Millet, S.A. Volobuev, and V.N. Fateev. Optimization of porous current collectors for pem water electrolyzers. *International Journal of Hydrogen Energy*, 34(11):4968–4973, 2009. 15
- [85] P. Lettenmeier, S. Kolb, F. Burggraf, A.S. Gago, and K.A. Friedrich. Towards developing a backing layer for proton exchange membrane electrolyzers. *Journal of Power Sources*, 311:153–158, 2016. 15, 16
- [86] P. Lettenmeier, S. Kolb, N. Sata, A. Fallisch, L. Zielke, S. Thiele, A. S. Gago, and K. A. Friedrich. Comprehensive investigation of novel pore-graded gas diffusion layers for high-performance and cost-effective proton exchange membrane electrolyzers. *Energy Environ. Sci.*, 10:2521–2533, 2017. 15
- [87] Tobias Schuler, Joseph M. Ciccone, Bernd Krentscher, Federica Marone, Christian Peter, Thomas J. Schmidt, and Felix N. Büchi. Hierarchically structured porous transport layers for polymer electrolyte water electrolysis. *Advanced Energy Materials*, 10(2):1903216, 2019. 15

- [88] Michel Suermann, Thomas Gimpel, Lena V. Böhre, Wolfgang Schade, Boris Bensmann, and Richard Hanke-Rauschenbach. Femtosecond laser-induced surface structuring of the porous transport layers in proton exchange membrane water electrolysis. *J. Mater. Chem. A*, 8:4898–4910, 2020. 15
- [89] Christoph Rakousky, Uwe Reimer, Klaus Wippermann, Marcelo Carmo, Wiebke Lueke, and Detlef Stolten. An analysis of degradation phenomena in polymer electrolyte membrane water electrolysis. *Journal of Power Sources*, 326:120–128, 2016. 15
- [90] Wolfram Research. ElementData. <https://reference.wolfram.com/language/ref/ElementData.html>, 2014. Accessed: 12-May-2021. 15
- [91] Manuel Langemann, David L. Fritz, Martin Müller, and Detlef Stolten. Validation and characterization of suitable materials for bipolar plates in pem water electrolysis. *International Journal of Hydrogen Energy*, 40(35):11385–11391, 2015. 16
- [92] A.S. Gago, S.A. Ansar, B. Saruhan, U. Schulz, P. Lettenmeier, N.A. Cañas, P. Gazdzicki, T. Morawietz, R. Hiesgen, J. Arnold, and K.A. Friedrich. Protective coatings on stainless steel bipolar plates for proton exchange membrane (pem) electrolyzers. *Journal of Power Sources*, 307:815–825, 2016. 16
- [93] Philipp Lettenmeier, Aldo S. Gago, and K. Andreas Friedrich. 4 - protective coatings for low-cost bipolar plates and current collectors of proton exchange membrane electrolyzers for large scale energy storage from renewables. In Carlos Giudice and Guadalupe Canosa, editors, *New Technologies in Protective Coatings*, pages 69–86. IntechOpen, 2017. 16
- [94] Nuria Rojas, Margarita Sánchez-Molina, Gema Sevilla, Ernesto Amores, Eluxka Almandoz, Joseba Esparza, Marlon R. Cruz Vivas, and Carles Colominas. Coated stainless steels evaluation for bipolar plates in pem water electrolysis conditions. *International Journal of Hydrogen Energy*, 2021. 16
- [95] Gustav Wilhelm Sievers, Kirsten Anklam, Rouven Henkel, Thorsten Hickmann, and Volker Brüser. Corrosion-protection of moulded graphite conductive plastic bipolar plates in pem electrolysis by plasma processing. *International Journal of Hydrogen Energy*, 44(5):2435–2445, 2019. 16
- [96] Meilin Liu, Shahram Karimi, Norman Fraser, Bronwyn Roberts, and Frank R. Foulkes. A review of metallic bipolar plates for proton exchange membrane fuel cells: Materials and fabrication methods. *Advances in Materials Science and Engineering*, 2012:828070, 2012. 16
- [97] Steven G. Bratsch. Standard electrode potentials and temperature coefficients in water at 298.15 k. *Journal of Physical and Chemical Reference Data*, 18(1):1–21, 1989. 17
- [98] Arden L. Buck. New equations for computing vapor pressure and enhancement factor. *Journal of Applied Meteorology and Climatology*, 20(12):1527 – 1532, 1981. 17
- [99] E. Fabbri, A. Habereeder, K. Waltar, R. Kötz, and T. J. Schmidt. Developments and perspectives of oxide-based catalysts for the oxygen evolution reaction. *Catal. Sci. Technol.*, 4:3800–3821, 2014. 18
- [100] J.O’M. Bockris and A.K.N. Reddy. *Modern Electrochemistry*. Plenum Press, New York, 1970. 18, 19, 20

- [101] John S. Newman. *Electrochemical Systems*. Prentice Hall, New Jersey, 1991. 18
- [102] Mark C. Lefebvre. Characterization of ionic conductivity profiles within proton exchange membrane fuel cell gas diffusion electrodes by impedance spectroscopy. *Electrochemical and Solid-State Letters*, 2(6):259, 1999. 21
- [103] M. Maier, K. Smith, J. Dodwell, G. Hinds, P.R. Shearing, and D.J.L. Brett. Mass transport in pem water electrolyzers: A review. *International Journal of Hydrogen Energy*, 47(1):30–56, 2022. 21
- [104] Michael Schimpe, Maik Naumann, Nam Truong, Holger C. Hesse, Shriram Santhanagopalan, Aron Saxon, and Andreas Jossen. Energy efficiency evaluation of a stationary lithium-ion battery container storage system via electro-thermal modeling and detailed component analysis. *Applied Energy*, 210:211–229, 2018. 23
- [105] David Parra and Martin K. Patel. Techno-economic implications of the electrolyser technology and size for power-to-gas systems. *International Journal of Hydrogen Energy*, 41(6):3748–3761, 2016. 23
- [106] Morten Nymand and Michael A. E. Andersen. High-efficiency isolated boost dc-dc converter for high-power low-voltage fuel-cell applications. *IEEE Transactions on Industrial Electronics*, 57(2):505–514, 2010. 23
- [107] Fabian Scheepers, Markus Stähler, Andrea Stähler, Edward Rauls, Martin Müller, Marcelo Carmo, and Werner Lehnert. Temperature optimization for improving polymer electrolyte membrane-water electrolysis system efficiency. *Nature Communications*, 283:116270, 2021. 24
- [108] M. Chandesris, V. Médeau, N. Guillet, S. Chelghoum, D. Thoby, and F. Fouda-Onana. Membrane degradation in pem water electrolyzer: Numerical modeling and experimental evidence of the influence of temperature and current density. *International Journal of Hydrogen Energy*, 40(3):1353–1366, 2015. 24
- [109] Steffen Henrik Frensch, Frédéric Fouda-Onana, Guillaume Serre, Dominique Thoby, Samuel Simon Araya, and Søren Knudsen Kær. Influence of the operation mode on pem water electrolysis degradation. *International Journal of Hydrogen Energy*, 44(57):29889–29898, 2019. 24
- [110] B. Bensmann, R. Hanke-Rauschenbach, I.K. Peña Arias, and K. Sundmacher. Energetic evaluation of high pressure pem electrolyzer systems for intermediate storage of renewable energies. *Electrochimica Acta*, 110:570–580, 2013. 24
- [111] Majid Aasadnia and Mehdi Mehrpooya. Large-scale liquid hydrogen production methods and approaches: A review. *Applied Energy*, 212:57–83, 2018. 24
- [112] Geert Tjarks, Andrej Gibelhaus, Franz Lanzerath, Martin Müller, André Bardow, and Detlef Stolten. Energetically-optimal pem electrolyzer pressure in power-to-gas plants. *Applied Energy*, 218:192–198, 2018. 24
- [113] P. Trinke, B. Bensmann, and R. Hanke-Rauschenbach. Experimental evidence of increasing oxygen crossover with increasing current density during pem water electrolysis. *Electrochemistry Communications*, 82:98–102, 2017. 27

- [114] S. Litster and G. McLean. Pem fuel cell electrodes. *Journal of Power Sources*, 130(1):61–76, 2004. 34
- [115] Ugljesa Babic, Mohamed Tarik, Thomas Justus Schmidt, and Lorenz Gubler. Understanding the effects of material properties and operating conditions on component aging in polymer electrolyte water electrolyzers. *Journal of Power Sources*, 451:227778, 2020. 36
- [116] G. Bender, M. Carmo, T. Smolinka, A. Gago, N. Danilovic, M. Mueller, F. Ganci, A. Fallisch, P. Lettenmeier, K.A. Friedrich, K. Ayers, B. Pivovar, J. Mergel, and D. Stolten. Initial approaches in benchmarking and round robin testing for proton exchange membrane water electrolyzers. *International Journal of Hydrogen Energy*, 44(18):9174–9187, 2019. 39
- [117] M. Möckl, M. Bernt, J. Schröter, and A. Jossen. Proton exchange membrane water electrolysis at high current densities: Investigation of thermal limitations. *International Journal of Hydrogen Energy*, 45:1417–1428, 2020. 56
- [118] M. Bernt, J. Schröter, M. Möckl, and H. A. Gasteiger. Analysis of gas permeation phenomena in a PEM water electrolyzer operated at high pressure and high current density. *Journal of The Electrochemical Society*, 167(12):124502, 2020. 69
- [119] Julius Knöppel, Maximilian Möckl, Daniel Escalera-Lopez, Kevin Stojanovski, Markus Bierling, Thomas Böhm, Simon Thiele, Matthias Rzepka, and Serhiy Cherevko. On the limitations in assessing stability of oxygen evolution catalysts using aqueous model electrochemical cells. *Nature Communications*, 12:2231, 2021. 83
- [120] Maximilian Möckl, Matthias F. Ernst, Matthias Kornherr, Frank Allebrod, Maximilian Bernt, Jan Byrknes, Christian Eickes, Christian Gebauer, Antonina Moskovtseva, and Hubert A. Gasteiger. Durability testing of low-iridium PEM water electrolysis membrane electrode assemblies. *Journal of The Electrochemical Society*, 169(6):064505, 2022. 94
- [121] M. Bernt, C. Schramm, J. Schröter, C. Gebauer, J. Byrknes, C. Eickes, and H. A. Gasteiger. Effect of the IrO_x conductivity on the anode electrode/porous transport layer interfacial resistance in PEM water electrolyzers. *Journal of The Electrochemical Society*, 168(8):084513, 2021. 94

Acknowledgments

This thesis was written during my work as a research assistant at the Bavarian Center for Applied Energy Research e.V. (ZAE Bayern), Department of Energy Storage in Garching, within the working group Electrochemical Energy Storage.

First and foremost, I would like to express my sincere thanks to Prof. Dr.-Ing. Andreas Jossen (Institute for Electrical Energy Storage Technology (EES) of the Technical University of Munich (TUM)), whose excellent supervision of my work was always very constructive and motivating. I particularly appreciated the numerous fruitful doctoral discussions about the progress of my research.

I would also like to thank Prof. Dr.-Ing. Hartmut Spliethoff for kindly taking over the co-evaluation of my thesis.

A big thank you goes to Dr. Matthias Rzepka for his always positive and friendly support at ZAE Bayern, always willing to listen to problems of any kind. I would also like to thank Dr. Holger Hesse for his support and advice on numerous issues and for his friendly integration into the Stationary Energy Storage team at the Chair of Electrical Energy Storage Technology.

Prof. Dr. Hubert A. Gasteiger deserves my special thanks for many in-depth discussions, highly valuable suggestions and the excellent collaboration on the publication on the long-term stack test. At the same time, I would like to thank Dr. Kay Bareiß, Dr. Cristina de la Rúa, Dr. Julius Knöppel and Dr. Serhiy Cherevko for their outstanding and very constructive collaboration on the respective joint publications.

Furthermore, I would like to thank my colleagues from the electrolysis team at ZAE Bayern and the Chair of Technical Electrochemistry (TEC), especially Dr. Maximilian Bernt, Dr. Jonas Schröter, Matthias Ernst, Matthias Kornherr and Carina Schramm, for the inestimably valuable exchange, numerous productive meetings, joint projects and the strong team spirit.

Special thanks go to my direct office colleagues at ZAE Bayern, Petra Dotzauer, Dr. Tobias Greese and Dr. Amadeus Teuffel, for the wonderful time over many years. The inspiring conversations, shared joy and, above all, the solidarity and support in difficult times have enriched my experience in the team.

Likewise, I want to thank all my direct cooperation partners from the Kopernikus projects as well as the German Federal Ministry of Education and Research and the Bavarian Ministry of Economic Affairs, Regional Development and Energy for their kind project funding.

Finally, there is a very special thanks to my family, my friends and especially my partner Kerstin for their great support during my doctoral studies. Their love, commitment and encouragement have always given me the strength to continue and finally complete my work.